UNIVERSITÀ DEGLI STUDI DELL'AQUILA

Department of Civil, Construction-Architectural and Environmental Engineering

DOCTORAL THESIS

Reduced-Order Models for Vibration Analysis, Parameter Identification and Passive Control of Civil Engineering Structures

Ph.D Course in Civil, Construction-Architectural and Environmental Engineering

XXXVIII cycle

Candidate
Andrea De Flaviis

SSD
CEAR-06/A

Course Coordinator
Prof. Federico De Matteis

Thesis Tutor
Prof. Daniele Zulli

Co-Tutors
Prof. Rocco Alaggio
Eng. Gianluca Di Francesco

May 15, 2026

Reduced-Order Models for Vibration Analysis, Parameter Identification and Passive Control of Civil Engineering Structures

Andrea De Flaviis

Prof. Daniele Zulli

Reviewers:

Alessandro Cabboi *Delft University of Technology*
Giuseppe Habib *Budapest University of Technology and Economics*

Reduced-Order Models for Vibration Analysis, Parameter Identification and Passive Control of Civil Engineering Structures

Andrea De Flaviis
Candidate ID number: 289590

Department of Civil, Construction-Architectural and Environmental Engineering- DICEAA
University of L'Aquila

 This thesis has been typeset by LaTeX and phdiceaa class.

Website: http://diceaa.univaq.it/

To what comes next.

[Blank page]

Acknowledgements

I would like to take a few lines to express my acknowledgments. I want to start by thanking Professor Daniele Zulli. I am honored to have been mentored by him. He has taught me so much over these years and has been the best guide I could have, and probably ever will have. I am deeply grateful to him for the knowledge he has passed on to me, for showing me what it means to work with professionalism, to truly believe in what one does, and to pursue one's own mission despite countless sacrifices. I am also grateful to him for never making me lose trust. I am sincerely grateful for all of this.

I am thankful to Professor Rocco Alaggio for his humanity, his expertise, and the true passion he brings to his experiments in the Laboratory.

I would like to express my gratitude to Professor Alireza Ture Savadkoohi for having guided me during my months in France, for everything he taught me, for his great kindness, and for his support. I would also like to thank the entire ENTPE community for the unforgettable memories.

I would like to thank the friends that I met in Dimensione Solare for welcoming me from the very first day and for the moments we shared.

Special thanks to Chiara, with whom I shared ambitions, hopes, disappointments, and new beginnings throughout a large part of our academic journey, and to Simona and Manuel for their valuable advice and for their support.

I also want to thank all those who have shared part of my academic journey, which is now coming to an end with this Thesis: to those who were there at the beginning, to those who accompanied me the longest, and to those I met at the end. Each of you has been part of this chapter of my life and has contributed to my growth.

A heartfelt thank you to my dear friends outside the university (all of you) for always being there and for bringing so many moments of joy and carefree happiness into my life.

I am grateful to my mother, my father, my brother and Giulia for always being there, for helping me in everyday life, and for giving me the peace I need. I know I can always count on you, and I am aware of the sacrifices you make and have always made, compared to which mine are nothing.

Finally, thanks to my love Giulia. For your boundless love, our laughter, and the bond we share. I could not wish for anything more.

[Blank page]

Abstract

Adequate mathematical models are essential for investigating the static and dynamic behaviors of structures; it would be useful to employ efficient models that require limited computational effort and can be readily adapted to address a wide range of problems. In the framework of civil engineering structures, almost all of them have one element in common: they are composed of beams. They are always present in bridges, either as main structural components or as secondary elements; furthermore, the largest part of buildings, both residential and industrial, is composed of beams (and columns as well), especially those constructed in reinforced concrete or steel. Thus, because of their central role in structures, different aspects of them are analyzed in the Thesis, investigating new features especially in nonlinear dynamics, with complementary points of view, but always aimed at a thorough understanding of the mechanical behavior.

Moreover, being the main purpose of the Thesis the development of efficient models to study linear and nonlinear systems, modeling aspects related to other types of structural elements are considered too, like cables and three-dimensional frames. For the former, a nonlinear model is used and the interaction of the cable with vortices that shed from its surface is investigated, whereas for the latter a model, based on the homogenization of the building to a Timoshenko beam, is used to get modal properties comparable with those experimentally found.

Consequently, reduced-order models are developed for the different types of structures, existing models are extended to incorporate new features and comparisons are made with results obtained from experimental data, when available, to validate the accuracy of the models and to test their limits. In general, each chapter of the Thesis corresponds to a main structural system – beams, cables or three-dimensional frames – where new problems are addressed and interesting findings are obtained in both linear and nonlinear fields, proving the importance of having models that are both simple and rigorous.

The main original contributions of the Thesis are in order of appearance: the comparison of analytical results, obtained for Thin-Walled Beams modeled through the Generalized Beam Theory, with those found on full-scale viaducts, the vibration control of this kind of beams using a Nonlinear Energy Sink, the introduction of a newly developed model-based procedure to identify parameters of nonlinear continuous systems, the extension of an analytical formulation for the suspended cable subjected to Vortex-Induced Vibrations using the Multiple Scale Method directly on the non-discretized equations and, finally, the implementation of some new features on the homogenization technique to model three-dimensional frames in order to compare their modal properties to those of full-scale buildings. The results reveal new and significant findings, and several additional aspects remain to be explored.

[Blank page]

Sommario

Avere a disposizione modelli matematici adeguati è una condizione necessaria per investigare il comportamento statico e dinamico delle strutture; sarebbe bene utilizzare modelli efficienti che richiedano un onere computazionale ridotto e che possano essere prontamente adattati per affrontare un'ampia gamma di problemi. Nell'ingegneria civile, quasi tutte le strutture hanno un elemento in comune: sono composte da travi. Queste sono sempre presenti nei ponti, o come componenti strutturali principali o come elementi secondari; in aggiunta, la maggior parte degli edifici, residenziali ed industriali, è composta da travi (e colonne ovviamente), soprattutto quelli in calcestruzzo armato o in acciaio. Quindi, visto il loro ruolo cruciale nelle strutture, diversi aspetti sono analizzati nella Tesi, investigando nuove peculiarità soprattutto in dinamica nonlineare, con punti di vista complementari, ma sempre rivolti ad una comprensione approfondita del comportamento meccanico.

Inoltre, essendo l'obiettivo principale della Tesi lo sviluppo di modelli efficienti per lo studio di sistemi lineari e nonlineari, sono considerati anche aspetti di modellazione per altri tipi di elementi strutturali, come cavi e telai tridimensionali. Per i primi, viene usato un modello nonlineare ed è investigata l'interazione del cavo con i vortici che si distaccano dalla sua superficie, mentre per i secondi viene usato un modello, basato sull'omogeneizzazione dell'edificio ad una trave di Timoshenko, per ottenere proprietà modali comparabili a quelle sperimentali.

Di conseguenza, si sviluppano modelli ridotti per i diversi tipi di strutture, si estendono modelli esistenti per incorporare nuove funzionalità e si fanno confronti con i risultati ottenuti da dati sperimentali, quando disponibili, per validare l'accuratezza dei modelli e testarne i limiti. In generale, ogni capitolo corrisponde ad un elemento strutturale principale – travi, cavi o telai tridimensionali – in cui si affrontano nuovi problemi e si ottengono risultati interessanti sia in campo lineare che nonlineare, dimostrando l'importanza di avere modelli che siano sia semplici che rigorosi.

I principali contributi originali della Tesi, così come compaiono nel testo, sono: il confronto dei risultati analitici, ottenuti per le travi a parete sottile modellate tramite la teoria generalizzata di trave, con quelli trovati su viadotti reali, il controllo delle vibrazioni di questo tipo di travi tramite l'uso di un Nonlinear Energy Sink, l'introduzione di una nuova procedura di identificazione parametrica basata sul modello per sistemi continui nonlineari, l'estensione di una formulazione analitica per il cavo sospeso soggetto a vibrazioni dovute al distacco dei vortici usando il metodo delle scale multiple direttamente sulle equazioni non discretizzate e, infine, l'implementazione di nuove funzionalità nella tecnica dell'omogeneizzazione per modellare telai tridimensionali al fine di confrontarne le proprietà modali con quelle di edifici reali. I risultati mettono in luce nuove e rilevanti evidenze, e molti aspetti restano da esplorare.

[Blank page]

Contents

[Blank page]

List of Figures

List of Tables

Introduction

This chapter introduces the main topic of the Thesis and provides the essential information to guide toward a clear and focused reading of the entire work. First, the motivations which pushed to investigate this subject are resumed together with the proposed goal, highlighting the existing link among the investigated problems. Then, the underlying approach followed throughout the entire study is described and properly motivated. Among civil engineering structures, beams, cables and three–dimensional frames are examined. For each structural type, the relevant aspects concerning modeling, monitoring, vibration control and parameter identification are addressed, depending on the context. The Introduction is closed with an index of the subsequent Chapters and a brief description of each of them.

1.1 Introduction

In latest decades a growing interest was born around the theme of monitoring of existing structures due to many reasons: one is without doubts the happening of some alarming collapses, that are starting to become more and more frequent, that moved the attention of citizens and industries on the topic of Structural Health Monitoring (SHM) making more urgent the need to keep an eye on those buildings, viaducts and bridges which were realized more than 40/50 years ago, in most of the cases in reinforced concrete (or pre-stressed reinforced concrete), which inevitably starts to show some symptoms of aging; another reason is that, at least in Italy, and probably in other countries too, national governments started to provide incentives to restore existing building, including the possibility of installing sensors to collect information from them [1],[2].

When dealing with monitoring of structures, the two principal approaches are the data-driven and the model-based ones. Data-driven approaches, which are quite common, rely on techniques such as Machine Learning or Artificial Neural Networks and are generally easier to implement, since they do not require the formulation of a physical model and have the merit of processing a big amount of data giving the user an equally big amount of information. However, the results which are obtained could be less easy to interpret and, in some cases, it could be tough to understand which of them has a real physical meaning and which ones have to be discarded. On the other hand, model-based approaches could be more complex to implement, since they require the development of a model which, in function of the complexity of the structure, could be more or less involving, but, at the end, results are easier to interpret and the model can be eventually modified, through the so-called model updating procedure, in order to make it as accurate as possible: this represents the preferred approach in the present work.

The most widespread models when talking about monitoring of civil structures are those based on Finite Element Analysis (FEA) which can be easily developed and updated using powerful commercial software. On the other hand, the main goal of this Thesis is the introduction of Reduced-Order Models (ROM), chosen in function of the structures under study, realized following other strategies, trying to obtain, whenever possible, analytical solutions in exact or approximate form, while models based on Finite Elements (FE) are here used is some cases as a means of comparison.

So, given that the models play a central role in the Thesis, they must be able to describe as accurately as possible the behavior of real structures, taking into account the assumptions introduced in each of them. Then, once they are built and proven effective for vibration analysis, they can be used for a range of applications: for SHM purposes in case experimental data are available, or to study the vibration control of structures when subjected to external dynamical loads, or they can be used to identify the parameters of a structure, developing strategies that can take as input experimental signals, helping to understand if something unexpected is happening. All this is done to have a wider vision of how these structures relate to the external world and to open different possibilities for future investigations.

Finally, peculiar aspects of SHM are addressed too, in the sense of periodic observation of structures and tracking of their health status, also discussing the possibility of updating the developed models to match the experimental outcomes and trying to understand, based on the acquired experience, the best sensors placement on them for future campaigns.

1.2 Motivations

This Thesis was born with the aim of giving a contribution to the big topic of SHM (in its most general sense), trying to develop and give answers to some of the uncountable topics of research developed by many scholars during the years. If one wants to present the main motivations behind this work, three main aspects can be detected:

- The need to extend existing and widespread studies on well-known problems to some new specific applications that were not already conceived or at least investigated, to further validate and disseminate them.

- The need to compare results found applying established theories on ROM with different orders of complexity (such as beams or three-dimensional frames) with experimental results, obtained, in most of the cases, in operational condition, without directly exciting the structure.

- The need to develop analytical procedures in place of purely numerical techniques to study complicated problems, to have a better understanding of the systems responses. This idea is the crucial one that motivated the whole research project, even when purely numerical methods would have been an easier way to go.

Furthermore, another classification of the motivations can be proposed by focusing on the four main areas that were investigated throughout the Thesis:

- The modeling, which forms the cornerstone of each chapter, since it is stressed that the main idea is to follow model-based approaches, being purely data-driven ones more immediate but also less controllable and more difficult to interpret.

- The monitoring, related to the previous point, realized when experimental data were available or when it was possible to produce them, comparing them with model results, making use algorithms that are able to track some key parameters of the structure, checking their variation over time to understand if some damage is present and how it evolves.

- The vibration control, realized in a passive way through the implementation of some specific devices in some key position of the structure (for beams and in perspective for cables), which can aid to reduce their vibrations in case of dynamic excitation.

- The parameter identification, both related to modeling and to monitoring, performed mixing analytical and numerical tools to retrieve important structure parameters based on the evolution of the system response over time.

1.3 Objectives

The objectives that this Thesis is aimed to reach, strictly related to the motivations which guided the work, can be summarized as follows:

- The development of analytical models, capable of giving results both in the static and in the dynamic fields, which are coherent with the real behavior of monitored structures, and which can be further refined with minor modifications. To reach this goal, such models are based on algorithms that are parametric, simple to use, modify and adapt, for the study of different types of structures.

- The introduction in the systems of some sources of nonlinearity, which can be representative of characteristics of the structures (common phenomena like the loss of pre-stress in pre-stressed concrete beams), accounted to obtain more realistic responses, or could be given by external devices having a specific role (e.g. vibration control).

- The implementation of procedures able to detect at least if defects or damages are present on a structure, with the idea, in future, to localize and quantify them and analyze their evolution.

- The understanding, based on the experience gained by comparing results offered by analytical models with experimental ones, if the type and the position of sensors used to monitor the status of beams and buildings is adequate or, if not, to provide some suggestions to better chose and locate them according to the need.

- The definition of strategies to reduce vibrations on structures in case of dynamic actions through reliable devices, in order to avoid the onset of damage or to limit its expansion if present.

In Fig. 1.1, the different aspects investigated throughout the Thesis are resumed: three main types of civil engineering structural systems, corresponding to the three main chapters of the Thesis, are identified as beams, cables and three-dimensional frames, and for each of them different topics are further explored as better explained in Sect. 1.5.

As previously highlighted, the underlying concept connecting the different chapters is the common starting point, consistently represented by tailored reduced-order models. Moreover, all the problems addressed in this Thesis clearly fall within the framework of structural dynamics, which therefore serves as the unifying thread throughout the work. In fact, all the developed models are suitable for investigating the linear dynamics of the corresponding structures, under both free and forced vibration conditions. At the same time, nonlinear dynamics is also considered in several contexts: in vibration control (through nonlinearities in the external control device), in parameter identification (accounting for geometric or material nonlinearities of the structure), and in the interaction between cables and wind action (involving a nonlinear structural model coupled with an additional nonlinear oscillator). Finally, experimental dynamics plays a significant role in the discussion of beams and three-dimensional frames within the framework of Operational Modal Analysis.

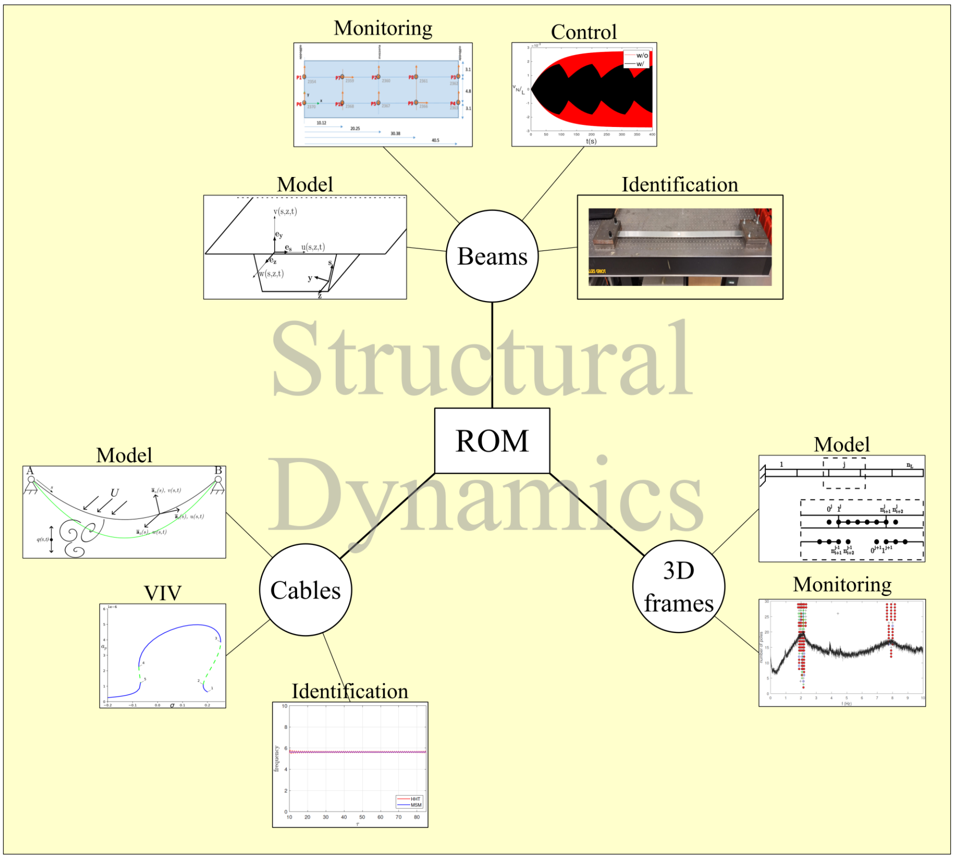

Figure 1.1. Schematic representation of the investigated topics.

1.4 Approach

As already mentioned, throughout all the Thesis, the main idea was to develop each problem in an analytical way trying to obtain closed-form solutions, even if approximated. At the same time, numerical approaches were not neglected: they were used to verify the analytical results and to ensure their consistency. Finally, FEA was used when necessary.

This approach went hand-in-hand with the central idea of this work, namely the preference for a model-based strategy to a complete data-driven procedure, which was limited to a secondary role, with the idea of studying problems that, even if apparently simple, could have been representative of a larger number of cases and easy to adapt. Among these analytical methods, a massive use was made of the Multiple Scale Method (MSM), a perturbation method sometimes applied on continuous problems which, through the introduction of different (time) scales, permits to find approximate yet really precise solutions.

Then, in addition to classical beam models like Euler-Bernoulli and Timoshenko ones, more refined theories, as Generalized Beam Theory (GBT), were implemented to get reduced order models able to describe complex phenomena; this one in particular was used to study beam viaducts having thin-walled cross-sections. On the other hand, to study the response of real dimension buildings, the homogenization procedure was used, through an equivalence between a three-dimensional frame and a Timoshenko beam.

Finally, experimental validation is provided for some of the investigated problems addressed in this Thesis. In particular, either previously acquired experimental data were used and processed for specific purposes, as in the case of Operational Modal Analysis (OMA), or new experimental campaigns were conducted, for example to validate the new proposed model-based identification procedure for the beams.

1.5 Organization

Beyond **Chapter 1**, where the subject of research is introduced, providing motivations, objectives and the approach, this Thesis is organized as follows.

In **Chapter 2**, a discussion of the current state of the art of the main topics covered in this work is given, dividing them by fields of application and trying to underline the current research gaps which were covered in the Thesis.

Chapter 3, which is the central chapter of the Thesis, starts by describing the behavior of Thin-Walled Beams (TWB) using the well known Generalized Beam Theory (GBT). More specifically, the variant known in literature as GBT with complete dynamic approach in cross-section analysis (GBT-D), is here extended to the dynamic case, also considering different configurations for the boundary conditions (b.c.). Then, the method is applied to a beam having dimensions of a full-scale pre-stressed concrete beam collecting static and dynamic results that are compared with those obtained from experimental data, the latter obtained applying algorithms from OMA. Then, for vibration control purposes, a Nonlinear Energy Sink (NES) is applied on the same beam, always modeled through GBT-D, to reduce its displacements under different load cases. Finally, a novel model-based procedure is proposed, based on the combination of the Multiple Scale Method (MSM) with the Hilbert-Huang Transform (HHT), to identify parameters of a nonlinear Euler-

Bernoulli beam, starting from signals which are either numerically-generated (for verification purpose) or experimentally acquired (for real cases).

In **Chapter 4**, always in the framework of one-dimensional continuous systems, the nonlinear model of suspended cable is recalled and free and forced dynamics is studied through MSM. Having as future scope the design and implementation of passive vibration strategies for wind-induced vibrations, the cable itself is analyzed under the action of Vortex-Induced Vibrations (VIV), developing its equations always through MSM and comparing results with those numerically found. Finally, the identification procedure developed for beams is applied here too, extending its range of application.

In **Chapter 5**, three-dimensional frames are studied. In particular, as in the previous sections, an analytical formulation, realized here through the homogenization procedure – which permits to treat the structure as an equivalent Timoshenko beam – is recalled and slightly modified to account for buildings having different mass and stiffness properties at each stage. The obtained natural frequencies and mode shapes are then compared to those found through OMA algorithms on existing buildings monitored by the company Dimensione Solare s.r.l. (where part of the PhD research was carried out). Data coming from the latter are used to track the modal properties over time and considerations on the updating of model parameters are made.

Finally, in **Chapter 6**, the main conclusions of the Thesis are drawn and ongoing and future research is discussed.

State of the art

This chapter presents the state of the art concerning the main topics addressed in this Thesis. It is organized into homogeneous sections, each devoted to a specific structural element and reflecting the structure of the subsequent chapters.

These sections are unified by the underlying themes that connect the entire work: the development of reduced-order models and the investigation of structural dynamics in its various facets.

First, beams are addressed starting from models, based on the Generalized Beam Theory, for the study of Thin-Walled Beams, moving to aspects related to system identification methods, both for modal properties and system parameters (a feature shared with the other chapters of this Thesis), to conclude with passive vibration control through nonlinear devices.

Then, cables are addressed, focusing on the topic of Vortex-Induced Vibrations and finally, three-dimensional frames are treated, with particular attention to analytical models developed through the homogenization procedure.

2.1 Introduction

This PhD Thesis primarily aims to develop and extend reduced-order models for the analysis of civil engineering structures like beams, cables, and three-dimensional frames, to study a wide range of topics, with a specific focus on their dynamic behavior: the modeling and subsequent analytical approach, together with the dynamic framework within which they are developed, constitute the common basis of all the subjects treated, as underlined in Sect. 1.3. Consequently, this chapter aims at giving to the reader a clear view of the current state of the art, highlighting the research gaps and questions arising from them, whose answers can be found through the Thesis.

2.2 Beams

In this section, beam-related problems in dynamics (linear, nonlinear, inverse, and experimental) are addressed within the framework of reduced-order modeling, with a view toward Structural Health Monitoring (SHM) applications ranging from the comparison of model results with experimental ones to the identification of parameters of nonlinear beams to the reduction of their vibrations through nonlinear devices.

2.2.1 Thin-Walled Beams

Thin-Walled Beams (TWB) are a widely used class of beams, whose main characteristic is to be made of elements having small thickness compared to the other section dimensions: they are undoubtedly very stiff and efficient in terms of load bearing capacity, but they can undergo non-negligible deformations both in-plane and out-of-plane. They are used in many fields from mechanics to aeronautics to civil engineering: just to cite a relevant example they are really common in bridges.

In order to correctly catch their behavior, adequate models have to be realized. A particularly widespread and valuable approach is the one based on the Generalized Beam Theory (GBT) introduced for the first time by Schardt in 1966 [119] and developed by the same author and Davies in the following years [120], [30], [31]: they established the main ideas like the concept of deformation modes (including warping components), studying different kinds of problems like beams with classical global restraints subjected to static loads or buckling analysis using Finite Differences or Finite Elements.

The work of Schardt and Davies sparked the interest of many scholars in this topic, and numerous subsequent studies were developed, aiming either to extend the original formulation to more complex problems or to modify the methodology adopted in certain steps. A fundamental contribution to the development of the GBT was given by the group of the Technical University of Lisbon and coworkers which investigated a really wide spectrum of problems. The starting and fundamental works of the group are those of Silvestre and Camotim [122], [123] that derived the equations of the problem for orthotropic materials for statics and for buckling analysis, where geometrically nonlinear terms were accounted too; moreover, they explained step by step how to obtain the deformation modes and how to solve the problems. Based on these initial works, other aspects were studied: for example in [124] a geometrically nonlinear formulation is developed to consider the post-buckling of isotropic TWB making use of FE, in [17] arbitrary support conditions, as punctual ones, are allowed in place of global ones (as better explained in the Thesis) and post-buckling is considered in [7]. Then, in [8] the free and forced dynamics of TWB is analyzed and the effectiveness of the method is proven also in this case. In [9] the procedure to obtain the deformation modes is improved and made automatic for different kind of sections. Finally, other works of the same group not directly cited here, are reported in the review [49].

In the meanwhile, the group of Luongo and Piccardo gave a massive contribution to the GBT since, through the so-called GBT-D, a new strategy was introduced to perform the first part of the theory – the so-called cross-section analysis – recalled and used in the Thesis. This new approach, used in works as [109], [105], [106], [38] simplifies the existing procedure, making the determination of deformation modes easier. Finally, the same group, or their coworkers, also investigated the case of beams showing a geometric nonlinear behavior as in [107] or used GBT to consider beams having a curvilinear cross-section as in [72].

Overall, GBT is a powerful reduced-order modeling strategy for beam-like structures such as TWB, overcoming the complexity of FE models and the simplifications of classical beam models like Euler-Bernoulli, Timoshenko, Vlasov which, above all, are not able to account for the deformations of the cross-section (in-plane and out-of-plane) that may occur on bridges and viaducts in some cases. In the Thesis a comparison is realized between models based on GBT-D, FE and Euler-Bernoulli to prove this statement.

Moreover, previous studies have not provided a direct comparison between results obtained from GBT models and experimental data for full-scale prestressed reinforced concrete girder bridges (where this model proves particularly well suited), considering both static load configurations and free-vibration dynamics. This validation would be fundamental in the context of SHM and could lead to future works regarding the updating of the GBT model, while its lack may raise questions about the capability of the model to represent realistic structural scenarios. Such a comparison is carried out in this Thesis, demonstrating the reliability of the model even in cases where classical beam models fail (e.g., under nonsymmetric static load configurations). Furthermore, while the ability of GBT models to account for punctual restraints has already been established, it remains unclear whether the same holds for GBT-D models: this Thesis investigates this aspect as well.

2.2.2 System identification methods

The identification of parameters of structures can be traced back to the resolution of the inverse problem [43], i.e. to the identification of the characteristics of the dynamical system once its response is known. The literature is rich about the identification of the modal properties of linear dynamical systems, for example in terms of Operational Modal Analysis (OMA), where structures are not directly excited. Here, the main distinguishing factor is between techniques operating in frequency domain, as established by Brinker et al. in [13], or in time domain as introduced in [135] and recalled in works as [103], [114]. A comprehensive list of papers including also other techniques is reported in [54] (focusing on bridges), while some particularly interesting applications may be found in [86] on an arch bridge where the modal properties are automatically obtained through a cluster algorithm, in [16] where further improvements were introduced with tracking purposes or in [3] where the case study is represented by a masonry church.

On the other side, many scholars have also focused themselves on the parameter identification of nonlinear dynamical systems [143]. Since the studies of Ibáñez [58], many other contributions started to appear, some of which are collected in the reviews [64], [97]. Among them, the SINDy algorithm was recently developed by Brunton et al. [15] following a data-driven approach based on a sparse regression, which allows to identify the coefficients of previously defined nonlinear functions and thus to reconstruct the nonlinear dynamical system [14]. Some applications can be found in [25], [98], [116] proving its effectiveness.

Then, among the different signal processing techniques, the Hilbert-Huang Transform (HHT) [55] has been used by many for identification purposes, in a data-driven or model-based approach, as resumed in [21] where the applications are aimed at monitoring the health status of structures or their components, or in [117] where HHT is used to detect damages on bridges under traveling loads. More recently, Scozzese and Dall'Asta used it for the parameter identification of post-tensioned beams with a bilinear elastic force-displacement constitutive relationship [121]. A really important work by Kerschen et al. [65] combines the HHT with the Complexification-Averaging Method to identify parameters of discrete nonlinear systems. Moreover, other uses of the HHT with the same aim are made in [101] in combination with a perturbation method, in [99], [100] with the concept of nonlinear modal analysis and in other works as [37].

Focusing on parameter identification, in all the previous cases, discrete (or discretized) systems were considered, without directly working on the continuous systems and this opens up a research direction that the present Thesis aims to address. In fact, it is known from literature that an a priori discretization of a continuous problem (e.g. through Galerkin's method) can lead to erroneous results, especially for systems with quadratic and cubic nonlinearities or presenting internal resonances as shown in [94], [113], [85] [52]. Thus, a central research question addressed in this work is whether a model-based identification procedure can be proposed for nonlinear continuous systems (beams and cables in particular) by applying the Multiple Scale Method directly to the continuous (non-discretized) equations; this was done in the Thesis combining the MSM with the HHT obtaining valuable findings. The introduction of such a method can be seen as a valid alternative to the existing ones and may open the way to further studies in the framework of SHM as in the detection and quantification of damage on beams.

2.2.3 Vibration control

Vibration control is a key topic in civil engineering, particularly in bridges, where vibrations generated by various sources, such as vehicles, wind, or earthquakes, can reach excessive amplitudes, making it necessary to implement appropriate mitigation systems. In particular, passive vibration control, which does not require an external source of power, was studied by many, starting from the patent of Frahm [41]. First, Tuned Mass Damper (TMD), made of a mass, a linear spring and a dashpot, started to be used and some applications can be found in works as [32], [59], [42], [44], [138], [6], [20] which prove its effectiveness.

However, this kind of device also presents some drawbacks, above all the necessity to be tuned to a specific frequency, meaning that its effectiveness in reducing vibrations significantly decreases when the excitation frequency deviates from the tuned value. For these reasons, nonlinear devices were introduced and realized in the meanwhile, starting from the work of Roberson [115] which introduced the cubic term in the spring.

The devices that originate from this concept are commonly referred to as Nonlinear Energy Sinks (NES). The principal difference with respect to Tuned Mass Dampers is that the stiffness is nonlinear ([69], [85], [95], [102], [142]) and it cannot be linearized (so it does not present linear terms) and this allows to act on a wider range of frequencies. The most studied and widespread ones are those having cubic nonlinearity as in [46], [45], [47], [127] [128], [77], [79], [151], [136], [134] with experimental validation too [89]. However, other types of nonlinearities can be realized, like non-smooth behaviors, nonlinearities due to impact, negative stiffness, presence of nonlinear damping as reported in [50], [71], [56], [57], [24], [33], [26], [118], [132], [92].

Among these works, a certain number focuses on continuous systems like beams as [48], [74], [149], strings as [80], [150] and cables as [140]. However, it was observed that the use of NES on box-girder bridge decks, considered as TWB, has not yet been addressed in the literature. Consequently, part of this Thesis is devoted to modeling the interaction between such a beam, modeled using the previously introduced GBT-D, with the NES, in order to evaluate whether and to what extent an attached nonlinear device can reduce vibrations under different loading conditions, with the ultimate goal of extending the beam service life; equations are developed making use of the Complexification-Averaging Method (Cx-A). Modeling the beam with GBT is necessary to account for specific load distributions and to capture resonances involving mixed modes, which cannot be identified using simpler theories.

2.3 Cables

In this section, wind-related problems on cables are addressed. In particular, after an overview of modeling aspects related to the cables themselves, their interaction with wind – specifically Vortex-Induced Vibrations (VIV), which involve complex nonlinear dynamic phenomena – is analyzed. This phenomenon can produce significant oscillations in cable structures, making it essential to understand how to model it effectively.

2.3.1 Cable models

One of the first works on vibrations of suspended cables is the one of Irvine and Caughey [60] which then found expression in what can be considered as a milestone of the study of cables in civil engineering, i.e. the book from Irvine [61], which provided one of the first and most complete treatments on cables modeling.

In the same years, other brilliant researchers dealt with cable-related problems in linear and nonlinear dynamics. An example is the work of Rega and Luongo [112] which studied the free dynamics of cables having flexible supports or [82], [83] where Luongo, Rega and Vestroni considered the nonlinear behavior of suspended cables, making the problem discrete and solving the equations through the Multiple Scale Method (MSM).

Significant contributions were given by Benedettini in many works among which [10] where the coupling between the in-plane and out-of plane motions is considered for cables showing high amplitude oscillations and [11] where a four-degrees-of-freedom system is used to account for internal resonances in both cases using the MSM to develop the discretized equations. Other interesting applications can be found in [104] where one support oscillates in the tangential direction resulting in parametric excitation and in [70] where the flexural stiffness is considered too for cables showing flexural curvature.

An extended review of nonlinear vibrations of suspended cables, accounting both for modeling aspects and bifurcation analyses, is realized in [111], [110]. In addition to the cited works, in recent times, two valuable references are the books [78], [69], where the governing equations for many kinds of beams and cables are derived following rigorous approaches: these works contain the information to properly realize many cable models. The model of cable used in this Thesis is based on the aforementioned references.

2.3.2 Vortex-Induced Vibrations

Wind-induced cable vibrations are classified in [62] as Vortex-Induced Vibrations, Rain-Wind-Induced Vibrations and galloping (of dry, ice and wake type): there, a selection of representative works is cited to provide a general overview of the current state of the art on the topic. Among the aforementioned phenomena, the topic of Vortex-Induced Vibrations (VIV) is analyzed in the Thesis, with the future goal of reducing the cable vibrations due to wind.

The problem of a structure subjected to VIV, which is a phenomenon that affects bodies immersed in a fluid due to fluid-structure interaction, is usually considered from an analytical point of view introducing the so-called wake oscillator: a non-linear (van der Pol) oscillator which has to account for the action of the wind and which was interpreted in many ways by different scholars [129]. The first work on the topic was from Hartlen and Currie [53] which studied a rigid cylinder giving to the wake oscillator the meaning of the fluctuating lift coefficient acting on the structure. Building upon this work, many subsequent studies have been developed as [125] which added the so-called stall term in the model, limiting the system response (damping term), based on the observations made in [130]. Moreover, a relevant work is the one of Kim and Perkins [67] where a flexible cable was studied and a drag model was adopted in addition to the lift one (since the out-of-plane behavior of the cable was considered too) and the two wake oscillators are considered as coupled or uncoupled, making use of the Multiple Scale Method (MSM), applied on the discretized problem. In addition, the work of Facchinetti et al. [35] constitutes a reference in the study of VIV, giving proven values for the experimental parameters. On the other side, Tamura and coworkers give a different meaning to the parameters involved as explained for example in [129], while in [126], [144], [147], [66] considerations are made on peculiar aspects about long cables as the need to consider higher vibrations modes, the presence of multimodal vibrations, the reduction of modal damping and the presence of traveling waves; some of these phenomena were also experimentally found [22], [23].

Other valuable works on VIV, involving cables or other kind of structures, are [137], [139] where marine risers are studied, [91] for a tethered sphere, [145] where a procedure is introduce to identify the experimental parameters and [93] where wind is effectively considered as a random action. Finally, in [90], [27], [148] the vibrations are controlled through nonlinear devices.

Many of the previous works share a common feature: the investigation of VIV through the wake oscillator approach, applied to different types of structures immersed in air or water. However, when the focus is on cables, they are typically modeled either as Euler–Bernoulli beams or, when explicitly treated as cables, the governing equations are discretized beforehand. Since an a priori discretization may lead to misleading results, as already discussed in Sect. 2.2.2, especially for systems with quadratic and cubic nonlinearities like the one at hand, the present work aims to propose a complete analytical procedure based on the application of the MSM directly to the continuous equations of a suspended cable subjected to VIV. This study is conceived as the first step of a broader research effort, whose ultimate goal is to mitigate cable vibrations through appropriate devices (such as those introduced in Sect. 2.2.3), thereby extending the service life of cables and, consequently, of the structures connected to them.

2.4 Homogenized models for three-dimensional frames

In this Thesis, also driven by industrial interests, three-dimensional frames are modeled with reduced-order approaches, alternative to classical FE models, with the aim of investigating the linear free dynamic properties of buildings; in addition, experimental dynamics is investigated within the framework of OMA. The present section focuses on the state of the art concerning the first of these two aspects, with particular emphasis on modeling strategies based on the homogenization procedure.

Models describing the response of three-dimensional frames are generally developed using the Finite Element Method, as it allows complex structural features to be accurately represented and provides reliable approximations of displacements and internal forces throughout all structural elements. However, when the structure under investigation consists of elements which are regularly repeated along the building height, alternative approaches may be adopted. One such approach is the so-called homogenization procedure, through which an equivalent yet simpler model of the three-dimensional frame is realized, while still enabling the evaluation of the structural response of the original frame based on the homogenized representation.

The literature on homogenization techniques is vast, owing to the wide range of applications spanning from metamaterials and periodic composites to structural engineering, wave propagation problems, and multi-scale modeling of complex media. This broad applicability has led to the development of numerous theoretical and computational approaches, tailored to different physical contexts and scales of interest. In this section the most recent contributions, relevant to the present study, are reviewed, with particular attention to works in which multi-frame structures are modeled and compared to equivalent beam representations.

In [108] a 3D Timoshenko beam is used to describe the building response, while in [28] a nonlinear shear-shear-torsional beam model is proposed. In [29], [40] attention is turned on the micro-scale and on the out-of-plane deformability (warping) of the cross-section of the equivalent beam. Then, in [81] the shear-shear-torsional beam model is considered in presence of earthquake and with multiple sources of damping, with particular attention to how the mass of the top floor is accounted for.

The chapter of the Thesis devoted to three-dimensional frames pursues two main objectives. The first is to employ a reduced-order model for periodic structures to describe the linear free dynamics of a structure having the properties of a full-scale building. To achieve this in a rigorous manner, one main feature is introduced: the possibility of assigning different properties to each story, accounting for variations in stiffness and/or mass distribution from one level to another, in order to represent the real structure more accurately. The second objective is to compare the resulting model with experimental results obtained through OMA on the full-scale building, with the future idea of enabling model updating which, if realized, would represent a novelty, since model updating techniques typically rely on FE models.

Beams

Beams are studied in this Chapter with the goal of developing a Reduced-Order Model (ROM) whose results are akin to experimental ones, and to properly control the amplitude of their vibrations; another goal is the establishment of an identification procedure based on another nonlinear beam model to get system parameters from experimental data. Thin-Walled Beams, like those often used in prestressed reinforced concrete girder bridges, are first investigated, applying a reduced order model based on the Generalized Beam Theory (GBT) able to catch the deformation of the cross-section in and out-of-plane. The static and dynamic responses are studied, considering different types of boundary conditions and comparing results to those obtained through a FE model implemented on a commercial software. Results are then compared to those collected on a full-scale beam in a previous campaign on existing bridges through Operational Modal Analysis (OMA) and to those found with an Euler-Bernoulli beam model, highlighting the inaccuracy of the latter to correctly describe the behavior of this kind of beams. Then, vibrations of the TWB are controlled through a Nonlinear Energy Sink (NES) considering different load cases which can act on the bridge, among which vehicles and earthquake. Finally, always in the framework of beams, the parameters of a nonlinear Euler-Bernoulli beam are identified introducing a new procedure which combines the Multiple Scale Method (MSM) with the Hilbert-Huang Transform (HHT) and the procedure is experimentally validated. Conclusions and future developments are resumed at the end of the chapter.

3.1 Introduction

Beams are fundamental structural elements in uncountable applications of civil engineering like buildings, bridge decks, large roofs and so on. For this reason, it is fundamental to have a deep knowledge of their behavior and to be able to predict and govern their reaction in static and dynamic conditions. This is the largest and most important chapter of the Thesis, highlighting once again the importance of this topic.

In particular, this chapter is divided as follows: first, a model based on the Generalized Beam Theory with complete dynamic approach in cross-section analysis (GBT-D) is introduced to accurately describe Thin-Walled Beams (TWB) and some applications are realized; some features already used in other GBT models are implemented for GBT-D, like the study of dynamical problems and the possibility to consider punctual support conditions, which could be, in some cases, more representative of the real situation. An existing beam viaduct is modeled through GBT-D and its results are collected both in statics and in dynamics, with the goal of comparing them to experimental findings.

Next, results obtained in a previous monitoring campaign on an existing viaduct, both in statics (static load tests) and in dynamics (vibrations recorded in operational conditions processed through well-known OMA algorithms in time and in frequency domains) are compared to those furnished by the model showing good agreement.

Subsequently, a new application is shown, with the TWB equipped with a cubic nonlinear device (Nonlinear Energy Sink, NES) to control its vibrations: first, generic harmonic loads are applied and then, the response under more realistic loading scenarios for bridges in operational conditions is also evaluated, e.g. the regular transit of vehicles on the bridge or the seismic action, discussing the efficiency of this device on this type of structure.

The last section of the chapter is focused on a novel procedure to identify the parameters of nonlinear discrete and continuous systems: in particular, it combines the Hilbert-Huang Transform (HHT) and the Multiple Scale Method (MSM) with the aim of realizing a model-based identification procedure. It is tested on discrete nonlinear systems before and on a nonlinear Euler-Bernoulli beam later, paving the way to new interesting applications. At the end, main results, novelties and future aspects related to beams are resumed.

3.2 Model

Bridge viaducts are usually made of slender elements, better known as Thin-Walled Beams (TWB). Besides being slender (in the longitudinal direction), their cross-section is made of thin elements, as suggested by the name, in order to optimize their load bearing capacity without increasing their weight. However, this aspect implies that these beams can undergo some phenomena that cannot be taken into account by simpler beam theories. For example, starting from models which generates from the de Saint-Venant theory, the Euler-Bernoulli model does not account for shear deformations, implying that the cross-section has to remain orthogonal to the beam axis, while the Timoshenko beam admits shear deformations but, as is the case for the previous one, does not consider the deformation of the cross-section in its own plane. Finally, the Vlasov model is richer, admitting a variable warping along the beam axis (due to a non-uniform torsion) but is not yet able to conceive the distortional deformation of the cross-section.

For these reasons, with the idea of studying a TWB subjected to different static and dynamical loads, which can act in a symmetric or non-symmetric way, a Reduced Order Model (ROM) based on the well-known Generalized beam Theory (GBT) is introduced. More specifically, the GBT-D version is here used and extended to dynamics and to the case of beams with non-classical restraints.

3.2.1 Formulation

The beam investigated in this section is a simply supported elastic beam with an initial length L and a boxed cross-section shown in Fig. 3.1: it is representative of one span of a bridge, where the hypotheses is made that the deformation effect of the pillars is negligible and that the spans are completely independent between each other. This model could be considered representative of a full-scale pre-stressed reinforced concrete beam; the type of restraint is investigated in more detail in the following, while at this stage it is sufficient to state that the beam is simply supported.

To introduce GBT-D (but in general for GBT), it has to be stated that, adopting the classical nomenclature, the displacement field of the beam can be written as a linear combination of pre-determined "deformation modes" which only depend on the curvilinear abscissa of the element of the cross-section (s in Fig. 3.1), with

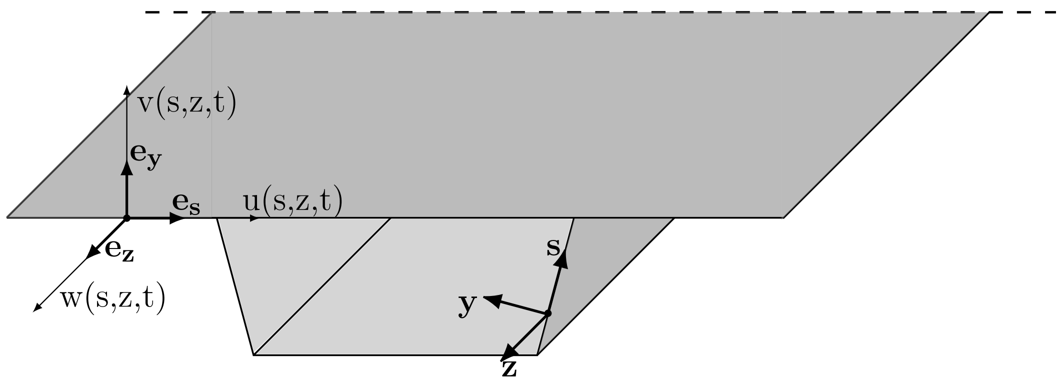

Figure 3.1. Cross-section of the TWB with displacement field.

unknown "amplitude functions", which depend on the axial coordinate z and eventually on time t. In this way, a problem which is inherently three-dimensional is transformed into a one-dimensional one, with z as the only variable, thus the definition of ROM. As it will become clear later, deformation modes do not coincide with vibration modes of the beam, since the first ones describe the deformation of the cross section and are independent on the type of analysis (i.e. they are common to static, dynamic, buckling problems), while the second ones are obtained studying the free dynamics of the beam, capturing its full behavior along both the cross-sectional and longitudinal directions (thus the definition of doubly modal representation given in [8] which is recalled in the following).

To understand how the reduction is made, the two main phases of GBT have to be introduced: the first and fundamental phase of the procedure is the cross-section analysis, where the deformation modes are obtained, while the second one is the member analysis, where the equilibrium equations are solved to get the amplitude functions which allows to completely determine the solution: both are described in the following. The main difference of GBT-D with respect to the classical GBT is about the first phase, namely on the determination of the deformation modes.

With reference to Fig. 3.1, s, y and z are the tangential, transversal and axial, or longitudinal, coordinates respectively of the different elements of the section and $u(s,z,t)$, $v(s,z,t)$ and $w(s,z,t)$ are the associated displacements on the middle surface (measured in m) written as:

$$\mathbf{u}(s,z,t) = u(s,z,t)\mathbf{e}_s(s) + v(s,z,t)\mathbf{e}_y(s) + w(s,z,t)\mathbf{e}_z(s) \tag{3.1}$$

being $(\mathbf{e}_s, \mathbf{e}_y, \mathbf{e}_z)^T$ the standard basis. Based on Eq. (3.1), the displacement of a point in the thickness of a generic element can be written, considering the Kirchhoff plate model, as:

$$\mathbf{d}_y(s,y,z,t) = (d_s(s,y,z,t)\ d_y(\ldots)\ d_z(\ldots))^T = (u - yv_{,s}\ v\ w - yv_{,z})^T \tag{3.2}$$

where the comma is used here to indicate the derivative with respect to s or z.

Writing the displacement field of Eq. (3.1) through linear combinations of known (to be determined) deformation modes $\bar{u}_k(s)$, $\bar{v}_k(s)$, $\Omega_k(s)$ and $\bar{w}_j(s)$ and unknown amplitude functions $\varphi_k(z,t)$ and $\Psi_j(z,t)$, one gets:

$$\begin{aligned} u(s,z,t) &= \sum_{k=1}^{K} \bar{u}_k(s)\varphi_k(z,t) = \bar{\mathbf{u}}^T(s)\boldsymbol{\varphi}(z,t) \\ v(s,z,t) &= \sum_{k=1}^{K} \bar{v}_k(s)\varphi_k(z,t) = \bar{\mathbf{v}}^T(s)\boldsymbol{\varphi}(z,t) \\ w(s,z,t) &= \sum_{k=1}^{K} \Omega_k(s)\varphi'_k(z,t) + \sum_{j=1}^{J} \bar{w}_j(s)\Psi_j(z,t) = \boldsymbol{\Omega}^T(s)\boldsymbol{\varphi}'(z,t) + \bar{\mathbf{w}}^T(s)\boldsymbol{\Psi}(z,t) \end{aligned} \tag{3.3}$$

where K represents the maximum number of conventional and extensional modes, while J is the maximum number of shear modes (their meaning is explained in a few lines). It is assumed that $\boldsymbol{\varphi}$ and $\boldsymbol{\Psi}$ have physical dimensions of a length, while $\bar{\mathbf{u}}$, $\bar{\mathbf{v}}$ and $\bar{\mathbf{w}}$ are non-dimensional and $\boldsymbol{\Omega}$ is a length too. Moreover, in the last equation, the first derivative with respect to z on $\boldsymbol{\varphi}$ is due to the hypothesis of null membrane shear strains (introduced in the aftermath) [105]. Finally, $\bar{u}_k(s)$ and $\bar{v}_k(s)$ are the in-plane components, while $\Omega_k(s)$ and $\bar{w}_j(s)$ are out-of-plane ones.

Before going on, it is necessary to give some more details in order to clarify the different nature of deformation modes. To do that, using a classical nomenclature, "natural nodes", i.e. those in correspondence of crossings of different branches of the section and those in correspondence of free ends are distinguished from "intermediate nodes", i.e. those included between natural nodes (descending from a certain discretization of the element): it should be noted that this distinction for GBT-D is just a formality, while in classical GBT is necessary to correctly determine deformation modes. Given that, three main groups can be defined:

- Conventional modes: the fundamental group respecting the 2 Vlasov's hypotheses of membrane inextensibility in the tangential direction $\varepsilon_s^m = 0$ and membrane shear indeformability $\gamma_{zs}^m = 0$; this latter becomes $\gamma_{zs}^m = const$ stepwise for closed loops following the Bredt's theory (the deformation components are introduced in a few lines). This group is characterized by both in-plane and out-of-plane components and, inside it, another classification can be made distinguishing "rigid modes", which, how suggested by their name, are such that the cross-section remains undeformed: they are the Vlasov's modes, i.e. three translations (two flexures and one extension) and one rotation (torsion); "distortional modes" for which the natural nodes show in-plane displacement and "local modes" for which the intermediate nodes show flexural displacement (as written before, except for rigid modes, this further classification is more important in the classical GBT). This group of deformation modes can be sufficient to describe a lot of phenomena, as shown later on.

- Extensional modes: in this case the inextensibility condition previously imposed is removed, thus one gets a set of purely in-plane modes, orthogonal to the previous ones. This group of deformation modes is necessary if one wants to consider a nonlinear behavior of the TWB, where membrane and flexural behavior are coupled, while they can have a minor effect in linear problems.

- Shear modes: also known as warping modes, they are purely out-of-plane, and they are fundamental when dealing with short beams that may suffer the phenomenon of shear lag.

Other details about the nature, number and importance of the different deformation modes can be found in Sect. 3.2.2.

From the displacement field of Eq. (3.3), the strain field, with axial and shear strain components (ε and γ respectively), with membrane and flexural components (superscripts m and f respectively), can be written as:

$$\begin{pmatrix} \varepsilon_s^m \\ \varepsilon_z^m \\ \gamma_{zs}^m \\ \varepsilon_s^f \\ \varepsilon_z^f \\ \gamma_{zs}^f \end{pmatrix} = \begin{pmatrix} u_{,s} \\ w_{,z} \\ u_{,z} + w_{,s} \\ -yv_{,ss} \\ -yv_{,zz} \\ -2yv_{,sz} \end{pmatrix} = \begin{pmatrix} \bar{\mathbf{u}}'^T \boldsymbol{\varphi} \\ \boldsymbol{\Omega}^T \boldsymbol{\varphi}'' + \bar{\mathbf{w}}^T \boldsymbol{\Psi}' \\ \left(\bar{\mathbf{u}}^T + \boldsymbol{\Omega}'^T\right) \boldsymbol{\varphi}' + \bar{\mathbf{w}}'^T \boldsymbol{\Psi} \\ -y\bar{\mathbf{v}}''^T \boldsymbol{\varphi} \\ -y\bar{\mathbf{v}}^T \boldsymbol{\varphi}'' \\ -2y\bar{\mathbf{v}}'^T \boldsymbol{\varphi}' \end{pmatrix} \tag{3.4}$$

Then, a linear elastic behavior is considered in order to write the active plane stress vector, where E is the Young modulus (in N/m^2), G is the shear modulus (in N/m^2), ν is the Poisson's ratio and σ and τ are the axial and shear components respectively:

$$\begin{pmatrix} \sigma_s^m \\ \sigma_z^m \\ \tau_{zs}^m \\ \sigma_s^f \\ \sigma_z^f \\ \tau_{zs}^f \end{pmatrix} = \begin{bmatrix} E & 0 & 0 & 0 & 0 & 0 \\ 0 & E & 0 & 0 & 0 & 0 \\ 0 & 0 & G & 0 & 0 & 0 \\ 0 & 0 & 0 & \frac{E}{1-\nu^2} & \frac{\nu E}{1-\nu^2} & 0 \\ 0 & 0 & 0 & \frac{\nu E}{1-\nu^2} & \frac{E}{1-\nu^2} & 0 \\ 0 & 0 & 0 & 0 & 0 & G \end{bmatrix} \begin{pmatrix} \varepsilon_s^m \\ \varepsilon_z^m \\ \gamma_{zs}^m \\ \varepsilon_s^f \\ \varepsilon_z^f \\ \gamma_{zs}^f \end{pmatrix} = \begin{pmatrix} E\bar{\mathbf{u}}'^T\boldsymbol{\varphi} \\ E\left(\boldsymbol{\Omega}^T\boldsymbol{\varphi}'' + \bar{\mathbf{w}}^T\boldsymbol{\Psi}'\right) \\ G(\bar{\mathbf{u}}^T + \boldsymbol{\Omega}'^T)\boldsymbol{\varphi}' + G\bar{\mathbf{w}}'^T\boldsymbol{\Psi} \\ -\frac{yE}{1-\nu^2}\left(\bar{\mathbf{v}}''^T\boldsymbol{\varphi} + \nu\bar{\mathbf{v}}^T\boldsymbol{\varphi}''\right) \\ -\frac{yE}{1-\nu^2}\left(\nu\bar{\mathbf{v}}''^T\boldsymbol{\varphi} + \bar{\mathbf{v}}^T\boldsymbol{\varphi}''\right) \\ -2yG\bar{\mathbf{v}}'^T\boldsymbol{\varphi}' \end{pmatrix} \tag{3.5}$$

The equations of motion in terms of the amplitude functions can be derived in a weak form using either the Principle of Virtual Work or the Hamilton's Principle in a variational way; the latter reads as:

$$\delta\mathcal{H} = \int_{t_1}^{t_2} \left(\delta\mathcal{T} - \delta\mathcal{U}_e - \delta\mathcal{U}_l\right) dt = 0 \tag{3.6}$$

subjected to the following condition on the generalized displacements at the extreme time instants t_1 and t_2 (represented by the operator δ):

$$\delta\boldsymbol{\varphi}\left(z, t_1\right) = \delta\boldsymbol{\varphi}\left(z, t_2\right) = 0 \tag{3.7}$$

$$\delta\boldsymbol{\Psi}\left(z, t_1\right) = \delta\boldsymbol{\Psi}\left(z, t_2\right) = 0 \tag{3.8}$$

The term $\mathcal{U}_e$ is the elastic potential energy, which can be written as:

$$\mathcal{U}_e = \frac{1}{2}\int_{\mathcal{V}} \boldsymbol{\sigma}^T\boldsymbol{\varepsilon} d\mathcal{V} = \frac{1}{2}\int_{\mathcal{V}} \left(\sigma_s^m\varepsilon_s^m + \sigma_z^m\varepsilon_z^m + \tau_{zs}^m\gamma_{zs}^m + \sigma_s^f\varepsilon_s^f + \sigma_z^f\varepsilon_z^f + \tau_{zs}^f\gamma_{zs}^f\right) d\mathcal{V} \tag{3.9}$$

where $\mathcal{V}$ indicates the total volume of the beam and $d\mathcal{V} = dsdydz$. Substituting Eq. (3.4) and Eq. (3.5) inside Eq. (3.9), the following expression is obtained:

$$\begin{aligned} \mathcal{U}_e = \frac{1}{2}\int_z & \left[\boldsymbol{\varphi}^T\mathbf{B}^e\boldsymbol{\varphi} + \boldsymbol{\varphi}''^T\left(\mathbf{C}^a_{\Omega\Omega}\boldsymbol{\varphi}'' + \mathbf{C}^a_{\Omega W}\boldsymbol{\Psi}'\right) + \boldsymbol{\Psi}'^T\left(\mathbf{C}^a_{W\Omega}\boldsymbol{\varphi}'' + \mathbf{C}^a_{WW}\boldsymbol{\Psi}'\right)\right. \\ & + \boldsymbol{\varphi}'^T\left(\mathbf{D}^s_{\Omega\Omega}\boldsymbol{\varphi}' + \mathbf{D}^s_{\Omega W}\boldsymbol{\Psi}\right) + \boldsymbol{\Psi}^T\left(\mathbf{D}^s_{W\Omega}\boldsymbol{\varphi}' + \mathbf{D}^s_{WW}\boldsymbol{\Psi}\right) + \boldsymbol{\varphi}^T\mathbf{B}^f\boldsymbol{\varphi} \\ & \left. + \boldsymbol{\varphi}''^T\mathbf{D}^f\boldsymbol{\varphi} + \boldsymbol{\varphi}^T\mathbf{D}^{f^T}\boldsymbol{\varphi}'' + \boldsymbol{\varphi}''^T\mathbf{C}^f\boldsymbol{\varphi}'' + \boldsymbol{\varphi}'^T\mathbf{D}^t\boldsymbol{\varphi}'\right] dz \end{aligned} \tag{3.10}$$

where the stiffness matrices are:

$$\begin{aligned} \mathbf{C}^f &= \int_{\mathcal{C}} \frac{Eh^3}{12\left(1-\nu^2\right)}\bar{\mathbf{v}}\bar{\mathbf{v}}^T ds, \\ \mathbf{C}^a &= \begin{bmatrix} \mathbf{C}^a_{\Omega\Omega} & \mathbf{C}^a_{\Omega W} \\ \mathbf{C}^a_{W\Omega} & \mathbf{C}^a_{WW} \end{bmatrix} = \begin{bmatrix} \int_{\mathcal{C}} Eh\boldsymbol{\Omega}\boldsymbol{\Omega}^T ds & \int_{\mathcal{C}} Eh\boldsymbol{\Omega}\bar{\mathbf{w}}^T ds \\ \int_{\mathcal{C}} Eh\bar{\mathbf{w}}\boldsymbol{\Omega}^T ds & \int_{\mathcal{C}} Eh\bar{\mathbf{w}}\bar{\mathbf{w}}^T ds \end{bmatrix} \end{aligned} \tag{3.11}$$

$$
\begin{aligned}
&\mathbf{D}^f = \int_{\mathcal{C}} \frac{\nu E h^3}{12\left(1-\nu^2\right)} \bar{\mathbf{v}} \bar{\mathbf{v}}''^T ds, \quad \mathbf{D}^t = \int_{\mathcal{C}} \frac{G h^3}{3} \bar{\mathbf{v}}' \bar{\mathbf{v}}'^T ds \\
&\mathbf{D}^s = \begin{bmatrix} \mathbf{D}^s_{\Omega\Omega} & \mathbf{D}^s_{\Omega W} \\ \mathbf{D}^s_{W\Omega} & \mathbf{D}^s_{WW} \end{bmatrix} \\
&= \begin{bmatrix} \int_{\mathcal{C}} Gh \left(\mathbf{\Omega}'^T + \bar{\mathbf{u}}^T\right)^T \left(\mathbf{\Omega}'^T + \bar{\mathbf{u}}^T\right) ds & \int_{\mathcal{C}} Gh \left(\mathbf{\Omega}'^T + \bar{\mathbf{u}}^T\right)^T \bar{\mathbf{w}}'^T ds \\ \int_{\mathcal{C}} Gh \bar{\mathbf{w}}' \left(\mathbf{\Omega}'^T + \bar{\mathbf{u}}^T\right) ds & \int_{\mathcal{C}} Gh \bar{\mathbf{w}}' \bar{\mathbf{w}}'^T ds \end{bmatrix}
\end{aligned} \tag{3.12}
$$

$$
\mathbf{B}^f = \int_{\mathcal{C}} \frac{E h^3}{12\left(1-\nu^2\right)} \bar{\mathbf{v}}'' \bar{\mathbf{v}}''^T ds, \quad \mathbf{B}^e = \int_{\mathcal{C}} E h \bar{\mathbf{u}}' \bar{\mathbf{u}}'^T ds \tag{3.13}
$$

being h the thickness of the generic element (in m). All the previous matrices are square and symmetric, and their dimension depends on the number of considered deformation modes.

The term $\mathcal{U}_l$ is the potential energy of conservative external loads (equal to the opposite of the work made by those load), which can be written as:

$$
\mathcal{U}_l = -\int_{\mathcal{S}} \mathbf{f}^T \mathbf{u} d\mathcal{S} - \int_{\mathcal{C}} \sum_H \mathbf{F}_H^T \mathbf{u}_H ds \tag{3.14}
$$

where $\mathcal{S}$ is the middle surface thus $d\mathcal{S} = ds dz$ and $\mathbf{f} = \mathbf{f}(s,z,t) = f_s(s,z,t)\mathbf{e}_s(s) + f_y(s,z,t)\mathbf{e}_y(s) + f_z(s,z,t)\mathbf{e}_z(s)$ are forces per unit area (in N/m^2) applied on $\mathcal{S}$, while $\mathcal{C}$ is the middle line at the end cross-sections $H = 0, L$, thus $\mathbf{F}_H = \mathbf{F}_H(s,t) = F_{Hs}(s,t)\mathbf{e}_s(s) + F_{Hy}(s,t)\mathbf{e}_y(s) + F_{Hz}(s,t)\mathbf{e}_z(s)$ are forces per unit length (in N/m) applied on $\mathcal{C}$. Substituting Eq. (3.3) inside Eq. (3.14) and integrating by parts, the following expression is obtained:

$$
\mathcal{U}_l = -\int_z \left(\boldsymbol{\varphi}^T \mathbf{p}_\Omega + \mathbf{\Psi}^T \mathbf{p}_W\right) dz - \left[\boldsymbol{\varphi}^T \mathbf{P}_\Omega\right]_0^L - \left[\boldsymbol{\varphi}'^T \mathbf{P}_M\right]_0^L - \left[\mathbf{\Psi}^T \mathbf{P}_W\right]_0^L \tag{3.15}
$$

where the load vectors are the following:

$$
\begin{aligned}
&\mathbf{p}_\Omega = \int_{\mathcal{C}} \left(f_s \bar{\mathbf{u}} + f_y \bar{\mathbf{v}} - f_z' \mathbf{\Omega}\right) ds, \quad \mathbf{p}_W = \int_{\mathcal{C}} f_z \bar{\mathbf{w}} ds \\
&\mathbf{P}_\Omega = \int_{\mathcal{C}} \sum_H \left(F_{Hs} \bar{\mathbf{u}} + F_{Hy} \bar{\mathbf{v}}\right) ds + \int_{\mathcal{C}} f_z \mathbf{\Omega} ds \\
&\mathbf{P}_M = \int_{\mathcal{C}} \sum_H F_{Hz} \mathbf{\Omega} ds, \quad \mathbf{P}_W = \int_{\mathcal{C}} \sum_H F_{Hz} \bar{\mathbf{w}} ds
\end{aligned} \tag{3.16}
$$

Finally, the term $\mathcal{T}$ is the kinetic energy which can be written as:

$$
\mathcal{T} = \frac{1}{2} \int_{\mathcal{S}} \left(m\dot{u}^2 + m\dot{v}^2 + m\dot{w}^2\right) d\mathcal{S} \tag{3.17}
$$

where m is the mass per unit area (in kg/m^2) applied on $\mathcal{S}$. Substituting Eq. (3.3) inside Eq. (3.17), the following expression is obtained:

$$\mathcal{T} = \frac{1}{2}\int_z \left[\dot{\boldsymbol{\varphi}}^T\mathbf{M}\dot{\boldsymbol{\varphi}} + \dot{\boldsymbol{\varphi}}'^T\left(\mathbf{Q}^m_{\Omega\Omega}\dot{\boldsymbol{\varphi}}' + \mathbf{Q}^m_{\Omega W}\dot{\boldsymbol{\Psi}}\right) + \dot{\boldsymbol{\Psi}}^T\left(\mathbf{Q}^m_{W\Omega}\dot{\boldsymbol{\varphi}}' + \mathbf{Q}^m_{WW}\dot{\boldsymbol{\Psi}}\right)\right] dz \tag{3.18}$$

where the square and symmetric mass matrices are:

$$\begin{aligned} \mathbf{M} &= \int_{\mathcal{C}} m(\bar{\mathbf{u}}\bar{\mathbf{u}}^T + \bar{\mathbf{v}}\bar{\mathbf{v}}^T)ds, \\ \mathbf{Q}^m &= \begin{bmatrix} \mathbf{Q}^m_{\Omega\Omega} & \mathbf{Q}^m_{\Omega W} \\ \mathbf{Q}^m_{W\Omega} & \mathbf{Q}^m_{WW} \end{bmatrix} = \begin{bmatrix} \int_{\mathcal{C}} m\boldsymbol{\Omega}\boldsymbol{\Omega}^T ds & \int_{\mathcal{C}} m\boldsymbol{\Omega}\bar{\mathbf{w}}^T ds \\ \int_{\mathcal{C}} m\bar{\mathbf{w}}\boldsymbol{\Omega}^T ds & \int_{\mathcal{C}} m\bar{\mathbf{w}}\bar{\mathbf{w}}^T ds \end{bmatrix} \end{aligned} \tag{3.19}$$

The variation of Eq. (3.10), Eq. (3.15) and Eq. (3.18) is performed making use of integral by parts with respect to z (and also with respect to t for the kinetic energy). The so-obtained $\delta\mathcal{U}_e$, $\delta\mathcal{U}_l$ and $\delta\mathcal{T}$ are substituted inside Eq. (3.6) which, keeping in mind Eq. (3.7) and Eq. (3.8), leads to the two coupled differential equations of motion of the beam in terms of the unknown amplitude functions:

$$\begin{aligned} &\mathbf{M}\ddot{\boldsymbol{\varphi}} - \mathbf{Q}^m_{\Omega\Omega}\ddot{\boldsymbol{\varphi}}'' - \mathbf{Q}^m_{\Omega W}\ddot{\boldsymbol{\Psi}}' + \left(\mathbf{C}^f + \mathbf{C}^a_{\Omega\Omega}\right)\boldsymbol{\varphi}'''' + \mathbf{C}^a_{\Omega W}\boldsymbol{\Psi}''' \\ &+ \left(\mathbf{D}^f + \mathbf{D}^{f^T} - \mathbf{D}^s_{\Omega\Omega} - \mathbf{D}^t\right)\boldsymbol{\varphi}'' - \mathbf{D}^s_{\Omega W}\boldsymbol{\Psi}' + \left(\mathbf{B}^f + \mathbf{B}^e\right)\boldsymbol{\varphi} = \mathbf{p}_\Omega \end{aligned} \tag{3.20}$$

$$\mathbf{Q}^m_{W\Omega}\ddot{\boldsymbol{\varphi}}' + \mathbf{Q}^m_{WW}\ddot{\boldsymbol{\Psi}} - \mathbf{C}^a_{W\Omega}\boldsymbol{\varphi}''' - \mathbf{C}^a_{WW}\boldsymbol{\Psi}'' + \mathbf{D}^s_{W\Omega}\boldsymbol{\varphi}' + \mathbf{D}^s_{WW}\boldsymbol{\Psi} = \mathbf{p}_W \tag{3.21}$$

with the following global boundary conditions at $z = 0, L$:

$$\delta\boldsymbol{\varphi}'^T\left[\left(\mathbf{C}^f + \mathbf{C}^a_{\Omega\Omega}\right)\boldsymbol{\varphi}'' + \mathbf{C}^a_{\Omega W}\boldsymbol{\Psi}' + \mathbf{D}^f\boldsymbol{\varphi} - \mathbf{P}_M\right] = 0 \quad \forall t \tag{3.22}$$

$$\begin{aligned} \delta\boldsymbol{\varphi}^T\Big[&-\left(\mathbf{Q}^m_{\Omega\Omega}\ddot{\boldsymbol{\varphi}}' + \mathbf{Q}^m_{\Omega W}\ddot{\boldsymbol{\Psi}}\right) + \left(\mathbf{C}^f + \mathbf{C}^a_{\Omega\Omega}\right)\boldsymbol{\varphi}''' + \mathbf{C}^a_{\Omega W}\boldsymbol{\Psi}'' \\ &+ \left(\mathbf{D}^f - \mathbf{D}^s_{\Omega\Omega} - \mathbf{D}^t\right)\boldsymbol{\varphi}' - \mathbf{D}^s_{\Omega W}\boldsymbol{\Psi} + \mathbf{P}_\Omega\Big] = 0 \quad \forall t \end{aligned} \tag{3.23}$$

$$\delta\boldsymbol{\Psi}^T\left[\mathbf{C}^a_{W\Omega}\boldsymbol{\varphi}'' + \mathbf{C}^a_{WW}\boldsymbol{\Psi}' - \mathbf{P}_W\right] = 0 \quad \forall t \tag{3.24}$$

where of course $\boldsymbol{\varphi} = \boldsymbol{\varphi}(z,t)$, $\boldsymbol{\Psi} = \boldsymbol{\Psi}(z,t)$, $\mathbf{p}_\Omega = \mathbf{p}_\Omega(z,t)$, $\mathbf{p}_W = \mathbf{p}_W(z,t)$. It is important to stress that the boundary conditions here reported are global since they are directly applied on the deformation modes and not on the physical nodes of the end sections, meaning that they can only describe the cases where all of them are restrained at the same way (free, clamped or hinged). The case where only some nodes are restrained and others are free, denoted as punctual or non-standard boundary conditions, is investigated in Sect. 3.2.3.

From these equations, it is evident that (except for time t in dynamics) the equations now depend only on the longitudinal variable z, thus the model order is reduced to one dimension. Furthermore, it can be remarked that, if shear deformation modes are neglected in the previous equations, i.e. all the terms multiplying $\boldsymbol{\Psi}$ are set equal to 0, the classical GBT equations are obtained and, of course, if all inertia terms are neglected, the static problem is obtained.

3.2.2 Cross-section analysis

The cross-section analysis is the core of models based on the GBT. As already mentioned, in this Thesis the approach introduced in [105], known as GBT-D was followed since it significantly simplifies this phase with respect to the classical procedure, reducing the determination of the deformation modes, which are only dependent on the cross-section properties, to the resolution of dynamic eigenvalue problems for of the externally unconstrained cross-section. More specifically, the so-called 1^{st} Planar Eigenvalue Problem (PEP) is performed to find conventional modes (this is the only unavoidable eigenvalue problem), then the extensional modes are obtained through the 2^{nd} PEP and finally shear modes through the Warping Eigenvalue Problem (WEP) as suggested by the authors in [105].

First Planar Eigenvalue Problem

To find conventional deformation modes, the cross-section is discretized in Finite Elements (FE) including a certain number of intermediate nodes between the natural ones. Each of them has 3 degree(s)-of-freedom (d.o.f.) in the plan, two translations and one rotation, meaning that the total number of d.o.f. of the unrestrained cross-section is $N_T = 3n_n$ where n_n is the total number of nodes while the total number of elements is called n_e. The global reference systems of the cross-section (X, Y) and the local one of the element e (x_e, y_e) are illustrated in Fig. 3.2 where the cross-section is divided in $n_n = 19$ nodes corresponding for this type of section to $n_e = 19$ elements. Capital letters (U_i, V_i) are used to indicate the displacements associated to a generic node i in the first system and small letters (u_i, v_i) that refer to the second one; the rotation θ_i is the same and it is always assumed positive in the counterclockwise direction.

The classical stiffness and mass (consistent) matrices of each element are built

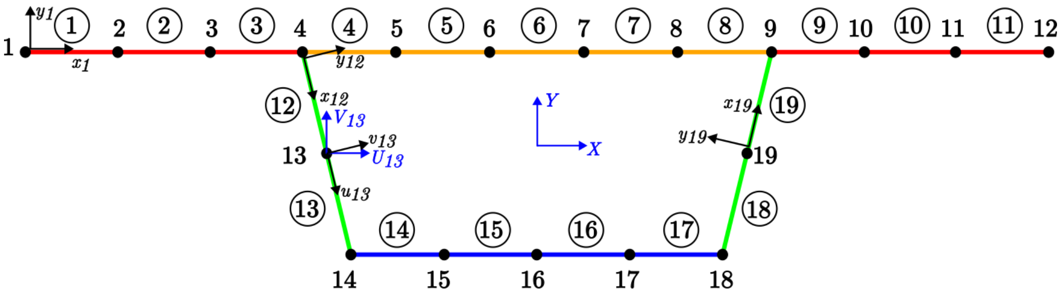

Figure 3.2. Global and local reference systems of the cross-section of the TWB.

considering that each of them is modeled as an Euler-Bernoulli beam:

$$
\mathbf{K}_{cs}^{e}=\begin{bmatrix}
\dfrac{E_eA_e}{L_e} & 0 & 0 & -\dfrac{E_eA_e}{L_e} & 0 & 0\\
0 & \dfrac{12E_eI_e}{L_e^3} & \dfrac{6E_eI_e}{L_e^2} & 0 & -\dfrac{12E_eI_e}{L_e^3} & \dfrac{6E_eI_e}{L_e^2}\\
0 & \dfrac{6E_eI_e}{L_e^2} & \dfrac{4E_eI_e}{L_e} & 0 & -\dfrac{6E_eI_e}{L_e^2} & \dfrac{2E_eI_e}{L_e}\\
-\dfrac{E_eA}{L_e} & 0 & 0 & \dfrac{E_eA_e}{L_e} & 0 & 0\\
0 & -\dfrac{12E_eI_e}{L_e^3} & -\dfrac{6E_eI_e}{L_e^2} & 0 & \dfrac{12E_eI_e}{L_e^3} & -\dfrac{6E_eI_e}{L_e^2}\\
0 & \dfrac{6E_eI_e}{L_e^2} & \dfrac{2E_eI_e}{L_e} & 0 & -\dfrac{6E_eI_e}{L_e^2} & \dfrac{4E_eI_e}{L_e}
\end{bmatrix} \tag{3.25}
$$

$$
\mathbf{M}_{cs}^{e}=m_e\begin{bmatrix}
\dfrac{L_e}{3} & 0 & 0 & \dfrac{L_e}{6} & 0 & 0\\
0 & \dfrac{13L_e}{35} & \dfrac{11L_e^2}{210} & 0 & \dfrac{9L_e}{70} & -\dfrac{13L_e^2}{420}\\
0 & \dfrac{11L_e^2}{210} & \dfrac{L_e^3}{105} & 0 & \dfrac{13L_e^2}{420} & -\dfrac{L_e^3}{140}\\
\dfrac{L_e}{6} & 0 & 0 & \dfrac{L_e}{3} & 0 & 0\\
0 & \dfrac{9L_e}{70} & \dfrac{13L_e^2}{420} & 0 & \dfrac{13L_e}{35} & -\dfrac{11L_e^2}{210}\\
0 & -\dfrac{13L_e^2}{420} & -\dfrac{L_e^3}{140} & 0 & -\dfrac{11L_e^2}{210} & \dfrac{L_e^3}{105}
\end{bmatrix} \tag{3.26}
$$

where all the properties are referred to the element e. Then, they are assembled following classical steps of FEA in order to get the stiffness and mass matrices of the entire cross-section which lead to an algebraic eigenvalue problem written in the classical form as:

$$
(\mathbf{K}_{cs}-\lambda\mathbf{M}_{cs})\,\mathbf{q}=\mathbf{0} \tag{3.27}
$$

where $\mathbf{K}_{cs}$ and $\mathbf{M}_{cs}$ are the global $N_T\times N_T$ stiffness and mass matrices, λ is the eigenvalue, which is not relevant for the cross-section analysis, and $\mathbf{q}$ is a vector with N_T components which are the nodal displacements (two translations and one rotation) in the global reference system of the cross-section for the different deformation modes.

Being the goal of the 1^{st} PEP to obtain conventional modes, the first hypothesis of membrane inextensibility in the tangential direction, $\varepsilon_s^m = 0$, is imposed. This condition implies that the two nodes i and j of the element e, inclined of α_e with respect to the global direction X, have the same displacement along s, i.e. $u_i - u_j = 0$ which, in the global system, reads:

$$(U_j - U_i)\cos\alpha_e + (V_j - V_i)\sin\alpha_e = 0 \tag{3.28}$$

Once this condition is applied to all the elements of the cross-section, it can be rewritten in matrix form as:

$$\mathbf{A}_i\mathbf{q}_i = \mathbf{0} \rightarrow \begin{bmatrix}\mathbf{A}_{iM} & | & \mathbf{A}_{iS}\end{bmatrix}\begin{bmatrix}\mathbf{q}_{iM}\\ --\\ \mathbf{q}_{iS}\end{bmatrix} = \mathbf{0} \tag{3.29}$$

where the subscript i was here added with the meaning of "inextensional" case. The $n_e \times N_T$ matrix $\mathbf{A}_i$ is partitioned in a "master" matrix $\mathbf{A}_{iM}$ of dimensions $n_e \times (N_T - n_e)$ and a "slave" matrix $\mathbf{A}_{iS}$ of dimensions $n_e \times n_e$, being the choice of the $N_T - n_e$ master parameters $\mathbf{q}_{iM}$ and of the n_e slave parameters $\mathbf{q}_{iS}$ a consequence of Eq. (3.28) and of the arrangement of the elements of the cross-section. Eq. (3.29) can be rewritten as:

$$\begin{cases}\mathbf{q}_{iM} = \mathbf{q}_{iM}\\ \mathbf{A}_{iM}\mathbf{q}_{iM} + \mathbf{A}_{iS}\mathbf{q}_{iS} = 0 \rightarrow \mathbf{q}_{iS} = -\mathbf{A}_{iS}^{-1}\mathbf{A}_{iM}\mathbf{q}_{iM}\end{cases} \tag{3.30}$$

meaning that $\mathbf{A}_{iS}$ has to be non-singular. Finally, the problem can be rewritten as follows:

$$\mathbf{q}_i = \mathbf{R}_i\mathbf{q}_{iM} \rightarrow \begin{bmatrix}\mathbf{q}_{iM}\\ --\\ \mathbf{q}_{iS}\end{bmatrix} = \begin{bmatrix}\mathbf{I}\\ --\\ -\mathbf{A}_{iS}^{-1}\mathbf{A}_{iM}\end{bmatrix}\mathbf{q}_{iM} \tag{3.31}$$

where the $N_T \times (N_T - n_e)$ matrix $\mathbf{R}_i$ is used to obtain the constrained algebraic eigenvalue problem with the inextensibility condition. In fact, substituting Eq. (3.31) in $\delta\mathbf{q}^T(\mathbf{K}_{cs} - \lambda\mathbf{M}_{cs})\,\mathbf{q} = 0$ with $\mathbf{q} = \mathbf{q}_i$, one gets:

$$(\mathbf{K}_i - \lambda\mathbf{M}_i)\,\mathbf{q}_{iM} = \mathbf{0} \tag{3.32}$$

being $\mathbf{K}_i = \mathbf{R}_i^T\mathbf{K}_{cs}\mathbf{R}_i$ and $\mathbf{M}_i = \mathbf{R}_i^T\mathbf{M}_{cs}\mathbf{R}_i$. The resolution of the internally constrained eigenvalue problem of Eq. (3.32) allows to find the in-plane nodal displacements associated to the so-called conventional modes.

Solving Eq. (3.32), $N_T - n_e$ conventional deformation modes are found, whose components represent the displacements associated to the corresponding d.o.f. at the nodes. Then, in order to reconstruct them, i.e. to find $\bar{\mathbf{u}}(s)$ and $\bar{\mathbf{v}}(s)$ in the entire cross-section domain, adequate interpolation functions have to be used. So, first the nodal components of deformation modes in the local reference system of each element are found by applying:

$$\begin{bmatrix} u_i \\ v_i \\ \theta_i \end{bmatrix} = \begin{bmatrix} \cos\alpha_e & \sin\alpha_e & 0 \\ -\sin\alpha_e & \cos\alpha_e & 0 \\ 0 & 0 & 1 \end{bmatrix} \begin{bmatrix} U_i \\ V_i \\ \theta_i \end{bmatrix} \tag{3.33}$$

Then, the in-plane components of the deformation mode k of the element e can be found from the values at nodes i and j as follows:

$$\bar{u}_k(s) = \Psi_1(s)u_{i,k} + \Psi_2(s)u_{j,k} \tag{3.34}$$

$$\bar{v}_k(s) = \Psi_3(s)v_{i,k} + \Psi_4(s)\theta_{i,k} + \Psi_5(s)v_{j,k} + \Psi_6(s)\theta_{j,k} \tag{3.35}$$

the linear and cubic interpolation functions being respectively:

$$\Psi_1(s) = 1 - \frac{s}{L_e}, \quad \Psi_2(s) = \frac{s}{L_e} \tag{3.36}$$

$$\begin{aligned} \Psi_3(s) &= 1 - \frac{3s^2}{L_e^2} + \frac{2s^3}{L_e^3}, \quad \Psi_4(s) = s - \frac{2s^2}{L_e} + \frac{s^3}{L_e^2}, \\ \Psi_5(s) &= \frac{3s^2}{L_e^2} - \frac{2s^3}{L_e^3}, \quad \Psi_6(s) = -\frac{s^2}{L_e} + \frac{s^3}{L_e^2} \end{aligned} \tag{3.37}$$

As was written before, the conventional deformation modes have also out-of-plane components, also addressed to as warping components. These can be determined by enforcing the second hypothesis of membrane shear indeformability, $\gamma_{zs}^m = 0$, which becomes $\gamma_{zs}^m = const$ stepwise for closed loops. From Eq. (3.4), γ_{zs}^m can be written considering only conventional modes as:

$$\gamma_{zs}^m = \left(\bar{\mathbf{u}}^T + \mathbf{\Omega}'^T\right)\boldsymbol{\varphi}' = \sum_{k=1}^{K} \left[\bar{u}_k(s) + \Omega_{k,s}(s)\right]\varphi_{k,z}(z,t) = \sum_{k=1}^{K} \Gamma_k(s)\varphi_{k,z}(z,t) \tag{3.38}$$

where $\Gamma_k(s) = \bar{u}_k(s) + \Omega_{k,s}(s)$ is either 0 or constant. From the hypothesis of tangential membrane inextensibility, it results that $\bar{u}_k(s)$ is constant on each element and can thus be written as $\bar{u}_k^e$ and, from the second hypothesis, $\Gamma_k(s)$ is constant too, equal to Γ_k^e. As a consequence, $\Omega_{k,s}(s)$ has to be constant on s for each element implying that $\Omega_k(s)$ is linear and can be written as:

$$\Omega_k(s) = \Omega_{k,s}(s)s + \Omega_{i,k} = \frac{\Omega_{j,k} - \Omega_{i,k}}{L_e}s + \Omega_{i,k} \tag{3.39}$$

as a function of the warping values at its end nodes i and j. Thus, if the element of the cross-section is open, the following expression can be derived from Eq. (3.38):

$$\Gamma_k^e = \bar{u}_k^e + \frac{\Omega_{j,k} - \Omega_{i,k}}{L_e} \tag{3.40}$$

On the other hand, on closed loops Γ_k^e is related to the unknown tangential stress flow Q_k^l where l stands for the loop under consideration (since more than one cell can be present), as:

$$Gh_e\Gamma_k^e = Gh_e\left(\bar{u}_k^e + \frac{\Omega_{j,k} - \Omega_{i,k}}{L_e}\right)\sum_l \pm Q_k^l \tag{3.41}$$

In this way, in case of a partially-closed cross-section with just one loop like the one under study, one has n_e equations and $n_e + 1$ unknowns, due to the uniform extension along z; these unknowns are the warping displacement at each node ($\Omega_{i,k}$) and the flow on the loop (Q_k^l). In order to be able to solve the system, the last equation to be satisfied is:

$$\int_{\mathcal{C}} \Omega_k(s)ds = 0 \rightarrow \sum_{e=1}^{n_e} \frac{\Omega_{i,k}^e + \Omega_{j,k}^e}{2} L_e = 0 \tag{3.42}$$

which is the condition of zero-mean value of the warping along the middle line of the cross-section. Attention has to be paid to the direction of the shear flow on each element, assigning a positive value when the conventional direction of the element coincides with the one chosen for the flow and a negative value vice versa. Thus, the system obtained considering Eq. (3.40), Eq. (3.41) and Eq. (3.42) is solved and the out-of-plane warping modes $\Omega_k(s)$ are reconstructed through Eq. (3.39).

At the end, a total number of $N_T - n_e$ modes is obtained having both in-plane and out-of-plane components $(\bar{u}_{ik}(s), \bar{v}_{ik}(s), \Omega_{ik}(s))$, the subscript i is added always standing for "inextensional". It is important to underline that, being the cross-section externally unrestrained, the first three deformation modes have a nil eigenvalue, representative of the first three rigid modes.

Second Planar Eigenvalue Problem

Once these conventional deformation modes are found, a 2^{nd} PEP is solved in order to obtain the extensional deformation modes for which $\varepsilon_s^m \neq 0$; this basis of modes has to be orthogonal to the conventional, inextensible ones. To impose this condition, the inextensional modes are collected in a $N_T \times (N_T - n_e)$ matrix which is obtained from Eq. (3.31) as $\mathbf{Q}_i = \mathbf{q}_i$. Once again a constrained eigenvalue problem has to be solved starting from Eq. (3.27) being the constraint exactly the aforementioned orthogonality condition expressed as:

$$\mathbf{Q}_i^T \mathbf{I} \mathbf{q}_e = \mathbf{0} \rightarrow \begin{bmatrix} \mathbf{Q}_{iM}^T & | & \mathbf{Q}_{iS}^T \end{bmatrix} \begin{bmatrix} \mathbf{q}_{eM} \\ -- \\ \mathbf{q}_{eS} \end{bmatrix} = \mathbf{0} \tag{3.43}$$

where the subscript e was here added with the meaning of "extensional" case. The choice of the n_e master parameters $\mathbf{q}_{eM}$ and of the $N_T - n_e$ slave parameters $\mathbf{q}_{eS}$ is a consequence of the choice made in the inextensible case. Then, proceeding as was done before, one gets:

$$\begin{cases} \mathbf{q}_{eM} = \mathbf{q}_{eM} \\ \mathbf{Q}_{iM}^T \mathbf{q}_{eM} + \mathbf{Q}_{iS}^T \mathbf{q}_{eS} = 0 \rightarrow \mathbf{q}_{eS} = -\mathbf{Q}_{iS}^{-T} \mathbf{Q}_{iM}^T \mathbf{q}_{eM} \end{cases} \tag{3.44}$$

with $\mathbf{Q}_{iS}^T$ which has to be non-singular. Finally, it is possible to write that:

$$\mathbf{q}_e = \mathbf{R}_e \mathbf{q}_{eM} \rightarrow \begin{bmatrix} \mathbf{q}_{eM} \\ -- \\ \mathbf{q}_{eS} \end{bmatrix} = \begin{bmatrix} \mathbf{I} \\ -- \\ -\mathbf{Q}_{iS}^{-T} \mathbf{Q}_{iM}^T \end{bmatrix} \mathbf{q}_{eM} \tag{3.45}$$

where through the $N_T \times n_e$ matrix $\mathbf{R}_e$, the eigenvalue problem becomes:

$$(\mathbf{K}_e - \lambda \mathbf{M}_e)\, \mathbf{q}_{eM} = \mathbf{0} \tag{3.46}$$

where $\mathbf{K}_e = \mathbf{R}_e^T \mathbf{K}_{cs} \mathbf{R}_e$ and $\mathbf{M}_e = \mathbf{R}_e^T \mathbf{M}_{cs} \mathbf{R}_e$. Solving the eigensystem of Eq. (3.46), the in-plane nodal displacements associated to the so-called extensional modes are obtained. Through the same interpolation functions written in Eq. (3.36) and Eq. (3.37) a total number of n_e modes is obtained having just in-plane components as $(\bar{u}_{eh}(s), \bar{v}_{eh}(s), 0)$.

Warping Eigenvalue Problem

To completely determine the deformation modes of the cross-section, the shear or warping modes are found solving an unconstrained WEP. The steps are the same followed for the 1^{st} PEP, but in this case the cross-section is studied as a shear beam, meaning that $\gamma_{zs}^m \neq 0$, i.e. the cross-section admits only membrane shear deformations (only out-of-plane components exist). The stiffness and mass matrices of the single elements represented in Fig. 3.2 are:

$$\mathbf{K}_w^e = \begin{bmatrix} \dfrac{G_e h_e}{L_e} & -\dfrac{G_e h_e}{L_e} \\ -\dfrac{G_e h_e}{L_e} & \dfrac{G_e h_e}{L_e} \end{bmatrix} \tag{3.47}$$

$$\mathbf{M}_w^e = \begin{bmatrix} \frac{m_e L_e}{3} & \frac{m_e L_e}{6} \\ \frac{m_e L_e}{6} & \frac{m_e L_e}{3} \end{bmatrix} \tag{3.48}$$

and, following a classical FE procedure, the eigenvalue problem reads as:

$$\left(\mathbf{K}_w - \lambda \mathbf{M}_w\right) \mathbf{q}_w = \mathbf{0} \tag{3.49}$$

where $\mathbf{K}_w$ and $\mathbf{M}_w$ are the global square stiffness and mass matrices with dimension $n_n \times n_n$, since each node has just one d.o.f. (axial displacement) and they are all collected in the vector $\mathbf{q}_w$ of n_n components.

Eq. (3.49) is solved obtaining the longitudinal displacement at each node. Using the linear interpolation functions of Eq. (3.36), the n_n modes are found with only out-of-plane components $(0, 0, \bar{w}_j(s))$ and, since the problem is externally unrestrained, the first mode has a nil eigenvalue and represents the uniform warping.

So, after performing the two PEP and the WEP, a total number of $4n_n$ modes is found, distributed among the different problems as follows:

- $N_T - n_e = 3n_n - n_e$ conventional modes with in-plane and out-of-plane components $(\bar{u}_{ik}(s), \bar{v}_{ik}(s), \Omega_{ik}(s))$.
- n_e extensional modes with only in-plane components $(\bar{u}_{eh}(s), \bar{v}_{eh}(s), 0)$.
- n_n shear or warping modes with only out-of-plane components $(0, 0, \bar{w}_j(s))$.

3.2.3 Member analysis

Once the deformation modes are found through the cross-section analysis, the equilibrium equations (in statics) or the equations of motion (in dynamics) of the problem can be solved. Various techniques can be followed and, in this section, three main approaches have been used in function of the problem under study: an analytical and two numerical methods (based on Finite Differences (FD) and on FE respectively). They are briefly resumed here and explained in the following:

- Member analysis with analytical solution (MA1): it can be used in the case of simply supported beams, i.e. globally hinged at both ends but still free to warp for which a closed-form solution is known. This approach was used here both for statics and dynamics considering all types of deformation modes.
- Member analysis with finite differences (MA2): it was introduced with the goal of having a first numerical comparison with the analytical results. This

approach was used here both for statics and dynamics considering only conventional deformation modes.

- Member analysis with finite elements (MA3): it was introduced when it was necessary to account for more complex load distributions (like piece-wise constant loads along z) and moreover non-standard restraints on the bridge, like punctual hinges applied only in some nodes of the end sections. This approach was used here both for statics and dynamics considering conventional and extensional deformation modes.

MA1

The procedure named MA1 is based on two distinct works realized by two different research groups in the same period: the first one is [105] where this analytical approach is applied to statics, while the second one is [8] which studies both statics and dynamics. They were grouped under the same section of this Thesis since they essentially address the same problem; however, as they were examined by the author at different stages and for different purposes, it was decided to include both, using the first for statics and the second for dynamics.

The procedure developed by Piccardo, Ranzi and Luongo in [105] allows to solve the equilibrium equations of the simply supported beam, restrained to torsion and free to warp at the ends taking into account all deformation modes, including the shear ones. In fact, considering the problem written in Eqs. (3.20) - (3.24) where the inertia forces are neglected, one can say that a solution that satisfies the equations and the aforementioned boundary conditions (which are $\boldsymbol{\varphi}(0) = \mathbf{0}$, $\boldsymbol{\varphi}(L) = \mathbf{0}$ and the terms inside the square brackets of Eqs. (3.22), (3.24) equal to $\mathbf{0}$) is:

$$\boldsymbol{\varphi}(z) = \sum_{n_j=1}^{N_j} \mathbf{a}_{n_j} \sin\left(\frac{n_j \pi z}{L}\right) \tag{3.50}$$

$$\boldsymbol{\Psi}(z) = \sum_{n_j=1}^{N_j} \mathbf{b}_{n_j} \cos\left(\frac{n_j \pi z}{L}\right) \tag{3.51}$$

where N_j is the maximum half-wave number considered. This formulation is a close relative to what in [8] is called doubly modal representation (recalled in the aftermath), since n_j represents the number of the sine wave which, in this case, is typical of a Fourier series formulation, thus accounting for the contribution of different harmonics along the beam axis, while $\mathbf{a}_{n_j}$ and $\mathbf{b}_{n_j}$ account for the deformation of the cross-section; if all the deformation modes are taken, $\mathbf{a}_{n_j}$ and $\mathbf{b}_{n_j}$ are vectors of respectively $3n_n$ and n_n components for each harmonic n_j.

Considering that no external forces are applied in correspondence of the end sections and considering for the distributed load vector $\mathbf{f}(s,z)$ of Eq. (3.16) the following laws:

$$\begin{aligned} f_s &= \sum_{n_j=1}^{N_j} f_{s,n_j}(s)\sin\left(\frac{n_j\pi z}{L}\right), \quad f_y = \sum_{n_j=1}^{N_j} f_{y,n_j}(s)\sin\left(\frac{n_j\pi z}{L}\right), \\ f_z &= \sum_{n_j=1}^{N_j} f_{z,n_j}(s)\cos\left(\frac{n_j\pi z}{L}\right) \end{aligned} \tag{3.52}$$

the external loads of Eq. (3.16) can be written as:

$$\mathbf{p}_\Omega = \sum_{n_j=1}^{N_j} \mathbf{p}_{\Omega,n_j}\sin\left(\frac{n_j\pi z}{L}\right), \quad \mathbf{p}_W = \sum_{n_j=1}^{N_j} \mathbf{p}_{W,n_j}\cos\left(\frac{n_j\pi z}{L}\right) \tag{3.53}$$

where, as a consequence of Eq. (3.16), one has for each n_j:

$$\mathbf{p}_{\Omega,n_j} = \int_{\mathcal{C}} \left(f_{s,n_j}\bar{\mathbf{u}} + f_{y,n_j}\bar{\mathbf{v}} - f'_{z,n_j}\boldsymbol{\Omega}\right) ds, \quad \mathbf{p}_{W,n_j} = \int_{\mathcal{C}} f_{z,n_j}\bar{\mathbf{w}} d\mathcal{S} \tag{3.54}$$

whose coefficients can be found as:

$$\begin{aligned} f_{s,n_j} &= \frac{2}{L}\int_0^L f_s(s,z)\sin\left(\frac{n_j\pi z}{L}\right)dz, \quad f_{y,n_j} = \frac{2}{L}\int_0^L f_y(s,z)\sin\left(\frac{n_j\pi z}{L}\right)dz, \\ f_{z,n_j} &= \frac{2}{L}\int_0^L f_z(s,z)\cos\left(\frac{n_j\pi z}{L}\right)dz \end{aligned} \tag{3.55}$$

Thus, the substitution of Eq. (3.50) into Eqs. (3.20), (3.21) leads to the following problem for each nj:

$$\begin{bmatrix} \mathbf{K}_{\Omega a} & \mathbf{K}_{\Omega b} \\ \mathbf{K}_{Wa} & \mathbf{K}_{Wb} \end{bmatrix} \begin{pmatrix} \mathbf{a}_{n_j} \\ \mathbf{b}_{n_j} \end{pmatrix} = \begin{pmatrix} \mathbf{p}_{\Omega,n_j} \\ \mathbf{p}_{W,n_j} \end{pmatrix} \tag{3.56}$$

where:

$$\begin{aligned} \mathbf{K}_{\Omega a} &= \left(\mathbf{C}^f + \mathbf{C}^a_{\Omega\Omega}\right)\left(\frac{n_j\pi}{L}\right)^4 - \left(\mathbf{D}^f + \mathbf{D}^{fT} - \mathbf{D}^s_{\Omega\Omega} - \mathbf{D}^t\right)\left(\frac{n_j\pi}{L}\right)^2 + \left(\mathbf{B}^f + \mathbf{B}^e\right) \\ \mathbf{K}_{\Omega b} &= -\mathbf{C}^a_{\Omega W}\left(\frac{n_j\pi}{L}\right)^3 + \mathbf{D}^s_{\Omega W}\left(\frac{n_j\pi}{L}\right) \\ \mathbf{K}_{Wa} &= \mathbf{C}^a_{W\Omega}\left(\frac{n_j\pi}{L}\right)^3 + \mathbf{D}^s_{W\Omega}\left(\frac{n_j\pi}{L}\right) \\ \mathbf{K}_{Wb} &= \mathbf{C}^a_{WW}\left(\frac{n_j\pi}{L}\right)^2 + \mathbf{D}^s_{WW} \end{aligned} \tag{3.57}$$

The problem written in Eq. (3.56) allows to study the static response of a simply supported TWB to different types of loads applied along the entire length of the beam, accounting for the contribution of all possible deformation modes. So, its resolution allows to obtain $\mathbf{a}_{n_j}$ and $\mathbf{b}_{n_j}$ for each harmonic n_j and reconstruct the amplitude functions through Eq. (3.50).

A similar procedure, always with the goal of finding an analytical solution, is the one developed by Bebiano, Camotim and Silvestre in [8] which was used in this work to study dynamics. There, the so-called doubly modal displacement representation is introduced. In particular, if the j^{th} vibration mode is considered, keeping only conventional modes, Eqs. (3.20), (3.22) and (3.23) for the simply supported beam in free dynamics are rewritten as:

$$\begin{aligned} &\mathbf{M}\ddot{\boldsymbol{\varphi}}_j(z,t) - \mathbf{Q}^m_{\Omega\Omega}\ddot{\boldsymbol{\varphi}}''_j(z,t) + \left(\mathbf{C}^f + \mathbf{C}^a_{\Omega\Omega}\right)\boldsymbol{\varphi}''''_j(z,t) \\ &+ \left(\mathbf{D}^f + \mathbf{D}^{fT} - \mathbf{D}^s_{\Omega\Omega} - \mathbf{D}^t\right)\boldsymbol{\varphi}''_j(z,t) + \mathbf{B}^f\boldsymbol{\varphi}_j(z,t) = \mathbf{0} \end{aligned} \tag{3.58}$$

with boundary conditions at $z = 0, L$:

$$\left[\left(\mathbf{C}^f + \mathbf{C}^a_{\Omega\Omega}\right)\boldsymbol{\varphi}''_j(z,t) + \mathbf{D}^f\boldsymbol{\varphi}_j(z,t)\right]_0^L = 0 \quad \forall t \tag{3.59}$$

$$\left[\boldsymbol{\varphi}_j(z,t)\right]_0^L = 0 \quad \forall t \tag{3.60}$$

Considering that n_d indicates the chosen number of deformation modes among those explained in Sect. 3.2.2, $\boldsymbol{\varphi}_j$ can be the seen as the amplitude function which accounts for the contribution of each of the n_d deformation modes to the j^{th} vibration mode along z. So, separating space and time, the j^{th} amplitude function can be written as:

$$\boldsymbol{\varphi}_j(z,t) = \boldsymbol{\Phi}_j(z)Y_j(t) \tag{3.61}$$

where the n_d column vector $\boldsymbol{\Phi}_j(z)$ accounts for the longitudinal evolution of the contribution of deformation modes to the j^{th} vibration mode and $Y_j(t)$ is the modal coordinate. Thus, using Eq. (3.61), Eq. (3.58) can be split into the following two equations, where ω_j is the j^{th} angular frequency (in rad/s):

$$\ddot{Y}_j(t) + \omega_j^2 Y_j(t) = 0 \tag{3.62}$$

$$\begin{aligned} &\left(\mathbf{C}^f + \mathbf{C}^a_{\Omega\Omega}\right)\boldsymbol{\Phi}''''_j(z) + \left(\mathbf{D}^f + \mathbf{D}^{fT} - \mathbf{D}^s_{\Omega\Omega} - \mathbf{D}^t\right)\boldsymbol{\Phi}''_j(z) \\ &+ \mathbf{B}^f\boldsymbol{\Phi}_j(z) - \omega_j^2\left(\mathbf{M}\boldsymbol{\Phi}_j(z) - \mathbf{Q}^m_{\Omega\Omega}\boldsymbol{\Phi}''_j(z)\right) = \mathbf{0} \end{aligned} \tag{3.63}$$

The objective is to analytically solve Eq. (3.63) in order to find natural frequencies and vibration modes and a solution that satisfies boundary conditions (3.59), (3.60) is:

$$\boldsymbol{\Phi}_j(z) = \boldsymbol{\Theta}_j \sin\left(\frac{n_j \pi z}{L}\right) \tag{3.64}$$

where $\boldsymbol{\Theta}_j$ and n_j are the magnitude and the longitudinal half-wave number of the j^{th}

vibration mode, respectively. The magnitudes and the squared angular frequencies ω_j^2, are found substituting Eq. (3.64) into Eq. (3.63), obtaining:

$$\left(\mathbf{K}_j - \omega_j^2 \mathbf{M}_j\right) \boldsymbol{\Theta}_j = \mathbf{0} \tag{3.65}$$

where the stiffness and mass matrices are respectively:

$$\mathbf{K}_j = \left(\mathbf{C}^f + \mathbf{C}^a_{\Omega\Omega}\right)\left(\frac{n_j\pi}{L}\right)^4 - \left(\mathbf{D}^f + \mathbf{D}^{fT} - \mathbf{D}^s_{\Omega\Omega} - \mathbf{D}^t\right)\left(\frac{n_j\pi}{L}\right)^2 + \mathbf{B}^f \tag{3.66}$$

$$\mathbf{M}_j = \mathbf{M} + \mathbf{Q}^m_{\Omega\Omega}\left(\frac{n_j\pi}{L}\right)^2 \tag{3.67}$$

and, as can be noted, $\mathbf{K}_j$ has the same expression of $\mathbf{K}_{\Omega a}$ in Eq. (3.57) except for the term related to extensional modes $\mathbf{B}^e$, highlighting again the correspondence with the previous procedure. The resolution of the eigenvalue problem (3.65) gives a total number of $n_v = n_d \times N_j$ vibration modes where N_j represents again the maximum considered half-wave number.

It can be proven, following classical steps, that orthogonality with respect to the mass and stiffness matrices $\mathbf{M}_j$ and $\mathbf{K}_j$ exists among all found vibration modes. This implies that if one wants to study the forced dynamics (as for Sect. 3.4), uncoupled equations can be solved for every vibration mode and then superimposed, retaining only a limited number of modes as:

$$\boldsymbol{\varphi}(z,t) = \sum_{j=1}^{n_v} \boldsymbol{\Phi}_j(z) Y_j(t) = \boldsymbol{\Phi}(z)\mathbf{Y}(t) \tag{3.68}$$

where $\boldsymbol{\Phi}(z)$ is the $n_d \times n_v$ matrix containing the longitudinal amplitude functions where each row is related to a deformation mode and each column to a vibration mode and $\mathbf{Y}(t)$ is a column vector function of n_v components, where each row is the time response of a vibration mode to a given load. Hence, the definition of doubly modal displacement representation given in [8] which can be better highlighted when substituting Eq. (3.68) in Eq. (3.3). In this way one can obtain the displacement field of the TWB; for example, the transversal displacement reads:

$$\begin{aligned} v(s,z,t) &= \bar{\mathbf{v}}^T(s)\boldsymbol{\Phi}(z)\mathbf{Y}(t) \\ &= \begin{pmatrix} \bar{v}_1(s) & \dots & \bar{v}_{n_d}(s) \end{pmatrix} \begin{bmatrix} \Phi_{11}(z) & \dots & \Phi_{1n_v}(z) \\ \vdots & \ddots & \vdots \\ \Phi_{n_d1}(z) & \dots & \Phi_{n_dn_v}(z) \end{bmatrix} \begin{pmatrix} Y_1(t) \\ \vdots \\ Y_{n_v}(t) \end{pmatrix} \end{aligned} \tag{3.69}$$

This representation shows the difference between the contribution of the deformation modes (vector $\bar{\mathbf{v}}(s)$ and rows of $\boldsymbol{\Phi}(z)$) and that of vibration modes (vector $\mathbf{Y}(t)$ and columns of $\boldsymbol{\Phi}(z)$) and highlights the possibility of choosing an arbitrary number of each of them to better describe the response of the beam or of excluding non-interesting deformation or vibration modes. More details on the application of this representation to static and forced dynamic problems can be found in [8].

MA2

As an alternative to MA1, a numerical approach can be followed to find the amplitude functions, based on Finite Differences FD, here addressed as MA2. This approach was followed to have numerical results to compare to analytical ones.

In order to do that, first the contribution of shear modes is neglected from Eqs. (3.20), (3.22) and (3.23) since, as it will be clear in the following, for the case study considered in the following they are not fundamental. Then, it is assumed that $\bar{\boldsymbol{\varphi}}_1 = \boldsymbol{\varphi}$, $\bar{\boldsymbol{\varphi}}_2 = \boldsymbol{\varphi}'$, $\bar{\boldsymbol{\varphi}}_3 = \boldsymbol{\varphi}''$ and $\bar{\boldsymbol{\varphi}}_4 = \boldsymbol{\varphi}'''$, so that the problem can be rewritten for the simply supported beam as follows:

$$\begin{aligned} &\bar{\boldsymbol{\varphi}}_1' = \bar{\boldsymbol{\varphi}}_2 \\ &\bar{\boldsymbol{\varphi}}_2' = \bar{\boldsymbol{\varphi}}_3 \\ &\bar{\boldsymbol{\varphi}}_3' = \bar{\boldsymbol{\varphi}}_4 \\ &\bar{\boldsymbol{\varphi}}_4' = \left(\mathbf{C}^f + \mathbf{C}^a_{\Omega\Omega}\right)^{-1} \left[\mathbf{M}\omega^2 - \left(\mathbf{B}^f + \mathbf{B}^e\right)\right] \bar{\boldsymbol{\varphi}}_1 - \left(\mathbf{C}^f + \mathbf{C}^a_{\Omega\Omega}\right)^{-1} \\ &\times \left[\mathbf{Q}^m_{\Omega\Omega}\omega^2 + \left(\mathbf{D}^f + {\mathbf{D}^f}^T - \mathbf{D}^s_{\Omega\Omega} - \mathbf{D}^t\right)\right] \bar{\boldsymbol{\varphi}}_3 + \left(\mathbf{C}^f + \mathbf{C}^a_{\Omega\Omega}\right)^{-1} \mathbf{p}_\Omega \end{aligned} \tag{3.70}$$

with boundary conditions:

$$\begin{aligned} &\mathbf{D}^f \bar{\boldsymbol{\varphi}}_1|_{0,L} + \left(\mathbf{C}^f + \mathbf{C}^a_{\Omega\Omega}\right) \bar{\boldsymbol{\varphi}}_3|_{0,L} = 0 \\ &\bar{\boldsymbol{\varphi}}_1|_{0,L} = 0 \end{aligned} \tag{3.71}$$

Another boundary condition has to be imposed when studying the dynamical problem, as a normalization condition, in order to find the further unknown represented by the natural frequency ω. Finite differences are used to solve Eq. (3.70) through the Matlab function bvp4c [88] after giving an (appropriate) initial guess to $\bar{\boldsymbol{\varphi}}_i$.

MA3

Finally, another numerical way to perform the member analysis in order to solve the problem and obtain the unknown amplitude functions is using Finite Elements, here called MA3; in this way, it is possible to combine the positive aspects of GBT-D and FEA. This approach was introduced in this Thesis to take into account more complex load distributions, like the presence of trucks which do not cover the entire span of the bridge for load test purposes but also to model different boundary conditions with respect to the classical global ones which are free, hinged or clamped end sections: this kind of restraints are intrinsic to GBT, due to its modal nature, descending from the deformation modes, which implies that restraint cannot be directly applied on nodes, but on the amplitude functions which do not depend on s; if all nodes of the end sections are restrained in the same way, the two things coincide. However, this means that it is not possible to account for punctual restraints at the end sections or elsewhere. In the author's opinion, the procedure here explained as MA3 based on [7, 17] is the most suitable method to consider this situation.

The procedure to carry on the member analysis using FE is here illustrated, considering the possible presence of non-standard support conditions. Of course, differently from what was done in Sect. 3.2.2 where FE were used to discretize the cross-section, here they are used to discretize the TWB along the axial direction z. The beam is divided into $n_z - 1$ elements, being n_z the number of nodes along z and considering always just the conventional and extensional deformation modes, the contribution of the k^{th} deformation mode to the unknown amplitude function on the finite element e can be written as:

$$\varphi_k(z) = \Psi_3(z)d_{k,i} + \Psi_4(z)d_{k,i+1} + \Psi_5(z)d_{k,i+2} + \Psi_6(z)d_{k,i+3} \tag{3.72}$$

where $d_{k,\alpha}$ are the generalized displacements of the finite element e, with $\alpha = i, \ldots, i+3$, being $i = 1+2\,(n_z^e - 1)$ the index associated to the vertical displacement of the first node of the element e, and the cubic polynomials Ψ_β (with $\beta = 3, \ldots, 6$) can be of Lagrange or Hermite type; the latter were considered in this work and their expressions are the same of Eq. (3.37) in function of z. The generalized displacements, shown in Fig. 3.3, have to be chosen in order to respect the compatibility between two following FE as:

$$d_{k,i} = \varphi_k(0), \quad d_{k,i+1} = \varphi_{k,z}(0), \quad d_{k,i+2} = \varphi_k(L_e), \quad d_{k,i+3} = \varphi_{k,z}(L_e) \tag{3.73}$$

where comma indicates derivative with respect to z. So, the vector of the generalized modal displacements of the finite element e is:

$$\mathbf{d}_k^e = [d_{k,i}, d_{k,i+1}, d_{k,i+2}, d_{k,i+3}]^T \tag{3.74}$$

To write the equilibrium equations in a FE form, the Hamilton's principle written in Eq. (3.6) is applied considering the expressions of the energies written in

Eq. (3.10), Eq. (3.15) and Eq. (3.18), after substituting $\varphi_k(z) = \Psi_\beta d_{k,\alpha}$ inside them. Doing that, one gets the following stiffness and mass matrices and load vector for each element:

$$\mathbf{K}^e_{FE} = \begin{bmatrix} \mathbf{K}^e_{11} & \dots & \mathbf{K}^e_{1n_d} \\ \vdots & \ddots & \vdots \\ \mathbf{K}^e_{n_d1} & \dots & \mathbf{K}^e_{n_dn_d} \end{bmatrix}, \mathbf{M}^e_{FE} = \begin{bmatrix} \mathbf{M}^e_{11} & \dots & \mathbf{M}^e_{1n_d} \\ \vdots & \ddots & \vdots \\ \mathbf{M}^e_{n_d1} & \dots & \mathbf{M}^e_{n_dn_d} \end{bmatrix}, \mathbf{P}^e_{FE} = \begin{bmatrix} \mathbf{P}^e_1 \\ \vdots \\ \mathbf{P}^e_{n_d} \end{bmatrix} \tag{3.75}$$

where each sub-matrix $\mathbf{K}^e_{hk}$, $\mathbf{M}^e_{hk}$ has dimensions 4×4 and each vector $\mathbf{P}^e_h$ is 4×1. More specifically, applying the aforementioned procedure, their expressions are:

$$\begin{aligned}
\mathbf{K}^e_{hk} = &\left(C^f_{hk} + C^a_{\Omega\Omega hk}\right) \begin{bmatrix} \int_{L_e} \Psi_1''\Psi_1''dz & \dots & \int_{L_e} \Psi_1''\Psi_4''dz \\ \vdots & \ddots & \vdots \\ \int_{L_e} \Psi_4''\Psi_1''dz & \dots & \int_{L_e} \Psi_4''\Psi_4''dz \end{bmatrix} \\
&+ \left(D^t_{hk} + D^s_{\Omega\Omega hk}\right) \begin{bmatrix} \int_{L_e} \Psi_1'\Psi_1'dz & \dots & \int_{L_e} \Psi_1'\Psi_4'dz \\ \vdots & \ddots & \vdots \\ \int_{L_e} \Psi_4'\Psi_1'dz & \dots & \int_{L_e} \Psi_4'\Psi_4'dz \end{bmatrix} \\
&+ D^f_{hk} \begin{bmatrix} \int_{L_e} \Psi_1\Psi_1''dz & \dots & \int_{L_e} \Psi_1\Psi_4''dz \\ \vdots & \ddots & \vdots \\ \int_{L_e} \Psi_4\Psi_1''dz & \dots & \int_{L_e} \Psi_4\Psi_4''dz \end{bmatrix} + D^f_{kh} \begin{bmatrix} \int_{L_e} \Psi_1''\Psi_1dz & \dots & \int_{L_e} \Psi_1''\Psi_4dz \\ \vdots & \ddots & \vdots \\ \int_{L_e} \Psi_4''\Psi_1dz & \dots & \int_{L_e} \Psi_4''\Psi_4dz \end{bmatrix} \\
&+ \left(B^e_{hk} + B^f_{hk}\right) \begin{bmatrix} \int_{L_e} \Psi_1\Psi_1dz & \dots & \int_{L_e} \Psi_1\Psi_4dz \\ \vdots & \ddots & \vdots \\ \int_{L_e} \Psi_4\Psi_1dz & \dots & \int_{L_e} \Psi_4\Psi_4dz \end{bmatrix}
\end{aligned} \tag{3.76}$$

$$\mathbf{M}^e_{hk} = M_{hk} \begin{bmatrix} \int_{L_e} \Psi_1\Psi_1dz & \dots & \int_{L_e} \Psi_1\Psi_4dz \\ \vdots & \ddots & \vdots \\ \int_{L_e} \Psi_4\Psi_1dz & \dots & \int_{L_e} \Psi_4\Psi_4dz \end{bmatrix} + Q^m_{\Omega\Omega hk} \begin{bmatrix} \int_{L_e} \Psi_1'\Psi_1'dz & \dots & \int_{L_e} \Psi_1'\Psi_4'dz \\ \vdots & \ddots & \vdots \\ \int_{L_e} \Psi_4'\Psi_1'dze & \dots & \int_{L_e} \Psi_4'\Psi_4'dz \end{bmatrix} \tag{3.77}$$

$$\mathbf{P}^e_h = \begin{bmatrix} p_{\Omega h} \int_{L_e} \Psi_1 dz + P_{Mh}\Psi_1' + P_{\Omega h}\Psi_1 \\ \vdots \\ p_{\Omega h} \int_{L_e} \Psi_4 dz + P_{Mh}\Psi_4' + P_{\Omega h}\Psi_4 \end{bmatrix} \tag{3.78}$$

So, in Eq. (3.75), $\mathbf{K}^e_{FE}$ and $\mathbf{M}^e_{FE}$ are $4n_d \times 4n_d$ matrices and $\mathbf{P}^e_{FE}$ is a $4n_d \times 1$ vector. The matrices of the single elements can be assembled following the classical steps of FEA, getting the global stiffness and mass matrices and load vector. The static and free dynamics problems of the beam can be written respectively as:

$$\mathbf{K}_{FE}\mathbf{d}_{FE} = \mathbf{P}_{FE}, \quad \left(\mathbf{K}_{FE} - \omega^2\mathbf{M}_{FE}\right)\mathbf{d}_{FE} = \mathbf{0} \tag{3.79}$$

where finally $\mathbf{K}_{FE}$ and $\mathbf{M}_{FE}$ are $2n_dn_z \times 2n_dn_z$ matrices and $\mathbf{P}_{FE}$ and $\mathbf{d}_{FE}$ are $2n_dn_z \times 1$ vectors.

Once the matrices are obtained, in case global boundary conditions involving all the nodes of the end sections are applied, it is possible to proceed in the classical way deleting from the matrices the rows and the columns in correspondence of the restraints and solving the problem, thus finding $\mathbf{d}_{FE}$ (and also ω^2 for dynamics) and reconstructing the unknown amplitude functions through Eq. (3.72).

On the other hand, if one wants to assign non-standard restraints (which is the main reason for using this approach), the constrained problem has to be written, similarly to what was done in the cross-section analysis with a different goal. To explain it, in Fig. 3.3 a vertical support is applied in the point P at the middle of the bottom flange (in addition to the global restraints at the end sections). From Eq. (3.1), one can write:

$$v(s_P, z_P) = \sum_{k=1}^{K} \bar{v}_k(s_P)\varphi_k(z_P) = \bar{v}_1(s_P)\varphi_1(z_P) + \ldots + \bar{v}_{n_d}(s_P)\varphi_{n_d}(z_P) = 0 \quad (3.80)$$

where the different $\bar{v}_k(s_P)$ are known from the cross-section analysis. Using the FE discretization of Eq. (3.72), it is possible to rewrite Eq. (3.80) as:

$$\begin{aligned} v(s_P, z_P) &= \bar{v}_1(s_P)\varphi_1(z_P) + \ldots + \bar{v}_{n_d}(s_P)\varphi_{n_d}(z_P) \\ &= \bar{v}_1(s_P)d_{1,11} + \ldots + \bar{v}_{n_d}(s_P)d_{n_d,11} = 0 \end{aligned} \quad (3.81)$$

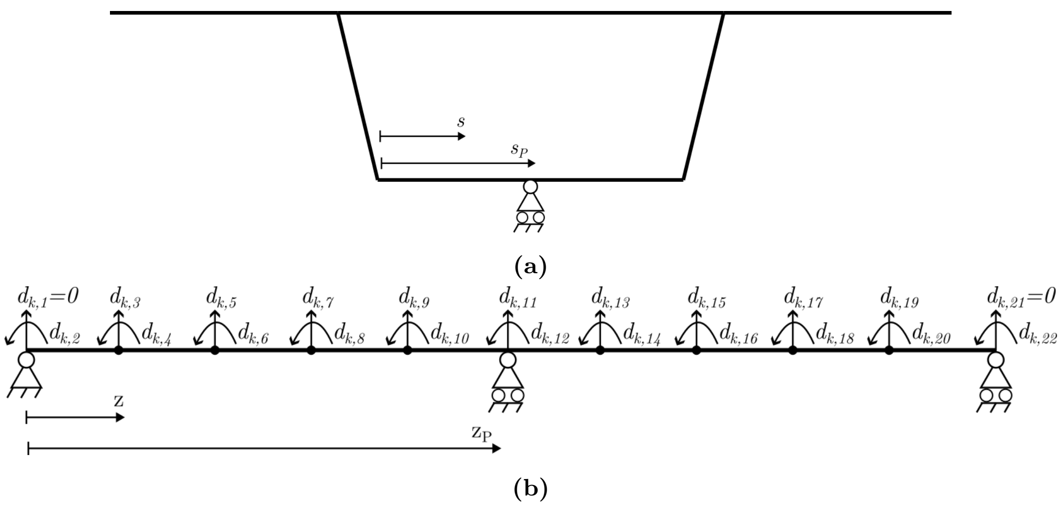

Figure 3.3. Example of punctual restraint on the TWB applied in a point at $z = L/2$: (a) cross-section at $z = L/2$; (b) longitudinal view with $n_z = 11$ nodes.

From Eq. (3.81), one can write one of the generalized displacements (slave) in function of the others (master) as:

$$
\begin{aligned}
d_{7,11} = -\frac{1}{\bar{v}_7(s_P)} & \left[\bar{v}_1(s_P)d_{1,11} + \ldots + \bar{v}_6(s_P)d_{6,11}\right. \\
& \left. + \bar{v}_8(s_P)d_{8,11} + \ldots + \bar{v}_{n_d}(s_P)d_{n_d,11}\right]
\end{aligned}
\tag{3.82}
$$

where the choice of $k = 7$ is not casual, since the slave node has to be selected in order to have $\bar{v}_i(s_P)$, which is $\bar{v}_7(s_P)$ in the example, different from 0. This means that one can write $\mathbf{d}_{FE} = \mathbf{\Gamma}_{FE}\mathbf{d}_{FE,M}$ where:

$$
\begin{aligned}
\mathbf{d}_{FE} &= \mathbf{d_{1,2}}, \mathbf{d_{1,3}}, \ldots, \mathbf{d_{1,20}}, \mathbf{d_{1,22}}, \ldots, \mathbf{d_{7,10}}, \mathbf{d_{7,11}}, \mathbf{d_{7,12}}, \ldots, \mathbf{d_{39,22}} \\
\mathbf{d}_{FE,M} &= \mathbf{d_{1,2}}, \mathbf{d_{1,3}}, \ldots, \mathbf{d_{1,20}}, \mathbf{d_{1,22}}, \ldots, \mathbf{d_{7,10}}, \mathbf{d_{7,12}}, \ldots, \mathbf{d_{39,22}}
\end{aligned}
\tag{3.83}
$$

In this example with global restraints at the end sections and vertical support added in P, the vector $\mathbf{d}_{FE}$ has dimension $2n_d n_z - 2n_d$, while the vector $\mathbf{d}_{FE,M}$ is a $2n_d n_z - 2n_d - 1$.

In order to generalize the procedure in case a generic number of non-standard supports are applied on the beam, Eq. (3.81) can be written as:

$$
\mathbf{A}_{FE}\mathbf{d}_{FE} = \mathbf{s} \rightarrow \begin{bmatrix} \mathbf{A}_{FE,M} & | & \mathbf{A}_{FE,S} \end{bmatrix} \begin{bmatrix} \mathbf{d}_{FE,M} \\ -- \\ \mathbf{d}_{FE,S} \end{bmatrix} = \mathbf{s}
\tag{3.84}
$$

where, if n_c is the number of introduced punctual restraints, $\mathbf{A}_{FE,M}$ has dimensions $n_c \times 2n_d n_z - n_c$ in case no global restraints are present while it is a $n_c \times 2n_d n_z - 2n_d - n_c$ matrix if also global restraints are applied at the end sections. On the other hand, $\mathbf{A}_{FE,S}$ is always a $n_c \times n_c$ non-singular matrix and $\mathbf{s}$ in a vector of n_c components accounting for possible settlements. As a consequence, the "master" generalized displacements are either $2n_d n_z - n_c \times 1$ or $2n_d n_z - 2n_d - n_c \times 1$ vectors while the "slave" generalized displacements are always $n_c \times 1$ vectors; so Eq. 3.84 can be rewritten as:

$$
\begin{cases}
\mathbf{d}_{FE,M} = \mathbf{d}_{FE,M} \\
\mathbf{A}_{FE,M}\mathbf{d}_{FE,M} + \mathbf{A}_{FE,S}\mathbf{d}_{FE,S} = \mathbf{s} \\
\rightarrow \mathbf{d}_{FE,S} = -\mathbf{A}_{FE,S}^{-1}\mathbf{A}_{FE,M}\mathbf{d}_{FE,M} + \mathbf{A}_{FE,S}^{-1}\mathbf{s}
\end{cases}
\tag{3.85}
$$

and finally, it is possible to write:

$$
\mathbf{d}_{FE} = \mathbf{\Gamma}_{FE}\mathbf{d}_{FE,M} + \hat{\mathbf{s}} \rightarrow \begin{bmatrix} \mathbf{d}_{FE,M} \\ -- \\ \mathbf{d}_{FE,S} \end{bmatrix} = \begin{bmatrix} \mathbf{I} \\ -- \\ -\mathbf{A}_{FE,S}^{-1}\mathbf{A}_{FE,M} \end{bmatrix} \mathbf{d}_{FE,M} + \begin{bmatrix} \mathbf{0} \\ -- \\ -\mathbf{A}_{FE,S}^{-1}\mathbf{s} \end{bmatrix}
\tag{3.86}
$$

where the matrix $\mathbf{\Gamma}_{FE}$ can have dimensions $2n_dn_z \times 2n_dn_z - n_c$ or $2n_dn_z - 2n_d \times 2n_dn_z - 2n_d - n_c$ and it is used to obtain the constrained stiffness and mass matrices and load vector $\mathbf{K}_{FE,r} = \mathbf{\Gamma}_{FE}^T\mathbf{K}_{FE}\mathbf{\Gamma}_{FE}$, $\mathbf{M}_{FE,r} = \mathbf{\Gamma}_{FE}^T\mathbf{M}_{FE}\mathbf{\Gamma}_{FE}$ and $\mathbf{P}_{FE,r} = \mathbf{\Gamma}_{FE}^T\mathbf{P}_{FE}$ (the subscript r means reduced). Doing that, the static and free dynamic problems for the beam with non-standard supports can be rewritten respectively as:

$$\mathbf{K}_{FE,r}\mathbf{d}_{FE,M} = \mathbf{P}_{FE,r}, \quad \left(\mathbf{K}_{FE,r} - \omega^2\mathbf{M}_{FE,r}\right)\mathbf{d}_{FE,M} = \mathbf{0} \tag{3.87}$$

and once the generalized displacements (and the angular frequency in dynamics) are obtained, the solution can be reconstructed.

3.2.4 Case study

As already mentioned, the system under analysis is constituted by a simply supported elastic beam having initial length L and boxed cross-section with a single cell. This kind of viaduct is really widespread in Italy as it was typically used for highways realized around the 80s. It is a slender beam realized in post-tensioned reinforced concrete and some typical problems of this kind of structures are the loss of pre-stress in the steel strands and the opening of cracks due to bending in the midspan or due to shear in correspondence of the end sections; if the intensity of these phenomena becomes important, the structure could also start to manifest a nonlinear behavior.

The beam under study is part of the San Nicola Viaduct of the A24 highway in Italy and its fundamental geometrical and mechanical properties are resumed in Tab. 3.1 where L is the length of the beam, b_1 is a representative length equal to the first branch of the upper flange, used in Sect. 3.4, A and I are the area and moment of inertia (with respect to the central axis of inertia along X) of the cross-section, ρ_c is the specific weight of the material (reinforced concrete), m_{tot} is the total mass of the bridge deck, E is the Young modulus and ξ_j is the considered modal damping coefficient. In Fig. 3.4 some more details on the measures of the cross-section are given.

Table 3.1. Geometrical and mechanical properties of the TWB case study.

L (m)	b_1 (m)	A (m^2)	I (m^4)	ρ_c (kN/m^3)	m_{tot} (ton)	E (N/m^2)	ξ_j
40.5	3.15	5.64	3.51	25	571	3.108×10^{10}	0.1%

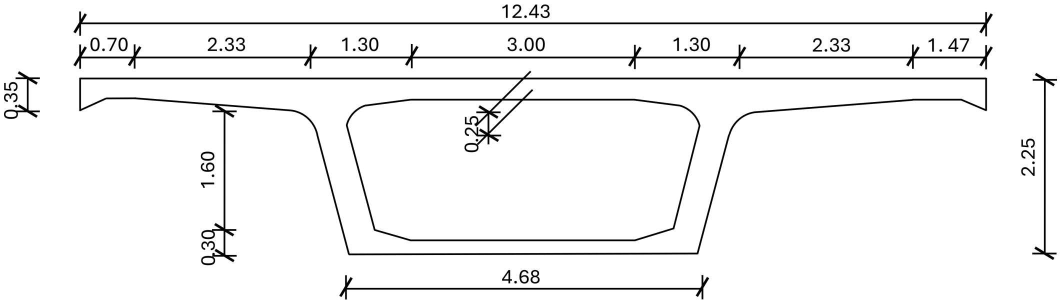

Figure 3.4. Measurements (in m) of the cross-section for the TWB case study.

3.2.5 Deformation modes

The procedure developed in Sect. 3.2.2 is here applied for the beam having the properties reported in Sect. 3.2.4. The deformation modes, fundamental for all the analyses, are here reported and discussed, based on their classification on conventional, extensional and shear modes.

Starting from conventional modes, i.e. those obtained from the 1^{st} PEP, which, as already written, are the most important modes in most of the cases, the first 8 are reported in Fig. 3.5. One can immediately notice that the first 4 are the rigid modes representing respectively the extension in the longitudinal direction (strictly speaking this mode was found solving the WEP, however it has to be included among the conventional ones), the translation in the global X and Y directions and the rotation around an arbitrary point. Beyond them, other 4 conventional modes are represented, and they can either be of distortional or local type. As explained in Sect. 3.2.2, the out-of-plane components $\Omega_k(s)$ are linear according to the way they were obtained.

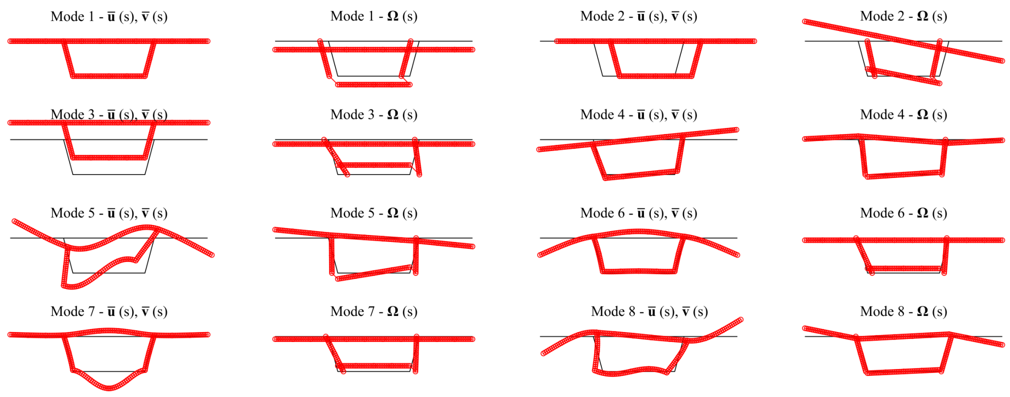

Figure 3.5. Some conventional deformation modes for the TWB case study.

Moving to extensional modes, which comes from the 2^{nd} PEP, the first 8 are illustrated in Fig. 3.6 and the extensional nature of these modes is evident from the elongation of the elements of the cross-section. They are orthogonal to the modes of the 1^{st} PEP since that was the condition imposed to find them, and they just present in-plane components $\bar{u}_k(s)$ and $\bar{v}_k(s)$.

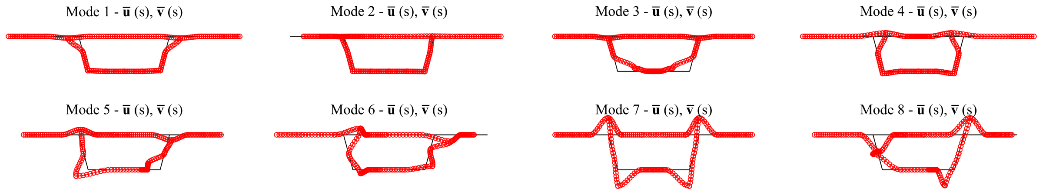

Figure 3.6. Some extensional deformation modes for the TWB case study.

Finally, the first 5 shear modes of the WEP are depicted in Fig. 3.7 (beyond the rigid one which was included in the conventional ones). In this case only out-of-plane components $\bar{w}_j(s)$ exist. However, for this case study, these components are not really useful to improve the system response, as explained later.

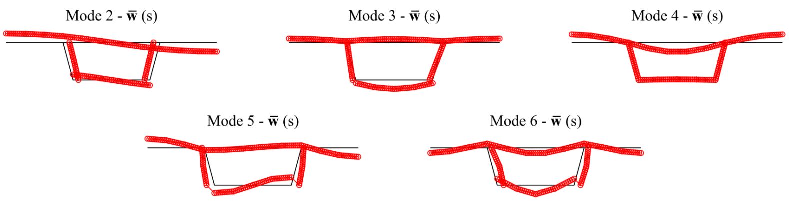

Figure 3.7. Some shear deformation modes for the TWB case study.

3.2.6 Statics

The equations developed in Sect. 3.2.3 are here applied under different static loading scenarios considering just global boundary conditions of simply supported beam, while punctual restraints are considered in the following section. This section is needed to test the model and to appreciate its capacity to consider non-classical loading conditions which could not be considered in simpler beam theories (or they could be taken into account, albeit less accurately) as loads that are not constantly applied along the global transverse direction of the beam, involving the deformation of the cross-section in and out-of-plane. After this validation of the model, in Sect. 3.3.1 the static response of the TWB obtained through GBT-D is compared with experimental results.

The validation of the model is here realized by comparing its results to those obtained on a beam model realized through a FE commercial software as SAP2000 [133]. Without going into too much detail, which is not the objective of this Thesis, the beam was modeled in SAP2000 using quadrilateral shell elements having the same thickness of the different pieces of the real beam and with the same type of material and it is shown in Fig. 3.8. The cross-section dimensions are those depicted in Fig. 3.4 and its total length is the same of Tab. 3.1. The shell elements were discretized in a convenient yet important number of FE with a total number of almost 21000 joints and 19000 shells. The restraints are applied at the two end sections in order to simulate the same conditions of the GBT-D model.

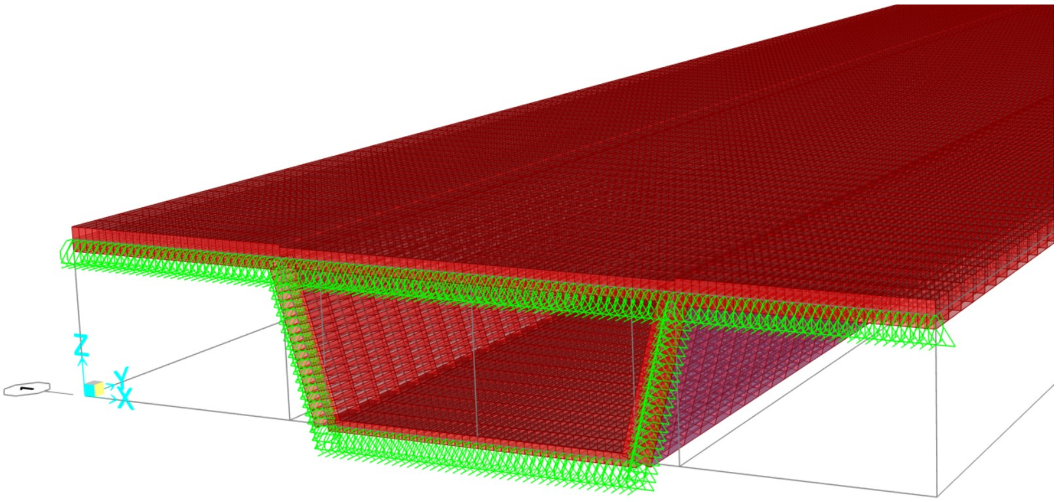

Figure 3.8. Particular of the TWB case study modeled through shell elements in SAP2000.

In Fig. 3.9 the load cases which were tested are resumed. They were applied along the entire length of the beam and are representative of classical loading scenarios, as can be the uniformly distributed load on the top flange or non-classical ones, which can act on it in some moments of its life, like the torsional one.

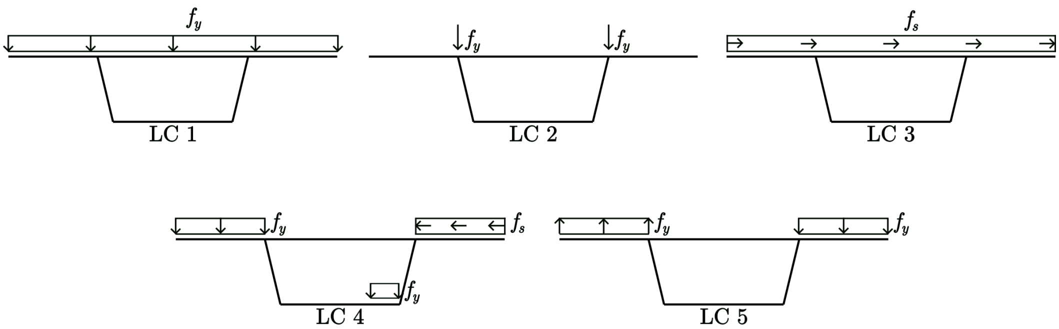

Figure 3.9. Load cases considered in statics for the TWB case study.

In Tab. 3.2, the displacements of some particularly interesting points are recorded and compared to those detected in correspondence of the same point for the FE model realized with SAP2000. The displacements are referred to the global reference system (capital letters (U_i, V_i, W_i) are used) for a direct comparison with those found with the software. The position of the monitored points in the cross-section is shown in Fig. 3.10, while their longitudinal abscissa is reported in the same figure in parentheses.

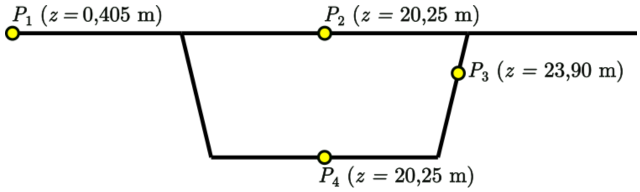

Figure 3.10. Monitored points in statics for the TWB case study.

Moving to results reported in Tab. 3.2, no differences were found using the different approaches MA1, MA2 and MA3 and, as can be seen by examining them, the same consideration are valid for all the considered load distributions. In particular, looking at the case named as LC1, for all the considered points (P_1, P_2, P_3, P_4), the vertical displacement V_{Pi}, which is the most important one due to the nature of the load, has almost the same value between GBT-D and SAP2000. Also the longitudinal displacements W_{Pi} show a good agreement. The horizontal one is not as good as the other two components, but it is evidently totally negligible compared to their values; the same holds true for the other load cases with their prevalent displacements. Moreover, no significant difference was found by accounting for only conventional modes or adding extensional modes too; on the contrary, if also shear modes are considered, a bigger difference with respect to FE results arises, meaning that for this type of beam (not short) and for this type of loads (not directly acting along z), their contribution has to be neglected.

3.2.7 Free dynamics

The free dynamics behavior of the TWB under study is here analyzed, considering different numbers of deformation modes to understand the minimum needed to correctly identify the vibration modes and also considering different types of restraints (global or local ones). A comparison is made with the same FE model realized with SAP2000 shown in Sect. 3.2.6. In addition to the information reported there, for the calculation of the dynamical properties, it should be specified that two mass sources were considered: the first one is the self-weight of the beam (reported in Tab. 3.1) and the second one is a distributed mass on the top flange of the TWB, comparable to a 10 cm layer of road pavement with a mass of 2.5 ton/m^3 representative of a real scenario.

Table 3.2. Displacement (in m) of points of Fig. 3.10 under different static load cases.

		P_1			P_2		
		U_{P1}	V_{P1}	W_{P1}	U_{P2}	V_{P2}	W_{P2}
LC 1	GBT-D	2.0×10^{-10}	-1.4×10^{-3}	1.6×10^{-3}	6.5×10^{-9}	-3.9×10^{-2}	0.0
	SAP2000	-7.0×10^{-6}	-1.5×10^{-3}	1.5×10^{-3}	0.0	-4.0×10^{-2}	0.0
LC 2	GBT-D	5.2×10^{-8}	-4.2×10^{-4}	5.6×10^{-4}	1.5×10^{-6}	-1.3×10^{-2}	0.0
	SAP2000	-2.3×10^{-6}	-4.5×10^{-4}	5.2×10^{-4}	0.0	-1.4×10^{-2}	0.0
LC 3	GBT-D	9.0×10^{-5}	4.4×10^{-5}	1.2×10^{-3}	2.8×10^{-3}	-6.8×10^{-9}	0.0
	SAP2000	1.1×10^{-4}	4.6×10^{-5}	1.2×10^{-3}	3.2×10^{-3}	0.0	0.0
LC 4	GBT-D	-3.2×10^{-5}	-7.4×10^{-4}	2.3×10^{-4}	-9.6×10^{-4}	-1.4×10^{-2}	0.0
	SAP2000	-3.9×10^{-5}	-7.6×10^{-4}	1.9×10^{-4}	-1.1×10^{-3}	-1.4×10^{-2}	0.0
LC 5	GBT-D	1.6×10^{-5}	3.5×10^{-4}	3.7×10^{-5}	4.6×10^{-4}	-5.5×10^{-9}	0.0
	SAP2000	1.7×10^{-5}	3.4×10^{-4}	4.4×10^{-5}	4.6×10^{-4}	0.0	0.0

		P_3			P_4		
		U_{P3}	V_{P3}	W_{P3}	U_{P4}	V_{P4}	W_{P4}
LC 1	GBT-D	-4.2×10^{-5}	-3.7×10^{-2}	6.8×10^{-5}	2.7×10^{-9}	-3.9×10^{-2}	0.00
	SAP2000	-3.7×10^{-5}	-3.9×10^{-2}	6.0×10^{-5}	0.00	-4.0×10^{-2}	0.00
LC 2	GBT-D	1.6×10^{-6}	-1.3×10^{-2}	2.3×10^{-5}	2.0×10^{-6}	-1.3×10^{-2}	0.0
	SAP2000	6.5×10^{-7}	-1.3×10^{-2}	2.1×10^{-5}	0.0	-1.4×10^{-2}	0.0
LC 3	GBT-D	2.5×10^{-3}	-3.6×10^{-4}	1.3×10^{-4}	2.2×10^{-3}	-8.2×10^{-9}	0.0
	SAP2000	3.0×10^{-3}	-4.0×10^{-4}	1.3×10^{-4}	2.7×10^{-3}	0.0	0.0
LC 4	GBT-D	-7.3×10^{-4}	-1.2×10^{-2}	-1.0×10^{-5}	-2.7×10^{-4}	-1.4×10^{-2}	0.0
	SAP2000	-8.6×10^{-4}	-1.3×10^{-2}	-1.0×10^{-5}	-4.0×10^{-4}	-1.4×10^{-2}	0.0
LC 5	GBT-D	1.1×10^{-4}	-2.0×10^{-3}	-2.4×10^{-6}	-4.0×10^{-4}	-2.4×10^{-8}	0.0
	SAP2000	1.0×10^{-4}	-1.9×10^{-3}	-2.5×10^{-6}	-4.6×10^{-4}	0.0	0.0

LC 1: Uniform vertical load $f_y = -10$ kN/m^2 on the upper flange.
LC 2: Linear vertical load $f_y = -20$ kN/m between the upper and inclined flanges.
LC 3: Uniform horizontal load of $f_s = 10$ kN/m^2 on the upper flange.
LC 4: Uniform vertical load of $f_y = -10$ kN/m^2 on the upper and lower flanges and horizontal load of $f_s = -10$ kN/m^2 in part of the upper flange.
LC 5: Uniform "torsional" vertical load $f_y = 10$ kN/m^2 on the upper flange.

Results in terms of frequencies and Modal Assurance Criterion (MAC) for the beam with global restraints are resumed in Tab. 3.3, and in Fig. 3.11 five vibration modes are shown (the first three global bending modes, the first torsional one and another mode mainly involving the upper flange). For completeness, the MAC is a well-known way to compare two vibration modes furnishing a measure of the consistency between them as a scalar value between 0 and 1 going from a completely inconsistent to a consistent correspondence (more details can be found in [4, 5]). If two generic modes $\boldsymbol{\phi}_j$ and $\boldsymbol{\phi}_k$ are considered (note that a general notation was used to indicate vibration modes not necessarily related to the one used in previous or following sections), the MAC in its classical form reads:

$$\mathrm{MAC}_{jk} = \frac{\boldsymbol{\phi}_j^T \boldsymbol{\phi}_k \boldsymbol{\phi}_k^T \boldsymbol{\phi}_j}{\boldsymbol{\phi}_j^T \boldsymbol{\phi}_j \boldsymbol{\phi}_k^T \boldsymbol{\phi}_k} \tag{3.88}$$

Its values in Tab. 3.3 are referred to the same vibration mode between GBT-D and SAP2000 (in other words they are the terms on the diagonal of the MAC matrix) and are calculated for each case with respect to the case called SAP1d, which is taken as benchmark.

All the models based on GBT-D in Tab. 3.3 are realized dividing the section in $n_e = 19$ elements (and as a consequence $n_n = 19$ nodes) and, if not specified, all the conventional modes, equal to $3n_n - n_e = 38$ plus the rigid mode representing the uniform extension along z, are considered. In addition, the model labeled as SAP2d, realized with punctual restraints and stiffeners at the end sections, is used in order to have a comparison with the model SAP1d; the stiffeners, which are typically placed in this type of beams to prevent from an excessive deformation, were realized through thick vertical plates modeled as shell elements in correspondence of the end sections.

From Tab. 3.3 it is evident that all the models are equivalent for the 1^{st} bending and the 1^{st} torsional modes with close values of frequencies and MAC almost equal to 1. The only model with a higher difference on the frequency of the 1^{st} torsional mode is GBT5d, i.e. the model whose member analysis was realized through FE (called MA3) which also accounts for the first 4 extensional modes in the cross-section analysis; however, this value is closer to the one determined from experimental data in Sect. 3.3.2 and this can be due to a more precise approximation of the membrane extension of the cross-section. On the other hand, higher differences are found comparing the frequencies of the 2^{nd} bending mode for the different models.

Something more can be said about the minimum number of deformation modes necessary to properly describe the different vibration modes. Given that convergence analyses are performed in Sect. 3.3.2, from GBT1d and GBT4d, where 9 and 8 conventional modes are kept respectively, it is evident that a small number of them is sufficient to have a clear representation of the free dynamics of the beam. Finally, about GBT2d (member analysis performed with the function bvp4c from Matlab), a proper initial guess has to be imposed to the solution, and a good idea is to use an adequate guess obtained solving the static problem.

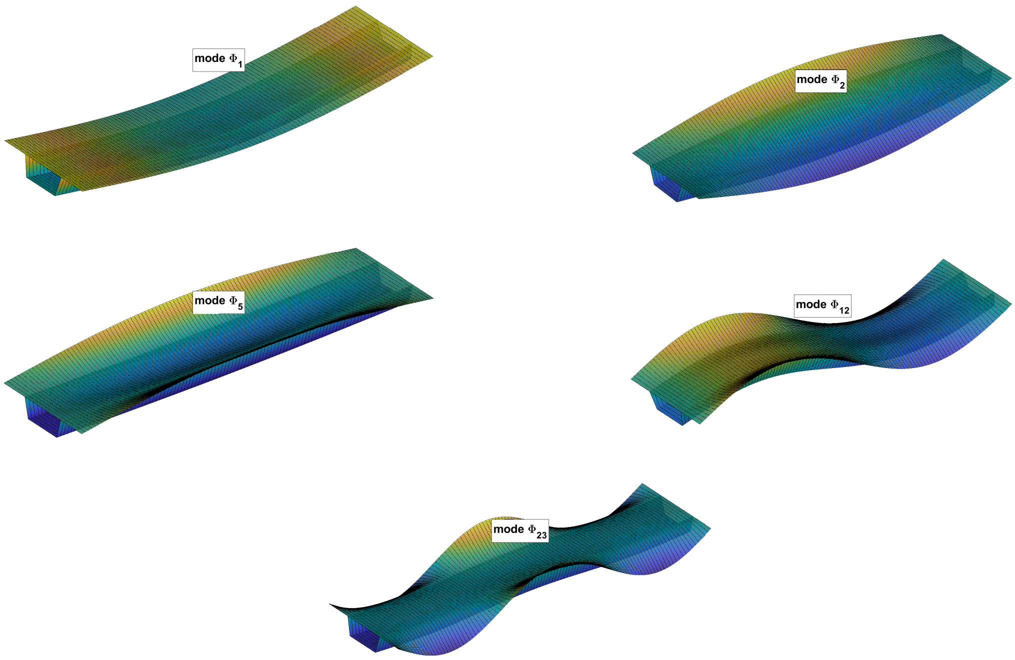

Figure 3.11. Some vibration modes of the TWB case study named after their longitudinal variation $\mathbf{\Phi}_j(z)$ found through the MA1 approach.

Table 3.3. Modal properties of the TWB case study found with GBT-D (and SAP2000) for different cases with global restraints.

mode	SAP1d		SAP2d		GBT1d		GBT2d	
	f (Hz)	-	f (Hz)	MAC	f (Hz)	MAC	f (Hz)	MAC
1^{st} BEND	2.30	-	2.27	0.97	2.39	1.00	2.39	1.00
1^{st} TORS	7.22	-	7.16	0.98	7.27	0.97	7.26	0.97
2^{nd} BEND	8.10	-	7.70	0.88	8.89	0.99	8.83	1.00

mode	GBT3d		GBT4d		GBT5d	
	f (Hz)	MAC	f (Hz)	MAC	f (Hz)	MAC
1^{st} BEND	2.37	1.00	2.38	0.99	2.37	0.99
1^{st} TORS	7.20	0.98	7.26	0.98	6.86	0.94
2^{nd} BEND	8.77	0.99	9.08	0.99	8.55	0.97

SAP1d: SAP2000 model with shell elements with global restraints.
SAP2d: SAP2000 model with shell elements with two punctual hinges at each end section and stiffeners.
GBT1d: simply supported beam (global restraints), 9 conv. modes solved with MA1.
GBT2d: simply supported beam (global restraints), conv. modes solved with MA2.
GBT3d: simply supported beam (global restraints), conv. modes solved with MA3.
GBT4d: simply supported beam (global restraints), 8 conv. modes solved with MA3.
GBT5d: simply supported beam (global restraints), conv. and 4 ext. modes solved with MA3.

Furthermore, in Tab. 3.4, results are reported for the beam with punctual restraints, whose vibration modes are represented in Fig. 3.12. No stiffeners are modeled in the SAP2000 model, in order to test the reliability of the GBT-D model with non-standard supports developed in Sect. 3.2.3. Three models are compared: SAP1p realized with SAP2000 with punctual restraints and the same mesh seen in the distributed case, GBT1p and GBT2p with the local restraints written in the table, either with only conventional modes or with the addition of all the available extensional modes respectively. In this case, a different discretization for the elements of the cross-section in the GBT-D model was chosen ($n_e = 11$, thus the number of conventional and extensional modes is $22 + 1$ and 11 respectively). The MAC with respect to the benchmark SAP1p is almost perfect and also the frequencies match really well, with higher differences for the 2^{nd} bending mode as highlighted for the case with distributed restraints.

Table 3.4. Modal properties of the TWB vase study found with GBT-D for different cases with punctual restraints.

mode	SAP1p		GBT1p		GBT2p	
	f (Hz)	-	f (Hz)	MAC	f (Hz)	MAC
1^{st} BEND	2.26	-	2.34	1.00	2.34	1.00
1^{st} TORS	7.18	-	7.23	0.99	7.16	0.99
2^{nd} BEND	7.46	-	8.23	0.98	8.18	0.97

SAP1p: SAP2000 model with shell elements two punctual hinges at each end section.
GBT1p: beam two punctual hinges at each end section, conv. modes solved with MA3.
GBT2p: beam two punctual hinges at each end section, conv. and ext. modes solved with MA3.

To sum up, the comparison of modal properties between the different GBT-D and FE models, together with the comparison of displacements realized in Sec. 3.2.6, proves the accuracy of the GBT-D models to describe the beam behavior both in statics and in dynamics for different kinds of support conditions (global or punctual). Moreover, the small number of conventional deformation modes needed to describe different scenarios, together with the lower computational cost (once the model is realized) and the possibility to evaluate how results vary by simply changing some parameters, makes the GBT-D model valid and even more convenient than classical FE models realized with commercial software.

3.3 Monitoring

In this section, the same viaduct of Sect. 3.2.4, the San Nicola Viaduct, is considered from an experimental point of view. In particular, data acquired in a previous

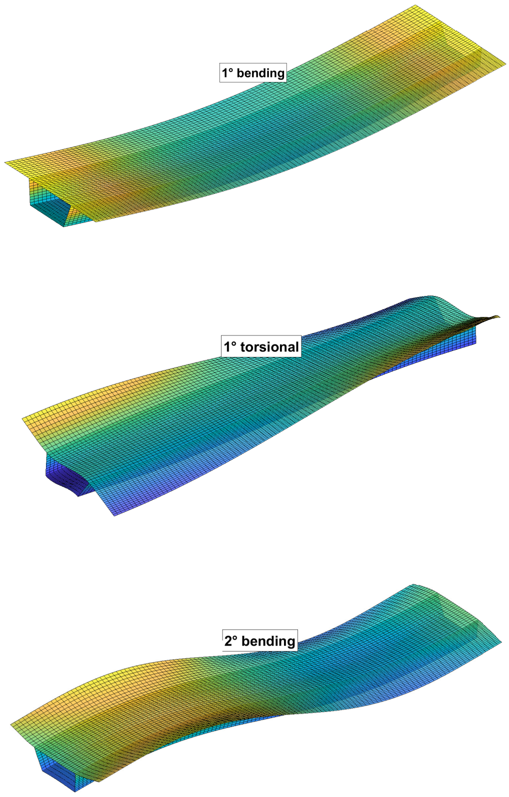

Figure 3.12. Some vibration modes of the TWB case study with punctual restraints found through the MA3 approach.

campaign are processed and their results are compared to those found in Sect. 3.2.6 for statics and in Sect. 3.2.7 for dynamics. The goal is to check if the GBT-D model is adequate to describe the beam response and to verify if any damage is present on it.

The experimental campaign from which data were collected was realized in 2019 by the research group of Structural Mechanics at University of L'Aquila, led by Professor Angelo Luongo. During the campaign, some viaducts of the highway A24 in Italy were tested: among them in this Thesis this span of the San Nicola Viaduct was studied.

3.3.1 Statics

In this section, results coming from the static load test on the bridge are processed and compared to those found by applying the model developed in Sect. 3.2.1 with the same type of static load. In particular, the goal is to check if the model is able to track the displacements found on the beam during all the phases of loading and to establish the minimum number of deformation modes that ensures response convergence.

The static test was realized placing some trucks with known weight along and across the upper flange of the beam and measuring the sag in some control points. The test configuration is shown in Fig. 3.13 where the trucks are identified as A_i, B_i and C_i, while the measurements points as P_i.

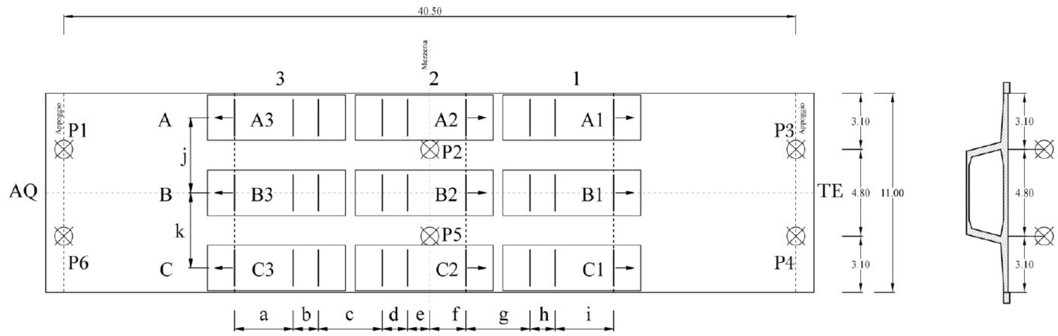

Figure 3.13. Position of trucks and measurement points in the static load test realized in 2019 (taken from [76]).

In particular, the trucks were positioned on the bridge during three phases: first the column A, then the column B and finally the column C. A certain amount of time was left between one phase and the next in order to allow the displacements to settle; they were measured through high precision digital electronic levels.

The results collected during the test were compared to those found through the GBT-D model, SAP2000 and an Euler-Bernoulli model, to understand if they are able to describe all the three phases of loading. The experimental displacements in points P_2 and P_5 were taken as the absolute measured displacements in correspondence of the same points minus the mean value of the displacements measured at the end sections of the bridge deck (P_1 and P_3 for P_2, P_4 and P_6 for P_5) since all the analytical and numerical considered models are realized with the hypothesis of perfect support (no vertical displacement). Finally, the displacement in correspondence of the center point of the upper flange of the bridge P_m was calculated as an average of measures in P_2 and in P_5.

Additional details are here given in order to provide a clear view of the results. The value of the elastic modulus E, already reported in Tab. 3.4 was taken from the available documentation. The mean load of each truck is approximately of 24 tons (about 235 kN) applied on three axles as shown in the figure. Since it was checked that no significant difference occurs, they were applied as distributed loads in models based on GBT-D and SAP2000, while on the Euler-Bernoulli beam model they were effectively considered as punctual loads; moreover, the latter model was adapted to consider also the torsional effect due to the eccentric position of the trucks with respect to the beam axis.

Results are reported in Fig. 3.14 as moment-sag diagrams (the moment was calculated through static schemes) and convergence analysis for the GBT-D model. The curve for the GBT-D case where extensional deformation modes were added to conventional ones was not reported since, at least at midspan, it is perfectly coincident with the case with just conventional modes. In the legend of the plots, the first two entries are the GBT-D models with conventional modes and global or punctual restraints respectively, the third one is about experimental measures, the fourth is related to the Euler-Bernoulli model and the last one comes from the SAP2000 model with global restraints (or, which is the same, with punctual restraint and stiffeners at the end sections).

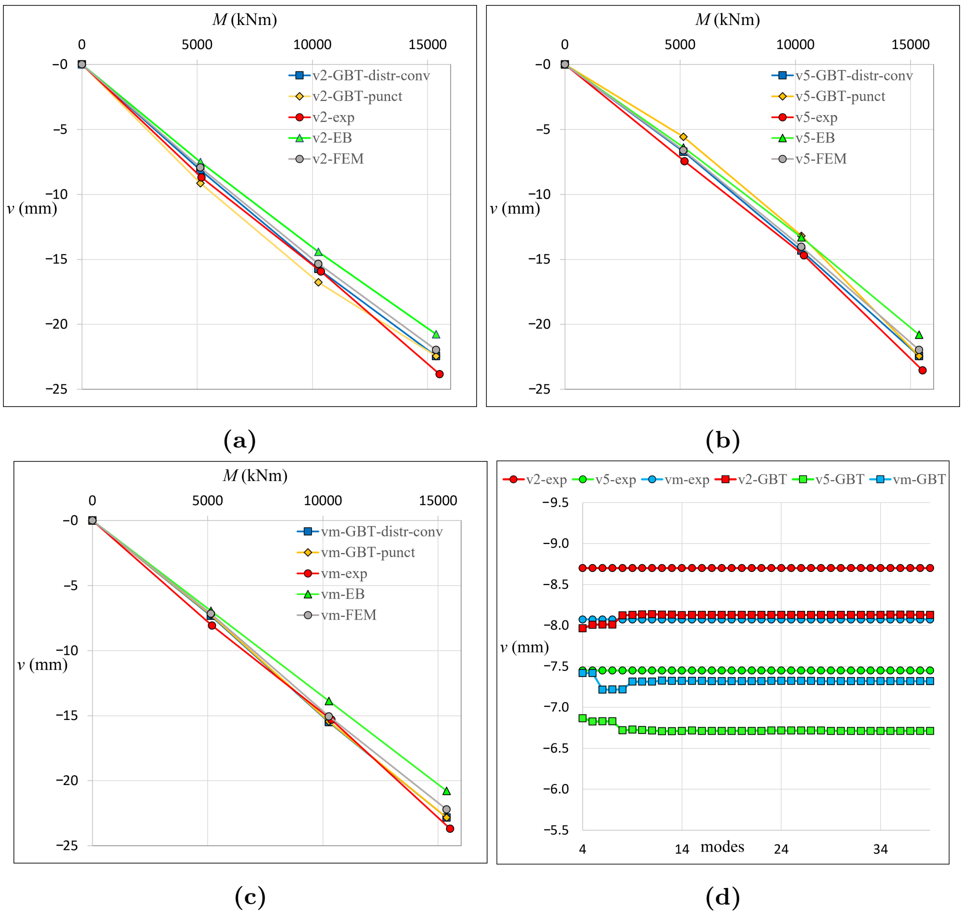

Figure 3.14. Moment-sag diagrams resulting from the application of trucks on the bridge deck for different models: (a) Vertical displacement in P_2; (b) Vertical displacement in P_5; (c) Vertical displacement in the center of the deck; (d) Convergence analysis for the GBT-D model.

Looking at the red curves, one can immediately say that the experimental behavior of the beam is linear, even if when the last column of trucks C is applied, a slightly nonlinear behavior seems to occur, probably linked to the opening of small cracks in the concrete or to an initial loss of pre-stress. Turning the attention to the models, a comparison of the two based on GBT-D shows that, even if they lead to the same results when all the trucks are applied on the bridge, they differ at the intermediate stages, i.e. when only the column of trucks A or A and B of Fig. 3.13 are applied, so that the load distribution is not symmetric: in these stages, the model based on punctual supports tends to overestimate the displacement in the point directly under the load (P_2) and to underestimate it in the point far from the load (P_5). This means that, since on the real bridge stiffeners are realized at the end sections as reinforced concrete plates, the model with global restraints is more accurate in capturing the beam response, while the model with punctual restraints does not really catch it. Moving to the Euler-Bernoulli model, it underestimates the beam displacements at all phases in all the monitored points, meaning that it could be used with an acceptable approximation for preliminary analyses, but more refined models (like the one based on GBT-D) have to be considered for precise analyses on this kind of beams. Subsequently, the model realized through the FE commercial software SAP2000 gives results really close to the GBT-D model, as also underlined in Sect. 3.2.6.

A final comment can be done on the apparent nonlinear behavior in some of the plots. Since all the models are linear, the different slope between one segment and another is necessarily due to some torsional effects, related to the fact that the load is increased, but it is not applied always in the same positions along the transversal direction of the beam. On the other hand, about the nonlinearity in the experimental curve previously mentioned, it looks like the experimental response of the bridge starts to be slightly nonlinear when the last column of trucks C is applied and this could be due to the high level of loads on the bridge which triggers the opening of some cracks at the bottom surface of the beam. A future work could be focused on the improvement of the GBT-D model to account for this material nonlinearity, like already done in some other works, to gain a clearer understanding of the phenomenon.

Finally, looking at Fig. 3.14(d), a convergence analysis on deformation modes is reported considering the displacements of the three points when the sole column of tracks A is applied. The comparison is between the experimentally measured values of the sag with respect to those obtained from the GBT-D model with distributed restraints, increasing the number of conventional modes from 4 (only the rigid ones) to 39. As can be seen, once almost 9 deformation modes are considered (thus just 5 non-rigid modes), the response converges to the experimental value, meaning that a small number of deformation modes is usually sufficient to describe the beam response.

3.3.2 Free dynamics

In this section, results coming from the dynamic test in operational condition are processed and compared to those found with the model developed in Sect. 3.2.1. In particular, the hypothesis is made that the low-intensity external excitation can be treated as white noise. Different boundary conditions were considered (global and punctual) to understand which are the most coherent with this type of structure as done for statics in Sect. 3.3.1.

The dynamic test was realized without directly exciting the bridge but making use of white noise which, by definition, is a signal having the same intensity at all frequencies, generated in this case with the aid of the irregular transit of a vehicle on the deck. The acceleration time histories were measured putting bi-axial accelerometers in some control points as shown in Fig. 3.15: they are oriented such that they can all track the acceleration in the direction of gravity and one between the longitudinal and the transverse components.

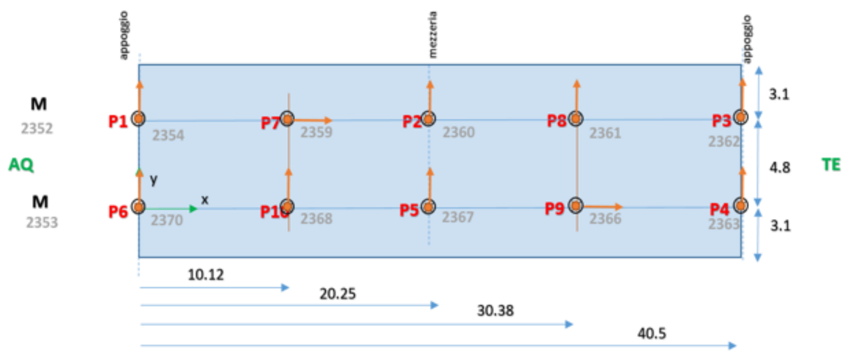

Figure 3.15. Position and orientation of accelerometers in the dynamic test realized in 2019 (taken from [76]).

To give some details, Force Balance Accelerometers (FBA) were used since they are highly sensitive to this kind of excitation, i.e. white noise on stiff structures; this statement was confirmed by other applications realized with the research group, being this devices able to record significant accelerations also on extremely stiff and massive structures as medieval masonry towers. The FBA were placed along two lines (in correspondence of the intersection between the top flange and the inclined ones) and connected by wires. The test lasted about 40 minutes, with a sampling frequency of 200 Hz.

Then, the accelerograms collected by the accelerometers were used to characterize the dynamics of the beam with the goal of determining natural frequencies, vibration modes and eventually modal damping ratios. The process which characterizes the free dynamics of the structure processing experimental data acquired in operational conditions, i.e. under white noise, goes under the name of Operational Modal Analysis (OMA). In particular, this can be performed both in frequency domain through the Frequency Domain Decomposition (FDD) or in time domain through the Stochastic Subspace Identification (SSI). Both techniques were used in this Thesis and compared to results found in Sect. 3.2. Just fundamental details are here given on these two methods since they are strongly consolidated in literature (some more details can be found in Sect. 2.2.2). For both types of analyses, trustworthy Matlab algorithms were used [88].

Starting from frequency domain, FDD can be seen as an extension of the peak peaking technique which is able to identify also close modes with high accuracy. In order to identify the modal parameters, the algorithms perform the following steps:

- The Power Spectral Density (PSD) matrix is estimated at discrete frequencies ω_i through Welch's averaged, modified periodogram method of spectral estimation (it involves sectioning the record, taking modified periodograms of these sections, and averaging them. The calculation of modified periodograms is explained in [141]).

- A Singular Value Decomposition (SVD) of the PSD is performed.

- The dominating peaks in the PSD are selected, manually or automatically, based on the value of the MAC between singular vectors and the estimate of the mode shape, to get the sought dynamical properties.

Results are better identified if the signal can be classified as white noise with small damping and for orthogonal mode shapes.

On the other hand, SSI, is an identification technique in the time domain. In this method the space state model is computed from output data with the states that are first estimated and the matrices which are successively obtained through Least Squares. Among the different SSI algorithm, the Covariance-driven SSI (SSI-COV) [16, 86, 103] was used and its main steps are here resumed:

- The covariance matrices of the output data are calculated.
- The block Toeplitz matrix is constructed from them and its SVD is performed.
- The matrices obtained from the SVD are used to identify the modal parameters solving an eigenvalue problem.
- A stability checking procedure is realized in order to determine the stability status of each mode obtained for two adjacent poles (meaning with this expression the states evaluated at two consecutive steps). Different cases can be obtained, involving a new pole, a stable one, a stable pole just for frequency and MAC or just for frequency and damping or just for frequency or even an unstable pole based on some chosen tolerances. Stable poles are selected among them.
- Finally, a cluster algorithm is realized in order to automatically collect the modes and hierarchically separate the physical ones, excluding the spurious modes which inevitably arise when high model orders are considered.

The best way to represent the identified modes is through the stabilization diagram which contains the frequencies along the x-axis and the order of the model on the y-axis.

Results are reported in Fig. 3.16 in terms of PSD for the FDD and in Fig. 3.17 in terms of the stabilization diagram for the SSI. Moreover, in Tab. 3.5, a comparison is made between results found using the two OMA methods and a reconstruction of the mode shapes based on the position of accelerometers of Fig. 3.15 is reported in Fig. 3.18. As can be seen, from Fig. 3.16 and Fig. 3.17, other modes are found with lower frequencies than those related to the bridge deck: they are mixed modes involving also the piers which were are not relevant for the present work.

First of all, comparing results obtained from experimental data in time and frequency domain, it is evident from Tab. 3.5 that they are equivalent in terms of frequency and mode shape. Some problems are encountered in the correct identification of modal damping coefficients with FDD, which is usually more difficult to

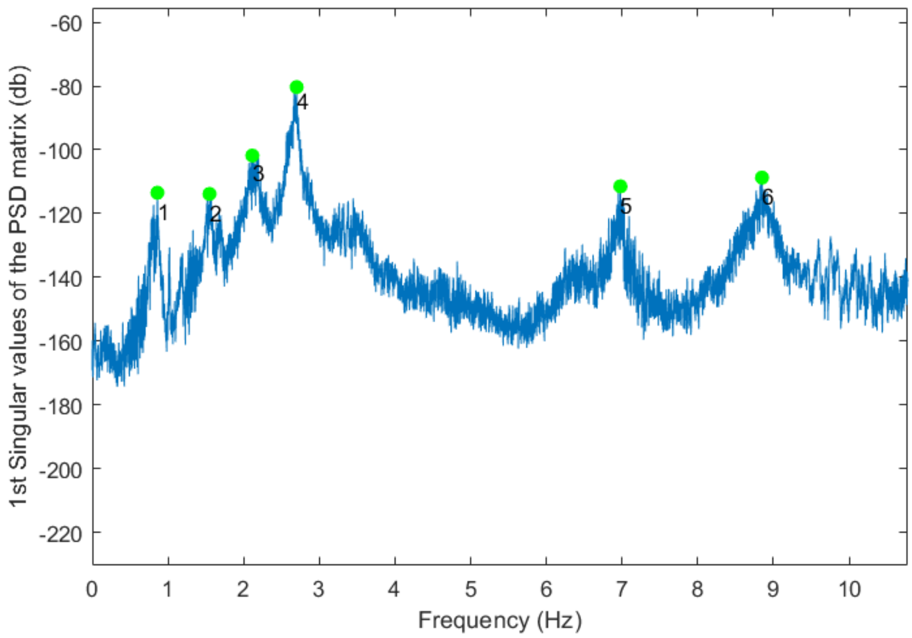

Figure 3.16. Power Spectral Density with identified vibrations modes using FDD on time series acquired during the experimental campaign of 2019.

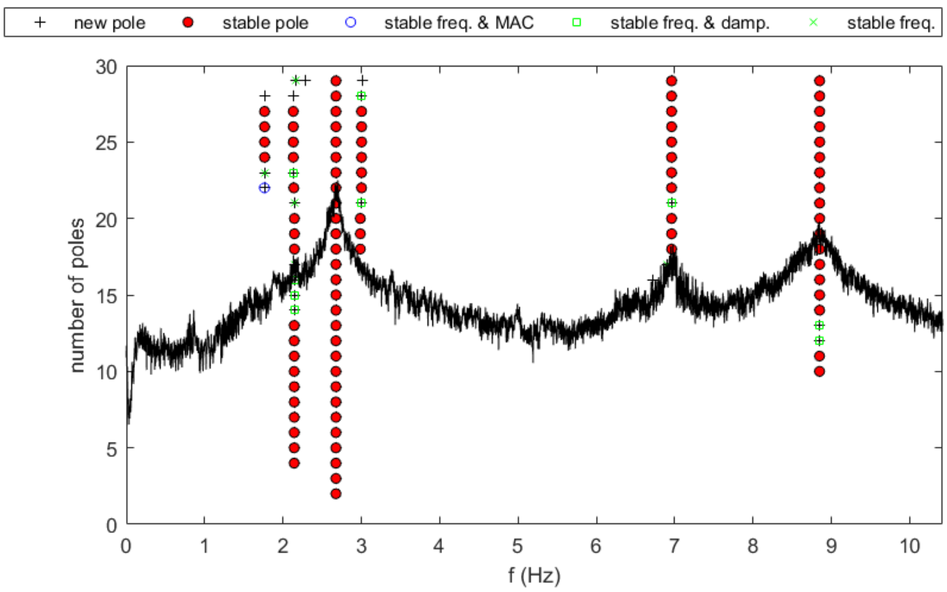

Figure 3.17. Stabilization Diagram with identified vibrations modes using SSI-COV on time series acquired during the experimental campaign of 2019.

estimate with these techniques, but this can be considered a minor problem for this analysis.

On the other hand, in Tab. 3.6, results obtained with OMA are compared to those found in Sect. 3.2 using the GBT-D with distributed (Tab. 3.3) and punctual (Tab. 3.4) restraints. The values of frequencies are almost the same among the three

Table 3.5. Modal properties of the beam case study found with OMA in frequency and time domains.

mode	FDD		SSI-COV		
	f (Hz)	ξ_j	f (Hz)	ξ_j	MAC
1^{st} BEND	2.70	1.32	2.68	1.26	1.00
1^{st} TORS	6.98	-	6.98	0.70	0.94
2^{nd} BEND	8.85	-	8.85	1.55	0.99

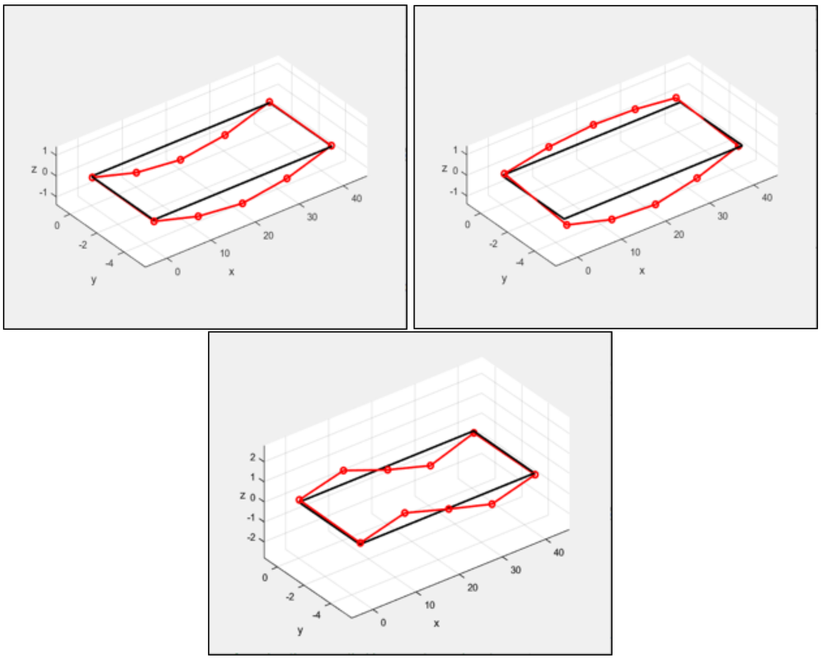

Figure 3.18. Schematic representation of vibration modes obtained through OMA (FDD or SSI-COV) on time series acquired during the experimental campaign of 2019.

Table 3.6. Modal properties of the beam case study found with OMA and GBT-D.

mode	OMA		GBTd		GBTp	
	f (Hz)	-	f (Hz)	MAC	f (Hz)	MAC
1^{st} BEND	2.70	-	2.37	0.99	2.34	0.95
1^{st} TORS	6.98	-	7.20	0.81	7.23	0.08
2^{nd} BEND	8.85	-	8.77	0.90	8.23	0.60

OMA: results obtained with SSI-COV in Tab. 3.5.
GBTd: results obtained with GBT3d in Tab. 3.3.
GBTp: results obtained with GBT1p in Tab. 3.4.

models, with the GBT models that underestimate the frequency for the bending modes and overestimate it for the torsional one: this could be due to the contribution of the adjacent decks, not considered in the model, which is stronger in bending than in torsion; however, looking at the MAC, it is evident that the model with distributed restraints can properly catch the free dynamics of the viaduct as also highlighted by comparing Fig. 3.11 with Fig. 3.18, while important differences are featured for the beam with punctual restraints especially for the mode shapes as can be seen from Fig. 3.12 and Fig. 3.18 which is in accordance with the value of the MAC, showing that the 1^{st} torsional mode is completely different and also the 2^{nd} bending mode is not the same. The explanation to these differences is the same given in statics: even if the real supports of the viaduct are represented by punctual restraints on the top of the piers, the presence of reinforced concrete stiffeners at the end-section is such that the actual boundary conditions are of global (or distributed) type.

To conclude, a convergence analyses is shown in Fig. 3.19 in order to check the minimum number of deformation modes necessary to have relevant vibration modes using as benchmarks the frequencies identified from the experimental records. The same conclusion drawn in statics hold also for dynamics, i.e. 4/5 deformation modes (in addition to the first 4 rigid ones) are enough to ensure convergence, underlying once again the low computational cost of this approach.

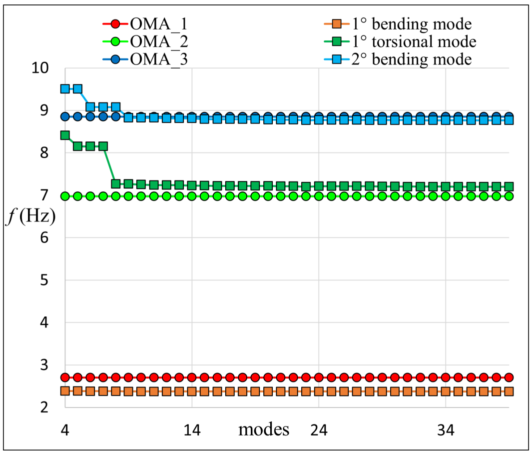

Figure 3.19. Convergence analysis for the GBT-D model in dynamics.

From this and the previous sections, it is evident that the model, based on GBT-D works properly both in statics and in dynamics and for the case under study, a small number of deformation modes is sufficient with no necessity of considering shear modes too; moreover, global restraints are preferable to study this type of bridge if stiffeners are present at the end sections.

However, it could also happen that for the same type of bridge, one could not get the same excellent results, for different reasons, among which the impossibility to neglect the contribution of the adjacent beams or that of the pier or a partial knowledge of the mass permanently applied on the bridge or even the impossibility to correctly determine the mechanical properties of the beam as the Young modulus. For these reasons, it would be advisable to implement in the future some model updating techniques in order to modify some crucial parameters of the GBT-D model to make its response closer to that of the real beam.

3.4 Control

In this section, for the first time a Nonlinear Energy Sink (NES) is coupled to a TWB modeled through GBT (as always in the GBT-D version), with the aim of mitigating vibrations induced by different types of loading. The problem is addressed analytically by deriving the governing equations through the Cx-A. The NES typically consists of a mass (small with the respect to the primary structure), a nonlinear spring, and a dashpot; it is employed as an alternative to a Tuned Mass Damper (TMD) since its nonlinear (and nonlinearizable) stiffness enables the device to operate effectively over a broader frequency range using a single configuration: this characteristic is particularly advantageous for real bridge applications, especially when the amplitude of the external load triggers relevant displacements, allowing to fully exploit the device's capabilities. Finally, as for TMD, the energy which is transferred from the beam to the device is dissipated through the viscous damper. The NES used in this Thesis is such that its nonlinearity is of cubic type, other possibilities are discussed.

3.4.1 Formulation

The NES is shown in Fig. 3.20 together with a sketch of the simply supported beam in the longitudinal direction of the bridge, where m_N, k_N and c_N are the mass (in kg), cubic stiffness (in N/m^3) and damping (in Ns/m) of the NES respectively, while z_N is its position along the beam axis and $y_N(t)$ its absolute vertical displacement (in m).

The equations of motion of the simply supported undamped beam with the attached NES, considering only conventional modes (which, as seen in the previous sections, are enough for the case under study), can be derived from Eqs. (3.20),

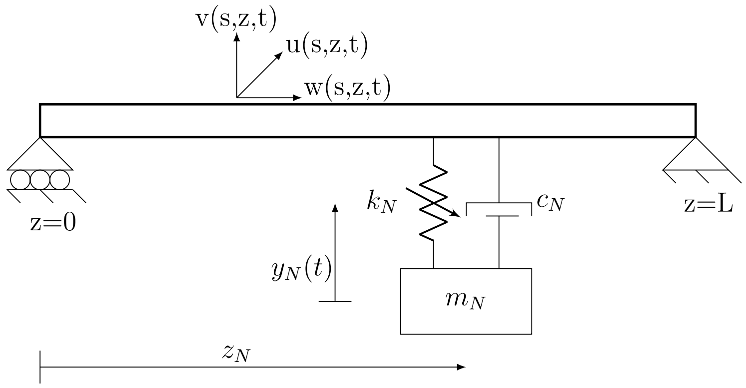

Figure 3.20. Longitudinal view of the beam coupled with NES.

(3.22) and (3.23) as:

$$\begin{aligned}&\mathbf{M}\ddot{\boldsymbol{\varphi}}(z,t)-\mathbf{Q}^m_{\Omega\Omega}\ddot{\boldsymbol{\varphi}}''(z,t)+\left(\mathbf{C}^f+\mathbf{C}^a_{\Omega\Omega}\right)\boldsymbol{\varphi}''''(z,t)+\left(\mathbf{D}^f+\mathbf{D}^{f^T}\right.\\&\left.-\mathbf{D}^s_{\Omega\Omega}-\mathbf{D}^t\right)\boldsymbol{\varphi}''(z,t)+\mathbf{B}^f\boldsymbol{\varphi}(z,t)+\bar{\mathbf{v}}(s_N)\left[k_N\left(\bar{\mathbf{v}}^T(s_N)\boldsymbol{\varphi}(z,t)-y_N(t)\right)^3\right.\\&\left.+c_N\left(\bar{\mathbf{v}}^T(s_N)\dot{\boldsymbol{\varphi}}(z,t)-\dot{y}_N(t)\right)\right]\delta(z-z_N)=\mathbf{p}_\Omega(z,t)\end{aligned} \tag{3.89}$$

$$\begin{aligned}&m_N\ddot{y}_N(t)-\left[k_N\left(\bar{\mathbf{v}}^T(s_N)\boldsymbol{\varphi}(z_N,t)-y_N(t)\right)^3\right.\\&\left.+c_N\left(\bar{\mathbf{v}}^T(s_N)\dot{\boldsymbol{\varphi}}(z_N,t)-\dot{y}_N(t)\right)\right]=0\end{aligned} \tag{3.90}$$

with boundary conditions at $z=0,L$:

$$\left[\left(\mathbf{C}^f+\mathbf{C}^a_{\Omega\Omega}\right)\boldsymbol{\varphi}''(z,t)+\mathbf{D}^f\boldsymbol{\varphi}(z,t)\right]_0^L=0\quad\forall t \tag{3.91}$$

$$[\boldsymbol{\varphi}(z,t)]_0^L=0\quad\forall t \tag{3.92}$$

where $\delta(z-z_N)$ is the Dirac function, which provides the position of the NES along the beam.

Being the main goal to study 1:1 resonance neglecting possible internal resonances, thanks to the presence of damping that is added on the beam, it can be assumed that the response of the system is dominated by its j^{th} vibration mode $\boldsymbol{\varphi}(z,t)=\boldsymbol{\Phi}_j(z)Y_j(t)$ which has to respect the boundary conditions in Eqs. (3.91), (3.92); the procedure to analytically obtain vibration modes for the simply supported beam explained in Sect. 3.2.3 under the name of MA1 is here followed. So, adding damping to the beam as $C_j=2\xi_jM_j\omega_j$ where ξ_j is the modal damping coefficient and projecting the equations of motion on the j^{th} mode, one can write:

$$\begin{aligned}&M_j\ddot{Y}_j(t)+C_j\dot{Y}_j(t)+K_jY_j(t)+\boldsymbol{\Phi}_j^T(z_N)\bar{\mathbf{v}}(s_N)\left[k_N\left(\bar{\mathbf{v}}^T(s_N)\boldsymbol{\Phi}_j(z_N)Y_j(t)\right.\right.\\&\left.\left.-y_N(t)\right)^3+c_N\left(\bar{\mathbf{v}}^T(s_N)\boldsymbol{\Phi}_j(z_N)\dot{Y}_j(t)-\dot{y}_N(t)\right)\right]=\int_0^L\boldsymbol{\Phi}_j^T(z)\mathbf{p}_\Omega(z,t)dz\end{aligned} \tag{3.93}$$

$$\begin{aligned} & m_N \ddot{y}_N(t) - \Big[k_N \left(\bar{\mathbf{v}}^T(s_N)\mathbf{\Phi}_j(z_N)Y_j(t) - y_N(t)\right)^3 \\ & + c_N \left(\bar{\mathbf{v}}^T(s_N)\mathbf{\Phi}_j(z_N)\dot{Y}_j(t) - \dot{y}_N(t)\right)\Big] = 0 \end{aligned} \tag{3.94}$$

where mass and stiffness terms are:

$$M_j = \int_0^L \mathbf{\Phi}_j^T(z) \left[\mathbf{M}\mathbf{\Phi}_j(z) - \mathbf{Q}^m_{\Omega\Omega}\mathbf{\Phi}''_j(z)\right] dz \tag{3.95}$$

$$\begin{aligned} K_j = & \int_0^L \mathbf{\Phi}_j^T(z) \Big[\left(\mathbf{C}^f + \mathbf{C}^a_{\Omega\Omega}\right)\mathbf{\Phi}''''_j(z) \\ & + \left(\mathbf{D}^f + \mathbf{D}^{f^T} - \mathbf{D}^s_{\Omega\Omega} - \mathbf{D}^t\right)\mathbf{\Phi}''_j(z) + \mathbf{B}^f\mathbf{\Phi}_j(z)\Big] dz \end{aligned} \tag{3.96}$$

At this point, in order to write the equations in a more convenient form, some non-dimensional parameters are introduced as follows:

$$\begin{aligned} & \tilde{z} = \frac{z}{b_1}, && \tau = \omega_j t, && \tilde{y}_N(\tau) = \frac{y_N(t)}{b_1} \\ & \varepsilon\tilde{k}_N = \frac{k_N b_1^2}{K_j}, && \varepsilon\tilde{c}_N = \frac{c_N\omega_j}{K_j}, && \varepsilon\hat{C}_j = 2\xi_j \\ & \tilde{\bar{\mathbf{v}}}(\tilde{s}_N) = \bar{\mathbf{v}}(s_N), && \tilde{\mathbf{\Phi}}_j(\tilde{z}_N) = \mathbf{\Phi}_j(z_N), && \tilde{Y}_j(\tau) = \frac{Y_j(t)}{b_1} \end{aligned} \tag{3.97}$$

$$\varepsilon\Gamma = \frac{1}{M_j\omega_j^2 b_1}\int_0^L \mathbf{\Phi}_j^T(z)\mathbf{p}_\Omega(z,t)dz \tag{3.98}$$

where b_1 is a characteristic length of the beam, which can be properly chosen, and ε is a small non-dimensional parameter that, in this case, has a clear physical meaning (differently for example from Sect. 3.5 where it is just a bookkeeping parameter) accounting for the ratio between the mass of the NES and that of the beam to be controlled as:

$$0 < \varepsilon = \frac{m_N}{M_j} \ll 1 \tag{3.99}$$

Non-dimensional variables are put inside Eqs. (3.93), (3.94) and, neglecting tilde to keep the notation light, they can be rewritten as follows:

$$\begin{aligned} & \ddot{Y}_j(\tau) + \varepsilon\hat{C}_j\dot{Y}_j(\tau) + Y_j(\tau) + \mathbf{\Phi}_j^T(z_N)\bar{\mathbf{v}}(\tilde{s}_N)\Big[\varepsilon k_N \left(\bar{\mathbf{v}}^T(s_N)\mathbf{\Phi}_j(z_N)Y_j(\tau)\right. \\ & \left.-y_N(\tau)\right)^3 + \varepsilon c_N\left(\bar{\mathbf{v}}^T(s_N)\mathbf{\Phi}_j(z_N)\dot{Y}_j(\tau) - \dot{y}_N(\tau)\right)\Big] = \varepsilon\Gamma \end{aligned} \tag{3.100}$$

$$\begin{aligned} & \varepsilon\ddot{y}_N(\tau) - \Big[\varepsilon k_N \left(\bar{\mathbf{v}}^T(s_N)\mathbf{\Phi}_j(z_N)Y_j(\tau) - y_N(\tau)\right)^3 \\ & + \varepsilon c_N\left(\bar{\mathbf{v}}^T(s_N)\mathbf{\Phi}_j(z_N)\dot{Y}_j(\tau) - \dot{y}_N(\tau)\right)\Big] = 0 \end{aligned} \tag{3.101}$$

where $\dot{()} = d/d\tau$. Equations are rearranged introducing new variables r_2 and r_1 which are representative of the relative displacement between the beam and the NES in the point where the NES is attached, and of the displacement of the center of mass of the coupled system respectively as:

$$\begin{pmatrix} r_2 \\ r_1 \end{pmatrix} = \begin{bmatrix} \bar{\mathbf{v}}^T(s_N)\mathbf{\Phi}_j(z_N) & -1 \\ 1 & \varepsilon \end{bmatrix} \begin{pmatrix} Y_j \\ y_N \end{pmatrix} \tag{3.102}$$

So, equilibrium equations are rewritten with these new coordinates, putting $\chi_j = \mathbf{\Phi}_j^T(z_N)\bar{\mathbf{v}}(s_N)$ and $D_j = 1 + \varepsilon\chi_j$, as:

$$\ddot{r_1} + \frac{\varepsilon\hat{C}_j}{D_j}(\varepsilon\dot{r_2} + \dot{r_1}) + \frac{1}{D_j}(\varepsilon r_2 + r_1) + \varepsilon k_N\left(\chi_j - 1\right) r_2^3 + \varepsilon c_N\left(\chi_j - 1\right)\dot{r_2} = \varepsilon\Gamma \tag{3.103}$$

$$\ddot{r_2} + \frac{\varepsilon\chi_j\hat{C}_j}{D_j}(\varepsilon\dot{r_2} + \dot{r_1}) + \frac{\chi_j}{D_j}(\varepsilon r_2 + r_1) + k_N\left(\varepsilon\chi_j^2 + 1\right) r_2^3 + c_N\left(\varepsilon\chi_j^2 + 1\right)\dot{r_2} = \varepsilon\chi_j\Gamma \tag{3.104}$$

In the spirit of the Complexification Averaging Method, complex variables β_1, β_2 by Manevitch [87] are introduced (i is the imaginary unit) as:

$$\begin{aligned} \beta_1 e^{i\Omega_R\tau} &= \dot{r_1} + i\Omega_R r_1 \\ \beta_2 e^{i\Omega_R\tau} &= \dot{r_2} + i\Omega_R r_2 \end{aligned} \tag{3.105}$$

Since the goal is to solve the problem through MSM [95], different time scales are introduced, and complex variables are rewritten respectively as:

$$\tau_i = \varepsilon^i\tau, \quad \beta_j(\tau) = \beta_j(\tau_0, \tau_1, \ldots), \quad i = 1, 2 \tag{3.106}$$

so that the derivative with respect to non-dimensional time becomes:

$$\frac{d(..)}{d\tau} = \frac{\partial(...)}{\partial\tau_0} + \varepsilon\frac{\partial(...)}{\partial\tau_1} + \varepsilon^2\frac{\partial(...)}{\partial\tau_2} + \ldots = D_0 + \varepsilon D_1 + \varepsilon^2 D_2 + \ldots \tag{3.107}$$

Then, the Galerkin's method is applied keeping only the harmonic of frequency Ω_R as:

$$x\left(\beta_1, \beta_2, \bar{\beta}_1, \bar{\beta}_2\right) = \frac{\Omega_R}{2\pi}\int_0^{\frac{2\pi}{\Omega_R}} X\left(\beta_1, \beta_2, \bar{\beta}_1, \bar{\beta}_2\right) e^{-i\Omega_R\tau} d\tau \tag{3.108}$$

where $\bar{(\cdot)}$ is used to denote the complex conjugate of these variables. It is made the hypothesis, to be proved, that variables β_j do not depend on the fast time scale $\tau_0 = \tau$ and, if it is not true, the system has to be studied at the infinity of fast time scale, i.e. for $\tau_0 \to \infty$. So, equilibrium equations can be finally rewritten as:

$$\begin{aligned} &\dot{\beta_1} + \frac{i\Omega_R}{2}\beta_1 + \frac{\varepsilon\hat{C}_j}{2D_j}\left(\beta_1 + \varepsilon\beta_2\right) + \frac{1}{2i\Omega_R D_j}\left(\beta_1 + \varepsilon\beta_2\right) \\ &+ \frac{3}{8i\Omega_R^3}\varepsilon k_N\left(\chi_j - 1\right)\beta_2^2\bar{\beta}_2 + \frac{1}{2}\varepsilon c_N\left(\chi_j - 1\right)\beta_2 = \frac{\Omega_R}{2\pi}\int_0^{\frac{2\pi}{\Omega_R}} \varepsilon\Gamma e^{-i\Omega_R\tau} d\tau \end{aligned} \tag{3.109}$$

$$\begin{aligned} &\dot{\beta}_2 + \frac{i\Omega_R}{2}\beta_2 + \frac{\varepsilon\chi_j\hat{C}_j}{2D_j}\left(\beta_1 + \varepsilon\beta_2\right) + \frac{\chi_j}{2i\Omega_R D_j}\left(\beta_1 + \varepsilon\beta_2\right) \\ &+ \frac{3}{8i\Omega_R^3}k_N\left(\varepsilon\chi_j^2 + 1\right)\beta_2^2\bar{\beta}_2 + \frac{1}{2}c_N\left(\varepsilon\chi_j^2 + 1\right)\beta_2 = \frac{\Omega_R}{2\pi}\int_0^{\frac{2\pi}{\Omega_R}} \varepsilon\chi_j\Gamma e^{-i\Omega_R\tau}d\tau \end{aligned} \tag{3.110}$$

The introduction of multiple time scales (fast, slow and eventually slower ones) implies that the system behavior has to be studied at different orders of ε, i.e. at different scales of time, with the higher orders ε being corrections to the lower order ones. In addition, given that the goal is to study the system response around a 1:1 resonance, it has to be set:

$$\Omega_R = \frac{\Omega_F}{\omega_j} = 1 + \varepsilon\sigma \tag{3.111}$$

where Ω_F is the angular frequency (in rad/s) of the external load (Ω_R being its non-dimensional counterpart) and σ is a detuning parameter that permits to study the system near resonance. Collecting all terms at the same order of ε until ε^1, so just the first two time scales, the perturbation equations are obtained as:

$$\text{ord. } \varepsilon^0 : D_0\beta_1 + \frac{i}{2}\beta_1 + \frac{1}{2iD_j}\beta_1 = 0 \tag{3.112}$$

$$D_0\beta_2 + \frac{i}{2}\beta_2 + \frac{\chi_j}{2iD_j}\beta_1 + \frac{3}{8i}\tilde{k}_N\beta_2^2\bar{\beta}_2 + \frac{1}{2}c_N\beta_2 = 0 \tag{3.113}$$

$$\begin{aligned} &\text{ord. } \varepsilon^1 : D_1\beta_1 + \frac{i\sigma}{2}\beta_1 + \frac{\hat{C}_j}{2D_j}\beta_1 + \frac{1}{2iD_j}\left(\beta_2 - \sigma\beta_1\right) \\ &+ \frac{3}{8i}k_N\left(\chi_j - 1\right)\beta_2^2\bar{\beta}_2 + \frac{1}{2}c_N\left(\chi_j - 1\right)\beta_2 = \frac{\Omega_R}{2\pi}\int_0^{\frac{2\pi}{\Omega_R}} \Gamma e^{-i\Omega_R\tau}d\tau \end{aligned} \tag{3.114}$$

$$\begin{aligned} &D_1\beta_2 + \frac{i\sigma}{2}\beta_2 + \frac{\chi_j\hat{C}_j}{2D_j}\beta_1 + \frac{\chi_j}{2iD_j}\left(\beta_2 - \sigma\beta_1\right) \\ &+ \frac{3}{8i}k_N\left(\chi_j^2 - 3\sigma\right)\beta_2^2\bar{\beta}_2 + \frac{1}{2}c_N\chi_j^2\beta_2 = \frac{\Omega_R}{2\pi}\int_0^{\frac{2\pi}{\Omega_R}} \chi_j\Gamma e^{-i\Omega_R\tau}d\tau \end{aligned} \tag{3.115}$$

First, the response of the system at fast time scale τ_0 is studied. Starting from Eq. (3.112), it can be verified that $D_j \approx 1$, so that $D_0\beta_1 = 0$, which means that β_1 is independent of fast time τ_0 in accordance to the hypothesis made before. About Eq. (3.113), an asymptotic state is searched for $\tau_0 \to \infty$, such that $D_0\beta_2 = 0$, i.e. the equilibrium (fixed) points of the system are searched, obtaining the following:

$$\mathbb{S}\left(\beta_1, \beta_2, \bar{\beta}_1, \bar{\beta}_2\right) = \frac{\chi_j}{2i}\beta_1 - \frac{1}{2i}\beta_2 + \frac{3}{8i}k_N\beta_2^2\bar{\beta}_2 + \frac{1}{2}c_N\beta_2 = 0 \tag{3.116}$$

which is the equation of the Slow Invariant Manifold (SIM), a topological manifold, invariant under the action of a dynamical system [18, 131]. In order to study it, complex variables introduced before are written in polar form as:

$$\beta_j = N_j e^{i\delta_j}, \quad j = 1, 2 \tag{3.117}$$

where $N_j \in \mathbb{R}^+$, $\delta_j \in \mathbb{R}$. Then, Eq. (3.117) is put inside Eq. (3.116) to get the SIM in the real domain, obtaining the equilibrium points as:

$$N_1 = \frac{N_2}{\chi_j}\sqrt{c_N^2 + \left(1 - \frac{3}{4}k_N N_2^2\right)^2} \tag{3.118}$$

To study the stability of the SIM, a small linear perturbation $|\Delta\beta_2| \ll |\beta_2|$ is applied to β_2 as $\beta_2 \to \beta_2 + \Delta\beta_2$ and to its complex conjugate. Then, as usual, the real part of the eigenvalues of the resulting matrix is studied: if it is negative, the equilibrium points are classified as stable, otherwise they are unstable. After neglecting higher order terms, the equation becomes:

$$\begin{pmatrix} \dfrac{\delta\Delta\beta_2}{\delta\tau_0} \\ \dfrac{\delta\Delta\bar{\beta}_2}{\delta\tau_0} \end{pmatrix} = \begin{bmatrix} \dfrac{1}{2i} - \dfrac{3}{4i}k_N\beta_2\bar{\beta}_2 - \dfrac{1}{2}c_N & -\dfrac{3}{8i}k_N\beta_2^2 \\ \dfrac{3}{8i}k_N\bar{\beta}_2^2 & -\dfrac{1}{2i} + \dfrac{3}{4i}k_N\beta_2\bar{\beta}_2 - \dfrac{1}{2}c_N \end{bmatrix} \begin{pmatrix} \Delta\beta_2 \\ \Delta\bar{\beta}_2 \end{pmatrix} \tag{3.119}$$

where the matrix is called $\mathbf{Z}$. Thus, the eigenvalues of $\mathbf{Z}$ can be found by solving the following characteristic polynomial:

$$\lambda^2 - (Z_{11} + Z_{22})\,\lambda + Z_{11}Z_{22} - Z_{12}Z_{21} = 0 \tag{3.120}$$

and the following relations can be identified:

$$\begin{cases} \lambda_1 + \lambda_2 = Z_{11} + Z_{22} = -c_N < 0 \\ \lambda_1\lambda_2 = Z_{11}Z_{22} - Z_{12}Z_{21} \end{cases} \tag{3.121}$$

So, it results that the sum between the real part of the eigenvalues is always negative (being the damping coefficient of the NES positive), thus if the product between them is positive, both of them have to be negative, so the equilibrium point is stable, while if the product is negative, the real part of one eigenvalue is necessarily positive, so the equilibrium point is unstable. From these considerations it is possible to state that the unstable zones of the SIM are those for which $Z_{11}Z_{22} - Z_{12}Z_{21} < 0$. An example of SIM found in this way is illustrated in Fig. 3.21.

Moving to the slow time scale τ_1, the objective is to track the evolution of the SIM at this time scale and to study the system at slow time scale around the SIM [127], to understand its behavior near a resonance condition. It means that equilibrium and singular points have to be found starting from the first equilibrium

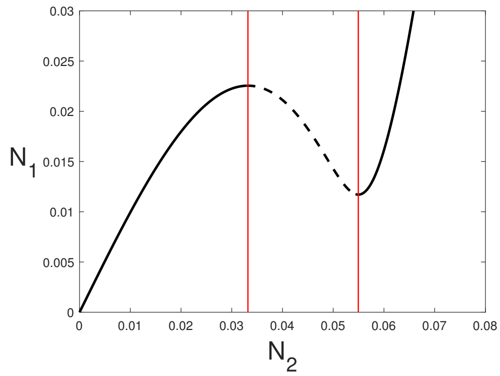

Figure 3.21. Analytical Slow Invariant Manifold with stable and unstable zones.

equation at order ε^1, Eq. (3.114), rewritten as:

$$\frac{\partial \beta_1}{\partial \tau_1} = \mathbb{E}_1\left(\beta_1, \beta_2, \bar{\beta}_1, \bar{\beta}_2\right) \tag{3.122}$$

where:

$$\begin{aligned} \mathbb{E}_1\left(\beta_1, \beta_2, \bar{\beta}_1, \bar{\beta}_2\right) &= \frac{\sigma}{2i}\beta_1 - \frac{\hat{C}_j}{2D_j}\beta_1 - \frac{1}{2i}\left(\beta_2 - \sigma\beta_1\right) \\ &- \frac{3}{8i}k_N\left(\chi_j - 1\right)\beta_2^2\bar{\beta}_2 - \frac{1}{2}c_N\left(\chi_j - 1\right)\beta_2 + \frac{\Omega_R}{2\pi}\int_0^{\frac{2\pi}{\Omega_R}} \Gamma e^{-i\Omega_R \tau} d\tau \end{aligned} \tag{3.123}$$

Then, the evolution of the SIM $\mathbb{S}$ at the current time scale τ_1 can be considered as follows:

$$\begin{cases} \dfrac{\partial \mathbb{S}}{\partial \tau_1} = \dfrac{\partial \mathbb{S}}{\partial \beta_1}\dfrac{\partial \beta_1}{\partial \tau_1} + \dfrac{\partial \mathbb{S}}{\partial \beta_2}\dfrac{\partial \beta_2}{\partial \tau_1} + \dfrac{\partial \mathbb{S}}{\partial \bar{\beta}_1}\dfrac{\partial \bar{\beta}_1}{\partial \tau_1} + \dfrac{\partial \mathbb{S}}{\partial \bar{\beta}_2}\dfrac{\partial \bar{\beta}_2}{\partial \tau_1} = 0 \\ \dfrac{\partial \bar{\mathbb{S}}}{\partial \tau_1} = \dfrac{\partial \bar{\mathbb{S}}}{\partial \beta_1}\dfrac{\partial \beta_1}{\partial \tau_1} + \dfrac{\partial \bar{\mathbb{S}}}{\partial \beta_2}\dfrac{\partial \beta_2}{\partial \tau_1} + \dfrac{\partial \bar{\mathbb{S}}}{\partial \bar{\beta}_1}\dfrac{\partial \bar{\beta}_1}{\partial \tau_1} + \dfrac{\partial \bar{\mathbb{S}}}{\partial \bar{\beta}_2}\dfrac{\partial \bar{\beta}_2}{\partial \tau_1} = 0 \end{cases} \tag{3.124}$$

A reorganization in matrix form of the system of equations can be realized as:

$$\underbrace{\begin{bmatrix} \dfrac{\partial \mathbb{S}}{\partial \beta_2} & \dfrac{\partial \mathbb{S}}{\partial \bar{\beta}_2} \\ \dfrac{\partial \bar{\mathbb{S}}}{\partial \beta_2} & \dfrac{\partial \bar{\mathbb{S}}}{\partial \bar{\beta}_2} \end{bmatrix}}_{\mathbf{J_2}} \begin{pmatrix} \dfrac{\partial \beta_2}{\partial \tau_1} \\ \dfrac{\partial \bar{\beta}_2}{\partial \tau_1} \end{pmatrix} = - \begin{bmatrix} \dfrac{\partial \mathbb{S}}{\partial \beta_1} & \dfrac{\partial \mathbb{S}}{\partial \bar{\beta}_1} \\ \dfrac{\partial \bar{\mathbb{S}}}{\partial \beta_1} & \dfrac{\partial \bar{\mathbb{S}}}{\partial \bar{\beta}_1} \end{bmatrix} \begin{pmatrix} \dfrac{\partial \beta_1}{\partial \tau_1} \\ \dfrac{\partial \bar{\beta}_1}{\partial \tau_1} \end{pmatrix} \tag{3.125}$$

where $\mathbf{J_2}$ is the Jacobian matrix of the SIM with respect to $\left(\beta_2, \bar{\beta}_2\right)$; thus, the following systems can be written, for equilibrium and singular points respectively:

$$\begin{cases} \mathbb{E}_1 = 0 \\ \mathbb{S} = 0 \\ \det(\mathbf{J_2}) \neq 0 \end{cases} \qquad \begin{cases} \mathbb{E}_1 = 0 \\ \mathbb{S} = 0 \\ \det(\mathbf{J_2}) = 0 \end{cases} \tag{3.126}$$

The calculation of the matrix $\mathbf{J_2}$, gives that $\mathbf{J_2} = -\mathbf{Z}$, which implies that the singular points of the system are found in correspondence of the stability borders.

On the other hand, to find equilibrium points, the subsystem given by the first two equations of the first system in Eq. (3.126) has to be solved, namely Eq. (3.123) and Eq. (3.116), to obtain an equation with N_2 and with the unknown variable as the detuning parameter σ; doing so, a simple second order algebraic equation has to be solved for different values of N_2 to find the equilibrium points. So, setting $\bar{F} = 3/4k_N\beta_2\bar{\beta}_2$ and $\bar{\gamma} = \Omega_R/(2\pi)\int_0^{2\pi/\Omega_R}\Gamma e^{-i\Omega_R\tau}d\tau$, the first two equations of the system give:

$$\bar{c}_1\sigma^2 + \bar{c}_2\sigma + \bar{c}_3 = 0 \tag{3.127}$$

where:

$$\bar{c}_1 = N_2^2\left[\left(\frac{1}{\chi_j} - \frac{\bar{F}}{\chi_j}\right)^2 + \frac{c_N^2}{\chi_j^2}\right] \tag{3.128}$$

$$\bar{c}_2 = N_2^2\left(\frac{\bar{F}^2(\chi_j-1)}{\chi_j} - \frac{\bar{F}(\chi_j-1)}{\chi_j} + \frac{\bar{F}}{\chi_j} - \frac{1}{\chi_j} + \frac{c_N^2(\chi_j-1)}{\chi_j}\right) \tag{3.129}$$

$$\begin{aligned}\bar{c}_3 = N_2^2\Bigg(&\frac{\bar{F}^2(\chi_j-1)^2}{4} + \frac{\bar{F}(\chi_j-1)}{2} + \frac{c_N^2(\chi_j-1)^2}{4} + \frac{1}{4}\\ &+\frac{\hat{C}_j^2\bar{F}^2}{4\chi_j^2} - \frac{\hat{C}_j^2\bar{F}}{2\chi_j^2} + \frac{\hat{C}_jc_N}{2} + \frac{\hat{C}_j^2}{4\chi_j^2} + \frac{\hat{C}_j^2c_N^2}{4\chi_j^2}\Bigg) - \left|\frac{-\bar{\gamma}}{i}\right|^2\end{aligned} \tag{3.130}$$

Resolution of Eq. (3.127) gives maximum two values of σ for each assigned value of N_2, with only real values of σ having a physical meaning. Then, the relationship between N_1 and σ can be easily obtained using Eq. (3.116), in order to get the Frequency Responce Curve (FRC), which are the relationships between the amplitudes of response N_1 and N_2 and the frequency, here represented in terms of σ. Studying these curves, different types of responses can be obtained in function of σ:

(i) Periodic Response: in case of stable equilibrium points the system oscillates in time with a certain period and asymptotically tends to a condition of equilibrium.

(ii) Modulated Response: in general this behavior can be detected if the system presents fold singularities, i.e. those when equilibrium points (obtained from $\mathbb{E}_1 = 0$ around the SIM) and singular points (for which $\det(\mathbf{J_2}) = 0$) coincide (see Eq. (3.126)) [45, 71, 127]. In addition, if the equilibrium point is positioned in the unstable zone of the SIM, the system will also present the modulated response, corresponding to repeated jumps between the limit points of the SIM [56].

(iii) Isola: the system can also present isolas which are isolated branches of the FRC that appear for some amplitudes of the external excitation and are re-absorbed to the main branch out of those amplitudes. In general, isolas have higher energy levels causing amplification in the response, being detrimental if the objective is, as in this case, to reduce the vibrations of the beam. More details about this phenomenon are found in [26].

As a final remark, another result of the analysis is the so-called backbone curve [95] which can be obtained from Eq. (3.127), via setting damping and external load equal to zero; for nonlinear conservative systems, this curve provides the amplitude dependency of the frequency.

3.4.2 Load cases

The model developed in the previous section is applied considering different types of external loads to test the capability of the NES to reduce vibrations related to them, at different frequency levels. In this section, the considered loads are specified, while results are presented in Sect. 3.4.3. Loading scenarios are resumed in Tab. 3.7 and shown in Fig. 3.22.

First of all, a vertical, sinusoidal, uniformly distributed load with frequency Ω_F is applied on the upper flange of the beam (the load p is in (N/m^2)). The frequency is then written in non-dimensional terms as in Eq. (3.111) as Ω_R in this and in following cases. Moreover, it can be useful to express the non-dimensional load Γ of Eq. (3.98) as:

$$\Gamma = \Gamma_p \sin(\Omega_R \tau) \tag{3.131}$$

and recalling Eq. (3.95), substituting to $\mathbf{\Phi}_j$ the expression obtained through MA1 in Eq. (3.64) and to $\mathbf{p}_\Omega$ the expression in Eq. (3.16), considering Eq. (3.67), for odd values of n_j it is possible to express Γ_p as:

$$\Gamma_p = \frac{4}{\varepsilon n_j \pi \omega_j^2 b_1} \frac{\mathbf{\Theta}_j^T \mathbf{p}_\Omega^0}{\mathbf{\Theta}_j^T \mathbf{M}_j \mathbf{\Theta}_j} \tag{3.132}$$

where $\mathbf{p}_\Omega^0$ is written in the table. In this way, one can find that $\bar{\gamma}$ appearing in Eq. (3.130) is equal to $\Gamma_p/(2i)$. This case is identified as UL-1 in Fig. 3.22(a) and the same procedure to determine Γ_p can be extended to the subsequent load cases.

Then, a case similar to UL-1 is considered, but with the load applied only in the mid upper flange of the cross section of the beam, i.e. between the points of intersection of inclined webs with the upper flange, identified as UL-2 in Fig. 3.22(b).

Subsequently, a vertical, sinusoidal, punctual load with frequency Ω_F is applied at the center of the upper flange of the beam (the load p is formally expressed in N/m, as it has to be written as the ratio between the punctual load in N and the cross-section dimension of the element along s following the discretization made in the cross-section analysis). Also in this case $\bar{\gamma}$ is equal to $\Gamma_p/(2i)$ where Γ_p was calculated as for UL-1. This case is identified as PL in Fig. 3.22(c).

Then, a train of moving loads p, representative of a series of N_v vehicles moving on the bridge at constant speed v_v and distance d_v, is applied on the upper flange of the beam. The frequency of each load is $\Omega_F = n_j \pi v_v / L$ [146]. Expressions in Tab. 3.7 are meant for each vehicle, where $t_j = (j-1)d_v/v_v$ is the arriving time of the j^{th} load on the beam and $t_j + L/v_v$ is the time at which the vehicle reaches the end of the beam. In this case, just the numerical solution of Eqs. (3.103), (3.104) was obtained using a Runge–Kutta method (ode45 on Matlab) since, due to the characteristics of the beam, if the goal is to have vehicles in a 1:1 resonance with one mode of the beam, an extremely high speed should be considered, which however would be unrealistic. This case is identified as ML in Fig. 3.22(d) and the expressions reported in Tab. 3.7 are found as before.

Finally, seismic action was considered too. For the beam without the NES, both analytical and numerical solutions can be obtained, while, for the beam with NES, just the numerical solution of Eqs. (3.103), (3.104) through a Runge–Kutta method is considered. In fact, as the earthquake has a wide spectrum of frequencies, it is not possible to consider a 1:1 resonance. Moreover, in general, in Eqs. (3.93), (3.94) the hypothesis that only the j^{th} vibration mode contributes to the beam response is not valid and a certain number of vibration modes should be considered to correctly describe the beam response, but the presence of nonlinear stiffness and damping terms of the NES couples all these vibration modes, making impossible to apply the procedure developed in the previous section. On the other hand, for the beam without NES it was seen that, due to the characteristics of the beam itself and those of the chosen earthquake, the difference between the analytical solution keeping only the 1^{st} vibration mode, and the one with more modes is negligible: this means that for this specific case it is possible to proceed with only one mode avoiding the coupling (always in a numerical way). So, the earthquake is considered as a vertical ground motion $v_g(t)$ (in m), applied to both supports of the beam, so that displacements $v(s,z,t)$ and $y_N(t)$ are relative to the base. Using the usual notation, the ground acceleration can be written as $\ddot{v}_g(t)$ and, considering the mass per unit area m seen in Eq. (3.19), the load terms are reported in Tab. 3.7. This case is identified as SL.

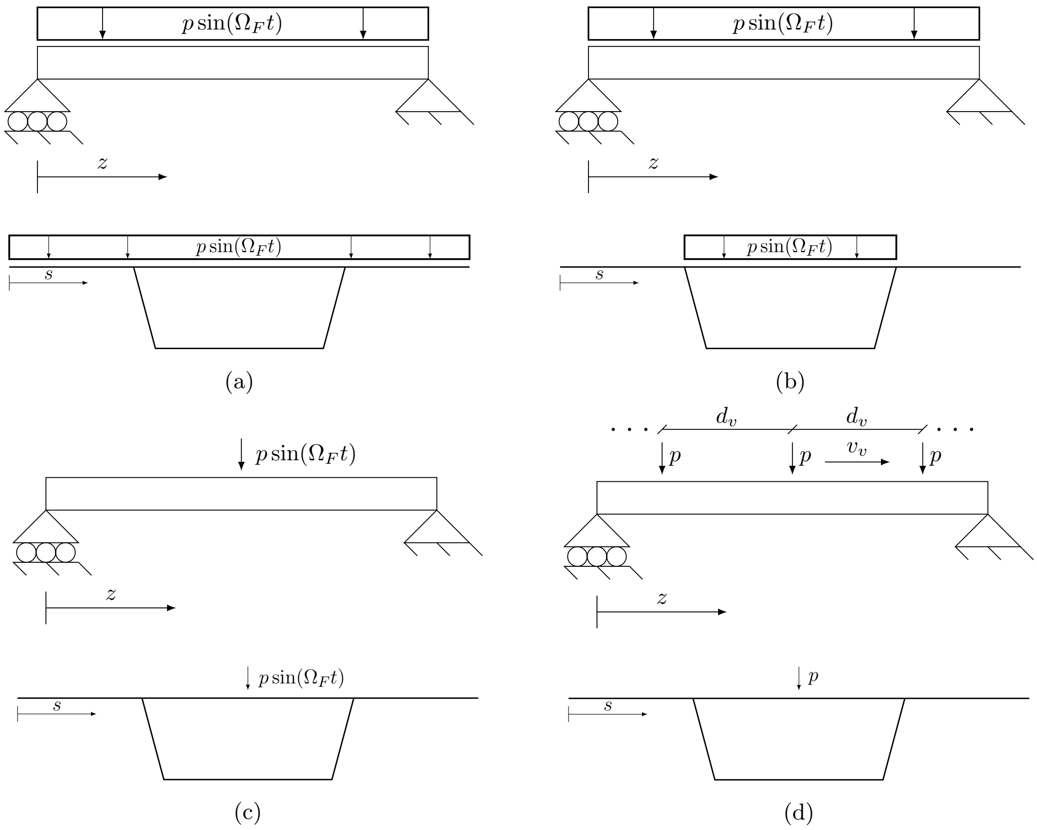

Figure 3.22. Schematic representation of different types of loads in longitudinal and transversal planes: (a) UL-1, (b) UL-2, (c) PL, (d) ML referred to Sect. 3.4.2.

Table 3.7. Characteristics of different types of loads for the TWB with NES.

Type of load	$f_y(s,z,t)$	$\mathbf{p}_\Omega^0$	$\varepsilon\Gamma$ for $n_j = 1, 5, \ldots$
Uniform	$p\sin(\Omega_F t)$	$\int_s p\bar{\mathbf{v}}(s)ds$	$\dfrac{4}{n_j\pi\omega_j^2 b_1}\dfrac{\mathbf{\Theta}_j^T\mathbf{p}_\Omega^0}{\mathbf{\Theta}_j^T\mathbf{M}_j\mathbf{\Theta}_j}\sin(\Omega_R\tau)$
Punctual	$p\sin(\Omega_F t)\delta(z-L/2)$	$\int_s p\bar{\mathbf{v}}(s)ds$	$\dfrac{2}{b_1 L\omega_j^2}\dfrac{\mathbf{\Theta}_j^T\mathbf{p}_\Omega^0}{\mathbf{\Theta}_j^T\mathbf{M}_j\mathbf{\Theta}_j}\sin(\Omega_R\tau)$
Moving	$p\delta(z-v_v(t-t_j))$	$\int_s p\bar{\mathbf{v}}(s)ds$	$\dfrac{2}{b_1 L\omega_j^2}\dfrac{\mathbf{\Theta}_j^T\mathbf{p}_\Omega^0}{\mathbf{\Theta}_j^T\mathbf{M}_j\mathbf{\Theta}_j}\sin(\Omega_R(\tau-\tau_j))$
Seismic	$m\ddot{v}_g(t)$	$\int_s m[\bar{\mathbf{u}}(s)\sin(\alpha(s))$ $+\bar{\mathbf{v}}(s)\cos(\alpha(s))]ds$	$\dfrac{4}{n_j\pi\omega_j^2 b_1}\dfrac{\mathbf{\Theta}_j^T\mathbf{p}_\Omega^0}{\mathbf{\Theta}_j^T\mathbf{M}_j\mathbf{\Theta}_j}\ddot{v}_g(\tau)$

3.4.3 Results

Geometrical and mechanical properties of the beam were already reported in Fig. 3.4 and in Tab. 3.1; those of the NES (the dimensional ones) are written in Tab. 3.8. The parameters of the NES were manually adjusted to minimize the beam displacements, thus they do not come from a rigorous optimization procedure [12], so it is likely that better results can be found by changing them (an example can be found in [71] where different trends of the SIM are identified as the parameters vary).

Table 3.8. Parameters of the NES applied on the TWB case study.

m_N (kg)	c_N (Ns/m)	k_N (N/m^3)	z_N (m)
650	2.0×10^3	6.0×10^6	$L/2$

First of all, in Fig. 3.23 the analytical SIM, found using Eq. (3.118), with the stability borders (in red) which are determined in accordance to Eq. (3.121), is shown together with a numerical solution given by the resolution of Eqs. (3.103), (3.104) with no external load, subjected to some non-trivial initial conditions (i.c.) marked as "x"; the unstable zone is represented by a dashed line. It can be noted that, for the chosen initial conditions, the solution oscillates in time around the right branch and then in correspondence of the stability border jumps on the left branch and finally goes to zero, since the unstable zone is physically unattainable.

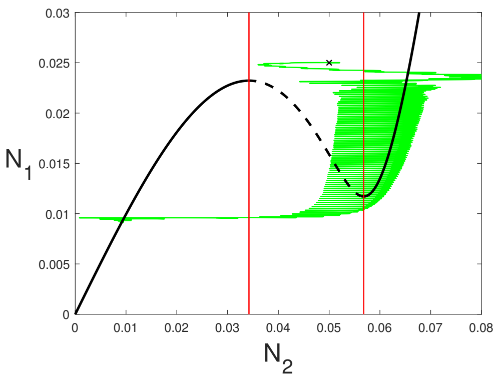

Figure 3.23. Analytical and numerical SIM for the TWB with NES.

Another important curve to describe the nonlinear system is the backbone curve, shown in Fig. 3.24 together with some FRC for different load amplitudes for the load case UL-1. The backbone curve is defined as the locus of the peak amplitudes and it is possible to note that by increasing the amplitude of the external load (e.g. from -10 N/m^2 to -200 N/m^2), the NES performance increases, in the sense that it really starts to manifest a nonlinear behavior, with different kinds of equilibrium points that can be obtained.

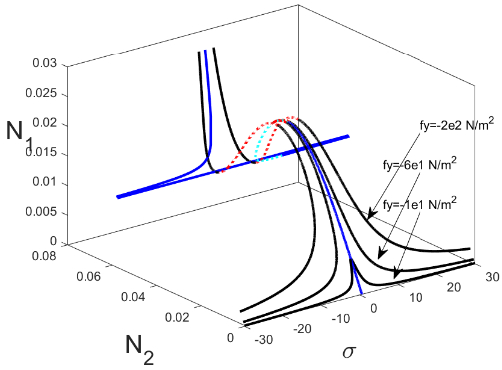

Figure 3.24. Frequency response curves and backbone curve (in blue and cyan) for the TWB with NES.

At this point, results for the different load cases are reported, in the same order they were presented (from UL-1 to SL). The first investigated case is a UL-1 with a load amplitude $p = 6.0 \times 10^1$ N/m^2 with the same frequency of the first vibration mode of the beam (the one whose longitudinal variation is indicated as $\mathbf{\Phi}_1$ in Fig. 3.11) equal to $\Omega_F = \omega_1 = 15.05$ rad/s.

From Fig. 3.25(a) it can be noticed that, in this case, the NES is well activated (the nonlinearity is evident) and, in Figs. 3.25(b), 3.25(c), it is shown that in function of the value of the detuning parameter, it is possible to have 1, 2 or in some cases even 3 solutions of different nature, depending on the value of the i.c.. Moreover, always in Fig. 3.25(b), a comparison between FRC of the beam with and without NES (the latter in magenta) highlights a general reduction of displacement on the beam when the nonlinear device is installed.

Fig. 3.26(a) shows that for a value of $\sigma = 0.65$, the equilibrium point (there represented by a circle) moves in time around the SIM and, when it attains the stability border, it bifurcates, jumping on the other branch. The same behavior, which clearly describes a Modulated Response, can be found in Figs. 3.26(b), 3.26(c) where bifurcations in time are evident; furthermore in the same figures N_1 and N_2 are plotted as envelopes of r_1 and r_2 respectively, with a clear meaning of energies.

In Fig. 3.27(a) the displacement of the beam at midspan and of the attached NES is shown, normalized with respect to the beam length, and it is evident while in Fig. 3.27(b) the response of the beam with and without NES is reported. Looking at the two figures, it is evident that when the NES is activated (high value of y_N)

the displacement of the beam is immediately reduced; moreover, the Modulated Response is evident once again.

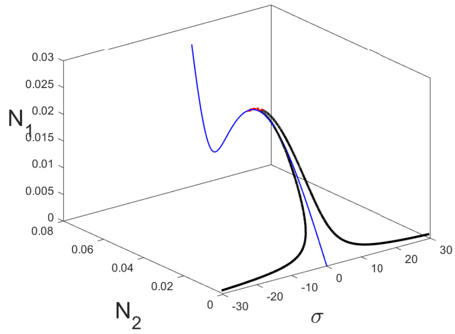

(a)

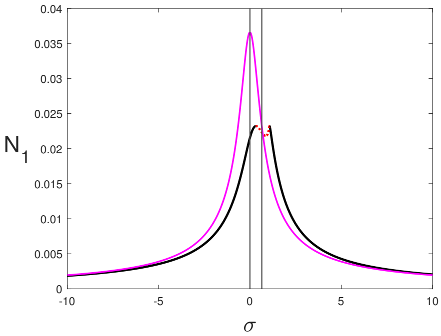

(b)

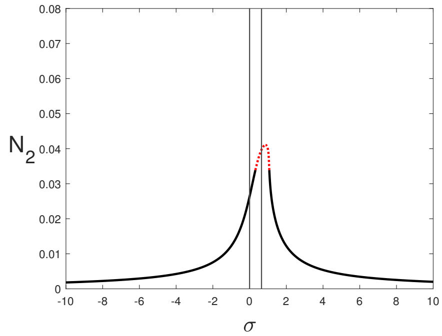

(c)

Figure 3.25. FRC for the TWB with NES under UL-1 load with $p = 6.0 \times 10^1$ N/m^2: (a) 3D view in $N_1 - N_2 - \sigma$ (unstable zone of the SIM in red) with SIM (in blue); (b) 2D view in $N_1 - \sigma$ with the FRC of the beam without NES (in magenta); (c) 2D view in $N_2 - \sigma$. Vertical lines represent values of σ investigated in next figures.

After that, the same UL-1 case with amplitude $p = 6.0 \times 10^1$ N/m^2 and frequency of the first vibration mode is considered but with a different value of the detuning parameter $\sigma = 0$. From Figs. 3.25(b), 3.25(c) it can be noticed that changing σ means that the response becomes periodic, with the equilibrium point oscillating in time and attaining to an asymptotic value, as shown in Figs. 3.28(a), 3.28(b); the values of N_1 and N_2 found solving the numerical problem are really close to the analytical ones identified by the vertical line at $\sigma = 0$ in Figs. 3.25(b), 3.25(c), confirming the validity of the analytical model. Moreover, in Fig. 3.29(a), it can be seen that the displacement of the NES is high enough to reduce the displacement of the beam as showed in Fig. 3.29(b); even if the behavior of the NES is not optimal, displacements are compatible with those expected on a real beam.

Moving on, a UL-2 case with amplitude $p = 2.0 \times 10^4$ N/m^2 and frequency equal to that of the fifth vibration mode (the one whose longitudinal variation is indicated

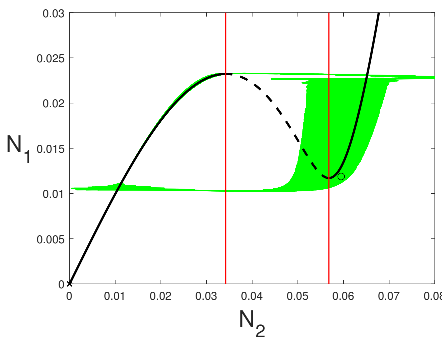

(a)

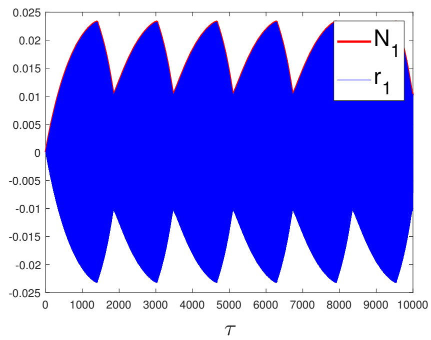

(b)

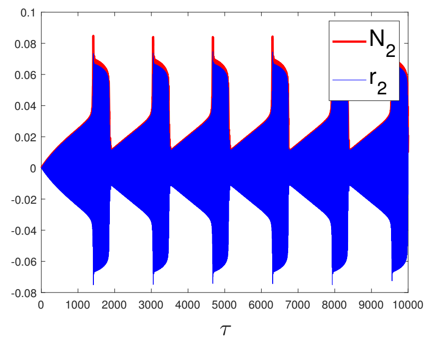

(c)

Figure 3.26. SIM and numerical results (from direct numerical integration of Eqs. (3.103), (3.104) with zero i.c.) for the TWB with NES under UL-1 load with $p = 6.0 \times 10^1$ N/m^2, $\sigma = 0.65$: (a) $N_1 - N_2$ with SIM ; (b) Time history of N_1 and r_1; (c) Time history of N_2 and r_2.

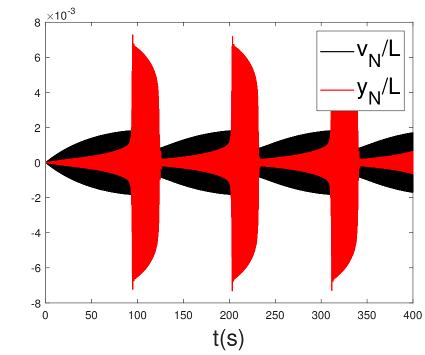

(a)

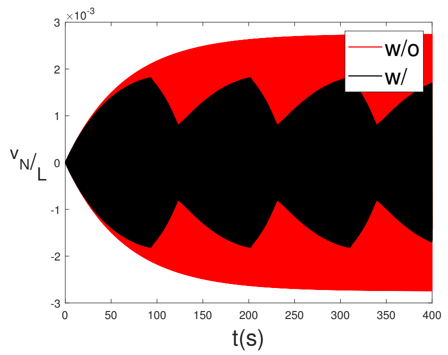

(b)

Figure 3.27. Numerical results (from direct numerical integration of Eqs. (3.103), (3.104) with zero i.c.) for the TWB with NES under UL-1 load with $p = 6.0 \times 10^1$ N/m^2, $\sigma = 0.65$: (a) Time histories of v_N/L and y_N/L; (b) Time histories of v_N/L with and without NES.

as $\mathbf{\Phi}_5$ in Fig. 3.11) equal to $\Omega_F = \omega_5 = 87.21$ rad/s is considered.

Results reported in Figs. 3.30(a), 3.30(b) and 3.30(c) are quite interesting, since they show the onset on an isolated response or Isola (see for example [51, 68]), which can be dangerous for the beam due to the higher energy level (note that in those

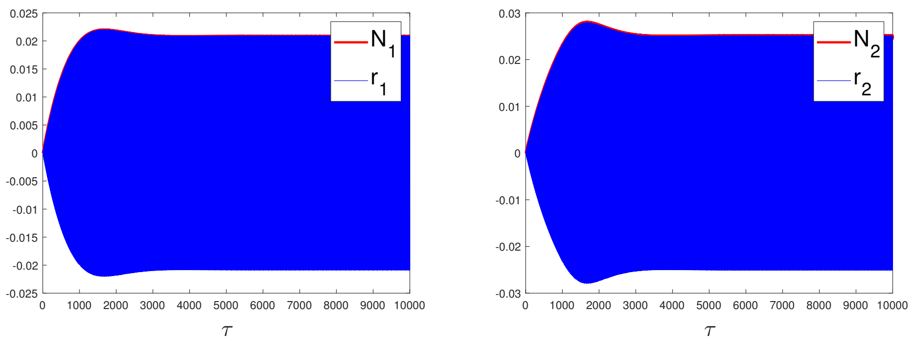

(a) (b)

Figure 3.28. Numerical results (from direct numerical integration of Eqs. (3.103), (3.104) with zero i.c.) for the TWB with NES under UL-1 load with $p = 6.0 \times 10^1$ N/m^2, $\sigma = 0$: (a) Time history of N_1 and r_1; (b) Time history of N_2 and r_2.

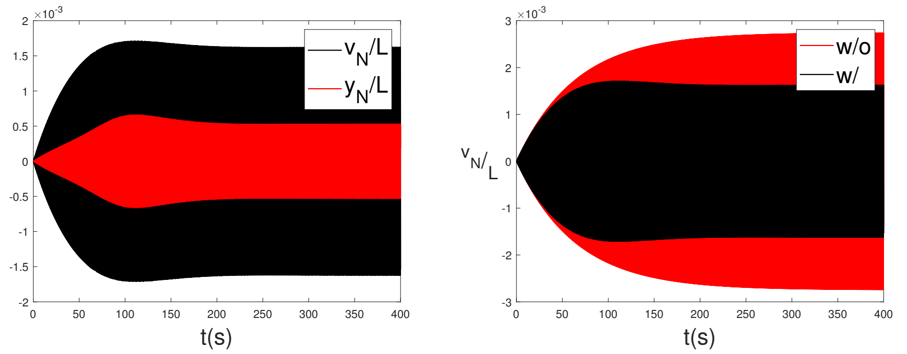

(a) (b)

Figure 3.29. Numerical results (from direct numerical integration of Eqs. (3.103), (3.104) with zero i.c.) for the TWB with NES under UL-1 load with $p = 6.0 \times 10^1$ N/m^2, $\sigma = 0$: (a) Time histories of v_N/L and y_N/L; (b) Time histories of v_N/L with and without NES.

figures, stable and unstable zones are referred to those of the SIM and not to the Isola itself). Figs. 3.31(a), 3.31(b) show once again the excellent correspondence of the numerical solution and the analytical one, as can be seen by looking at the values intercepted by the vertical lines in Fig. 3.30(c). Moreover, in Figs. 3.32(a), 3.32(b) the reduction of the displacement on the beam, thanks to the Modulated Response of the NES is still evident, meaning that the same NES can be used to control a different type of load (distributed just in the central part of the beam) with a different frequency associated to a mode which was detected thanks to GBT-D: in fact, it has to be stressed that the GBT-D was fundamental to detect this vibration mode, which, as can be seen in Fig. 3.11, exhibits the deformation of the cross-section in its own plane meaning that it could not be found through simpler beam theories, which, as a consequence, could not account for this resonance.

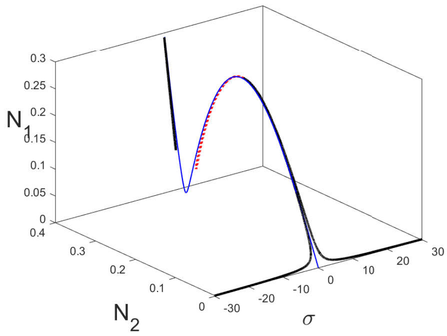

(a)

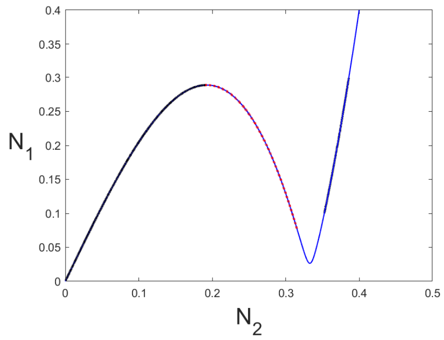

(b)

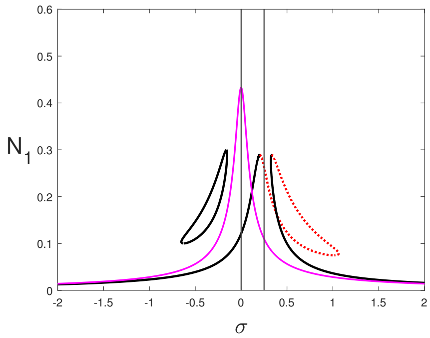

(c)

Figure 3.30. FRC for the TWB with NES under UL-2 load with $p = 2.0 \times 10^4$ N/m^2: (a) 3D view in $N_1 - N_2 - \sigma$ (unstable zone of the SIM in red) with SIM (in blue); (b) 2D view in $N_1 - N_2$ with SIM; (c) 2D view in $N_1 - \sigma$ with the FRC of the beam without NES (in magenta). Vertical lines represent values of σ investigated in next figures.

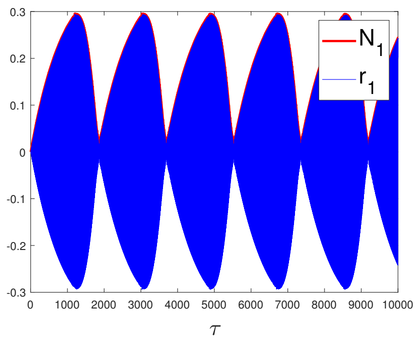

(a)

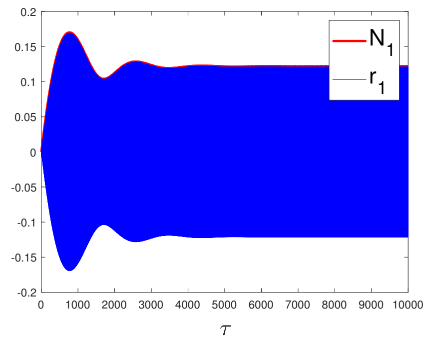

(b)

Figure 3.31. Numerical results (from direct numerical integration of Eqs. (3.103), (3.104) with zero i.c.) for the TWB with NES under UL-2 load with $p = 2.0 \times 10^4$ N/m^2: (a) Time history of N_1 and r_1 for $\sigma = 0.25$; (c) Time history of N_1 and r_1 for $\sigma = 0$.

Then, moving from uniform to punctual loads, a PL case with amplitude $p = 3.0 \times 10^4$ N (divided by the the dimension of the cross-section element along s to have a load per unit length) and frequency equal to that of the first vibration mode is considered. Results are qualitatively the same of those shown for uniform load,

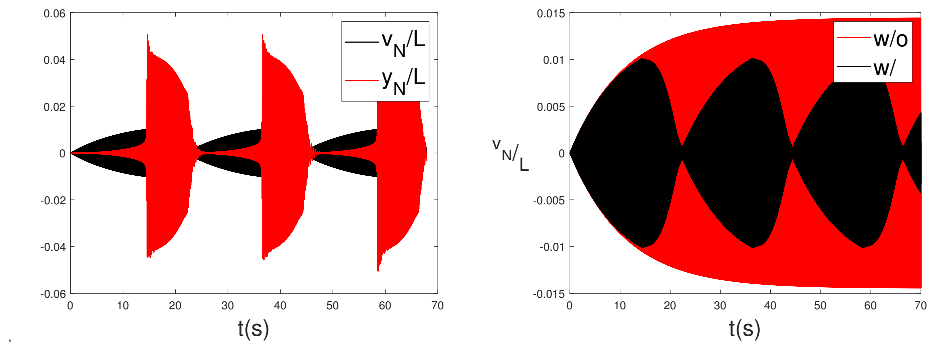

(a) (b)

Figure 3.32. Numerical results (from direct numerical integration of Eqs. (3.103), (3.104) with zero i.c.) for the TWB with NES under UL-2 load with $p = 2.0 \times 10^4$ N/m^2, $\sigma = 0.25$: (a) Time histories of v_N/L and y_N/L; (b) Time histories of v_N/L with and without NES.

as can be seen in Fig. 3.33(a) where the Isola is also present, and in Fig. 3.33(b), showing the ability of the NES to reduce vibrations on this type of beam also for this type of load. It can also be noted that, since the amplitude of the displacements is limited, a properly tuned TMD could also lead to an adequate reduction of vibrations having a periodic response in cases like the one at hand.

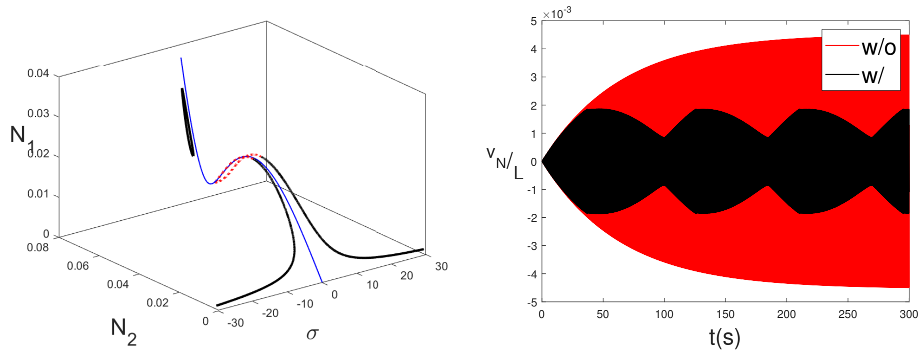

(a) (b)

Figure 3.33. (a) 3D view of the FRC for the TWB with NES under PL load with $p = 3.0 \times 10^4$ N (unstable zone of the SIM in red) with SIM (in blue); (b) Time histories of v_N/L with and without NES for $\sigma = 0.5$; numerical results from direct numerical integration of Eqs. (3.103), (3.104) with zero i.c.

Then, the moving load, considered as subsequent vehicles with the same speed at the same distance, is introduced. Different combinations of parameters can be considered for this type of load. In this case $N_v = 80$ vehicles, at a distance $d_v = 20$ m with a speed $v_v = 70$ m/s and with amplitude $p = 3.0 \times 10^5$ N are considered. Results reported in Figs. 3.34(a), 3.34(b) show a reduction of the vertical displacement of the beam with NES, both during the transit of vehicles on the bridge and in free oscillations. However, even though the NES is activated, the reduction is not so impressive in this case, and it can be better appreciated in the tail of the figures, when all the vehicles have passed through the beam; it is likely that the high number of parameters involved for the load, in addition to those of the NES, do not permit an ideal reduction in vibrations. In Tabs. 3.9, 3.10 some results are reported, showing the influence of different vehicle parameters on vibration control; values are $\left(v_N^{w/} - v_N^{w/o}\right)/v_N^{w/o}$ in percentage. In particular, from Tab. 3.9 it can be noticed that if vehicles are too close or too far, with respect to the beam length, the NES could increase the displacement (positive difference) rather than reducing it, especially for higher speed values. On the other hand, Tab. 3.10 shows that for some combinations of N_v and v_v the reduction is more effective. Furthermore, it should be stated that the chosen speed of vehicles is quite far from the critical one, which for the characteristics of this beam is too high to have a physical meaning, so the reduction may not be optimal.

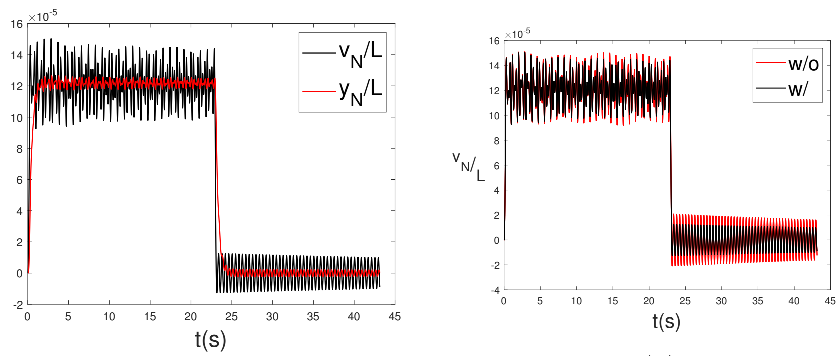

Figure 3.34. Numerical results (from direct numerical integration of Eqs. (3.103), (3.104) with zero i.c.) for the TWB with NES under ML load with $p = 3.0 \times 10^5$ N/m^2, $N_v = 80$, $d_v = 20$ m, $v_v = 70$ m/s: (a) Time histories of v_N/L and y_N/L; (b) Time histories of v_N/L with and without NES.

Table 3.9. Influence of d_v and v_v on vibrations reduction with $p = 3.0 \times 10^5$ N/m^2 and $N_v = 80$. Values represent $\left(v_N^{w/} - v_N^{w/o}\right)/v_N^{w/o}$ in percentage.

v_v \ d_v	15 (m)	20 (m)	30 (m)
36 (m/s)	-4.56	-29.41	-0.23
50 (m/s)	-6.25	-15.88	+30.12
70 (m/s)	+44.75	-38.85	+22.92

Finally, the earthquake is taken into account through a SL case with $\ddot{v}_g(t)$ taken

Table 3.10. Influence of N_v and v_v on vibrations reduction with $p = 3.0 \times 10^5$ N/m^2 and $d_v = 20$ m. Values represent $\left(v_N^{w/} - v_N^{w/o}\right)/v_N^{w/o}$ in percentage.

v_v \ N_v	10	20	50
36 (m/s)	-2.71	-6.90	-24.79
50 (m/s)	-2.06	+7.34	-28.49
70 (m/s)	-9.25	-13.43	+1.29

as the time history of a past earthquake (L'Aquila, 2009): it was chosen since the range of frequencies of the event, identified by its spectrum, was around the 1^{st} frequency of the beam, with a vertical Peak Ground Acceleration (PGA), slightly increased to a value of 0.52 g (Fig. 3.35(a)). Numerical results shown in Figs. 3.35(b), 3.35(c), put in evidence the instant when the NES is activated, almost corresponding to the moment when the seismic acceleration reaches its peak value, and show an evident reduction of displacement of the beam with the NES, even if the maximum displacement remains the same. This application demonstrates the validity of the NES in reducing vibrations related to real loading scenarios, which can otherwise cause severe problems on bridge decks.

To conclude this section resuming its main findings, a full-scale beam was studied with the goal of reducing vibrations caused by different types of loads with different frequencies. Due to its shape, the beam was modeled through Generalized Beam Theory to take into account aspects like the deformation of the cross-section in its own plane and to consider vibration modes (like torsional, local or mixed ones) which cannot be considered with simpler beam theories. The beam, linked to a Nonlinear Energy Sink, was studied through the Complexification Averaging Method, highlighting a good reduction in beam vibrations for 1:1 resonant loads, with different behaviors (periodic, modulated response, isolas). A lower reduction for non-resonant loads which normally act on the beam, like earthquake or train of moving loads, was found too.

3.5 Identification

In this section, a parameter identification procedure of a (geometrically and mechanically) nonlinear beam is presented, with the objective of estimating the value of its parameters from numerical or experimental data; the procedure could be lately

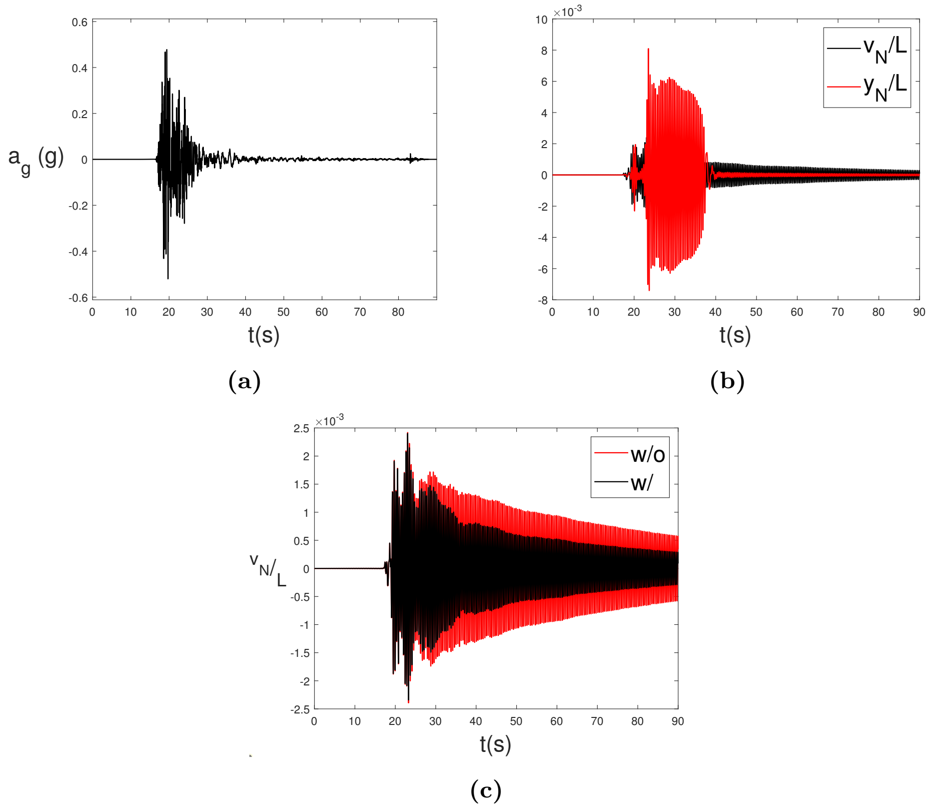

Figure 3.35. Numerical results (from direct numerical integration of Eqs. (3.103), (3.104) with zero i.c.) for the TWB with NES under SL load: (a) Time history of the event; (b) Time histories of v_N/L and y_N/L; (c) Time histories of v_N/L with and without NES.

used for damage detection purposes, not pursued here. First, discrete systems are studied, in order to validate the method and compare it to an equivalent technique taken from the literature, based on the combination of the Hilbert-Huang Transform (HHT) and of the Complexification Averaging Method (Cx-A) (whose results are presented in Appendix A), then the nonlinear continuous beam is studied.

The identification is model-based, being the model tackled through the Multiple Scale Method (MSM), while the input data coming from the signals are processed through the HHT. In this way, it is possible to exploit the advantages of both methods: for the MSM the advantage is that, using it directly on the continuous problem, it is not necessary to choose a priori the modal basis (e.g. through Galerkin's method), while for the HHT the advantage is that it allows to extract mono-component subsignals from a generic record.

In this section a nonlinear Euler-Bernoulli beam model is used, with the first goal being the establishment of this new model-based identification technique. However, it is not excluded that in the future the same technique could be applied to the GBT-D model of the previous sections with the possibility to localize the damage in a TWB.

3.5.1 Hilbert-Huang Transform

The fundamental aspects of the HHT are here recalled. This technique, which was developed in the field of signal processing, is used here in order to identify the parameters of nonlinear dynamical systems, in combination with MSM; better, it is used to process the signal and get the information needed by the identification procedure.

The HHT can be seen as an extension of the classical Hilbert Transform (HT). It was first introduced in this form by Huang and coworkers in [55] to deal with generic nonlinear and non-stationary signals with multiple components. The novelty introduced by Huang allows to deal with generic signals by dividing them into mono-component sub-signals. This step is unavoidable since, as demonstrated by many, the direct application of the HT on the original signal leads to wrong results (like negative values of the frequency).

The idea is to apply the Empirical Mode Decomposition (EMD) which, through the so-called sifting process, decomposes the signal into a small number of Intrinsic Mode Functions (IMF) and a residue as:

$$x(t) = \sum_{i=1}^{n} x_i(t) + r_n(t) \tag{3.133}$$

where each IMF is associated with a single frequency. The main steps of the EMD to find the IMF written in Eq. (3.133) and represented in Fig. 3.36 are the following:

- Local maxima and minima of the signal (according to certain time lapse) are identified.
- Their envelopes are constructed through two distinct splines.
- The mean between the two envelopes is calculated and the difference between the original signal and this mean is considered as the first component.
- Then, the sifting process is repeated starting from the identified first component (which in general is not an IMF yet) in order to overcome problems highlighted in [55] (as negative local maxima and positive local minima and asymmetry problems).
- The same process is repeated more times until an IMF is finally obtained as the first component $x_1(t)$ of the original signal $x(t)$.

- The first IMF is subtracted to the initial signal and the sifting process is repeated to find other IMF until a certain tolerance is reached on the residue $r_n(t)$.

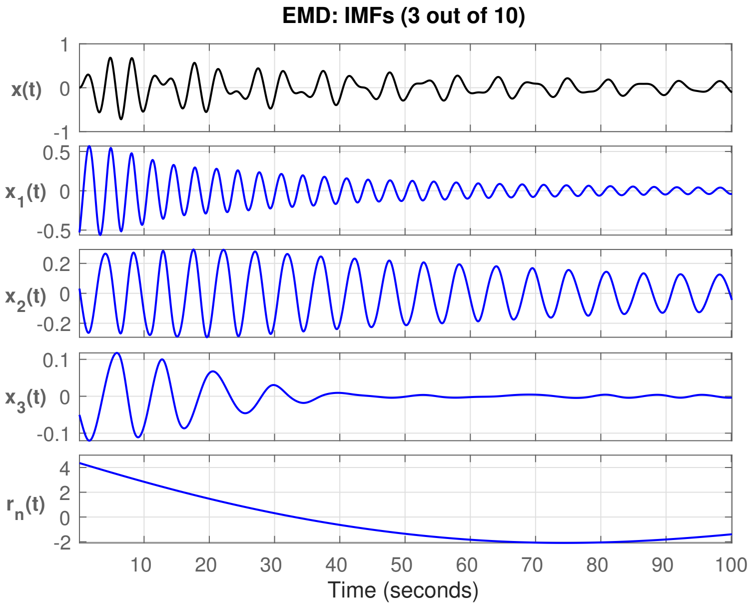

Figure 3.36. IMF obtained through the EMD of a generic signal $x(t)$.

To summarize, each IMF have to respect the following two conditions: (i) in the whole data set, the number of extrema and of zero crossings must either be equal or differ at most by one and (ii) at any point, the mean value of the envelope defined by the local maxima and that defined by the local minima has to be zero.

Once the EMD is performed, the classical HT can be applied separately on each IMF and the equations are here reported. The generic signal $x(t)$ is considered (where t is time), as its IMF are obtained through EMD and are referred to as $x_k(t)$, the HT (here indicated as $y_k(t)$) can be written as:

$$y_k(t) = H(x_k(t)) = \frac{1}{\pi} PV \int_{-\infty}^{\infty} \frac{x_k(\tau)}{t-\tau} d\tau \tag{3.134}$$

where PV is the Cauchy Principal Value, introduced to avoid the singularity at $t = \tau$. Therefore, the transform $H(x_k(t))$ can be seen as the convolution integral between $x_k(t)$ and $1/t$. The two signals $x_k(t)$ and $y_k(t)$ can be combined to give the complex analytic signal:

$$z_k(t) = x_k(t) + i y_k(t) = Q_{x_k}(t) e^{i\phi_{x_k}(t)} \tag{3.135}$$

where the amplitude and phase are respectively:

$$Q_{x_k}(t) = \sqrt{x_k(t)^2 + y_k(t)^2}, \quad \phi_{x_k}(t) = \arctan\left(\frac{y_k(t)}{x_k(t)}\right) \tag{3.136}$$

The instantaneous frequency is obtained deriving the instantaneous phase with respect to time:

$$\theta_{x_k}(t) = \frac{d\phi_{x_k}(t)}{dt} \tag{3.137}$$

The envelopes, phases and frequencies which are obtained through the application of the HHT to experimental or numerical signals are used in this section to identify the parameters of discrete systems before and those of a nonlinear Euler-Bernoulli beam after. This concept entails a fundamental similarity among HHT, Cx-A and MSM and is discussed in the following.

3.5.2 1-d.o.f. systems

The procedure to identify parameters using the HHT combined with MSM is described here and in Sect. 3.5.3 for discrete systems in order to validate and extend it to the beam in Sect. 3.5.4. The inspiration comes from [65] where HHT was used in combination with Cx-A with the same goal (parameter identification) for discrete systems (reported in Appendix A for comparison). The same two discrete systems are here studied for validation of the proposed technique.

A damped Duffing oscillator, with linear stiffness k (in N/m), nonlinear stiffness k_{nl} (in N/m^3) and damping coefficient c (in Ns/m) is considered:

$$\ddot{x} + c\dot{x} + kx + k_{nl}x^3 = 0 \tag{3.138}$$

Nontrivial initial conditions are applied: $x(0) = \hat{a}$, $\dot{x}(0) = \hat{b}$, where $\hat{a}$ and $\hat{b}$ are given coefficients. The small bookkeeping parameter $\varepsilon > 0$ is introduced, the variable x is scaled as $x = \varepsilon^{1/2}\tilde{x}$ and damping as $c = \varepsilon\tilde{c}$. After substitution in Eq. (3.138), dividing by $\varepsilon^{1/2}$ and omitting tilde, one gets:

$$\ddot{x} + \varepsilon c\dot{x} + kx + \varepsilon k_{nl}x^3 = 0 \tag{3.139}$$

Then, in the spirit of the Multiple Scale Method, different independent time scales are introduced as $T_i = \varepsilon^i t$ such that $T_0 = t$, $T_1 = \varepsilon t$, $T_2 = \varepsilon^2 t$ and so on. If only T_0 and T_1 are kept, a uniform first-order series expansion of the solution is looked for as $x(t) = x_0(T_0, T_1) + \varepsilon x_1(T_0, T_1)$. Derivatives with respect to new time scales can thus be written as:

$$\frac{d}{dt} = D_0 + \varepsilon D_1 + \ldots \qquad \frac{d^2}{dt^2} = D_0^2 + 2\varepsilon D_0 D_1 + \ldots \tag{3.140}$$

where $D_i = d/dT_i$. The expanded version of x is substituted inside Eq. (3.139) and high-order terms are discarded. Coefficients of like power of ε are collected and set equal to zero, thus obtaining perturbation equations (and initial conditions) at different orders of ε. For the case under study:

$$\text{ord. } \varepsilon^0 : D_0^2 x_0 + k x_0 = 0 \tag{3.141}$$

$$x_0(0,0) = \hat{a}, \quad D_0 x_0(0,0) = \hat{b} \tag{3.142}$$

$$\text{ord. } \varepsilon^1 : D_0^2 x_1 + k x_1 = -2D_0 D_1 x_0 - c D_0 x_0 - k_{nl} x_0^3 \tag{3.143}$$

$$x_1(0,0) = 0, \quad D_0 x_1(0,0) = -D_1 x_0(0,0) \tag{3.144}$$

Then, the generating solution of Eq. (3.141) is written as:

$$x_0(T_0, T_1) = A(T_1) e^{i\omega T_0} + c.c. \tag{3.145}$$

where $c.c.$ stands for complex conjugate, $A(T_1)$ is the complex slow time-dependent amplitude and $\omega = \sqrt{\frac{k}{m}}$ is the natural (angular) frequency of the associated linear undamped system (the mass m is considered equal to one for the 1-d.o.f. system). The generating solution, found at order ε^0, is then substituted in Eq. (3.143). Resonant terms, i.e. those multiplying $e^{i\omega T_0}$ are collected and set equal to zero in order to avoid the presence of secular terms in the solution, thus obtaining the Amplitude Modulation Equation (AME), which is a nonlinear differential equation governing the modulation of the leading response on the slow time scale (here T_1). For the 1-d.o.f. case under investigation, one obtains that:

$$D_1 A(T_1) = -\frac{c}{2} A + \frac{3ik_{nl}}{2\omega} A^2 \bar{A} \tag{3.146}$$

where $\bar{A}$ is the complex conjugate of A. The polar form of the complex amplitude is finally introduced as $A(T_1) = \frac{1}{2} a(T_1) e^{i\beta(T_1)}$ and the real and imaginary parts of Eq. (3.146) are evaluated after the perturbation parameter ε is reabsorbed, thus going back to the true time t, as follows:

$$\omega a \dot{\beta} = \frac{3}{8} k_{nl} a^3 \tag{3.147}$$

$$\omega \dot{a} = -\frac{1}{2} \omega c a \tag{3.148}$$

As a consequence, i.c. can be written as:

$$a(0) = \sqrt{\hat{a}^2 + \frac{\hat{b}^2}{\omega^2}} \tag{3.149}$$

$$\beta(0) = -\arctan\left(\frac{\hat{b}}{\omega\hat{a}}\right) \tag{3.150}$$

Eqs. (3.147), (3.148) are used here to identify the systems parameters, i.e., nonlinear stiffness and damping coefficients, and for this purpose they are rewritten in the matrix form $\mathbf{A}\boldsymbol{\eta} = \mathbf{b}$ as:

$$\begin{bmatrix} \frac{3}{8}a^3 & 0 \\ 0 & -\frac{1}{2}\omega a \end{bmatrix} \begin{pmatrix} k_{nl} \\ c \end{pmatrix} = \begin{pmatrix} \omega a\dot{\beta} \\ \omega\dot{a} \end{pmatrix} \tag{3.151}$$

where $\boldsymbol{\eta} = (k_{nl}\ c)^T$ is the column of the parameters to be identified. The model-based identification is carried out substituting to the time laws of a, β, and their derivatives in Eq. (3.151) the outcomes of the Hilbert-Huang Transform on the acquired signals, thus allowing one to evaluate $\boldsymbol{\eta}$. This step is possible because, after rewriting Eq. (3.145) with trigonometric functions as:

$$x_0(t) = a(t)\cos\left(\omega t + \beta(t)\right) \tag{3.152}$$

and, comparing the expression of $x_0(t)$ written in Eq. (3.152) with the analytical signal of Eq. (3.135), it is found that:

$$\begin{cases} a(t) = Q_x(t) \\ \beta(t) = \phi_x(t) - \omega t \rightarrow \dot{\beta}(t) = \theta_x(t) - \omega \end{cases} \tag{3.153}$$

which illustrates the link between HHT and MSM.

It should be highlighted that the matrix of coefficients $\mathbf{A}$ of Eq. (3.151) is not square: in fact a, β, $\dot{a}$, $\dot{\beta}$, used to solve the problem, come from the application of the Hilbert-Huang Transform on the time histories of the solution, thanks to the relationship written in Eq. (3.153); they can be either numerically generated or experimentally acquired, thus, in both cases, they are evaluated at different time instants (this means that the matrix $\mathbf{A}$ is tall). It is now possible to pseudo-invert the matrix of coefficients $\mathbf{A}$ of Eq. (3.151) and solve the system for $\boldsymbol{\eta}$, i.e., to find the unknown parameters k_{nl} and c, as:

$$\boldsymbol{\eta} = (\mathbf{A}^T\mathbf{A})^{-1}\mathbf{A}^T\mathbf{b} \tag{3.154}$$

3.5.3 2-d.o.f. systems

The 2-d.o.f. nonlinear oscillator, with masses m_1, m_2 (in kg), linear stiffness terms k_1, k_2, k_{12}, nonlinear stiffness k_{nl} and damping terms c_1, c_2, c_{12}, already analyzed in [65] through Cx-A, is considered. The equations of motion are:

$$\begin{aligned} &m_1\ddot{x} + c_1\dot{x} + c_{12}(\dot{x} - \dot{y}) + k_1 x + k_{12}(x - y) = 0 \\ &m_2\ddot{y} + c_2\dot{y} + c_{12}(\dot{y} - \dot{x}) + k_2 y + k_{12}(y - x) + k_{nl}y^3 = 0 \end{aligned} \tag{3.155}$$

Non-trivial initial conditions are applied, as $x(0) = \hat{x}$, $y(0) = \hat{y}$, $\dot{x}(0) = \hat{X}$, $\dot{y}(0) = \hat{Y}$, where $\hat{x}$, $\hat{y}$, $\hat{X}$, $\hat{Y}$ are given parameters. The goal here is the identification of the column $\boldsymbol{\eta} = (k_{nl}\ c_1\ c_2\ c_{12})^T$.

The MSM is applied once again, i.e. the bookkeeping parameter $\varepsilon > 0$ is introduced, variables x and y are scaled as $x = \varepsilon^{1/2}\tilde{x}$ and $y = \varepsilon^{1/2}\tilde{y}$ and, in the hypothesis of small damping, c_i is considered as $c_i = \varepsilon\tilde{c_i}$ ($i = 1, 2, 12$). Substituting in Eqs. (3.155), dividing by $\varepsilon^{1/2}$ and omitting tilde, provides:

$$\begin{aligned} &m_1\ddot{x} + \varepsilon c_1\dot{x} + \varepsilon c_{12}(\dot{x} - \dot{y}) + k_1 x + k_{12}(x - y) = 0 \\ &m_2\ddot{y} + \varepsilon c_2\dot{y} + \varepsilon c_{12}(\dot{y} - \dot{x}) + k_2 y + k_{12}(y - x) + \varepsilon k_{nl}y^3 = 0 \end{aligned} \tag{3.156}$$

Time scales $T_0 = t$ and $T_1 = \varepsilon t$ are introduced and the dependent variables are expanded in series as:

$$\begin{pmatrix} x(t) \\ y(t) \end{pmatrix} = \begin{pmatrix} x_0(T_0, T_1) \\ y_0(T_0, T_1) \end{pmatrix} + \varepsilon \begin{pmatrix} x_1(T_0, T_1) \\ y_1(T_0, T_1) \end{pmatrix} \tag{3.157}$$

After substitution of Eq. (3.157) in Eqs. (3.156), perturbation equations are obtained collecting and equating to zero the coefficients of the different powers of ε. Initial conditions are considered too:

$$\begin{aligned} \text{ord. } \varepsilon^0 : \ &m_1 D_0^2 x_0 + k_1 x_0 + k_{12}(x_0 - y_0) = 0 \\ &m_2 D_0^2 y_0 + k_2 y_0 + k_{12}(y_0 - x_0) = 0 \end{aligned} \tag{3.158}$$

$$\begin{aligned} &x_0(0,0) = \hat{x}, \quad y_0(0,0) = \hat{y} \\ &D_0 x_0(0,0) = \hat{X}, \quad D_0 y_0(0,0) = \hat{Y} \end{aligned} \tag{3.159}$$

$$
\begin{aligned}
\text{ord. } \varepsilon^1 : \; & m_1 D_0^2 x_1 + k_1 x_1 + k_{12}(x_1 - y_1) \\
& = -2m_1 D_0 D_1 x_0 - c_1 D_0 x_0 - c_{12}(D_0 x_0 - D_0 y_0) \\
& m_2 D_0^2 y_1 + k_2 y_1 + k_{12}(y_1 - x_1) \\
& = -2m_2 D_0 D_1 y_0 - c_2 D_0 y_0 - c_{12}(D_0 y_0 - D_0 x_0) - k_{nl} y_0^3
\end{aligned}
\tag{3.160}
$$

$$
\begin{aligned}
& x_1(0,0) = 0, \quad y_1(0,0) = 0 \\
& D_0 x_1(0,0) = -D_1 x_0(0,0), \quad D_0 y_1(0,0) = -D_1 y_0(0,0)
\end{aligned}
\tag{3.161}
$$

The linear eigenvalue problem descending from Eq. (3.158), namely:

$$
(\mathbf{K}_{ID} + \lambda^2 \mathbf{M}_{ID})\mathbf{v} = \mathbf{0} \tag{3.162}
$$

where

$$
\mathbf{M}_{ID} = \begin{bmatrix} m_1 & 0 \\ 0 & m_2 \end{bmatrix}, \quad \mathbf{K}_{ID} = \begin{bmatrix} k_1 + k_{12} & -k_{12} \\ -k_{12} & k_2 + k_{12} \end{bmatrix} \tag{3.163}
$$

are mass and stiffness matrices, respectively, is solved and the eigenvalues $\lambda_k = \pm i\omega_k$ and the (real) eigenvectors $\mathbf{v}_k = (v_{k,x} \; v_{k,y})^T$, $(k = 1, 2)$ are obtained.

The generating solution of Eq. (3.158) can thus be written as:

$$
\mathbf{x}_0(T_0, T_1) = \sum_{k=1}^{2} A_k(T_1)\mathbf{v}_k e^{i\omega_k T_0} + c.c. \tag{3.164}
$$

where $\mathbf{x}_0 = (x_0 \; y_0)^T$ and $A_k(T_1)$ are complex unknown amplitudes, depending on the slow time scale.

The i.c. of Eqs. (3.159) can be rewritten on the modal basis as:

$$
\mathbf{x}_0(0,0) = \sum_{k=1}^{2} \hat{a}_k \mathbf{v}_k, \quad D_0 \mathbf{x}_0(0,0) = \sum_{k=1}^{2} \hat{b}_k \mathbf{v}_k \tag{3.165}
$$

where:

$$
\hat{a}_k = \frac{(\hat{x} \;\; \hat{y})\mathbf{M}_{ID}\mathbf{v}_k}{\mathbf{v}_k^T \mathbf{M}_{ID} \mathbf{v}_k}, \quad \hat{b}_k = \frac{(\hat{X} \;\; \hat{Y})\mathbf{M}_{ID}\mathbf{v}_k}{\mathbf{v}_k^T \mathbf{M}_{ID} \mathbf{v}_k} \tag{3.166}
$$

Eq. (3.164) is substituted in Eq. (3.160) and, there, terms multiplying $e^{i\omega_k T_0}$ on the right-hand side are collected in a 2-components column vector $\mathbf{f}_k$. Solvability conditions require that $\mathbf{f}_k$ is orthogonal to the eigenvector $\mathbf{v}_k$, for $k = 1, 2$, giving rise to the following AME:

$$
\begin{aligned}
D_1 A_1(T_1) = & \frac{1}{2(m_1 {v_{1,x}}^2 + m_2 {v_{1,y}}^2)\omega_1} \left[-A_1(c_1 + c_{12}) {v_{1,x}}^2 \omega_1 \right. \\
& + 2A_1 c_{12} v_{1,x} v_{1,y} \omega_1 - A_1(c_2 + c_{12}) {v_{1,y}}^2 \omega_1 \\
& \left. + 3i \left(A_1^2 \bar{A}_1 k_{nl} {v_{1,y}}^4 + 2A_1 A_2 \bar{A}_2 k_{nl} {v_{1,y}}^2 {v_{2,y}}^2 \right) \right]
\end{aligned}
\tag{3.167}
$$

$$
\begin{aligned}
D_1A_2(T_1) = {} & \frac{1}{2(m_1{v_{2,x}}^2+m_2{v_{2,y}}^2)\omega_2}\left[-A_2(c_1+c_{12}){v_{2,x}}^2\omega_2\right.\\
& +2A_2c_{12}v_{2,x}v_{2,y}\omega_2 - A_2(c_2+c_{12}){v_{2,y}}^2\omega_2 \\
& \left.+3i\left(A_2^2\bar{A}_2k_{nl}{v_{2,y}}^4+2A_1A_2\bar{A}_1k_{nl}{v_{1,y}}^2{v_{2,y}}^2\right)\right]
\end{aligned}
\tag{3.168}
$$

Polar form is introduced as $A_k(T_1) = \frac{1}{2}a_k(T_1)e^{i\beta_k(T_1)}$ and, after reabsorbing ε, thus going back to the true time t, real and imaginary parts of the AME are collected, providing the real form of the equations, which can be written in the form $\mathbf{A}\boldsymbol{\eta}=\mathbf{b}$, as:

$$
\begin{bmatrix}
\mu_1a_1^3+\mu_2a_1a_2^2 & 0 & 0 & 0\\
0 & \mu_3a_1 & \mu_4a_1 & \mu_5a_1\\
\mu_6a_2^3+\mu_7a_1^2a_2 & 0 & 0 & 0\\
0 & \mu_8a_2 & \mu_9a_2 & \mu_{10}a_2
\end{bmatrix}
\begin{pmatrix} k_{nl}\\ c_1\\ c_2\\ c_{12}\end{pmatrix}
=
\begin{pmatrix} -\zeta_1a_1\dot{\beta}_1\\ \zeta_1\dot{a}_1\\ -\zeta_2a_2\dot{\beta}_2\\ \zeta_2\dot{a}_2\end{pmatrix}
\tag{3.169}
$$

where the expression of the coefficients μ_i and ζ_i are:

$$
\begin{aligned}
&\mu_1=-\frac{3{v_{1,y}}^4}{8},\quad \mu_2=-\frac{3{v_{1,y}}^2{v_{2,y}}^2}{4},\quad \mu_3=-\frac{{v_{1,x}}^2\omega_1}{2},\quad \mu_4=-\frac{{v_{1,y}}^2\omega_1}{2},\\
&\mu_5=-\frac{(v_{1,x}-v_{1,y})^2\omega_1}{2},\quad \mu_6=-\frac{3{v_{2,y}}^4}{8},\quad \mu_7=-\frac{3{v_{1,y}}^2{v_{2,y}}^2}{4},\quad \mu_8=-\frac{{v_{2,x}}^2\omega_2}{2},\\
&\mu_9=-\frac{{v_{2,y}}^2\omega_2}{2},\quad \mu_{10}=-\frac{(v_{2,x}-v_{2,y})^2\omega_2}{2},\\
&\zeta_1=(m_1{v_{1,x}}^2+m_2{v_{1,y}}^2)\omega_1,\quad \zeta_2=(m_1{v_{2,x}}^2+m_2{v_{2,y}}^2)\omega_2
\end{aligned}
\tag{3.170}
$$

Initial conditions become:

$$
a_k(0)=\sqrt{\hat{a}_k^2+\frac{\hat{b}_k^2}{\omega_k^2}},\quad \beta_k(0)=-\arctan\left(\frac{\hat{b}_k}{\omega_k\hat{a}_k}\right)
\tag{3.171}
$$

for $k=1,2$. Moreover, from Eq. (3.164) one gets:

$$
\mathbf{x}_0(t)=\sum_{k=1}^{2}a_k(t)\mathbf{v}_k\cos\left(\omega_kt+\beta_k(t)\right)
\tag{3.172}
$$

from which the k^{th} modal component of, e.g., the first component of the solution is deduced as:

$$
x_{0,k}(t)=a_k(t)v_{k,x}\cos\left(\omega_kt+\beta_k(t)\right)
\tag{3.173}
$$

The obtained fast-frequency mono-component of the multi-frequency signal is compared with Eq. (3.135), providing the following relationship:

$$
\begin{cases}
a_k(t)=Q_{x_k}(t)/v_{k,x}\\
\beta_k(t)=\phi_{x_k}(t)-\omega_kt\rightarrow\dot{\beta}_k(t)=\theta_{x_k}(t)-\omega_k
\end{cases}
\tag{3.174}
$$

Therefore, as for the 1-d.o.f. case, the outcomes of the HHT in terms of time series for

$a_k, \beta_k, \dot{a}_k, \dot{\beta}_k$ can be used in Eq. (3.169), and the resulting tall matrix of coefficients $\mathbf{A}$ can be pseudo-inverted and multiplied to $\mathbf{b}$ to provide the unknown parameters $\boldsymbol{\eta} = (k_{nl}\ c_1\ c_2\ c_{12})^T$.

It is worth noting that, if the i.c. of Eqs. (3.165) lie on a single eigenvector, e.g., $\hat{a}_2 = \hat{b}_2 = 0$ with $\hat{a}_1 \neq 0$ and/or $\hat{b}_1 \neq 0$ then, from Eqs. (3.169), (3.171), it turns out that $a_2(t) \equiv 0$. It means that, in such a case, the solution is mono-modal, i.e.:

$$\mathbf{x}_0(t) = a_1(t)\mathbf{v}_1 \cos(\omega_1 t + \beta_1(t)) \tag{3.175}$$

and the HHT would not be able to deduce the IMF related to the second mode. The real AME related only to mode 1 needs to be considered, namely:

$$\begin{bmatrix} \mu_1 a_1^3 & 0 & 0 & 0 \\ 0 & \mu_3 a_1 & \mu_4 a_1 & \mu_5 a_1 \end{bmatrix} \begin{pmatrix} k_{nl} \\ c_1 \\ c_2 \\ c_{12} \end{pmatrix} = \begin{pmatrix} -\zeta_1 a_1 \dot{\beta}_1 \\ \zeta_1 \dot{a}_1 \end{pmatrix} \tag{3.176}$$

3.5.4 Continuous Systems: hinged-hinged beam

In this section, the procedure developed in Sect. 3.5.2 and Sect. 3.5.3 is extended to the nonlinear beam. Both the transient dynamics associated with the imposition of non-trivial initial conditions and the steady-state response following the application of a harmonic forcing are investigated.

A hinged-hinged Euler-Bernoulli beam, with no internal resonances, is considered. The source of nonlinearity is twofold: on the one hand, it comes from the geometrical effect related to moderately large displacements, which induce a nonlinear cubic term associated to the phenomenon of stretching [85]; on the other hand, a second nonlinear effect is related to the bending moment-curvature relationship $M(w'') = EI(w'')w''$. The resulting equation of motion with boundary conditions [73, 84], in case of external harmonic load, is considered:

$$\rho \ddot{w} + \left(EI(w'')w''\right)'' + c\dot{w} = \frac{EA}{2L} w'' \int_0^L w'^2 dx + F \sin(\Omega_F t) \tag{3.177}$$

with:

$$\begin{aligned} w(0,t) &= w''(0,t) = 0 \\ w(L,t) &= w''(L,t) = 0 \end{aligned} \tag{3.178}$$

where $w(x,t)$ is the vertical displacement (in m), ρ is the mass per unit length (in kg/m), c is the damping coefficient (in kg/ms), EA is the axial stiffness (in N), L

is the length of the beam (in m) and F is the amplitude of the vertical load per unit length (in N/m) with angular frequency Ω_F (in rad/s); $()'$ denotes derivative with respect to x, $\dot{()}$ with respect to time t. The bending stiffness is assumed here as $EI(w'') = EI_c + k_3 w''^2$, where EI_c is the tangent stiffness at the origin (in Nm^2) and k_3 is an elastic coefficient describing a hardening ($k_3 > 0$) or softening ($k_3 < 0$) behavior (in Nm^4).

The following non-dimensional variables are introduced and properly scaled (with $\bar{\omega} = 1/L^2\sqrt{EI_c/\rho}$):

$$\begin{aligned}
&\tilde{x} = \frac{x}{L}, && \tau = \bar{\omega}t, && \tilde{w} = \frac{w}{L}, && \tilde{w} = \varepsilon^{1/2}\hat{w}, \\
&\xi = \frac{c}{2\rho\bar{\omega}}, && \xi = \varepsilon\hat{\xi}, && \alpha = \frac{AL^2}{2I_c}, && \chi = \frac{k_3}{(EI_c L^2)}, \\
&\tilde{F} = \frac{F}{\rho L\bar{\omega}^2}, && \tilde{F} = \varepsilon^{3/2}\hat{F}, && \Omega_R = \frac{\Omega_F}{\bar{\omega}}
\end{aligned} \tag{3.179}$$

Thus, the problem in non-dimensional form, after omitting tilde and hat, becomes:

$$\ddot{w} + w'''' + \varepsilon\chi\left(6w''w'''^2 + 3w''^2 w''''\right) + 2\varepsilon\xi\dot{w} = \varepsilon\alpha w''\int_0^1 w'^2 dx + \varepsilon F\sin\Omega_R\tau \tag{3.180}$$

with:

$$\begin{aligned}
w(0,\tau) = w''(0,\tau) = 0 \\
w(1,\tau) = w''(1,\tau) = 0
\end{aligned} \tag{3.181}$$

Here, $()'$ denotes derivative with respect to $\tilde{x}$, $\dot{()}$ with respect to non-dimensional time τ. Modal frequencies of the linearized beam are evaluated as $\omega_k = k^2\pi^2$ and (mass normalized) linear mode shapes as $\varphi_k(x) = \sqrt{2}\sin(k\pi x)$.

The identification procedure here has the scope to evaluate the parameters contained in the column $\boldsymbol{\eta} = (\alpha\ \chi\ \xi)^T$.

Non-zero initial conditions

The first analyzed case is the application of the Multiple Scale Method to a beam subjected to non-zero initial conditions so, from Eqs. (3.180), (3.181), neglecting the external load F, and considering i.c. in the modal basis, one has:

$$\begin{aligned}
w(x,0) = \sum_{k=1}^{\infty}\hat{a}_k\varphi_k(x) \\
\dot{w}(x,0) = \sum_{k=1}^{\infty}\hat{b}_k\varphi_k(x)
\end{aligned} \tag{3.182}$$

where $\hat{a}_k$ and $\hat{b}_k$ are assigned initial displacement and velocity modal amplitudes, respectively. After introduction of the bookkeeping parameter $\varepsilon > 0$ and time scales $T_0 = \tau$, $T_1 = \varepsilon\tau$, the series expansion of the vertical displacement is $w(x,\tau) = w_0(x,T_0,T_1)+\varepsilon w_1(x,T_0,T_1)$, and perturbation equations, boundary and initial conditions are obtained:

$$\text{ord. } \varepsilon^0 : D_0^2 w_0 + w_0'''' = 0 \tag{3.183}$$

$$\begin{aligned} &w_0(0,T_0,T_1) = w_0''(0,T_0,T_1) = 0 \\ &w_0(1,T_0,T_1) = w_0''(1,T_0,T_1) = 0 \end{aligned} \tag{3.184}$$

$$\begin{aligned} &w_0(x,0,0) = \sum_{k=1}^{\infty} \hat{a}_k \varphi_k(x) \\ &D_0 w_0(x,0,0) = \sum_{k=1}^{\infty} \hat{b}_k \varphi_k(x) \end{aligned} \tag{3.185}$$

$$\begin{aligned} \text{ord. } \varepsilon^1 : D_0^2 w_1 + w_1'''' &= -2D_0 D_1 w_0 - 2\xi D_0 w_0 \\ &+ \alpha w_0'' \int_0^1 w_0'^2 dx - 6\chi w_0'' w_0'''^2 - 3\chi w_0''^2 w_0'''' \end{aligned} \tag{3.186}$$

$$\begin{aligned} &w_1(0,T_0,T_1) = w_1''(0,T_0,T_1) = 0 \\ &w_1(1,T_0,T_1) = w_1''(1,T_0,T_1) = 0 \end{aligned} \tag{3.187}$$

$$\begin{aligned} &w_1(x,0,0) = 0 \\ &D_0 w_1(x,0,0) = -D_1 w_0(x,0,0) \end{aligned} \tag{3.188}$$

The generating solution of Eq. (3.183) is:

$$w_0(x,T_0,T_1) = \sum_{k=1}^{\infty} A_k(T_1)\varphi_k(x) e^{i\omega_k T_0} + c.c. \tag{3.189}$$

where $A_k(T_1)$ is the complex slow time-dependent amplitude. Eq. (3.189) is substituted in Eq. (3.186) and terms multiplying $e^{i\omega_k T_0}$ in the right-hand side are imposed to be orthogonal to the mode shape $\varphi_k(x)$, in order to apply solvability and avoid the occurrence of secular terms. The so-obtained AME referred to the k^{th} amplitude ($k = 1, 2, \ldots$), reads:

$$\begin{aligned} D_1 A_k(T_1) = -\frac{1}{2i\omega_k} \Bigg[& 2i\omega_k \xi A_k + 3k^4\pi^4 \alpha A_k^2 \bar{A}_k + \frac{9}{2} k^8 \pi^8 \chi A_k^2 \bar{A}_k \\ & + \sum_{p \neq k} \left(2k^2 p^2 \pi^4 \alpha A_k A_p \bar{A}_p + 6k^4 p^4 \pi^8 \chi A_k A_p \bar{A}_p \right) \Bigg] \end{aligned} \tag{3.190}$$

The polar form $A_k(T_1) = \dfrac{1}{2} a_k(T_1) e^{i\beta_k(T_1)}$ is introduced and ε reabsorbed, thus going back to true non-dimensional time τ, real and imaginary parts of the AME are obtained for each considered mode amplitude, which reads:

$$\begin{aligned}\omega_k a_k \dot{\beta}_k &= \frac{3}{8}k^4\pi^4\alpha a_k^3 + \frac{9}{16}k^8\pi^8\chi a_k^3 \\ &+ \sum_{p\neq k}\left(\frac{1}{4}k^2p^2\pi^4\alpha a_k a_p^2 + \frac{3}{4}k^4p^4\pi^8\chi a_k a_p^2\right)\end{aligned} \tag{3.191}$$

$$\omega_k \dot{a_k} = -\omega_k \xi a_k \tag{3.192}$$

with initial conditions:

$$a_k(0) = \sqrt{\hat{a}_k^2 + \frac{\hat{b}_k^2}{\omega_k^2}} \tag{3.193}$$

$$\beta_k(0) = -\arctan\frac{\hat{b}_k}{\omega_k \hat{a}_k} \tag{3.194}$$

As the system is damped and no internal resonances occur, if the initial conditions are trivial for a generic modal component, i.e., $\hat{a}_k = \hat{b}_k = 0$, from Eqs. (3.192), (3.193) it turns out that $a_k(\tau) \equiv 0$. Therefore, the effective number of modal amplitudes to be considered corresponds to the number of nontrivial modal amplitudes appearing in the i.c. (Eqs. (3.182)). For the sake of simplicity, assuming $\hat{a}_1 \neq 0$, $\hat{b}_1 \neq 0$ and $\hat{a}_k = \hat{b}_k = 0$ for $k \neq 1$ in Eq. (3.182), the real AME resulting from Eqs. (3.191), (3.192), put in the form $\mathbf{A}\boldsymbol{\eta} = \mathbf{b}$, read:

$$\begin{bmatrix} 6\pi^4 a_1^3 & 9\pi^8 a_1^3 & 0 \\ 0 & 0 & \omega_1 a_1 \end{bmatrix} \begin{pmatrix} \alpha \\ \chi \\ \xi \end{pmatrix} = \begin{pmatrix} 16\omega_1 a_1 \dot{\beta}_1 \\ -\omega_1 \dot{a}_1 \end{pmatrix} \tag{3.195}$$

which corresponds to assume as generating solution:

$$w_0(x,\tau) = a_1(\tau)\varphi_1(x)\cos(\omega_1\tau + \beta_1(\tau)) \tag{3.196}$$

However, if for instance two modes have nontrivial amplitudes in Eqs. (3.182), e.g. mode number 1 and p, then the real AME become:

$$\begin{bmatrix} 6\pi^4 a_1^3 + 4p^2\pi^4 a_1 a_p^2 & 9\pi^8 a_1^3 + 12p^4\pi^8 a_1 a_p^2 & 0 \\ 0 & 0 & \omega_1 a_1 \\ 4p^2\pi^4 a_1^2 a_p + 6p^4\pi^4 a_p^3 & 12p^4\pi^8 a_1^2 a_p + 9p^8\pi^8 a_p^3 & 0 \\ 0 & 0 & \omega_p a_p \end{bmatrix} \begin{pmatrix} \alpha \\ \chi \\ \xi \end{pmatrix} = \begin{pmatrix} 16\omega_1 a_1 \dot{\beta}_1 \\ -\omega_1 \dot{a}_1 \\ 16\omega_p a_p \dot{\beta}_p \\ -\omega_p \dot{a}_p \end{pmatrix} \tag{3.197}$$

which corresponds to the following generating solution:

$$w_0(x,\tau) = a_1(\tau)\varphi_1(x)\cos(\omega_1\tau + \beta_1(\tau)) + a_p(\tau)\varphi_p(x)\cos(\omega_p\tau + \beta_p(\tau)) \tag{3.198}$$

It is once again possible to use the formula in Eq. (3.154) to evaluate the system parameters either from Eq. (3.195) or (3.197).

At this point, to highlight the link between HHT and MSM, which is the idea at the basis of this identification process, one can evaluate the solution in Eq. (3.189) at the position $\bar{x}$, in the general case infinite modes are considered, in polar form and in terms of true time, as:

$$w_0(\bar{x},\tau) = \sum_{k=1}^{\infty} \frac{1}{2} a_k(\tau)\varphi_k(\bar{x}) e^{i(\omega_k \tau + \beta_k(\tau))} + c.c. \tag{3.199}$$

which becomes, using Euler's formula:

$$w_0(\bar{x},\tau) = \sum_{k=1}^{\infty} a_k(\tau)\varphi_k(\bar{x}) \cos\left(\omega_k \tau + \beta_k(\tau)\right) \tag{3.200}$$

From this one, the k^{th} modal component of the solution at the position $\bar{x}$ at the leading perturbation order is:

$$w_{0,k}(\bar{x},\tau) = a_k(\tau)\varphi_k(\bar{x}) \cos\left(\omega_k \tau + \beta_k(\tau)\right) \tag{3.201}$$

As for the discrete problems, the expression given in Eq. (3.201) can be compared to the analytical signal of Eq. (3.135) adopting a convenient notation, thus getting the following relationship:

$$\begin{cases} a_k(\tau) = Q_{w_k}(\tau)|_{\bar{x}} / \varphi_k(\bar{x}) \\ \beta_k(\tau) = \phi_{w_k}(\tau)|_{\bar{x}} - \omega_k \tau \rightarrow \dot{\beta}_k(\tau) = \theta_{w_k}(\tau)|_{\bar{x}} - \omega_k \end{cases} \tag{3.202}$$

provided that $\varphi_k(\bar{x}) \neq 0$, which represents the only requirement to be met when choosing $\bar{x}$ (i.e., $\bar{x}$ is not a node for the k^{th} mode).

Eq. (3.202) allows to use the outcomes of the HHT applied on acquired time series, to be put inside Eq. (3.195) if the initial condition is applied only on 1 mode or inside Eq. (3.197) if two modes are kept, or similar expressions written in the form $\mathbf{A}\boldsymbol{\eta} = \mathbf{b}$ if more modes are present, in terms of $a_k(\tau), \beta_k(\tau)$ and their derivatives to evaluate the relevant parameters.

It is worth mentioning that if one includes more modes in the generation solution (and then in the AME) than those involved in the initial conditions, the identification procedure fails, as the HHT will only allow to evaluate the IMF associated to the modes included in the initial conditions. However, if one includes in the generating solution (and then in AME) less modes than those involved in the initial conditions, the identification procedure works, even if it is generally less precise than the case in which the same exact modes of the initial condition are included.

External resonant load

Here the case of the beam subjected to a harmonic load $F\sin(\Omega_F t)$, in 1:1 external resonance with one of the modes of the system (e.g., the k^{th}), is considered (Eqs. (3.180), (3.181)). The procedure still leads to the identification of the parameters $\boldsymbol{\eta} = (\alpha\ \chi\ \xi)^T$ but, differently than the previous case, the steady-state response is exploited in addition to the transient one.

The non-dimensional angular frequency of the external load can be written as $\Omega_R = \omega_k + \sigma$ where σ is the (small) detuning parameter, which is scaled as $\sigma = \varepsilon\tilde{\sigma}$. Omitting tilde, the perturbation equations turn out to be:

$$\text{ord. } \varepsilon^0 : D_0^2 w_0 + w_0'''' = 0 \tag{3.203}$$

$$\begin{aligned} w_0(0, T_0, T_1) = w_0''(0, T_0, T_1) = 0 \\ w_0(1, T_0, T_1) = w_0''(1, T_0, T_1) = 0 \end{aligned} \tag{3.204}$$

$$\begin{aligned} \text{ord. } \varepsilon^1 : D_0^2 w_1 + w_1'''' &= -2D_0 D_1 w_0 - 2\xi D_0 w_0 \\ &+ \alpha w_0'' \int_0^1 w_0'^2 dx - 6\chi w_0'' w_0'''^2 - 3\chi w_0''^2 w_0'''' + F\sin(\omega_k T_0 + \sigma T_1) \end{aligned} \tag{3.205}$$

$$\begin{aligned} w_1(0, T_0, T_1) = w_1''(0, T_0, T_1) = 0 \\ w_1(1, T_0, T_1) = w_1''(1, T_0, T_1) = 0 \end{aligned} \tag{3.206}$$

As the system is damped and no internal resonances are assumed, the generating solution of Eq. (3.203) can be written as:

$$w_0(x, T_0, T_1) = A_k(T_1)\varphi_k(x)e^{i\omega_k T_0} + c.c. \tag{3.207}$$

Substituting Eq. (3.207) in right-hand side of Eq. (3.205) and imposing the solvability condition, the (single) AME is obtained:

$$D_1 A_k(T_1) = -\frac{1}{2i\omega_k}\left[2i\omega_k\xi A_k + 3k^4\pi^4\alpha A_k^2\bar{A}_k + \frac{9}{2}k^8\pi^8\chi A_k^2\bar{A}_k + \frac{i\sqrt{2}Fe^{i\sigma T_1}}{k\pi}\right] \tag{3.208}$$

The external load makes Eq. (3.208) non-autonomous. Therefore, the phase difference $\gamma_k = \sigma\tau - \beta_k$ is introduced and, using the polar decomposition and separating the real and imaginary parts of Eq. (3.208), the real form expressions of the AME are obtained:

$$\omega_k a_k \left(\sigma - \dot{\gamma}_k\right) = \frac{3}{8} k^4 \pi^4 \alpha a_k^3 + \frac{9}{16} k^8 \pi^8 \chi a_k^3 - \frac{\sqrt{2} F \sin\left(\gamma_k\right)}{k\pi} \tag{3.209}$$

$$\omega_k \dot{a_k} = -\omega_k \xi a_k - \frac{\sqrt{2} F \cos\left(\gamma_k\right)}{k\pi} \tag{3.210}$$

which can be written in the form $\mathbf{A}\boldsymbol{\eta} = \mathbf{b}$:

$$\begin{bmatrix} -3k^5\pi^5 a_k^3 & -9/2k^9\pi^9 a_k^3 & 0 \\ 0 & 0 & k\pi\omega_k a_k \end{bmatrix} \begin{pmatrix} \alpha \\ \chi \\ \xi \end{pmatrix} = \begin{pmatrix} -8\sqrt{2}F\sin(\gamma_k) - 8k\pi\omega_k a_k(\sigma - \dot{\gamma}_k) \\ -\sqrt{2}F\cos(\gamma_k) - k\pi\omega_k \dot{a}_k \end{pmatrix} \tag{3.211}$$

Also in this case, the link between HHT and MSM can be proven. To do that, the generating solution Eq. (3.207) evaluated at the position $\bar{x}$ and in term of true time can be rewritten as:

$$w_{0,k}(\bar{x}, \tau) = a_k(\tau)\varphi_k(\bar{x}) \cos\left(\omega_k \tau + \sigma\tau - \gamma_k(\tau)\right) \tag{3.212}$$

Therefore, comparing also for the forced beam Eq. (3.212) with the analytical signal of Eq. (3.135), the relationship holds if, using the right notation for the beam:

$$\begin{cases} a_k(\tau) = Q_{w_k}(\tau)|_{\bar{x}}/\varphi_k(\bar{x}) \\ \gamma_k(\tau) = -\phi_{w_k}(\tau)|_{\bar{x}} + \omega_k\tau + \sigma\tau \rightarrow \dot{\gamma}_k(\tau) = -\theta_{w_k}(\tau)|_{\bar{x}} + \omega_k + \sigma \end{cases} \tag{3.213}$$

provided that $\varphi_k(\bar{x}) \neq 0$. Therefore, making use of the outcomes of the HHT for a_k, γ_k and their derivatives, the system (3.211) can be pseudo-inverted to evaluate the unknown parameters $\boldsymbol{\eta} = (\alpha\ \chi\ \xi)^T$.

3.5.5 Continuous system: clamped-clamped beam

The procedure developed in Sect. 3.5.4 for the hinged-hinged beam is here extended to the clamped-clamped beam. The equations of motion and b.c. are formulated for a system with geometric nonlinearity subjected to a concentrated force as:

$$\rho\ddot{w} + EI_c w'''' + c\dot{w} = \frac{EA}{2L} w'' \int_0^L w'^2 dx + F_V \delta(x - x_V) \sin\left(\Omega_F t\right) \tag{3.214}$$

$$\begin{gathered} w(0,t) = w'(0,t) = 0 \\ w(L,t) = w'(L,t) = 0 \end{gathered} \tag{3.215}$$

where, differently from what written in Sect. 3.5.4, F_V has the dimension of a force and the term δ is the Dirac delta function to account for the position x_V of the force along the beam axis. The same nondimensional variables written in Eq. (3.179) are used, with the following differences:

$$\tilde{F}_V = \frac{F_V}{\rho L^2 \bar{\omega}^2}, \qquad \tilde{F}_V = \varepsilon^{3/2} \hat{F}_V, \qquad \delta\left(x - x_V\right) = \frac{1}{L}\delta\left(\tilde{x} - \tilde{x}_V\right) \tag{3.216}$$

Thus, the nondimensional problem can be rewritten, after omitting tilde and hat, as:

$$\ddot{w} + w'''' + 2\varepsilon\xi\dot{w} = \varepsilon\alpha w'' \int_0^1 w'^2 dx + \varepsilon F_V \delta(x - x_V) \sin \Omega_R \tau \tag{3.217}$$

$$\begin{aligned} w(0,\tau) = w'(0,\tau) = 0 \\ w(1,\tau) = w'(1,\tau) = 0 \end{aligned} \tag{3.218}$$

The external load is considered to be resonant with the 1^{st} natural mode of the clamped-clamped beam ($\Omega_R = \omega_1 + \sigma$), which reads:

$$\varphi_1(x) = \cos(\lambda_1 x) - \cosh(\lambda_1 x) - \frac{\cos(\lambda_1) - \cosh(\lambda_1)}{\sin(\lambda_1) - \sinh(\lambda_1)} \left(\sin(\lambda_1 x) - \sinh(\lambda_1 x)\right) \tag{3.219}$$

with nondimensional angular frequency $\omega_1 = \lambda_1^2$, where $\lambda_1 = 4.730$.

The same steps followed in Sect. 3.5.4 are repeated and the identification equations, written in the form $\mathbf{A}\boldsymbol{\eta} = \mathbf{b}$ with $\boldsymbol{\eta} = (\alpha\ \xi)^T$, reads:

$$\begin{aligned} &\begin{bmatrix} 3\left(\int_0^1 \varphi_1'^2 dx\right)\left(\int_0^1 \varphi_1 \varphi_1'' dx\right) a_1^3 & 0 \\ 0 & 2\left(\int_0^1 \varphi_1^2 dx\right)\omega_1 a_1 \end{bmatrix} \begin{pmatrix} \alpha \\ \xi \end{pmatrix} \\ &= \begin{pmatrix} -4F\sin(\gamma_1)\varphi_1(x_V) - 8\left(\int_0^1 \varphi_1^2 dx\right)\omega_1 a_1(\sigma - \dot{\gamma}_1) \\ -F\cos(\gamma_1)\varphi_1(x_V) - 2\left(\int_0^1 \varphi_1^2 dx\right)\omega_1 \dot{a}_1 \end{pmatrix} \end{aligned} \tag{3.220}$$

The relationship which highlights the similarity between the HHT and the MSM is the same written in Eq. (3.213).

3.5.6 Material nonlinearity

Since inside Eq. (3.177) a material nonlinearity is present, different possibilities could be considered to describe it. For instance, in case of post-tensioned reinforced concrete beams (see [121]), a bilinear constitutive elastic law between bending moment and curvature can be assumed:

$$M(w''(x)) = \begin{cases} EI_1 w''(x) \text{ for } \ w''(x) \leq \bar{k} \\ EI_2 w''(x) \text{ for } \ w''(x) > \bar{k} \end{cases} \tag{3.221}$$

where $\bar{k}$ is the limit curvature corresponding to the angular point of the relationship. The two constant stiffness values are such that $EI_2 < EI_1$ (softening behavior). The non-smooth relationship (3.221) can be processed in order to apply the MSM.

In particular, an alternative smooth representation of Eq. (3.221) is realized by introducing a polynomial relationship (linear and cubic terms), which can be made equivalent to the first one, e.g. by comparing the energies. In this way, the value of the cubic term related to the material nonlinearity can be evaluated using the identification procedure and then used to assess the stiffness of the second branch of the bilinear law. For this purpose, the nonlinear stiffness was considered as:

$$EI(w'') = EI_c + k_3 w''^2 \tag{3.222}$$

where EI_c and k_3 are constants, the latter having dimensions Nm^4, and, as a consequence, the bending moment-curvature relationship becomes:

$$M(w'') = EI(w'')w'' = EI_c w'' + k_3 w''^3 \tag{3.223}$$

Similarly to what was done in [19], it is possible to evaluate the elastic energy related to the bilinear (3.221) and polynomial (3.223) relationships, respectively:

$$A_b = \frac{M_u\left(w''_u - w''_e\right) + M_e w''_u}{2} \tag{3.224}$$

and

$$A_c = \frac{EI_c w''^2_u}{2} + \frac{k_3 w''^4_u}{4} \tag{3.225}$$

where $EI_c = EI_1$, w''_e is the first branch limit curvature for the bilinear case ($w''_e = \bar{k}$), w''_u is the ultimate limit curvature for both cases, $M_e = EI_1 w''_e$ and $M_u = M_e + EI_2\left(w''_u - w''_e\right)$ are the first branch and ultimate limit moments for the bilinear case, respectively. Imposing that $A_b = A_c$, the value of EI_2 is obtained as:

$$EI_2 = EI_c + \frac{k_3}{2}\frac{w''^4_u}{\left(w''_e - w''_u\right)^2} \tag{3.226}$$

Assuming that w''_e, w''_u, EI_c are known parameters, once k_3 (or its non-dimensional counterpart χ) is identified through the proposed procedure, then EI_2 is determined.

An example of constitutive laws is shown in Fig. 3.37, where the red curve is the bilinear relationship, the blue curve the polynomial equivalent representation and the filled areas correspond to the relevant elastic energy.

3.5.7 Numerical results

System parameters are here identified starting from numerically generated signals, obtained through the Matlab function ode45 [88]. In particular, all the system parameters are assigned in order to generate the numerical signals. The signals are then processed by the identification procedure, and the identified parameters are

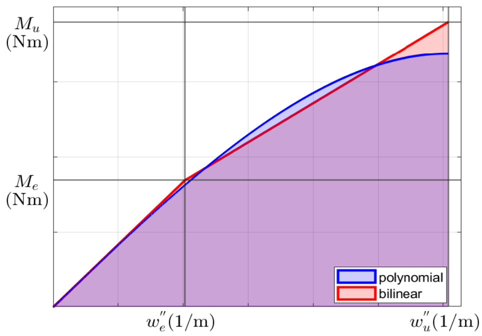

Figure 3.37. Equivalence in terms of energy between the moment-curvature constitutive laws of the bilinear (Eq. (3.221)) and polynomial (Eq. (3.222)) cases.

compared with the assigned ones.

1-d.o.f systems

With reference to the 1-d.o.f. system of Sect. 3.5.2, results are reported in Tab. 3.11, where the numerically acquired signals were generated by applying a non-zero initial condition on x. More specifically, in Tab. 3.11 the row "Real values" shows the values of all the system parameters (k, k_{nl}, c) used to generate the numerical data, whereas the row "Identified values" shows the values obtained by the identification procedure (here k_{nl} and c). The applied initial condition (i.c.) is shown as well. It can be seen that, for two different sets of parameters, the identification leads to a maximum difference of 5.9% on k_{nl}.

Table 3.11. Parameter identification for the 1-d.o.f. system of Eq. (3.138) using HHT+MSM.

	k (N/m)	k_{nl} (N/m^3)	c (Ns/m)
Real values	1.000	1.000	0.100
Identified values for $x(0) = 1.0$ m	-	0.941	0.098
Identified values for $x(0) = 0.5$ m	-	1.054	0.099
Real values	1.000	2.000	0.050
Identified values for $x(0) = 0.5$ m	-	1.944	0.048

As a further validation of the link among HHT, MSM and Cx-A, a comparison of amplitudes and instantaneous frequencies (see Eqs. (3.174)) as obtained from the three methods is shown in Fig. 3.38. There, in particular, the red lines represent the outcomes of the HHT on the numerically generated signal, the blue stars are the outcomes of the numerical integration of the real AME with the assigned parameters (Eqs. (3.169)), and the black-edged circles are the outcomes of the numerical integration of the averaged equations coming from the application of the Cx-A (taken from [65]), still with the assigned parameters. The superimposition is perfect, confirming the validity of what written before.

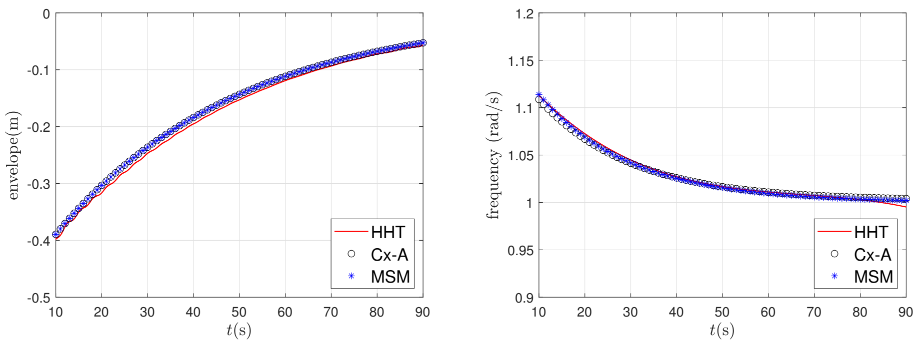

(a) **(b)**

Figure 3.38. Slow-time depending amplitudes and instantaneous frequencies of HHT, Cx-A and MSM for a 1-d.o.f. system with $k = 1$ N/m, $k_{nl} = 2$ N/m^3, $c = 0.05$ Ns/m and i.c. $x(0) = 0.5$ m, $\dot{x}(0) = 0$. (a) $Q_x(t)$ (HHT), $a_x(t)/\omega$ (Cx-A), $a(t)$ (MSM); (b) $\theta_x(t)$ (HHT), $\dot{\beta}_x(t) + \omega$ (Cx-A), $\dot{\beta}(t) + \omega$ (MSM).

2-d.o.f systems

With reference to the 2-d.o.f. system of Sect. 3.5.3, results are reported in Tab. 3.12, where the numerical solution was found by applying a non-zero i.c. either on x, $\dot{x}$ or y. Still, Tab. 3.12 shows the parameter values used to generate data ("Real values"), the identified values and the initial conditions (i.c.).

It can be seen that all parameters are well identified in all investigated cases, with a maximum difference of 25.8% on c_2 in the second last case. On the other hand, in the last case, c_1 is not well identified, as can also be pointed out when using Cx-A for the same problem (Tab. A.2): it was found that, with both methods, when dealing with 2 d.o.f. systems where nonlinear stiffness is considered only for one of them, it can be more difficult to correctly identify the value of damping associated to the other d.o.f.

The same relationship written in Eq. (3.174) is shown Fig. 3.39 where the different lines have the same meaning explained for 1 d.o.f. systems. Their correspondence, except for some fluctuations, validates once again the proposed procedure.

Table 3.12. Parameter identification for the 2-d.o.f. system of Eq. (3.155) using HHT+MSM.

	m_1 (kg)	m_2 (kg)	k_1 (N/m)	k_2 (N/m)	k_{12} (N/m)	k_{nl} (N/m^3)	c_1 (Ns/m)	c_2 (Ns/m)	c_{12} (Ns/m)
Real values	1.000	1.000	1.000	1.000	1.000	2.000	0.050	0.050	0.000
Identified values for $x(0) = 0.5$ m	-	-	-	-	-	1.968	0.050	0.050	-0.001
Identified values for $y(0) = 0.5$ m	-	-	-	-	-	2.007	0.051	0.051	-0.003
Identified values for $\dot{x}(0) = 1.0$ m/s	-	-	-	-	-	2.038	0.050	0.050	-0.001
Real values	1.000	1.000	1.000	2.000	2.000	3.000	0.050	0.050	0.010
Identified values for $x(0) = 0.5$ m	-	-	-	-	-	3.048	0.059	0.037	0.010
Real values	1.000	1.300	2.000	1.000	1.000	5.000	0.050	0.030	0.000
Identified values for $x(0) = 0.1$ m	-	-	-	-	-	5.128	0.015	0.034	0.018

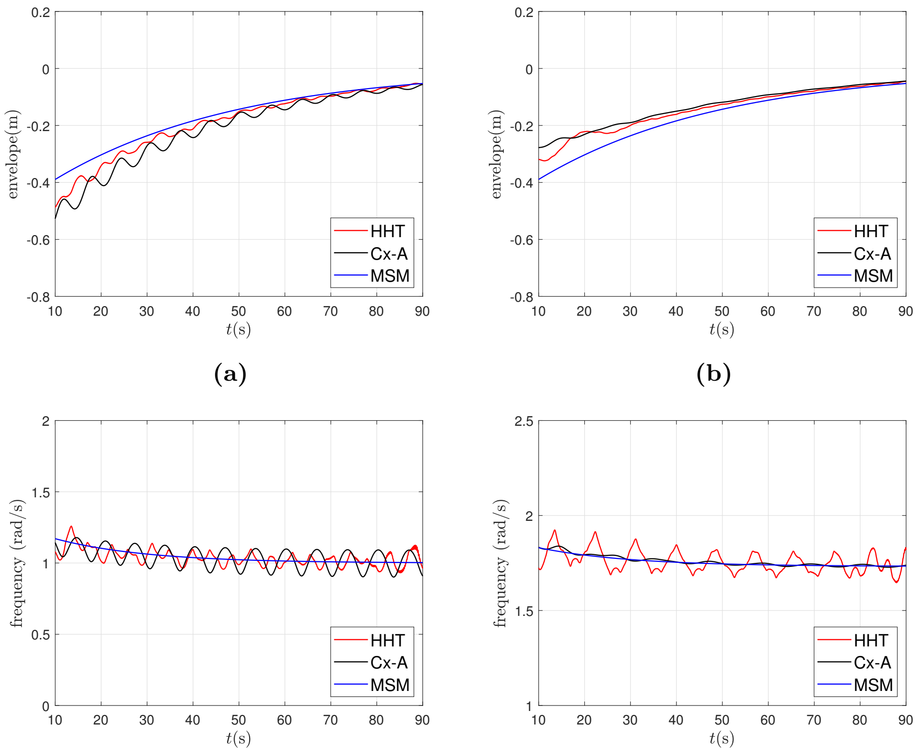

(a) **(b)** **(c)** **(d)**

Figure 3.39. Slow-time depending amplitudes and instantaneous frequencies of HHT, Cx-A and MSM for a 2-d.o.f. system with $m_1 = 1$ kg, $m_2 = 1$ kg, $k_1 = 1$ N/m, $k_2 = 1$ N/m, $k_{12} = 1$ N/m, $k_{nl} = 2$ N/m^3, $c_1 = 0.05$ Ns/m, $c_2 = 0.05$ Ns/m, $c_{12} = 0$ Ns/m and i.c. $x(0) = 1$ m, $\dot{x}(0) = y(0) = \dot{y}(0) = 0$. (a) $Q_{x_1}(t)$ (HHT), $a_{x_1}(t)/\omega_1$ (Cx-A), $a_1(t)v_{1,x}$ (MSM); (b) $Q_{x_2}(t)$ (HHT), $a_{x_2}(t)/\omega_2$ (Cx-A), $a_2(t)v_{2,x}$ (MSM); (c) $\theta_{x_1}(t)$ (HHT), $\dot{\beta}_{x_1}(t)+\omega_1$ (Cx-A), $\dot{\beta}_1(t)+\omega_1$ (MSM); (d) $\theta_{x_2}(t)$ (HHT), $\dot{\beta}_{x_2}(t)+\omega_2$ (Cx-A), $\dot{\beta}_2(t)+\omega_2$ (MSM).

Some differences between the proposed procedure and that which makes use of the Cx-A are finally highlighted, for the 2-d.o.f. system case. The application of

Cx-A provides one AME for each of the k-th modal components ($k = 1, 2$), for every degree-of-freedom. It means that the final number of equations is eight. On the other hand, MSM provides one AME for each modal component, leading to four final equations (Eqs. (3.169)). Another difference is that, using Cx-A, linear stiffness terms can be identified as well, whereas the MSM requires the knowledge in advance of the natural frequencies of the system. Moreover, the frequency ω_k dealt with Cx-A, reported in Appendix A, is not exactly the same of Eq. (3.174), since for Cx-A it represents the frequency which best describes the system response, as stated in [65], which can actually be identified in different ways (e.g., through Wavelet Transform or Fast Fourier Transform), while for MSM it unambiguously represents the frequency of the linear system.

Hinged-hinged beam

With reference to the hinged-hinged beam with non-zero initial conditions and no external force, results when the sole geometric nonlinearity is retained ($\chi = 0$) are reported in Tab. 3.13 for the single mode case, and in Tab. 3.14 when 2 modes are kept. The numerical solution was found by applying a non-zero initial condition either on displacement or on velocity (Eqs. (3.182)). It can be seen that all parameters are well identified both in the single mode case, with a maximum difference of 7.1% both on α and on ξ, and in the 2 modes case with a difference of 4.1%.

A comparison of slow time depending amplitudes and instantaneous frequencies, evaluated through HHT and MSM is reported in Fig. 3.40, confirming the validity of the procedure.

Results when the sole material nonlinearity is retained ($\alpha = 0$) are reported in Tab. 3.15 for the single mode case, while Tab. 3.16 is the case when both types of nonlinearity are taken into account, with 2 modes. It can be seen that all parameters are identified in a satisfactory way: in particular, in the first case, the maximum difference is of 5.3% on ξ, while in the second one is of 12.6% on χ with smaller values on ξ and α.

When dealing with the hinged-hinged beam subjected to a 1:1 resonant load, results are reported in Tab. 3.17, where initial conditions are kept equal to zero. Also in this case the identified parameters are in good agreement with the real ones for different cases, with the load in resonance with different modes (the first or the third one), with a maximum difference of 5.2% on α when considering the first

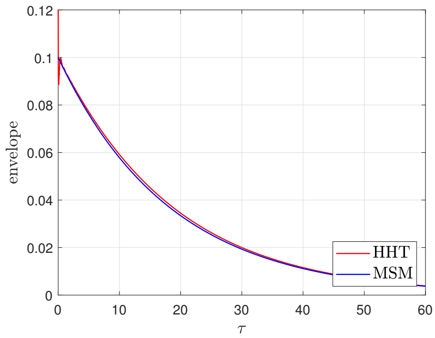

(a)

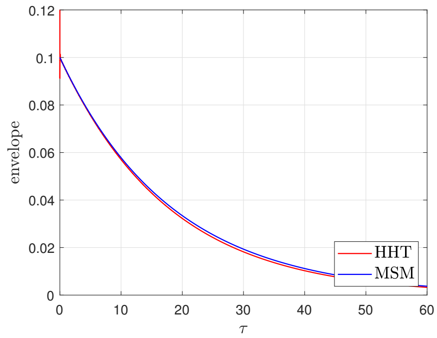

(b)

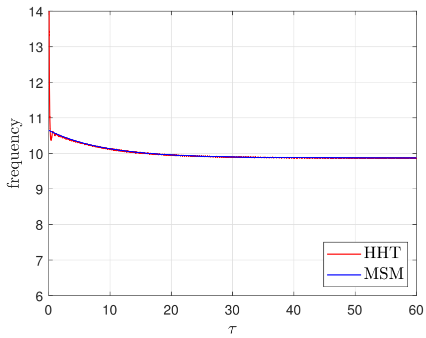

(c)

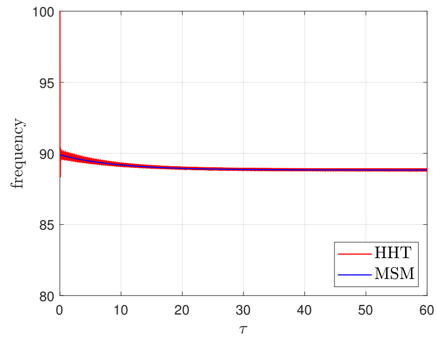

(d)

Figure 3.40. Slow time depending amplitudes and instantaneous frequencies of HHT and MSM for a beam with geometric nonlinearity with 2 modes (1 and $p = 3$) with $\xi = 0.055$, $\alpha = 6.0$, and i.c. $w(x, 0) = 0.1[\sin(\pi x) + \sin(p\pi x)]$, $\dot{w}_0(x, 0) = 0$ evaluated at midspan. (a) $Q_{w_1}(\tau)|_{\bar{x}}$ (HHT), $a_1(\tau)\varphi_1(\bar{x})$ (MSM); (b) $Q_{w_p}(\tau)|_{\bar{x}}$ (HHT), $a_p(\tau)\varphi_p(\bar{x})$ (MSM); (c) $\theta_{w_1}(\tau)|_{\bar{x}}$ (HHT), $\dot{\beta}_1(\tau) + \omega_1$ (MSM); (d) $\theta_{w_p}(\tau)|_{\bar{x}}$ (HHT), $\dot{\beta}_p(\tau) + \omega_p$ (MSM).

mode, and of 11.8%, still on α, for the third mode.

Table 3.13. Parameter identification for the beam of Eqs. (3.180), (3.181) with only geometric nonlinearity with i.c. on the 1^{st} mode using HHT+MSM.

	ξ -	α -
Real values	0.055	6.000
Identified values for $\hat{a}_1 = 0.071$	0.052	5.912
Identified values for $\hat{b}_1 = 3.873$	0.054	6.426
Real values	0.968	150.000
Identified values for $\hat{a}_1 = 0.141$	1.037	146.414

A last comparison of slow time depending amplitudes and instantaneous frequencies of HHT and MSM in the forced case which confirms what written in Eq. (3.213) is reported in Fig. 3.41 for two different data sets.

Table 3.14. Parameter identification for the beam of Eqs. (3.180), (3.181) with only geometric nonlinearity with i.c. on the 1^{st} and 3^{rd} modes using HHT+MSM.

	ξ -	α -
Real values	0.055	6.000
Identified values for $\hat{a}_{1,3} = 0.071$	0.053	6.238
Real values	0.968	150.000
Identified values for $\hat{a}_{1,3} = 0.014$	0.966	150.552

Table 3.15. Parameter identification for the beam of Eqs. (3.180), (3.181) with only material nonlinearity with i.c. on the 1^{st} mode using HHT+MSM.

	ξ -	χ -
Real values	0.055	-3.600×10^{-4}
Identified values for $\hat{a}_1 = 0.707$	0.056	-3.724×10^{-4}
Real values	0.219	-9.000×10^{-3}
Identified values for $\hat{a}_1 = 0.354$	0.207	-8.985×10^{-3}

Table 3.16. Parameter identification for the beam of Eqs. (3.180), (3.181) with geometric and material nonlinearities with i.c. on the 1^{st} and 3^{rd} modes using HHT+MSM.

	ξ -	α -	χ -
Real values	0.055	6.000	-3.600×10^{-4}
Identified values for $\hat{a}_{1,3} = 0.707$	0.055	6.177	-3.972×10^{-4}
Real values	0.968	150.000	-7.200×10^{-3}
Identified values for $\hat{a}_{1,3} = 0.141$	0.971	152.625	-8.106×10^{-3}

Table 3.17. Parameter identification for the beam of Eqs. (3.180), (3.181) with geometric nonlinearity and external sinusoidal resonant force using HHT+MSM.

	mode	ξ	α
	-	-	-
Real values	1	0.055	6.000
Identified values for $F = 0.120$, $\sigma = 0.0$	-	0.056	5.689
Real values	1	0.219	24.000
Identified values for $F = 0.480$, $\sigma = 0.0$	-	0.226	23.619
Real values	3	0.055	6.000
Identified values for $F = 12.00$, $\sigma = 0.0$	-	0.050	5.294
Real values	3	1.369	150.000
Identified values for $F = 15.00$, $\sigma = 0.0$	-	1.441	136.108

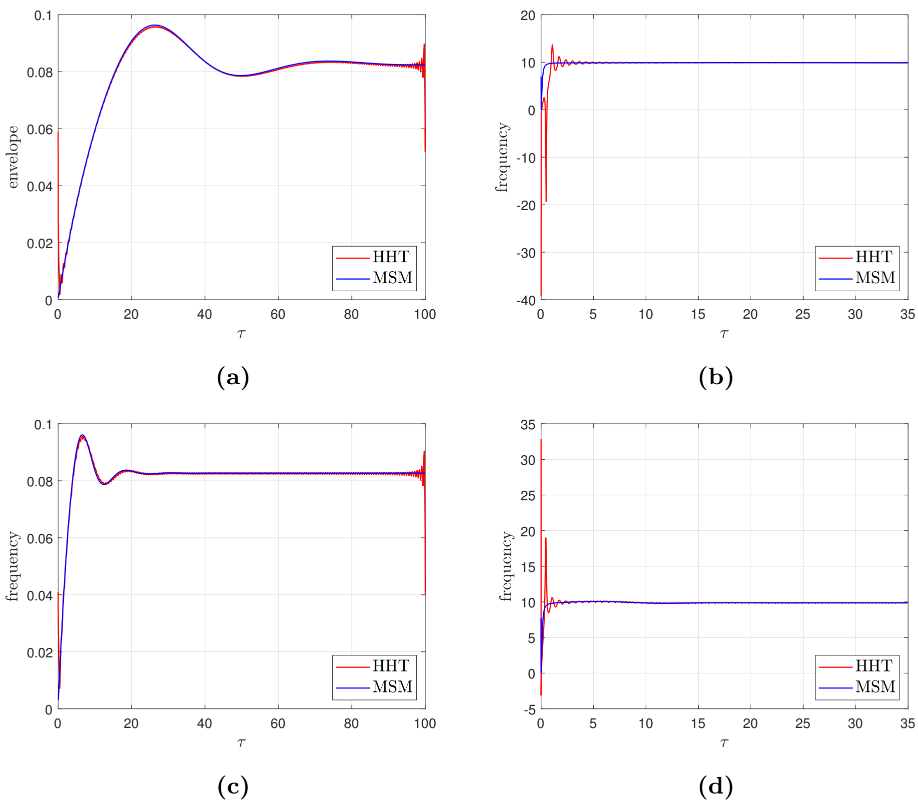

Figure 3.41. Slow time depending amplitudes and instantaneous frequencies of HHT and MSM for a forced beam (with respect to the 1^{st} mode) with geometric nonlinearity with $\xi = 0.055$, $\alpha = 6.0$, and $F = 0.12$ (on the top) or $\xi = 0.219$, $\alpha = 24.0$, and $F = 0.48$ (on the bottom) evaluated at midspan. (a)-(c) $Q_{w_1}(\tau)|_{\bar{x}}$ (HHT), $a_1(\tau)\varphi_1(\bar{x})$ (MSM); (b)-(d) $\theta_{w_1}(\tau)|_{\bar{x}}$ (HHT), $\dot{\beta}_1(\tau) + \omega_1$ (MSM).

3.5.8 Sensitivity to user-defined inputs

Some user-defined inputs have to be set for the identification process using HHT in combination with MSM. The same happens of course when, instead of MSM, Cx-A is used. The most important inputs are, in descending order of relevance: (i) the time interval within which envelopes, phases and their derivatives are evaluated, (ii) the amplitude of the initial condition, (iii) the time step to find the numerical solution, (iv) the tolerance and number of iterations in the Empirical Mode Decomposition (EMD) to obtain Intrinsic Mode Functions (IMF) which really bring information on single components, (v) the possible need of filters or fitting on envelopes and instantaneous frequencies to get rid of numerical errors. In this section it is discussed how some of these inputs affect the identification process, with the aim of testing its robustness.

With reference to both discrete and continuous systems under non-trivial initial conditions, it turns out that the most significant user-defined inputs are: (i) the amplitude of the initial condition (e.g., the value $x(0)$) to obtain the numerical solution which is fed into the HHT and (ii) the time range $[t_i, t_f]$, where t_i is the initial time and t_f the final time, within which envelopes and phases are evaluated.

Considering the 2-d.o.f. nonlinear system of Eq. (3.155), with $m_1 = 1$ kg, $m_2 = 1$ kg, $k_1 = 1$ N/m, $k_2 = 1$ N/m, $k_{12} = 1$ N/m, $k_{nl} = 2$ N/m^3, $c_1 = 0.05$ Ns/m, $c_2 = 0.05$ Ns/m, $c_{12} = 0$ Ns/m, Fig. 3.42(a) shows the dependency of the identified value of k_{nl} on the initial condition when using Cx-A and MSM with the time range fixed between $t_i = 20$ s and $t_f = 60$ s (for a signal which ranges between 0 and 100 seconds). In both cases, there is a range of $x(0)$ which guarantees a valid identification, outside which the identification fails. It can be seen that the working range of initial conditions is partially superimposed between Cx-A and MSM.

Once the range of valid initial conditions is identified, it is useful to create a 3D domain for $x(0)$, t_i and t_f to test the robustness of the procedure. Since this work focuses on MSM, the domain of Cx-A is not reported here. In Fig. 3.42(b) a domain in the space $x(0)$, t_i, t_f is shown for the identified values of k_{nl}. It is realized taking all the triplets which, starting from the numerical solution, are able to identify k_{nl} with a 10% difference with respect to the real value, by varying $x(0)$ between 0.1 m and 1 m, t_i between 10 s and 20 s and t_f between 60 s and 100 s; this means that the actual domain is wider than the represented one. Fig. 3.42(b) highlights that, at least for the problem under study, when using the proposed identification procedure,

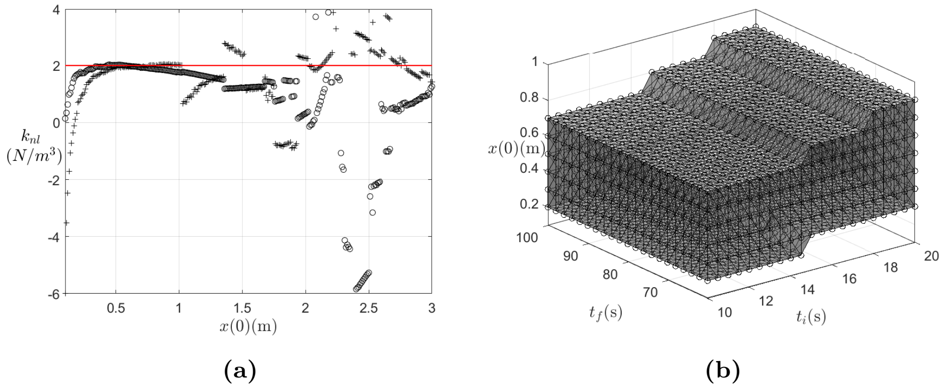

Figure 3.42. (a) Dependence of the identified k_{nl} value of Eq. (3.155) on the i.c. $x(0)$ when using HHT+Cx-A (+) and HHT+MSM (o) for $m_1 = 1$ kg, $m_2 = 1$ kg, $k_1 = 1$ N/m, $k_2 = 1$ N/m, $k_{12} = 1$ N/m, $k_{nl} = 2$ N/m^3, $c_1 = 0.05$ Ns/m, $c_2 = 0.05$ Ns/m, $c_{12} = 0$ Ns/m with time range fixed between 20 s and 60 s. (b) Domain of validity of the identified value of k_{nl} in the space $x(0)$, t_i, t_f when using HHT+MSM.

one could be able to correctly identify the system parameters (specifically k_{nl}) by choosing the three user-defined inputs in a wide interval, hence ensuring consistency to the identification process.

3.5.9 Simulation on a discrete nonlinear system

A preliminary experimental validation is realized on a discrete problem. In particular, a real time simulation of a nonlinear oscillator is set up with a MathWorks Simulink model [88] of the forced Duffing oscillator, whose code is then implemented on a dSPACE DS1005 real-time workstation. The real time fixed-step solver uses the fourth-order Runge-Kutta method to compute the model state variables at a rate of 20000 samples/second. Analog signals are generated at the same rate by a DS1103 16 bit DAC converter. The estimated value of quantization noise was less than 1mV RMS on the DAC output range of +/- 10V; the pass band of 5 kHz was considered adequate for the dynamics exhibited by the oscillator. Analog signals were acquired and saved by means of a National Instruments system equipped with PXIe-4499 board. A scheme of the system is depicted in Fig. 3.43.

Results are reported in Tab. 3.18, for the forced Duffing oscillator with the experimental signal $x(t)$ as input for the HHT. Both k_{nl} and c are well identified, considering perfect resonance, i.e., $\sigma = 0$ as well as a case with $\sigma = 0.1$ rad/s (being σ the detuning parameter).

The present preliminary experimental validation, together with results shown in Sect. 3.5.7, allows to conclude that the model-based identification procedure

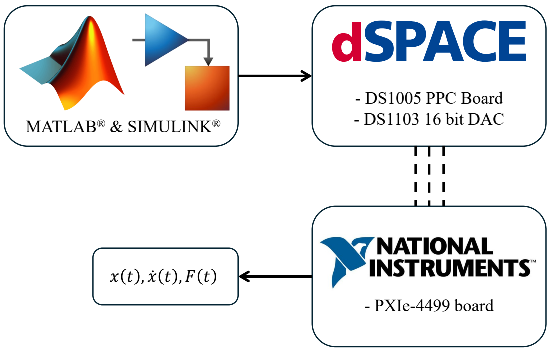

Figure 3.43. Scheme of the experimental setup for the parameter identification of the forced Duffing oscillator.

Table 3.18. Parameter identification for the 1-d.o.f. experimental forced Duffing oscillator using HHT+MSM.

	k (N/m)	k_{nl} (N/m^3)	c (Ns/m)
Real values	1.000	1.000	0.100
Identified values for $F = 0.100$ N/m, $\sigma = 0.0$ rad/s	-	1.035	0.109
Identified values for $F = 0.100$ N/m, $\sigma = 0.1$ rad/s	-	0.986	0.106

proposed in this Thesis, which had the goal of estimating parameters as damping and nonlinear stiffness, works well both for discrete and continuous systems, being possible for the latter to apply the MSM directly on the continuous (non-discretized) equations, using numerically generated or experimentally recorded signals, processed through the HHT.

3.5.10 Experimental validation on a clamped-clamped beam

To test the developed model-based identification procedure, an experimental validation is realized in laboratory making use of a nonlinear Euler-Bernoulli beam. In particular, the beam exhibits a nonlinear behavior triggered by the moderately large amplitude of transversal displacements (geometric nonlinearity). Moreover, the beam is realized as clamped-clamped and either a non-zero initial condition on the first mode is assigned by slightly hitting it at the center or a punctual harmonic force is applied always at midspan, and the experimentally acquired signals are used to identify the system parameters using the model developed in Sect. 3.5.5.

Experimental setup

The experimental setup used to generate and acquire the signal employed in the identification procedure is shown in Fig. 3.44. In the forced case, a resonant excitation with amplitude up to 10 V and frequency of 2 kHz is generated by operating a geophone in active configuration as an electrodynamic actuator, positioned close to the beam midspan ($x_V = 0.516$); its calibration constants, necessary to estimate the amplitude of the force in that configuration, were previously experimentally determined. The structural response is measured using a non-contact laser triangulation displacement sensor (optoNCDT ILD1420-500), centered at midspan ($\bar{x} = 0.5$); the sensor has a nominal measuring range of 500 mm, a repeatability of up to 20 μm, and a linearity up to $\pm 0.1\%$ of full scale. The displacement signal is acquired at a sampling frequency of 2 kHz, consistent with the sensor bandwidth. Data acquisition and storage are performed using a PXIe-4499 board.

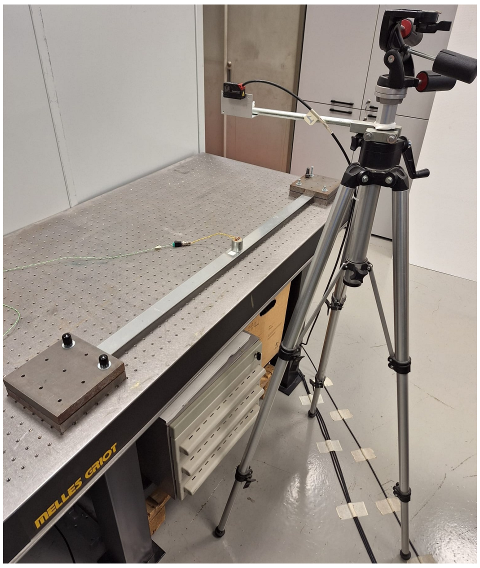

(a)

(b)

Figure 3.44. Experimental setup for the clamped-clamped beam: (a) view of the beam and of the laser (the geophone is installed at midspan); (b) front and top views of the beam.

The beam is realized using an aluminum alloy of width $b = 39.8$ mm, thickness $h = 2.82$ mm and free length $L = 0.975$ m. The mass per unit length is measured to be equal to $\rho = 0.300$ kg/m while the elastic modulus, which is required for the identification procedure, is calibrated by applying a series of small loads to the beam and fitting the measured static deflections to the corresponding analytical predictions via linear regression. An additional consistency check was performed using the calibrated modulus to compute the first natural frequency of the linear clamped–clamped beam model, which was found to be in really good agreement with the frequency estimated from FFT analysis of accelerograms recorded under white-noise excitation.

Finally, the benchmark values of ξ and α, which are then compared to the identified ones in order to validate the identification procedure (the so-called "Real values" in the tables), have to be established: the damping ξ is obtained from the modal one ξ_1 found through the logarithmic decrement on the acquired free oscillations: in fact, by applying the definition of modal damping to Eq. (3.217) as $2\xi_1\omega_1 = \dfrac{2\xi \int_0^1 \varphi_1^2 dx}{1 \int_0^1 \varphi_1^2 dx}$ with $\int_0^1 \varphi_1^2 dx = 1$, it results that $\xi = \xi_1\omega_1$. On the other hand, the real value of α is directly evaluated from Eq. (3.179) as $\alpha = \dfrac{AL^2}{2I_c}$.

Experimental results: non-zero initial condition

First, the identification procedure is carried out by applying a non-zero initial condition on the beam, in the absence of external forcing (the geophone is removed), by impacting it near the midspan. The acquired signal, converted in nondimensional form, is shown in Fig. 3.45(a), while in Fig. 3.45(b) a detailed view is shown, highlighting the presence of noise; before performing the identification procedure a moving average is realized to make the signal smoother.

The identified parameters found through the pseudo-inversion of Eq. (3.220), compared to the real values, are reported in Tab. 3.19 where two different acquisitions are considered (case 1 and case 2), realized hitting the beam at different intensities. First, it can be seen that the procedure is robust, as already highlighted in Sect. 3.5.8, since varying the time interval, the identified values slightly change in a meaningful way. Then, it can be observed that in case of free oscillations, the identified parameters are really close to the benchmark values with the maximum difference of 3.2% on ξ and 3.1% on α for the considered cases.

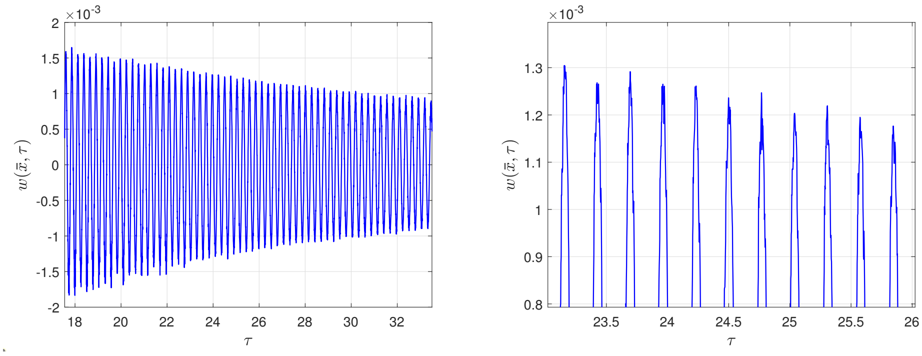

(a) **(b)**

Figure 3.45. Signal experimentally generated at x_V and acquired at $\bar{x}$: (a) free oscillations; (b) detail showing the presence of noise.

Table 3.19. Parameter identification for the experimental clamped-clamped beam with geometric nonlinearity in case of free oscillations using HHT+MSM.

	case	ξ	α
	-	-	-
Real values	-	0.0403	7.172×10^5
Identified values for $(\tau_i, \tau_f) = (21.94, 73.80)$	1	0.0403	7.088×10^5
Identified values for $(\tau_i, \tau_f) = (18.15, 97.73)$	1	0.0390	7.015×10^5
Identified values for $(\tau_i, \tau_f) = (12.96, 60.83)$	2	0.0402	7.238×10^5
Identified values for $(\tau_i, \tau_f) = (14.96, 50.96)$	2	0.0393	7.395×10^5

As a verification of the validity of the identified values, the acquired signal is compared with the response obtained by applying the MSM to Eqs. (3.217)-(3.218), using the identified parameters $\xi = 0.0403$ and $\alpha = 7.088 \times 10^5$. This comparison, which provides a further validation of the proposed procedure, shows that the time histories are in good agreement as long as envelopes and frequencies, as illustrated in Fig. 3.46. With regard to the frequency, it is worth noting its evolution from higher values toward the first natural frequency as the displacement amplitude decreases as also seen in Sect. 3.5.7.

Experimental results: resonant load

Then, the parameters are identified using as experimental signal the one generated by an external force F_V (geophone), resonant with the first natural mode, applied near midspan ($x_V = 0.516$). The signal is converted in nondimensional form and it is illustrated in Fig. 3.47(a), where the detail highlights the presence of noise; on the other hand, in Fig. 3.47(b) free oscillations are reported for the beam with the

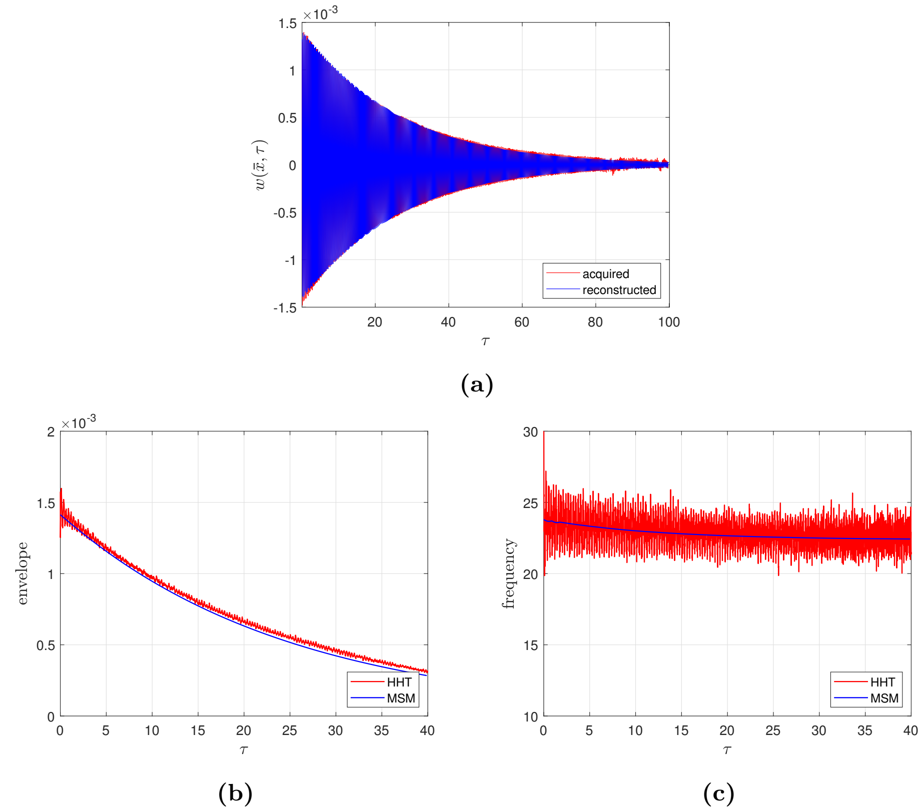

Figure 3.46. Comparison between HHT and MSM for the clamped-clamped nonlinear beam with geometric nonlinearity under non-zero initial displacement with $\xi = 0.0403$, $\alpha = 7.088 \times 10^5$ evaluated at $\bar{x} = 0.5$. (a) time histories $w(\bar{x}, \tau)$; (b) slow time depending amplitudes $Q_{w_1}(\tau)|_{\bar{x}}$ (HHT), $a_1(\tau)\varphi_1(\bar{x})$ (MSM); (c) instantaneous frequencies $\theta_{w_1}(\tau)|_{\bar{x}}$ (HHT), $\dot{\beta}_1(\tau) + \omega_1$ (MSM).

geophone installed on, to estimate the damping value used to find the benchmark value of ξ (labeled as "Real value"), since the presence of the geophone slightly varies the modal properties of the system.

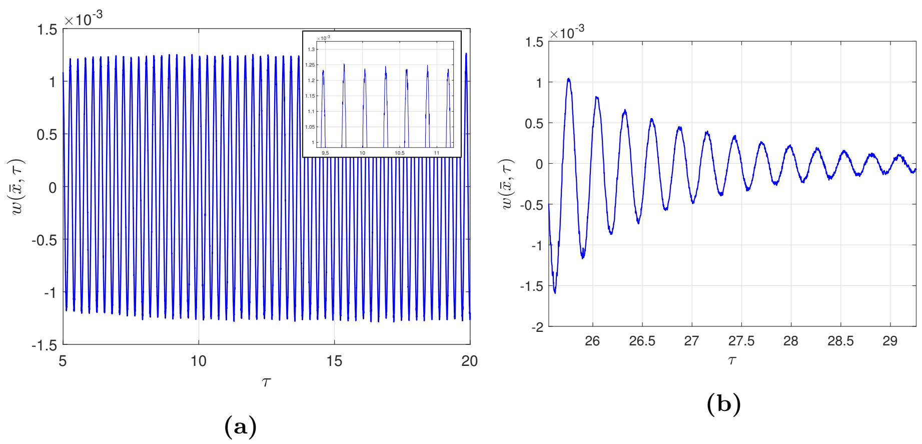

Figure 3.47. Signal experimentally generated at x_V and acquired at $\bar{x}$: (a) stationary part with detail showing the presence of noise; (b) free oscillations.

Table 3.20. Parameter identification for the experimental clamped-clamped beam with geometric nonlinearity and external punctual sinusoidal resonant force ($F_V = -0.028$, $\sigma = 0.0$) using HHT+MSM.

	mode	ξ	α
	-	-	-
Real values	1	0.738	7.172×10^5
Identified values for $(\tau_i, \tau_f) = (1.85, 31.48)$	-	0.741	7.298×10^5
Identified values for $(\tau_i, \tau_f) = (1.48, 37.04)$	-	0.768	7.109×10^5
Identified values for $(\tau_i, \tau_f) = (1.85, 22.22)$	-	0.692	7.668×10^5
Identified values for $(\tau_i, \tau_f) = (5.56, 31.48)$	-	0.753	7.064×10^5

The results of the model-based parameter identification procedure are reported in Tab. 3.20. As in the previous case the procedure is consistent, and the parameters are identified with a maximum difference of 6.2% on ξ and 6.9% on α.

Finally, a graphical interpretation of Eq. (3.213) is given in Fig. 3.48, where the time history, envelope, phase and frequency of the experimentally acquired signal, processed through the HHT, are compared to those found applying the MSM on Eqs. (3.217)-(3.218), where the identified values of $\xi = 0.768$ and $\alpha = 7.109 \times 10^5$ are used, showing a good correspondence between the experimental signal and the reconstructed solution.

3.6 Conclusions and future developments

In this Chapter, beams were studied. First, an existing model for Thin-Walled Beams (TWB) was introduced, namely the Generalized Beam Theory (GBT) here used in its GBT-D version; this theory allows to account for some specific aspects of TWB as the deformation of the cross-section in and out-of-plane and to account for non-classical load cases, without the necessity of realizing a Finite Element model which is more computationally expensive and in general non-parametric.

The GBT-D version, first developed in [109], proposes a non-classical approach to perform the cross-section analysis, which is one on the two main phases of GBT in a completely different way, through the study of the free dynamics of the externally unconstrained cross-section. This procedure for the cross-section analysis allows to find the deformation modes, which describe the section behavior. Then, the second phase, the member analysis, which allows to solve the equations, thus finding the solution along the z axis was explained, using different existing methods. It

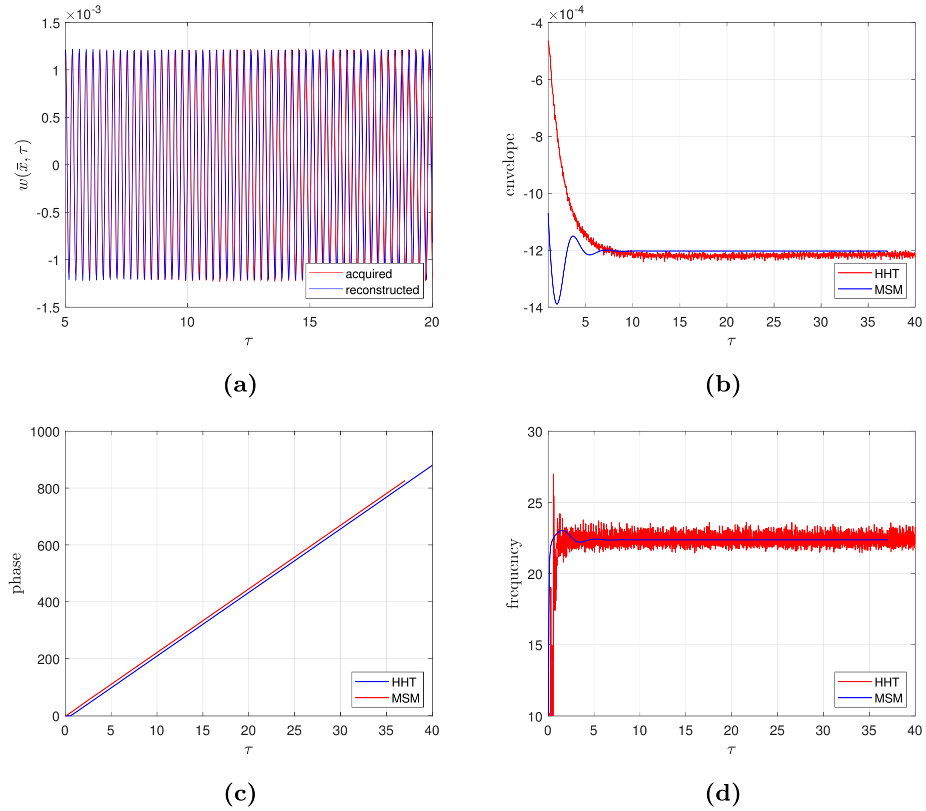

Figure 3.48. Comparison between HHT and MSM for a forced (with respect to the 1^{st} mode) clamped-clamped nonlinear beam with geometric nonlinearity with $\xi = 0.768$, $\alpha = 7.109 \times 10^5$ and $F = -0.028$ ($\sigma = 0.0$) evaluated at $\bar{x} = 0.5$. (a) time histories $w(\bar{x}, \tau)$; (b) slow time depending amplitudes $Q_{w_1}(\tau)|_{\bar{x}}$ (HHT), $a_1(\tau)\varphi_1(\bar{x})$ (MSM); (c) phases $\phi_{w_1}(\tau)|_{\bar{x}}$ (HHT), $-\gamma_1(\tau)+\omega_1\tau+\sigma\tau$ (MSM); (d) instantaneous frequencies $\theta_{w_1}(\tau)|_{\bar{x}}$ (HHT), $-\dot{\gamma}_1(\tau)+\omega_1+\sigma$ (MSM).

can be highlighted that, differently from the past, in this Thesis some concepts already developed for the GBT have been applied to the GBT-D as the study of the dynamics and the possible implementation of punctual restraints. Once the model was developed, its results were compared with those of a Finite Elements model realized through SAP2000 and it was seen that they were really close, both for statics and dynamics, with the advantage of being less computationally demanding and parametric.

Then, results coming from the GBT-D model were compared to those coming from an experimental campaign on a box-girder bridge deck. In particular, for statics the beam displacements in some points were compared, showing once again the great correspondence (differently from the Euler-Bernoulli model which is too simple to describe this kind of beam), and in dynamics accelerograms recorded in operational conditions on the beam were processed through specific algorithms in

Operational Modal Analysis (OMA) as FDD and SSI-COV finding the first natural frequencies and vibration modes of the bridge deck: once again the results of the model were in good agreement to the real ones and this proves the reliability of the GBT-D to represent full-scale bridge decks both in statics and dynamics.

After that, with the goal of controlling the vibration of the same TWB, a Nonlinear Energy Sink (NES) was applied on the beam and the problem was analytically solved. This section represents a novelty since for the first time a beam modeled through GBT-D was controlled through a NES. Equations were developed through the Complexification Averaging Method (Cx-A) and different load cases (harmonic loads, moving loads, seismic load) were tested. Various considerations about the nonlinear behavior of the system (thanks to the introduction of the NES) were made, highlighting different types of behaviors as Periodic Response, Modulated Response, Isolas.

Finally, always with the idea of proposing reduced-order models for SHM purposes, a new model-based procedure for the identification of system parameters on nonlinear continuous systems was developed. In particular, the procedure, based on the combination of the Multiple Scale Method (MSM) and of the Hilbert-Huang Transform (HHT) was first tested for discrete systems, comparing results to those found in a previous work with Cx-A in place of MSM, and then extended to the nonlinear beam. In this case a hinged-hinged Euler-Bernoulli beam was studied, with both geometric and material nonlinearities, with the idea of developing the MSM directly on the continuous system. So, once the model is developed writing the amplitude Modulation Equations (AME) in their real form, the identification procedure can be performed, taking as inputs (envelopes, phases, frequencies) those coming from the application of the HHT on numerical or experimental signals. In particular, an experimental validation was conducted on a clamped-clamped beam with time histories generated both considering non-zero initial conditions or an external resonant load, proving the validity of the method. This new procedure can be seen as an alternative to existing methods, especially for continuous systems with different kinds of nonlinearities and possible internal resonances.

Future developments regard the possibility to implement on the GBT-D model some geometrical or material nonlinearities since, experimental test highlighted a possible nonlinear behavior when heavy loads are applied on the bridge deck. Moreover, in the perspective of damage detection, it is possible to think to the extension of the identification procedure based on MSM+HHT to this model to eventually understand, based on the identified parameters, if damage is present and to localize and/or quantify it.

Always in the framework of identification, after the validation of the procedure on the experimental clamped-clamped beam, ongoing research is focusing on the possibility to account for internal resonances in order to study the problem of the curved or buckled beam (both using numerical and experimental time histories), but also to identify the beam parameters under different sources of excitation as in the case of moving loads, to extend the applicability of the method.

Finally, about the beam control realized through the NES, an optimization procedure should be developed to test the best NES parameters which in this Thesis were chosen by hand, and the implementation of other types of nonlinearity for the device (different from the cubic one) which, in the author's opinion, could lead to minor displacements on the controlled beam resulting in a better performance of the NES.

Cables

A model of nonlinear suspended cable (with quadratic and cubic nonlinearities) is introduced. The equations of motion of the cable are resumed before studying its behavior under the action of a harmonic resonant load. Then, having as future goal the control of the cable through one or more Nonlinear Energy Sinks and the monitoring of its vibrations when subjected to wind action, the interaction between the cable and the wind action is studied. In particular, Vortex-Induced Vibrations (VIV) are analyzed through a wake (van der Pol) oscillator. Analytical and numerical results are compared in view of further analyses. Finally, using the same model-based procedure introduced for beams, a first identification of the system parameters is realized for the cable subjected to non-zero initial conditions. Conclusions and future developments are resumed at the end of the chapter.

4.1 Introduction

Cable-based structures are extremely widespread in civil engineering applications, especially in bridge construction: from iconic suspension bridges (like the Golden Gate Bridge in San Francisco, USA or the Akashi Kaikyō Bridge in Kobe, Japan) to modern cable-stayed decks (like the Millau Viaduct in Millau, France or the Russky Bridge in Vladivostok, Russia). However, it would be simplistic to restrict the vision to bridges only since a massive use in made also in railway electrification (overhead contact wires and messenger wires) and in high-voltage power transmission lines.

Cables-related problems were studied by many scholars through the years and this Thesis tries to give a contribution to the existing literature. In particular, first the model of the nonlinear suspended cable is recalled and results in terms of free dynamics and when the cable is subjected to a resonant harmonic external load are given. Then, having as a future goal the vibrations control of this kind of structure when subjected to wind, the phenomenon of Vortex-Induced Vibrations (VIV) is studied. The idea is, differently from existing studies, to analytically solve the problem, through the Multiple Scale Method (MSM) and, as future development to introduce a Nonlinear Energy Sinks (NES) and use once again an analytical approach to solve the resulting problem. Finally, the identification algorithm developed for beams is tested for cables too. At the end, after recalling the main results and novelties introduced, what is meant to do in the future is explained.

4.2 Model

The model of suspended cable introduced in [78] is here recalled, also referred to as shallow cable (being the adjective shallow related to the small deviation of the cable from the chord that joins the two fixed ends in the horizontal configuration). The fundamental equations and hypotheses are here resumed.

4.2.1 Formulation

A flexible cable, whose position in the natural (and reference) configuration $\bar{\mathcal{C}}$ is $\bar{\mathbf{x}}(s)$, is considered in Fig. 4.1, being s the curvilinear abscissa going from the extreme A to the extreme B and $(\bar{\mathbf{a}}_t(s), \bar{\mathbf{a}}_n(s), \bar{\mathbf{a}}_b(s))$ the reference basis.

In the natural configuration, the (static) equilibrium of the cable subjected to static external loads on the domain $\bar{\mathbf{p}}(s)$ and on the boundaries $\bar{\mathbf{P}}_H$ with the internal

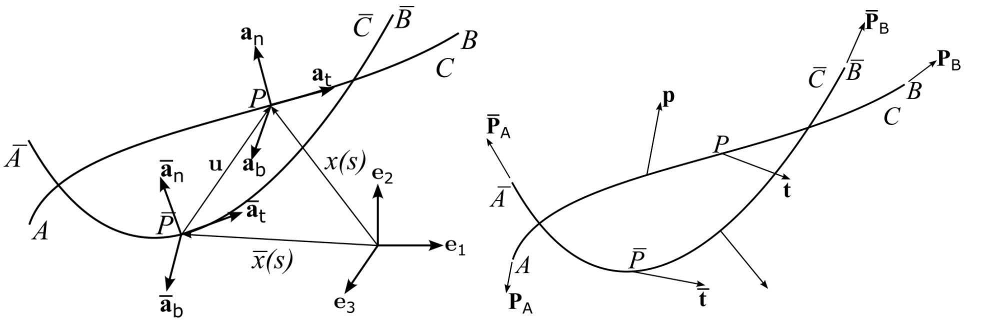

Figure 4.1. Pre-stressed cable: (a) kinematics with bases, positions and displacement; (b) dynamics with external loads and internal stress. The reference configuration is called $\bar{\mathcal{C}}$, the current one $\mathcal{C}$.

stresses $\bar{\mathbf{t}}(s)$ is written as:

$$\bar{\mathbf{t}}' + \bar{\mathbf{p}} = \mathbf{0} \tag{4.1}$$

$$\bar{\mathbf{t}}_H = \pm\bar{\mathbf{P}}_H \tag{4.2}$$

being $\bar{\mathbf{t}} = \bar{T}\bar{\mathbf{a}}_t$. In order to derive the equations of motion of the cable in terms of displacement, starting from kinematics, the position $\mathbf{x}(s,t)$ occupied by the cable at time t describes a current configuration $\mathcal{C}$ in the basis $(\mathbf{a}_t(s), \mathbf{a}_n(s), \mathbf{a}_b(s))$. Thus, the displacement vector and the geometric boundary conditions at the two ends of the cable are:

$$\mathbf{u} = \mathbf{x}(s,t) - \bar{\mathbf{x}}(s) \tag{4.3}$$

$$\mathbf{u}_H = \hat{\mathbf{u}}_H \tag{4.4}$$

The unit extension, which can be obtained as $e = \|x'\| - 1$ becomes, thanks to Eq. (4.3), the following:

$$e = \sqrt{1 + 2\mathbf{u}' \cdot \bar{\mathbf{a}}_t + \mathbf{u}' \cdot \mathbf{u}'} - 1 \tag{4.5}$$

So, expressing the cable displacement in the intrinsic reference (pre-stressed) basis as:

$$\mathbf{u} = u\bar{\mathbf{a}}_t + v\bar{\mathbf{a}}_n + w\bar{\mathbf{a}}_b \tag{4.6}$$

and making use of the Frenet formulas, $\mathbf{u}'$ can be derived and thus the unit extension can be rewritten as:

$$e = \sqrt{\left(1 + u' - \bar{k}v\right)^2 + \left(v' + \bar{k}u\right)^2 + w'^2} - 1 \tag{4.7}$$

where the torsion contribution is set equal to zero (in the hypothesis that in the reference configuration the cable is planar) and $\bar{k}$ is the Frenet curvature (in m^{-1}).

Moving on to dynamics, the balance equations between external loads on the domain $\mathbf{p}(s,t)$ (in N/m) and on the boundaries $\bar{\mathbf{P}}_H(t)$ (in N) with the internal stresses $\mathbf{t}(s,t)$ in the current configuration can be written as:

$$\mathbf{t}' + \mathbf{p} = m\ddot{\mathbf{u}} \tag{4.8}$$

$$\mathbf{t}_H = \pm \mathbf{P}_H \tag{4.9}$$

being m the mass per unit length (in kg/m) and $\mathbf{t} = T\mathbf{a}_t$. They can be expressed in terms of increments with respect to the reference configuration by subtracting Eq. (4.1) to Eq. (4.8), thus getting:

$$(\mathbf{t} - \bar{\mathbf{t}})' + \tilde{\mathbf{p}} = m\ddot{\mathbf{u}} \tag{4.10}$$

$$(\mathbf{t} - \bar{\mathbf{t}})_H = \pm \tilde{\mathbf{P}}_H \tag{4.11}$$

where $\tilde{\mathbf{p}} = \mathbf{p} - \bar{\mathbf{p}}$ and $\tilde{\mathbf{P}}_H = \mathbf{P}_H - \bar{\mathbf{P}}_H$

Finally, considering a hyperelastic material, the constitutive law reads:

$$T = \bar{T} + EAe \tag{4.12}$$

where EA is the axial stiffness and $\bar{T}$ the already introduced pre-stress in the reference configuration (both in N). So, collecting kinematics from Eq. (4.5), dynamics from Eqs. (4.10), the elastic law from Eq. (4.12) and boundary conditions from Eqs. (4.4), (4.11), the equations of motion in terms of displacement in the reference basis are:

$$(EAe)' + \left[\left(\bar{T} + EAe\right)\left(u' - \bar{k}v\right)\right] - \bar{k}\left(\bar{T} + EAe\right)\left(v' + \bar{k}u\right) + \tilde{p}_t = m\ddot{u} \tag{4.13}$$

$$(EAe)\,\bar{k} + \left[\left(\bar{T} + EAe\right)\left(v' + \bar{k}u\right)\right]' + \bar{k}\left(\bar{T} + EAe\right)\left(u' - \bar{k}v\right) + \tilde{p}_n = m\ddot{v} \tag{4.14}$$

$$\left[\left(\bar{T} + EAe\right)w'\right]' + \tilde{p}_b = m\ddot{w} \tag{4.15}$$

with geometric boundary conditions equal to Eq. (4.4) and mechanical ones rewritten as:

$$\left[EAe + \left(\bar{T} + EAe\right)\left(u' - \bar{k}v\right)\right]_H = \pm\tilde{P}_t \tag{4.16}$$

$$\left[\left(\bar{T} + EAe\right)\left(v' + \bar{k}u\right)\right]_H = \pm\tilde{P}_n \tag{4.17}$$

$$\left[\left(\bar{T} + EAe\right)w'\right]_H = \pm\tilde{P}_b \tag{4.18}$$

being e written in Eq. (4.7).

Then, some hypotheses have to be introduced to derive an approximated non-linear model for the shallow cable as the one represented in Fig. 4.2 with supports at the same height (horizontal configuration).

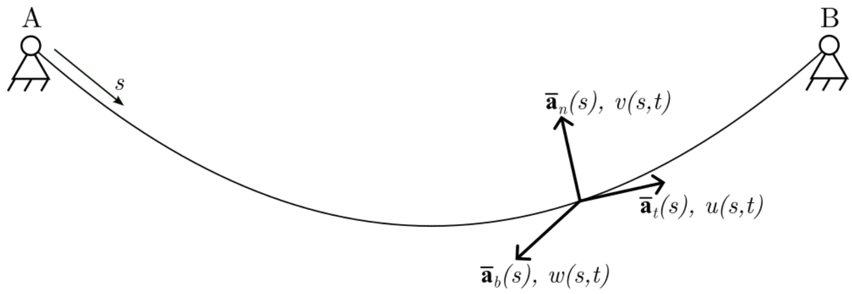

Figure 4.2. Longitudinal view of the suspended cable with supports at the same height.

The principal hypotheses (in addition to those already introduced) are that in the reference configuration the sag (ratio between the maximum vertical displacement and the length of the cable) is small, the curvature $\bar{k}$ is constant on s and small (shallow parabola), the pre-stress $\bar{T}$ is constant, the ratio $\bar{T}/EA$ is small, the displacements along the normal and binormal directions v and w are of the order of the sag, while the tangential one u is smaller and finally $\tilde{p}_t = 0$.

Starting from the tangential direction, with these hypotheses, if Eq. (4.7) is expanded in series for small displacements, neglecting squared linear terms, small terms (tangential displacement with respect to the transverse one) and higher order terms, the unit extension becomes:

$$e = u' - \bar{k}v + \frac{1}{2}\left(v'^2 + w'^2\right) \tag{4.19}$$

Then, from Eq. (4.13), the leading term among the internal forces is identified in $(EAe)'$ and, if the motion is considered to be prevalent in the transverse directions, it can be proven that $m\ddot{u} \ll (EAe)'$. Thus, the tangential inertia can be neglected and Eq. (4.13) becomes:

$$(EAe)' \approx 0 \rightarrow e(s,t) = e(t) \tag{4.20}$$

i.e. the unit extension can be approximately considered constant all along the cable. This allows to find the tangential displacement from Eq. (4.19) as:

$$u(s,t) = u(0,t) + e(t)s + \bar{k}\int_0^s v(\xi,t)d\xi - \frac{1}{2}\int_0^s \left(v(\xi,t)'^2 + w(\xi,t)'^2\right)d\xi \tag{4.21}$$

which goes under the name of static condensation, being the tangential displacement function of the transverse ones. Since in this case the cable is fixed at both ends, the unit extension can be found as:

$$e(t) = -\frac{\bar{k}}{L}\int_0^L v(s,t)ds + \frac{1}{2L}\int_0^L \left(v(s,t)'^2 + w(s,t)'^2\right)ds \tag{4.22}$$

being L the total length of the cable (in m).

Moving to the transverse directions, considering Eqs. (4.14), (4.15) with the constant pre-stress $\bar{T} + EAe$ on s according to the hypothesis on $\bar{T}$ and Eq. (4.20), and neglecting higher order terms in the normal direction, the equations of motion of the suspended cable fixed at both ends, together with Eq. (4.22) are rewritten as:

$$
\begin{aligned}
&\left(\bar{T} + EAe(t)\right) v(s,t)'' + EA\bar{k}e(t) - m\ddot{v}(s,t) = -p_v \\
&\left(\bar{T} + EAe(t)\right) w(s,t)'' - m\ddot{w}(s,t) = -p_w \\
&e(t) = -\frac{\bar{k}}{L}\int_0^L v(s,t)ds + \frac{1}{2L}\int_0^L \left(v(s,t)'^2 + w(s,t)'^2\right) ds
\end{aligned}
\tag{4.23}
$$

with:

$$
\begin{aligned}
v(0,t) = v(L,t) = 0 \\
w(0,t) = w(L,t) = 0
\end{aligned}
\tag{4.24}
$$

where the tilde on the external loads p_v and p_w is neglected. The initial pre-stress is equal to $\bar{T} = mgL^2/8d$ where d is the sag (in m) and the initial curvature is equal to $\bar{k} = -mg/\bar{T}$ constant on s.

Once the equations of motion of the cable are obtained, the hypothesis is made of neglecting the out-of-plane behavior. This hypothesis can be considered respected if the cable swinging is negligible and if, as can be seen in the following, only symmetric vibration modes are taken into account (since the frequencies of the anti-symmetric modes are the same of the out-of-plane ones) and if the frequencies of the symmetric modes under consideration are sufficiently far from those of the out-of-plane ones); however the idea is to remove this hypothesis in future works. Thus, one gets:

$$
\begin{aligned}
&\left(\bar{T} + EAe(t)\right) v(s,t)'' + EA\bar{k}e(t) - m\ddot{v}(s,t) = -p_v \\
&e(t) = -\frac{\bar{k}}{L}\int_0^L v(s,t)ds + \frac{1}{2L}\int_0^L v(s,t)'^2 ds \\
&v(0,t) = v(L,t) = 0
\end{aligned}
\tag{4.25}
$$

Introducing $h(t)$ with the meaning of dynamic tension as $h(t) = EAe(t)$ and remembering that the relation between the curvature and the pre-stress is $\bar{k} = -mg/\bar{T}$, the previous problem can be rewritten, adding linear external damping $c_e\dot{v}(s,t)$, with c_e in kg/(ms), as:

$$\begin{aligned}
&\left(\bar{T}+h(t)\right)v(s,t)''-\frac{mg}{\bar{T}}h(t)-m\ddot{v}(s,t)-c_e\dot{v}(s,t)=-p_v\\
&h(t)=\frac{mg}{\bar{T}}\frac{EA}{L}\int_0^L v(s,t)ds+\frac{EA}{2L}\int_0^L v(s,t)'^2ds\\
&v(0,t)=v(L,t)=0
\end{aligned}\tag{4.26}$$

Following [61], non-dimensional variables are introduced as follows, where $\bar{\omega}=\sqrt{\bar{T}/mL^2}$ is the reference angular frequency:

$$\tilde{s}=\frac{s}{L},\qquad \tau=\bar{\omega}t,\qquad \tilde{v}=\frac{v\bar{\omega}^2}{g},\qquad \tilde{h}=\frac{h}{\bar{T}},\qquad \tilde{c}_e=\frac{c_eL^2}{\bar{T}}\bar{\omega},\qquad \tilde{p}_v=\frac{p_v}{mg}\tag{4.27}$$

Thus, the problem can be finally rewritten as follows with $\lambda^2=\left(\frac{mgL}{\bar{T}}\right)^2\frac{EA}{\bar{T}}$:

$$\begin{aligned}
&\left(1+\tilde{h}(\tau)\right)\tilde{v}(\tilde{s},\tau)''-\tilde{h}(\tau)-\ddot{\tilde{v}}(\tilde{s},\tau)-\tilde{c}_e\dot{\tilde{v}}(\tilde{s},\tau)=\tilde{p}_v\\
&\tilde{h}(\tau)=\lambda^2\left(\int_0^1\tilde{v}(\tilde{s},\tau)d\tilde{s}+\frac{1}{2}\int_0^1\tilde{v}(\tilde{s},\tau)'^2d\tilde{s}\right)\\
&\tilde{v}(0,\tau)=\tilde{v}(1,\tau)=0
\end{aligned}\tag{4.28}$$

4.2.2 Free linear dynamics

To study the free dynamics of the equivalent linear cable, i.e. to find the in-plane vibration modes and natural frequencies, Eq. (4.28) is rewritten, neglecting tilde, as:

$$\begin{aligned}
&v(s,\tau)''-h(\tau)-\ddot{v}(s,\tau)=0\\
&h(\tau)=\lambda^2\int_0^1 v(s,\tau)ds\\
&v(0,\tau)=v(1,\tau)=0
\end{aligned}\tag{4.29}$$

Two different scenarios are possible depending on $h(\tau)$. In particular $h(\tau)=0$ implies that $\int_0^1 v(s,\tau)ds=0$, which means that the mode is anti-symmetric and so the free dynamics problem becomes:

$$\begin{aligned}
&v(s,\tau)''-\ddot{v}(s,\tau)=0\\
&v(0,\tau)=v(1,\tau)=0
\end{aligned}\tag{4.30}$$

This is the well-known problem of the taut string; so, the anti-symmetric modes are such that:

$$\omega_k=2k\pi,\quad \varphi_k(s)=\sqrt{2}\sin(2k\pi s),\quad k=1,2,\ldots\tag{4.31}$$

On the other hand, if $h(\tau)\neq 0$ the mode is symmetric and Eq. (4.29) has to be solved. If one looks for a solution as $v(s,\tau)=\varphi_k(s)e^{i\omega_k\tau}$, $h(\tau)=H_ke^{i\omega_k\tau}$, the problem becomes:

$$\begin{aligned}
&\varphi_k(s)'' + \omega_k^2 \varphi_k(s) = H_k \\
&H_k = \lambda^2 \int_0^1 \varphi_k(s) ds \\
&\varphi_k(0) = \varphi_k(1) = 0
\end{aligned} \tag{4.32}$$

Solving Eq. (4.32), one finds that the symmetric vibration mode is:

$$\varphi_k(s) = \frac{H_k}{\omega_k^2} \left[1 - \tan\left(\frac{\omega_k}{2}\right) \sin(\omega_k s) - \cos(\omega_k s) \right] \tag{4.33}$$

Integrating Eq. (4.33), after multiplying everything by λ^2, one finds the following transcendental equation which can be solved to find the frequency ω_k:

$$\tan\left(\frac{\omega_k}{2}\right) = \frac{\omega_k}{2} - \frac{\omega_k^3}{2\lambda^2} \tag{4.34}$$

Thus, the symmetric mode is completely determined after determining H_k by imposing a normalization condition, as can be for example $\int_0^1 \varphi_k(s,\tau)^2 ds = 1$.

The first three in-plane vibration modes of the cable are shown in Fig. 4.3. In particular, in Fig. 4.3(a) those found for a cable with $\lambda^2 < 4\pi^2$ are reported, while in Fig. 4.3(b) the case $\lambda^2 > 4\pi^2$ is depicted. As underlined by Irvine in [61] based on the value of λ^2 the first mode (in blue) does not present internal nodes (before crossover), or it has two internal nodes (after crossover). For completeness, the first three anti-symmetric vibration modes are reported too in Fig. 4.3(c).

4.2.3 Forced dynamics: harmonic load

Since the forced dynamics problem cannot be solved in closed form, the Multiple Scale Method (MSM) is used to find the solution: in this way, one can analytically solve the problem in an asymptotic way. The case of the cable subjected to a uniform vertical sinusoidal load is here studied.

If one considers $p_v = -F \sin \Omega_F t$ as the external sinusoidal load in Eq. (4.26), with F in N/m and Ω_F in rad/s, stating that $\tilde{F} = \frac{F}{mg}$ and that $\Omega_R = \frac{\Omega_F}{\bar{\omega}}$ in addition to non-dimensional terms introduced in Eq. (4.27), the non-dimensional problem becomes:

$$\begin{aligned}
&\left(1 + \tilde{h}(\tau)\right) \tilde{v}(\tilde{s},\tau)'' - \tilde{h}(\tau) - \ddot{\tilde{v}}(\tilde{s},\tau) - \tilde{c}_e \dot{\tilde{v}}(\tilde{s},\tau) = \tilde{F} \sin \Omega_R \tau \\
&\tilde{h}(\tau) = \lambda^2 \left(\int_0^1 \tilde{v}(\tilde{s},\tau) d\tilde{s} + \frac{1}{2} \int_0^1 \tilde{v}(\tilde{s},\tau)'^2 d\tilde{s} \right) \\
&\tilde{v}(0,\tau) = \tilde{v}(1,\tau) = 0
\end{aligned} \tag{4.35}$$

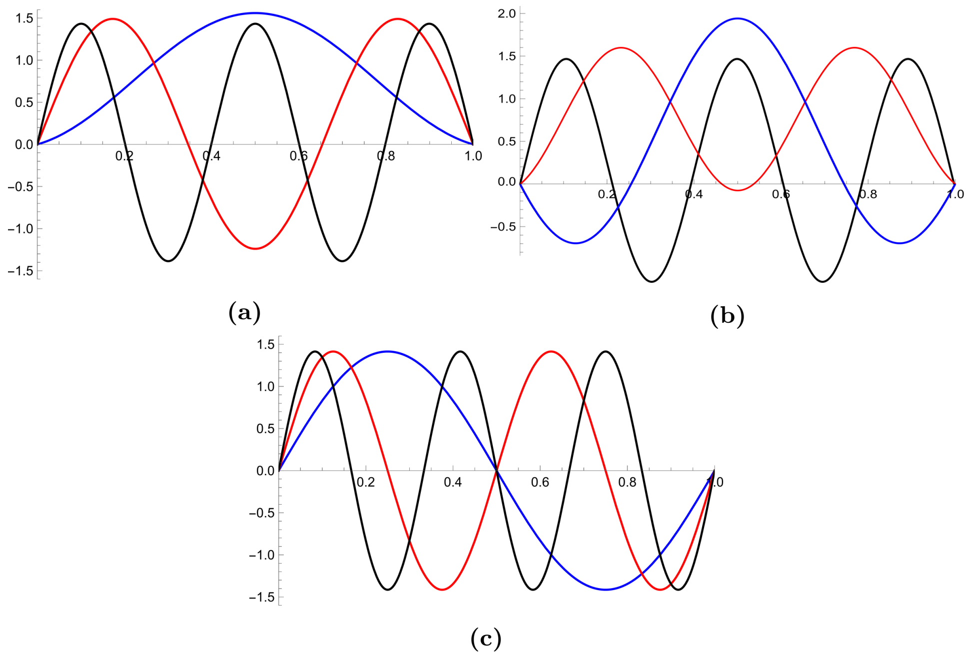

Figure 4.3. In-plane vibration modes of the cable (1^{st} = blue, 2^{nd} = red, 3^{rd} = black): (a) symmetric ones before crossover; (b) symmetric ones after crossover; (c) anti-symmetric ones.

The Multiple Scale Method is used directly on the continuous problem, with time scales $T_i = \varepsilon^i \tau$: in particular $T_0 = \tau$ and $T_2 = \varepsilon^2 \tau$ are kept, while $T_1 = \varepsilon\tau$ is not considered, since it can be demonstrated that the solution does not depend on T_1. So, derivatives are written as follows, where $D_i = d(...)/dT_i$:

$$\frac{d(...)}{d\tau} = D_0 + \varepsilon^2 D_2, \quad \frac{d^2(...)}{d\tau^2} = D_0^2 + 2\varepsilon^2 D_0 D_2 \tag{4.36}$$

and variables are rescaled as follows:

$$\tilde{v}(\tilde{s},\tau) = \varepsilon\tilde{v}_1(\tilde{s},T_0,T_2) + \varepsilon^2\tilde{v}_2(\tilde{s},T_0,T_2) + \varepsilon^3\tilde{v}_3(\tilde{s},T_0,T_2) \tag{4.37}$$

$$\tilde{h}(\tau) = \varepsilon\tilde{h}_1(T_0,T_2) + \varepsilon^2\tilde{h}_2(T_0,T_2) + \varepsilon^3\tilde{h}_3(T_0,T_2) \tag{4.38}$$

$$\tilde{c}_e = \varepsilon^2\hat{c}_e, \quad \tilde{F} = \varepsilon^3\hat{F} \tag{4.39}$$

Since a 1:1 resonance between the frequency of the external load and one of the natural frequencies of the cable is considered, the non-dimensional angular frequency of the external resonant load is related to the one of the cable through the relation $\Omega_R = \omega_k + \sigma$ where $\sigma = \varepsilon^2\tilde{\sigma}$ is a small detuning parameter to slightly modify the frequency of the force. Omitting tilde and hat, perturbation equations at different order of ε are collected as:

$$\begin{aligned}
\text{ord. } \varepsilon^1 : & \; v_1'' - h_1 - D_0^2 v_1 = 0 \\
& h_1 = \lambda^2 \int_0^1 v_1 ds \\
& v_1(0, T_0, T_2) = v_1(1, T_0, T_2) = 0
\end{aligned} \tag{4.40}$$

$$\begin{aligned}
\text{ord. } \varepsilon^2 : & \; v_2'' - h_2 - D_0^2 v_2 = -v_1'' h_1 \\
& h_2 = \lambda^2 \left(\int_0^1 v_2 ds + \frac{1}{2} \int_0^1 v_1'^2 ds \right) \\
& v_2(0, T_0, T_2) = v_2(1, T_0, T_2) = 0
\end{aligned} \tag{4.41}$$

$$\begin{aligned}
\text{ord. } \varepsilon^3 : & \; v_3'' - h_3 - D_0^2 v_3 = \tilde{c}_e D_0 v_1 \\
& - (v_2'' h_1 + v_1'' h_2) + 2 D_0 D_2 v_1 + F \sin(\omega_k T_0 + \sigma T_2) \\
& h_3 = \lambda^2 \left(\int_0^1 v_3 ds + \frac{1}{2} \int_0^1 v_1' v_2' ds \right) \\
& v_3(0, T_0, T_2) = v_3(1, T_0, T_2) = 0
\end{aligned} \tag{4.42}$$

Starting from order ε, the generating solution can be written as:

$$v_1(s, T_0, T_2) = A_k(T_2) \varphi_k(s) e^{i \omega_k T_0} + c.c. \tag{4.43}$$

$$h_1(T_0, T_2) = A_k(T_2) H_k e^{i \omega_k T_0} + c.c. \tag{4.44}$$

where $\varphi_k(s)$ and ω_k are those found in Sect. 4.2.2 for the considered vibration mode of the cable and H_k is constant on s.

The solution at order ε^2 can be found by examining the right-hand side of Eq. (4.41) knowing the solution found at the previous order ε [39]. It can be written as:

$$v_2(s, T_0, T_2) = A_k(T_2)^2 \chi_{22}(s) e^{2 i \omega_k T_0} + A_k(T_2) \bar{A}_k(T_2) \chi_{20}(s) + c.c. \tag{4.45}$$

$$h_2(T_0, T_2) = A_k(T_2) \eta_{22} e^{2 i \omega_k T_0} + A_k(T_2) \bar{A}_k(T_2) \eta_{20} + c.c. \tag{4.46}$$

where $\bar{A}_k(T_2)$ is the complex conjugate of $A_k(T_2)$ and $\chi_{22}(s)$, $\chi_{20}(s)$, η_{22} and η_{20} are called shape corrections. They can be found by substituting Eqs. (4.43), (4.44) and Eqs. (4.45), (4.46) inside Eq. (4.41) and separately collecting terms multiplying

$e^{2i\omega_k T_0}$ and e^0. Doing so, one gets for $\chi_{22}(s)$ and η_{22}:

$$\begin{aligned}
&\chi_{22}(s)'' + 4\omega_k^2 \chi_{22}(s) - \eta_{22} = H_k \varphi_k(s)'' \\
&\eta_{22} - \lambda^2 \int_0^1 \chi_{22}(s) ds = \frac{\lambda^2}{2} \int_0^1 \varphi_k(s)'^2 ds \\
&\chi_{22}(0) = \chi_{22}(1) = 0
\end{aligned} \tag{4.47}$$

while for $\chi_{20}(s)$ and η_{20} the problem is:

$$\begin{aligned}
&\chi_{20}(s)'' - \eta_{20} = -H_k \varphi_k(s)'' \\
&\eta_{20} - \lambda^2 \int_0^1 \chi_{20}(s) ds = \frac{\lambda^2}{2} \int_0^1 \varphi_k(s)'^2 ds \\
&\chi_{20}(0) = \chi_{20}(1) = 0
\end{aligned} \tag{4.48}$$

The solution of the system written in Eq. (4.47) can be obtained by solving the boundary value problem with η_{22} that remains undetermined; then, one can solve the second equation of (4.47) substituting to $\chi_{22}(s)$ the previously found expression and, in this way, η_{22} is determined; at this point it can be used to completely determine $\chi_{22}(s)$ found before. The same procedure holds for the system (4.48) with $\chi_{20}(s)$ and η_{20}.

Then, moving to order ε^3, Eqs. (4.43), (4.44) and Eqs. (4.45), (4.46) can be substituted inside Eq. (4.42). Secular terms, i.e. those multiplying $e^{i\omega_k T_0}$ which can bring the response to diverge, are collected and put equal to 0. Then, the solvability condition is imposed as the projection of the equation on the mode φ_k (the resonant one), thus getting the Amplitude Modulation Equation (AME) written in true time τ (meaning that the perturbation parameter ε is reabsorbed) as:

$$\begin{aligned}
\dot{A}_k(\tau) = &-\frac{\tilde{c}_e A_k}{2} + \frac{i A_k^2 \bar{A}_k}{2\omega_k} \Bigg[\lambda^2 \int_0^1 \varphi_k(s) ds \left(2 \int_0^1 \varphi_k'(s) \chi_{20}'(s) ds \right. \\
&\left. + \int_0^1 \varphi_k'(s) \chi_{22}'(s) ds \right) - \left(2 \int_0^1 \varphi_k(s) \chi_{20}''(s) ds + \int_0^1 \varphi_k(s) \chi_{22}''(s) ds \right) H_k \\
&- (2\eta_{20} + \eta_{22}) \int_0^1 \varphi_k(s) \varphi_k''(s) ds \Bigg] \\
&+ \frac{F e^{i\sigma\tau}}{4\omega_k} \int_0^1 \varphi_k(s) ds
\end{aligned} \tag{4.49}$$

Polar form is introduced as $A_k(\tau) = \frac{1}{2} a_k(\tau) e^{i\beta_k(\tau)}$ and the real and imaginary parts of the AME are collected thus giving two real equations. Then, the system is made autonomous by introducing the phase $\gamma_k(\tau)$ as $\gamma_k(\tau) = \sigma\tau - \beta_k(\tau)$ and the real and imaginary parts of the AME are rewritten as:

$$\dot{a_k} = F_1\left(a_k, \gamma_k\right) \tag{4.50}$$

$$\omega_k a_k \dot{\gamma_k} = F_2\left(a_k, \gamma_k\right) \tag{4.51}$$

4.2.4 Forced dynamics: results

Results are here resumed for the cable having the non-dimensional properties written in Tab. 4.1 (ξ_1 is the modal damping ratio).

Table 4.1. Geometrical and mechanical non-dimensional properties of the cable under harmonic resonant load.

λ^2	$\tilde{c}_e$	ξ_1	F	Ω_R	σ
$2.86\pi^2$	8.31×10^{-3}	$0.75‰$	1.00×10^{-3}	5.63	0.0

First, it can be commented that the value of λ^2 is such that the system is before the crossover, thus the vibration modes of the equivalent linear system are those reported in Fig. 4.3(a); in particular, the first symmetric mode, with frequency $\omega_1 = 5.63$ is taken.

In Fig. 4.4 the shape corrections $\chi_{22}(s)$ and $\chi_{20}(s)$ obtained from the resolution of Eqs. (4.47) and Eqs. (4.48) are shown. $\chi_{20}(s)$ is always real, while $\chi_{22}(s)$ could be complex if other types of damping in addition to the external one considered in this work are accounted for. Moreover, for this data set it results that $\eta_{22} = 209.77$ and $\eta_{20} = -124.68$.

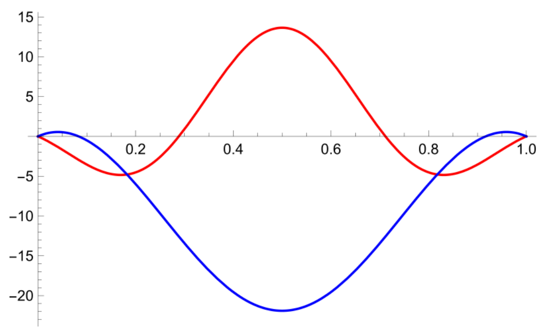

Figure 4.4. Shape corrections $\chi_{22}(s)$ (in red) and $\chi_{20}(s)$ (in blue) for the suspended cable of Tab. 4.1.

The Frequency Response Curve (FRC) of a_k is shown in Fig. 4.5. Equilibrium points can be found by solving Eqs. (4.50), (4.51) with $\dot{a}_k = 0$ and $\dot{\gamma}_k = 0$, summing and squaring them and considering that $\cos\gamma_k{}^2 + \sin\gamma_k{}^2 = 1$, thus getting an equation with a_k and σ; the equation is solved, so a_k is obtained in function of σ

and the FRC is found for different values of the frequency (or detuning parameter). Then, in order to find the stable and unstable equilibrium points (in blue and dashed green in Fig. 4.5 respectively), following the classical stability analysis, one has to evaluate the eigenvalues of the Jacobian matrix in correspondence of the investigated equilibrium point (a_{ke}, γ_{ke}), thus getting a problem as:

$$\begin{pmatrix} \delta \dot{a}_k \\ \delta \dot{\gamma}_k \end{pmatrix} = \mathbf{J}\left(a_{ke}, \gamma_{ke}\right) \begin{pmatrix} \delta a_k \\ \delta \gamma_k \end{pmatrix} \tag{4.52}$$

The eigenvalues of the Jacobian matrix $\mathbf{J}$ tell if the equilibrium point is stable (real part of all eigenvalues < 0) or unstable (at least one eigenvalue with real part > 0) [85]. The same results can be obtained by implementing Eqs. (4.50), (4.51) on a commercial software as AUTO [34].

Moreover, in the same figure the circles indicate the numerical solution. To find it, the transverse displacement of the cable is evaluated after the application of a Galerkin method involving just the resonant mode as $v(s,\tau) = \varphi_k(s)V_k(\tau)$ (other modes could be considered but due to orthogonality they would give negligible contribution), then it is substituted into Eq. (4.35), being the vibration mode $\varphi_k(s)$ known; finally, the resulting problem with assigned initial conditions is solved. The circles appearing in Fig. 4.5 are the values of $V_k(\tau)$ after the initial transient. It can

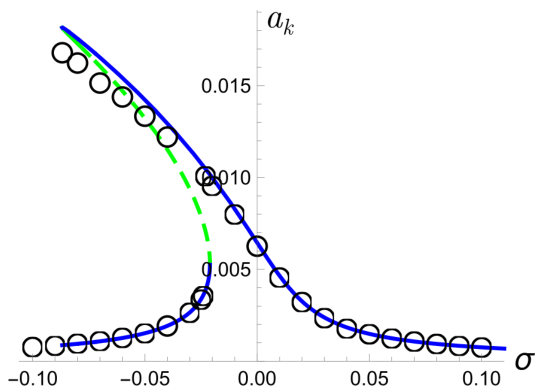

Figure 4.5. Frequency response curve for the suspended cable of Tab. 4.1 subjected to a resonant sinusoidal load (circles are obtained from the direct numerical integration of Eqs. (4.35)).

be commented that the stable and unstable zones of the FRC are the expected ones and that the numerical solution is well superimposed to the analytical one. This latter consideration in confirmed by Fig. 4.6 where the displacement time histories of the middle point $\bar{s} = 1/2$ of the cable analytically and numerically obtained are represented and they are in very good agreement.

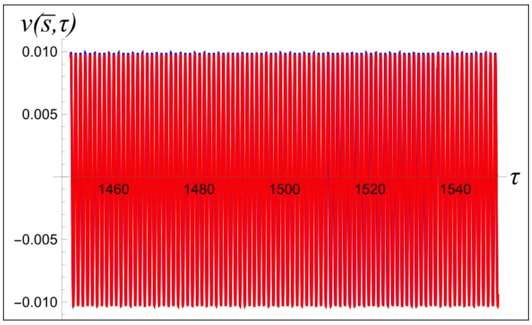

Figure 4.6. Displacement time history in terms of $v(\bar{s}, \tau)$ found analytically (blue) and numerically (red, from the direct numerical integration of Eqs. (4.35)) for the suspended cable of Tab. 4.1.

Finally, given that an infinite number of dimensional systems can be obtained from the non-dimensional parameters written in Tab. 4.1, one set of parameters corresponding to a cable having physically meaningful properties is reported in Tab. 4.2.

Table 4.2. Geometrical and mechanical dimensional properties of the cable under harmonic resonant load.

L (m)	m (kg/m)	EA (N)	c_e (kg/(ms))	$\bar{T}$ (N)	F (N/m)	σ (rad/s)
45	561	7.5×10^6	2.2	253125	5.5	0

4.3 Vortex-Induced Vibrations

This section of the Thesis is devoted to the analysis of cable behavior when subjected to Vortex-Induced Vibrations, which arise when vortices periodically shed from the surface of the cable which is hit by the wind at certain velocities, producing fluctuating aerodynamic forces. More specifically, when a fluid flows past a body, the interaction between the two depends on several factors, such as the fluid velocity (air, in this case), the angle of attack, and the geometry of the body. For a circular cross-section, as considered in this chapter, it is known that, for certain flow velocities – corresponding to a specific range of Reynolds numbers Re – vortices form and detach periodically from the body, giving rise to Vortex-Induced Vibrations. The range of frequencies over which the vortex shedding frequency (commonly related to the flow velocity through the Strouhal number) and the natural frequency of the structure (the cable, in this case) are close, defines the so-called lock-in region. This synchronization phenomenon is characterized by a strong fluid–structure interaction and a marked nonlinear behavior which can lead to non-negligible oscillations in the direction orthogonal to that of the wind (cross-flow), even if (smaller) motion happens also in the parallel one (in-line). A distinguishing trait of VIV is that they are both self-excited and self-limited.

The work here presented about VIV has a natural continuation in the control of these vibrations, making use of specific devices, as the NES already used on beams: at the end of the Section, some indications will be given on the planned next steps.

4.3.1 Wake oscillator

One common way to analytically model VIV is through the so-called wake oscillator, a nonlinear oscillator which represents a certain variable. In this case, the dimensionless wake variable q is considered to be representative of the fluctuating lift coefficient on the structure [35] as schematically shown in Fig. 4.7. So, starting

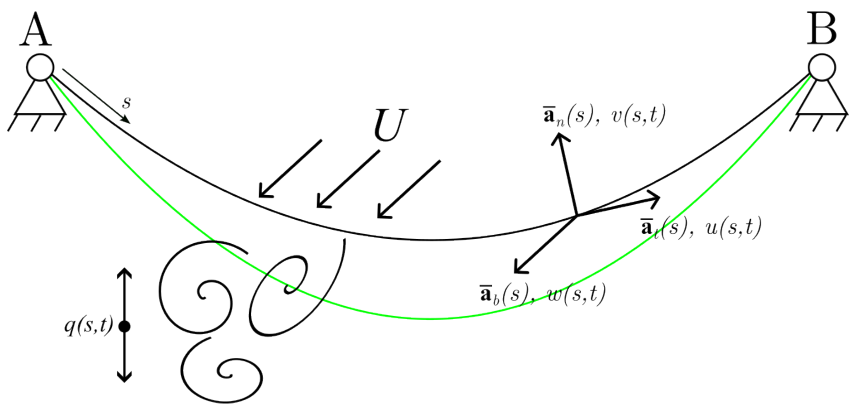

Figure 4.7. Schematic representation of the suspended cable subjected to VIV.

from Eq. (4.26), its contribution is reflected in a new equation which is that of a van der Pol oscillator:

$$
\begin{aligned}
&\left(\bar{T}+h(t)\right) v(s,t)'' - \frac{mg}{\bar{T}} h(t) - m\ddot{v}(s,t) - c_e\dot{v}(s,t) = -S(s,t) + c_F\dot{v}(s,t)\\
&h(t) = \frac{mg}{\bar{T}}\frac{EA}{L}\int_0^L v(s,t)ds + \frac{EA}{2L}\int_0^L v(s,t)'^2 ds\\
&v(0,t) = v(L,t) = 0\\
&\ddot{q}(s,t) + \alpha\Omega_F\left(q(s,t)^2-1\right)\dot{q}(s,t) + \Omega_F^2 q(s,t) = F(s,t)
\end{aligned}
\tag{4.53}
$$

where the new terms with respect to Sect. 4.2.1 are the fluid-added damping c_F in kg/(ms), the effects of the cylinder motion on the near wake $F(s,t)$ in s^{-2} and the effect of the wake oscillator on the cylinder motion $S(s,t)$ in N/m. They can be written as:

$$
\begin{aligned}
&c_F = \gamma\Omega_F\rho D^2, \quad \Omega_F = 2\pi St\frac{U}{D}, \\
&F(s,t) = \frac{A}{D}\ddot{v}(s,t), \quad S(s,t) = \frac{\rho U^2 D c_{L0} q(s,t)}{4}
\end{aligned}
\tag{4.54}
$$

where Ω_F is the vortex-shedding angular frequency in rad/s, ρ is the air fluid density in kg/m^3, D is the diameter of the cable in m, γ is the stall term (more details in [125, 130]), c_{L0} is the reference lift coefficient, U is the wind velocity in m/s, St is the Strouhal number, α is the van der Pol parameter and A is the scaling of the coupling force. Based on Eq. (4.28), the problem is rewritten in non-dimensional form as:

$$
\begin{aligned}
&\left(1+\tilde{h}(\tau)\right)\tilde{v}(\tilde{s},\tau)'' - \tilde{h}(\tau) - \ddot{\tilde{v}}(\tilde{s},\tau) - \tilde{c}_e\dot{\tilde{v}}(\tilde{s},\tau) = -s_V\Omega_R^2 q(\tilde{s},\tau) + \tilde{c}_F\Omega_R\dot{\tilde{v}}(\tilde{s},\tau) \\
&\tilde{h}(\tau) = \lambda^2\left(\int_0^1 \tilde{v}(\tilde{s},\tau)d\tilde{s} + \frac{1}{2}\int_0^1 \tilde{v}(\tilde{s},\tau)'^2 d\tilde{s}\right) \\
&\tilde{v}(0,\tau) = \tilde{v}(1,\tau) = 0 \\
&\ddot{q}(\tilde{s},\tau) + \varepsilon\tilde{\alpha}\Omega_R\left(q(\tilde{s},\tau)^2 - 1\right)\dot{q}(\tilde{s},\tau) + \Omega_R^2 q(\tilde{s},\tau) = f_V\ddot{\tilde{v}}(\tilde{s},\tau)
\end{aligned}
\tag{4.55}
$$

where, in addition to terms introduced in Eq. (4.27) and in Eq. (4.39), the new terms are written in non-dimensional form as:

$$\tilde{c}_F = \frac{\gamma\rho D^2}{m} \tag{4.56}$$

$$\frac{S}{mg} = s_V\Omega_R^2 q(\tilde{s},\tau), \quad s_V = \frac{\rho D^3 c_{L0}\bar{T}}{16\pi^2 m^2 g L^2 St^2} \tag{4.57}$$

$$f_V = \frac{A}{D}\frac{mgL^2}{\bar{T}} \tag{4.58}$$

and $\Omega_R = \Omega_F/\bar{\omega}$ is the non-dimensional vortex shedding frequency.

The MSM is used once again, assuming that $\tilde{v}(\tilde{s},\tau)$ and $\tilde{h}(\tau)$ depend on time scales T_0 and T_2, while the wake variable depends on T_1 too (since it is evident that the dependency here is no more trivial). Thus, while for $\tilde{v}$ and $\tilde{h}$, Eq. (4.36) still holds, for q derivatives are written as:

$$\frac{d(...)}{d\tau} = D_0 + \varepsilon D_1 + \varepsilon^2 D_2, \quad \frac{d^2(...)}{d\tau^2} = D_0^2 + 2\varepsilon D_0 D_1 + \varepsilon^2 D_1^2 + 2\varepsilon^2 D_0 D_2 \tag{4.59}$$

and, in addition to Eqs. (4.37), (4.39), $\tilde{q}$ and the other terms are rescaled as:

$$\tilde{q}(\tilde{s},\tau) = q_0(\tilde{s},T_0,T_1,T_2) + \varepsilon q_1(\tilde{s},T_0,T_1,T_2) + \varepsilon^2 q_2(\tilde{s},T_0,T_1,T_2) \tag{4.60}$$

$$\tilde{c}_F = \varepsilon^2\hat{c}_F, \quad \alpha = \varepsilon\tilde{\alpha}, \quad s_V = \varepsilon^3\hat{s_V}, \quad f_V = \varepsilon\hat{f_V} \tag{4.61}$$

This means that, after collecting terms at the same order of ε, the following perturbation equations are obtained, where tildes and hats are omitted:

$$\begin{aligned} \text{ord. } \varepsilon^1 : v_1'' - h_1 - D_0^2 v_1 = 0 \\ h_1 = \lambda^2 \int_0^1 v_1 ds \\ v_1(0, T_0, T_2) = v_1(1, T_0, T_2) = 0 \\ D_0^2 q_0 + \Omega_R^2 q_0 = 0 \end{aligned} \tag{4.62}$$

$$\begin{aligned} \text{ord. } \varepsilon^2 : v_2'' - h_2 - D_0^2 v_2 = -v_1'' h_1 \\ h_2 = \lambda^2 \left(\int_0^1 v_2 ds + \frac{1}{2} \int_0^1 v_1'^2 ds \right) \\ v_2(0, T_0, T_2) = v_2(1, T_0, T_2) = 0 \\ D_0^2 q_1 + \Omega_R^2 q_1 = \alpha \Omega_R D_0 q_0 - 2 D_0 D_1 q_0 - \alpha \Omega_R (D_0 q_0) q_0^2 \end{aligned} \tag{4.63}$$

$$\begin{aligned} \text{ord. } \varepsilon^3 : v_3'' - h_3 - D_0^2 v_3 = (\tilde{c}_e + \tilde{c}_F \Omega_R) D_0 v_1 - (v_2'' h_1 + v_1'' h_2) \\ + 2 D_0 D_2 v_1 - s_V \Omega_R^2 q_0 \\ h_3 = \lambda^2 \left(\int_0^1 v_3 ds + \frac{1}{2} \int_0^1 v_1' v_2' ds \right) \\ v_3(0, T_0, T_2) = v_3(1, T_0, T_2) = 0 \\ D_0^2 q_2 + \Omega_R^2 q_2 = \alpha \Omega_R D_0 q_1 - 2 D_0 D_1 q_1 + \alpha \Omega_R D_1 q_0 \\ - 2 D_0 D_2 q_0 - D_1^2 q_0 - \alpha \Omega_R (D_0 q_1) q_0^2 - \alpha \Omega_R (D_1 q_0) q_0^2 \\ - 2 \alpha \Omega_R (D_0 q_0) q_0 q_1 + f_V D_0^2 v_1 \end{aligned} \tag{4.64}$$

Developing the equations, what was written in Sect. 4.2.3 at the first two orders for v and h still holds. On the other hand, for the wake oscillator, the solution at order ε^1 is determined assuming that its dependency on s is the same of the cable:

$$q_0(s, T_0, T_1, T_2) = Q_k(T_1, T_2) \varphi_k(s) e^{i \Omega_R T_0} + c.c. \tag{4.65}$$

At the second order, Eq. (4.65) is substituted into Eq. (4.63) and secular terms arises. In particular one finds that:

$$D_1 Q_k(T_1, T_2) = -\frac{1}{2} \alpha \Omega_R Q_k (-1 + Q_k \varphi_k(s)^2 \bar{Q}_k) \tag{4.66}$$

Going to the third order, Eqs. (4.43), (4.44), Eqs. (4.45), (4.46) and (4.65) can be put inside Eq. (4.64). It should be noted that, from Eqs. (4.63) and (4.65), due to the elimination of secular terms written in Eq. (4.66), q_1 is redundant and can thus be neglected. To trigger the phenomenon of Vortex Induced Vibrations, the frequency of the vortex shedding, which is proportional to the wind velocity as written in Eq. (4.54), has to be close to one of the natural frequencies of the cable; this resonance condition can be expressed through the relation $\Omega_R = \omega_k + \sigma$ with $\sigma = \varepsilon^2\tilde{\sigma}$. So, secular terms are collected at the third order both for the cable, i.e. terms multiplying $e^{i\omega_k T_0}$, and for the wake, i.e. terms multiplying $e^{i\Omega_R T_0}$ and put equal to 0. For the wake oscillator one obtains:

$$\begin{aligned} D_2Q_k(T_1,T_2) = \frac{i}{2\Omega_R}\big(&-\alpha\Omega_R D_1Q_k + D_1^2Q_k \\ &+2\alpha\Omega_R Q_k\varphi_k(s)^2\bar{Q}_k D_1Q_k \\ &+\alpha\Omega_R Q_k^2\varphi_k(s)^2 D_1\bar{Q}_k + f_V e^{-i\sigma T_2}A_k(T_2)\omega_k^2\big) \end{aligned} \tag{4.67}$$

Then, substituting the secular term obtained from Eq. (4.66), one obtains:

$$\begin{aligned} D_2Q_k(T_1,T_2) = \frac{i}{8\Omega_R}\big(&-\alpha^2\Omega_R^2 Q_k + 4\alpha^2\Omega_R^2 Q_k^2\varphi_k(s)^2\bar{Q}_k \\ &-3\alpha^2\Omega_R^2 Q_k^3\varphi_k(s)^4\bar{Q}_k^2 + 4f_V e^{-i\sigma T_2}A_k(T_2)\omega_k^2\big) \end{aligned} \tag{4.68}$$

Finally, going back to true time τ, the reconstitution method is used in order to get the complete source of secular terms of the wake oscillator as the sum of Eq. (4.66) and Eq. (4.68) as:

$$\begin{aligned} \dot{Q}_k(\tau) = \frac{dQ_k}{d\tau} = \varepsilon D_1Q_k + \varepsilon^2 D_2Q_k = \frac{\alpha\Omega_R Q_k}{2} - \frac{\alpha\Omega_R Q_k^2\varphi_k(s)^2\bar{Q}_k}{2} \\ - \frac{i\alpha^2\Omega_R^2 Q_k}{8} + \frac{i\alpha^2\Omega_R Q_k^2\varphi_k(s)^2\bar{Q}_k}{2} \\ - \frac{3i\alpha^2\Omega_R Q_k^3\varphi_k(s)^4\bar{Q}_k^2}{8} + \frac{if_V e^{-i\sigma\tau}A_k(\tau)\omega_k^2}{2\Omega_R} \end{aligned} \tag{4.69}$$

Then, after applying the solvability conditions by projecting on the mode φ_k, the AME of the cable and of the wake in true time τ are respectively:

$$\begin{aligned} \dot{A}_k(\tau) = &-\frac{(\tilde{c}_e + \tilde{c}_F\Omega_R)A_k}{2} + \frac{iA_k^2\bar{A}_k}{2\omega_k}\Bigg[\lambda^2\int_0^1 \varphi_k(s)ds\left(2\int_0^1 \varphi_k'(s)\chi_{20}'(s)ds\right. \\ &\left.+\int_0^1 \varphi_k'(s)\chi_{22}'(s)ds\right) - \left(2\int_0^1 \varphi_k(s)\chi_{20}''(s)ds + \int_0^1 \varphi_k(s)\chi_{22}''(s)ds\right)H_k \\ &-(2\eta_{20}+\eta_{22})\int_0^1 \varphi_k(s)\varphi_k''(s)ds\Bigg] - \frac{is_V e^{i\sigma\tau}\Omega_R^2 Q_k}{2\omega_k} \end{aligned} \tag{4.70}$$

$$\begin{aligned} \dot{Q}_k(\tau) = \frac{\alpha\Omega_R Q_k}{8}\Bigg[4 - i\alpha + \frac{iQ_k\bar{Q}_k}{\int_0^1 \varphi_k(s)ds}\Bigg(4(i+\alpha)\int_0^1 \varphi_k(s)^3ds \\ -3\alpha Q_k(\tau)\bar{Q}_k(\tau)\int_0^1 \varphi_k(s)^5ds\Bigg)\Bigg] + \frac{if_V e^{-i\sigma\tau}\omega_k^2 A_k}{2\Omega_R} \end{aligned} \tag{4.71}$$

Thus, two coupled AME are obtained, one for $\dot{A}_k(\tau)$ and one for $\dot{Q}_k(\tau)$. Polar form is introduced as $A_k(\tau) = \frac{1}{2}a_k(\tau)e^{i\beta_k(\tau)}$ and $Q_k(\tau) = \frac{1}{2}z_k(\tau)e^{i\theta_k(\tau)}$ and real and imaginary parts are separated. Then, to make the system autonomous, the phase has to be written as $\gamma_k(\tau) = \sigma\tau - \beta_k(\tau) + \theta_k(\tau)$ and the following first order differential equations are obtained:

$$\dot{a_k} = F_1 \left(a_k, z_k, \gamma_k\right) \tag{4.72}$$

$$\dot{z_k} = F_2 \left(a_k, z_k, \gamma_k\right) \tag{4.73}$$

$$\dot{\beta_k} = F_3 \left(a_k, z_k, \gamma_k\right) \tag{4.74}$$

$$\dot{\theta_k} = F_4 \left(a_k, z_k, \gamma_k\right) \tag{4.75}$$

$$\dot{\gamma_k} = F_5 \left(a_k, z_k, \gamma_k\right) \tag{4.76}$$

4.3.2 VIV: results

The properties of the cable whose results are here presented are resumed in Tab. 4.3; modal damping ξ_1 also account for the fluid-added contribution.

Table 4.3. Geometrical and mechanical non-dimensional properties of the cable under VIV.

λ^2	$\tilde{c}_e$	ξ_1	Ω_R	σ
$6.28\pi^2$	2.68×10^{-2}	0.2%	7.27	0.1

About the wind parameters, following [35], fixed values are given to them, as $\gamma = 0.8$, $c_{L0} = 0.3$ in the large range of Reynolds' number, $St = 0.2$ in the sub-critical range where $300 < Re < 1.5 \times 10^5$, $A = 12$ and $\alpha = 0.3$. In this case, being λ^2 greater than $4\pi^2$, the system is after the crossover and vibration modes are those of Fig. 4.3(b); in particular, in this section the first symmetric mode, with frequency $\omega_1 = 7.27$ is considered.

The shape corrections $\chi_{22}(s)$ and $\chi_{20}(s)$ for this data set are represented in Fig. 4.8 and, in addition, $\eta_{22} = 915.49$ and $\eta_{20} = -211.75$.

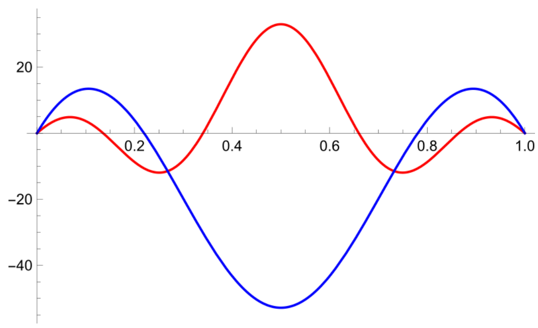

Figure 4.8. Shape corrections $\chi_{22}(s)$ (in red) and $\chi_{20}(s)$ (in blue) for the suspended cable of Tab. 4.3.

To obtain the Frequency Response Curves, one can use Eqs. (4.72), (4.73), (4.76) putting the left-hand side equal to zero. In particular, one can collect terms multiplying $\sin(\gamma_k)$ from Eqs. (4.72), (4.73) and set them equal, thus getting the first equation which is function of a_k, z_k and σ. The second one is obtained by collecting terms multiplying $\cos(\gamma_k)$ from Eq. (4.76) and using the Pythagorean trigonometric identity $\cos(\gamma_k)^2 + \sin(\gamma_k)^2 = 1$. In this way two equations are obtained in function of a_k, z_k and σ and it is possible to solve them to obtain a_k and z_k in function of the detuning parameter σ, i.e. the FRC and then eventually derive the FRC of γ_k. The stability of the equilibrium points is found as explained in Sect. 4.2.4. The FRC of a_k, z_k and of the phase γ_k are represented in Fig. 4.9 with stable (in blue) and unstable (in dashed green) branches.

First of all, it is evident that near $\sigma = 0$, which corresponds to the case when the frequency of the vortex shedding is exactly the same of the first natural mode of the cable, the amplitude of motion is higher for a certain range of frequencies, thus defining the lock-in or synchronization region, with the maximum value attained not exactly at $\sigma = 0$ (hardening behavior). Moreover, it can be seen from Fig. 4.9(c) that the jumps occur at the boundaries of the lock-in region; these results are in agreement with those obtained by Kim and Perkins in [67]. Finally, for some values of the detuning parameter σ, three equilibrium points are intercepted (two stables, one unstable): the solution will tend to one of them based on the initial conditions.

The analytical and numerical time histories of $v\left(\frac{1}{2}, \tau\right)$ and $q\left(\frac{1}{2}, \tau\right)$ are represented in Fig. 4.10 for the value of σ of Tab. 4.3. The analytical solution is obtained from the systems of Eqs. (4.72), (4.73), (4.74) and (4.75), which allows to find $a_k(\tau)$, $\beta_k(\tau)$ and thus $A_k(\tau)$ and $z_k(\tau)$, $\theta_k(\tau)$ and thus $Q_k(\tau)$, which means that both $v(s, \tau)$ and $q(s, \tau)$ are determined. The numerical solution is obtained directly from Eq. (4.55) using once again the Galerkin method retrieving only the resonant mode. In this case a value of $\sigma = 0.1$ was considered, and it can be seen that the analytical and numerical solutions represented in Fig. 4.10, obtained assigning non-zero i.c. on $v(s, 0)$, $q(s, 0)$ having the shape of the linear vibration mode (with different amplitudes) and trivial i.c. on $\dot{v}(s, 0)$ and $\dot{q}(s, 0)$, agree both in terms of v and q, confirming the validity of the analytical model. Moreover, their values (taking into account $\varphi_k(\bar{s})$) are coherent with those read in Fig. 4.9(a) and Fig. 4.9(b) in correspondence of the same value of σ.

Finally, one set of parameters corresponding to a cable having physically meaningful properties whose results correspond to those written in this section is reported in Tab. 4.4.

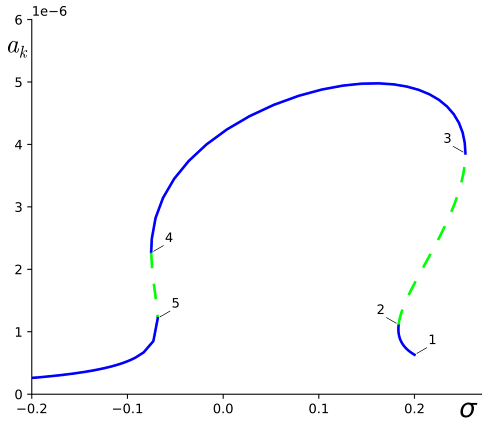

(a)

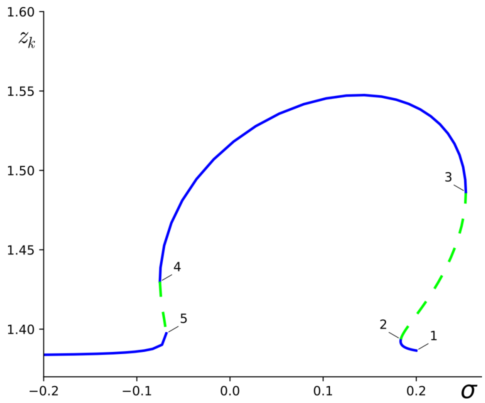

(b)

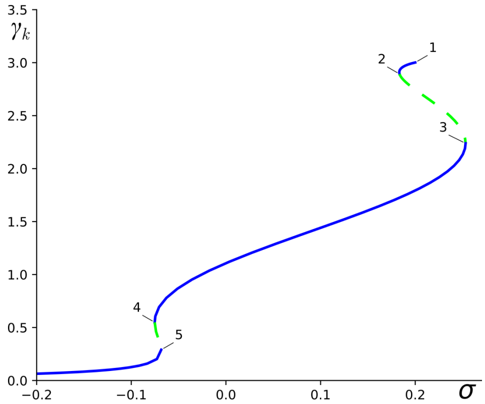

(c)

Figure 4.9. Frequency response curves for the suspended cable of Tab. 4.3 subjected to VIV: (a) FRC of the cable; (b) FRC of the wake oscillator; (c) FRC of the phase.

Table 4.4. Geometrical and mechanical dimensional properties of the cable under VIV.

L (m)	m (kg/m)	EA (N)	c_e (kg/(ms))	$\bar{T}$ (N)
267	1.8	2.97×10^7	0.02	22000

This first part, which had as main goal the development of an analytical model to study the problem of the cable subjected to VIV applying MSM directly on the continuous equations gave encouraging results, which have to be further investigated

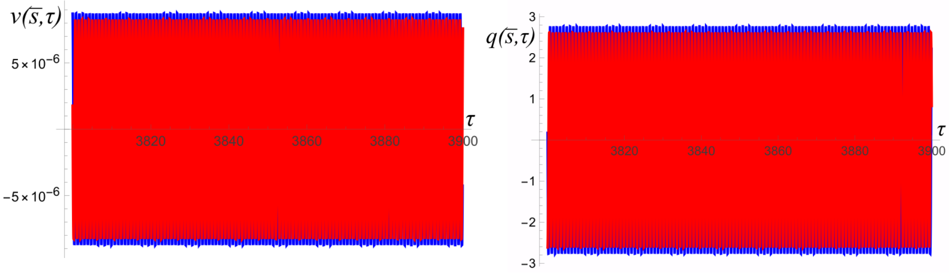

(a) **(b)**

Figure 4.10. Displacement time histories in terms of $v(\bar{s},\tau)$ (a) and of $q(\bar{s},\tau)$ (b) found analytically (blue) and numerically (red, from the direct numerical integration of Eqs. (4.55)) for the suspended cable of Tab. 4.3.

in order to obtain large displacements in correspondence of the lock-in region which thus justify the implementation of a passive vibrations control system. Just to give some details, the idea is to use one or more NES as done in Sect. 3.4 and to study the problem as in [150] with the idea of optimizing the behavior of the NES in order to get a massive vibration reduction and thus extend the service life of the cable.

4.4 Identification

The identification of system parameters of the cable is realized making use of the algorithm developed in Sect. 3.5 and here extended to cables subjected to non-zero initial conditions. This is a first application of the MSM+HHT approach to cables with the idea of making it more general and to consider also the external resonant load.

4.4.1 Non-zero initial conditions

The equations derived for the cable in Sect. 4.2.3 are here used. It is possible to restart from Eq. (4.35) with $\tilde{F}=0$. As written, in this first extension of the identification procedure to cables, for simplicity the initial condition involves just one mode and can be written in the modal basis as:

$$\begin{aligned} \tilde{v}(s,0) &= \hat{a}_k \varphi_k(s) \\ \dot{\tilde{v}}(s,0) &= \hat{b}_k \varphi_k(s) \end{aligned} \tag{4.77}$$

being $\hat{a}_k$ and $\hat{b}_k$ assigned initial displacement and velocity modal amplitudes, respectively. Scaling $\tilde{v}(\tilde{s},\tau)$ and $\tilde{h}(\tau)$ as in Eq. (4.37) and scaling the initial conditions as $\hat{a}_k=\varepsilon\tilde{\hat{a}}_k$ and $\hat{b}_k=\varepsilon\tilde{\hat{b}}_k$ and neglecting tilde everywhere, the perturbation equations, together with boundary and initial conditions, can be written as:

$$
\begin{aligned}
\text{ord. } \varepsilon^1 : \; & v_1'' - h_1 - D_0^2 v_1 = 0 \\
& h_1 = \lambda^2 \int_0^1 v_1 ds \\
& v_1(0, T_0, T_2) = v_1(1, T_0, T_2) = 0 \\
& v_1(s, 0, 0) = \hat{a}_k \varphi_k(s) \\
& D_0 v_1(s, 0, 0) = \hat{b}_k \varphi_k(s)
\end{aligned}
\tag{4.78}
$$

$$
\begin{aligned}
\text{ord. } \varepsilon^2 : \; & v_2'' - h_2 - D_0^2 v_2 = -v_1'' h_1 \\
& h_2 = \lambda^2 \left(\int_0^1 v_2 ds + \frac{1}{2} \int_0^1 v_1'^2 ds \right) \\
& v_2(0, T_0, T_2) = v_2(1, T_0, T_2) = 0 \\
& v_2(s, 0, 0) = 0 \\
& D_0 v_2(s, 0, 0) = 0
\end{aligned}
\tag{4.79}
$$

$$
\begin{aligned}
\text{ord. } \varepsilon^3 : \; & v_3'' - h_3 - D_0^2 v_3 = \tilde{c}_e D_0 v_1 - (v_2'' h_1 + v_1'' h_2) + 2 D_0 D_2 v_1 \\
& h_3 = \lambda^2 \left(\int_0^1 v_3 ds + \frac{1}{2} \int_0^1 v_1' v_2' ds \right) \\
& v_3(0, T_0, T_2) = v_3(1, T_0, T_2) = 0 \\
& v_3(s, 0, 0) = 0 \\
& D_0 v_3(s, 0, 0) = -D_2 v_1(s, 0, 0)
\end{aligned}
\tag{4.80}
$$

The solutions at order ε and ε^2 are those written in Eqs. (4.43), (4.44) and Eqs. (4.45), (4.46) respectively. Then, the only AME can be deducted as:

$$
\begin{aligned}
\dot{A}_k(\tau) = & -\frac{\tilde{c}_e A_k}{2} + \frac{i A_k^2 \bar{A}_k}{2\omega_k} \left[\lambda^2 \int_0^1 \varphi_k(s) ds \left(2 \int_0^1 \varphi_k'(s) \chi_{20}'(s) ds \right. \right. \\
& \left. + \int_0^1 \varphi_k'(s) \chi_{22}'(s) ds \right) - \left(2 \int_0^1 \varphi_k(s) \chi_{20}''(s) ds + \int_0^1 \varphi_k(s) \chi_{22}''(s) ds \right) H_k \\
& \left. - (2\eta_{20} + \eta_{22}) \int_0^1 \varphi_k(s) \varphi_k''(s) ds \right]
\end{aligned}
\tag{4.81}
$$

which, after the introduction of polar form as $A_k(\tau) = \frac{1}{2} a_k(\tau) e^{i\beta_k(\tau)}$, can be rewritten in real form as:

$$
\dot{a_k} = F_1 \left(a_k, \beta_k \right) \tag{4.82}
$$

$$
\omega_k a_k \dot{\beta}_k = F_2 \left(a_k, \beta \right) \tag{4.83}
$$

and, as already written for the beam in Sect. 3.5, the initial conditions can be expressed as:

$$a_k(0) = \sqrt{\hat{a}_k^2 + \frac{\hat{b}_k^2}{\omega_k^2}} \tag{4.84}$$

$$\beta_k(0) = -\arctan \frac{\hat{b}_k}{\omega_k \hat{a}_k} \tag{4.85}$$

Differently from the investigated discrete systems and from the beam in Sect. 3.5, in this case, the presence of the solution at order ε^2 does not allow to write the identification problem as $\mathbf{A}\boldsymbol{\eta} = \mathbf{b}$. In fact, considering as unknown parameters to identify the damping term $\tilde{c}_e$ and the parameter λ^2, which, as stated in [61], accounts for geometric and elastic effects, and collecting them inside the vector $\boldsymbol{\eta}$ as $\boldsymbol{\eta} = \left(\lambda^2\ \tilde{c}_e\right)^T$, if one explicitly writes Eqs. (4.82), (4.83), sees that the dependence on the unknown parameters is not linear, differently for example from Eq. (3.191) with respect to α, χ and ξ. This is due to the nonlinear dependence of shape corrections introduced in Eqs. (4.45), (4.45) on the parameter λ^2. So, the identification problem derived from Eqs. (4.82), (4.83) can be formally written as:

$$\mathbf{A}\left(a_k, \dot{a}_k, \beta_k, \dot{\beta}_k, \boldsymbol{\eta}\right) = \mathbf{b} \tag{4.86}$$

and Nonlinear Least Squares can be adopted to find the unknown parameters $\boldsymbol{\eta}$.

At this point, since the goal is to highlight the relationship between HHT and MSM, in order to put the outcomes of the former inside the equations of the latter to identify the system parameters, the solution of the cable given by the two contribution written in Eqs. (4.43), (4.44) and in Eqs. (4.45), (4.45) at the position $\bar{s}$, in polar form and in terms of true time (reabsorbing the bookkeeping parameter ε) can be written as:

$$\begin{aligned} v(\bar{s},\tau) = v_1(\bar{s},\tau) + v_2(\bar{s},\tau) = \frac{1}{2}a_k(\tau)\varphi_k(\bar{s})e^{i(\omega_k\tau+\beta_k(\tau))} \\ + \frac{1}{4}a_k(\tau)^2\chi_{22}(\bar{s})e^{2i(\omega_k\tau+\beta_k(\tau))} + \frac{1}{4}a_k(\tau)^2\chi_{20}(\bar{s}) + c.c. \end{aligned} \tag{4.87}$$

which becomes, using Euler's formula:

$$\begin{aligned} v(\bar{s},\tau) = a_k(\tau)\varphi_k(\bar{s})\cos\left(\omega_k\tau + \beta_k(\tau)\right) \\ + \frac{a_k(\tau)^2}{2}\chi_{22}(\bar{s})\cos\left[2\left(\omega_k\tau+\beta_k(\tau)\right)\right] + a_k^2(\tau)\chi_{20}(\bar{s}) \end{aligned} \tag{4.88}$$

As already done for the nonlinear beam and for the discrete problems, the expression given in Eq. (4.88) can be compared to the analytical signal of Eq. (3.135) retaining only terms of frequency ω_k as:

$$\begin{cases} a_k(\tau) = Q_{v_k}(\tau)|_{\bar{s}}/\varphi_k(\bar{s}) \\ \beta_k(\tau) = \phi_{v_k}(\tau)|_{\bar{s}} - \omega_k\tau \rightarrow \dot{\beta}_k(\tau) = \theta_{v_k}(\tau)|_{\bar{s}} - \omega_k \end{cases} \tag{4.89}$$

This simplification makes the comparison less rigorous (even if also for beams the solution was stopped at a certain time scale) but some initial results are collected in the Thesis leaving to future works the inclusion of the higher order terms which could improve and make the identification process more stable.

4.4.2 Results

As already done for beams, system parameters are identified for cables too starting from numerically generated signals, obtained through the Matlab function ode45 [88].

Results are reported in Tab. 4.5 together with the real values (used to generate the numerical solution). The numerical solution, whose results were fed to the HHT, was found by applying a non-zero i.c. on the vertical displacement of the cable (Eqs. (4.77)). Both damping $\tilde{c}_e$ and the parameter λ^2 are identified with a good approximation, with a maximum difference of 3.1% on $\tilde{c}_e$ and of 17.6% on λ^2 for the investigated case. This error, especially on λ^2, could be reduced taking into consideration a higher number of IMF. However, these results are undoubtedly encouraging and have to be reinforced with further analyses.

Table 4.5. Parameter identification for the cable of Eq. (4.35) with i.c. on the 1^{st} symmetric vibration mode using HHT+MSM.

	$\tilde{c}_e$	λ^2	i.c.
	-	-	-
Real values	8.310×10^{-3}	28.286	-
Identified values	8.569×10^{-3}	33.255	$\hat{a}_1 = -3.955 \times 10^{-2}$
Identified values	8.246×10^{-3}	30.951	$\hat{a}_1 = -3.955 \times 10^{-3}$

A further comparison of slow time depending amplitudes and instantaneous frequencies, evaluated through HHT and MSM for the data sets of Tab. 4.5 is reported in Fig. 4.11. A good correspondence can be found between the curves obtained with HHT and MSM despite the simplification made in Eq. (4.89) which is somehow highlighted in the figures, thus proving their “equivalence”.

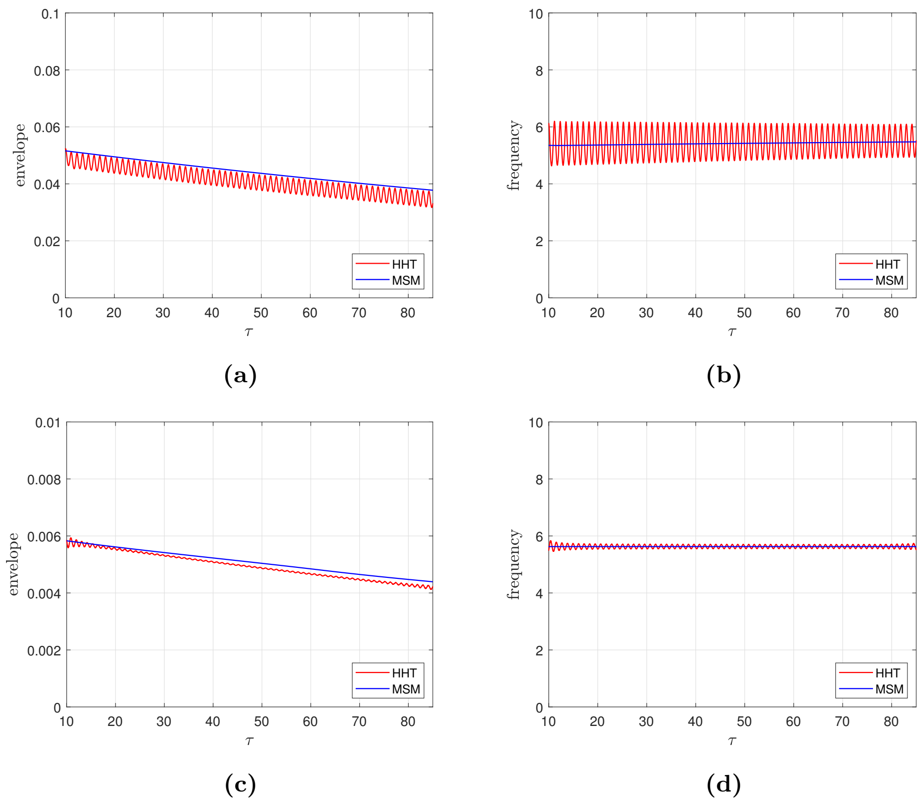

Figure 4.11. Slow time depending amplitudes and instantaneous frequencies of HHT and MSM for a cable with i.c on the 1^{st} symmetric mode with $\tilde{c}_e = 8.310\times10^{-3}$, $\lambda^2 = 28.286$, and i.c. $v(s,0) = -3.955\times10^{-2}\varphi_1(s)$, $\dot{v}(s,0) = 0$ (on the top) or $v(s,0) = -3.955\times10^{-3}\varphi_1(s)$, $\dot{v}(s,0) = 0$ (on the bottom) evaluated at midspan. (a)-(c) $Q_{v_1}(\tau)|_{\bar{s}}$ (HHT), $a_1(\tau)\varphi_1(\bar{s})$ (MSM); (b)-(d) $\theta_{v_1}(\tau)|_{\bar{s}}$ (HHT), $\dot{\beta}_1(\tau)+\omega_1$ (MSM).

4.5 Conclusions and future developments

In this chapter, cables were studied. First the analytical model of the nonlinear suspended cable was recalled. The model was obtained through classical hypotheses which lead to the equations of motion of the cable in the transverse directions both in-plane and out-of-plane while for the tangential behavior a static condensation was realized. Then, the out-of-plane behavior was neglected under certain assumptions, with the idea of reconsidering it in the future. The free and forced dynamics were studied, using for the latter the Multiple Scale Method (MSM) and numerical results confirmed the analytical ones.

After, the phenomenon of Vortex-Induced Vibrations (VIV) was introduced and the cable subjected to it was analytically studied for the first time through MSM directly applied on the continuous problem. In fact, it was proven by many works that in case of continuous nonlinear systems with quadratic and cubic nonlinearities (like cables or buckled beams) the a priori discretization of the equations of motion can lead to qualitative and quantitative errors. Once again, the comparison between analytical and numerical results confirmed the validity of the model which can thus be implemented to consider also the presence of one or more NES.

Finally, the same model-based identification procedure realized through the combination of the Multiple Scale Method (MSM) and the Hilbert-Huang Transform (HHT), first introduced for beams, was extended to the suspended cable and it was shown that the relationship between the two methods still holds, allowing to identify some particularly interesting parameters of the cable.

Future developments are expected to bring the work started in this Thesis to completion. In particular, the study of the cable subjected to VIV has to be further investigated to find a set of physical parameters for the cable which, under the wind action, manifest important displacements, thus requiring the introduction of the NES, especially focusing on long cables which can manifest more complex phenomena.

Related to the previous point there is the experimental realization of the model and the monitoring of vibrations. In particular, the idea is to realize an experimental model of the cable with multiple goals: the first one is the evaluation of some parameters introduced in Sect. 4.3 to model the wind action (A, γ, α) which can be checked and eventually updated to be more faithful to the real cable behavior; then, with the same experimental specimen, one can first of all investigate the modal properties of the cable with the same OMA algorithms considered for beams and then realize a monitoring campaign, for example exciting the cable with an harmonic force or applying non-zero initial conditions and compare results to those furnished by the model. Of course, adequate sensors should be used having low weight and high sensitivity.

Always related to the idea developed in Sect. 4.3 of controlling the cable vibrations, one could think to realize an experimental cubic Nonlinear Energy Sink (NES) using a combination of linear springs as in [89] and to verify that in case the NES is implemented on the cable the vibrations are reduced; this validation would be fundamental to extend the study on full-scale cables.

Finally, the procedure to identify the parameters of the cable has to be extended in order to account for the complete expression of the cable displacement obtained through MSM in the comparison with the one found with HHT involving also other

Intrinsic Mode Functions (IMF) to improve the identification procedure.

Three-dimensional frames

Three-dimensional frames, like those used in reinforced concrete buildings are studied. First a model is presented, based on the homogenization theory, with some little modifications to make it possible to consider frames with different mass and stiffness at different stages. Then, considering a model of a real case study, results are presented in terms of free dynamics. Subsequently, the same case study is analyzed through of Operational Modal Analysis (OMA) processing data collected from some sensors placed on it. These results are compared to those found with the model and the possibility to update the model is discussed. Then, another case study is considered and the tracking of modal properties in time is presented exploiting the permanent sensors, taking into consideration also the variation of the ambient temperature and the correlation among modes. Conclusions and future developments are resumed at the end of the chapter.

5.1 Introduction

Three-dimensional frames are extremely common in civil constructions. In fact, they represent the principal choice for residential and offices buildings, and they are usually realized in reinforced concrete or in steel, differently from small residential houses, usually realized, at least in Italy, in masonry.

This chapter of the Thesis was born to satisfy the demand of companies which on one side asked for models which were sufficiently simple, with a small number of parameters and easy to modify and interpret, able to describe this type of buildings and, on the other side, wanted to develop strategies to monitor the health status of those buildings through the use of specific sensors which acquired information continuously.

This chapter is divided as follows: first, an existing model for three-dimensional frames based on the so-called homogenization technique is introduced with some care to account for the real condition of this type of buildings, where the stiffness and mass properties usually slightly vary from a floor to another (due to different sizes of columns or to a different distribution of masses in plan). Based on it, an existing reinforced concrete building is modeled, with the aim of studying its behavior in free dynamics. After that, the natural frequencies and mode shapes of the same building are found through one of the two Operational Modal Analysis (OMA) algorithms introduced for beams in the Sect. 3.3 and compared to those coming from the model.

Subsequently, another case study is considered and, making use of the same OMA algorithms, its modal properties are obtained and tracked in time, to understand if they vary and if this variation is due to seasonal effects or to some kind of damage. At the end, main findings and future perspectives are reported.

The content of this chapter was developed during the period the candidate spent at the company Dimensione Solare s.r.l., which provided the instruments and experimental data required to carry out these investigations.

5.2 Model

This section was conceived with the idea of developing an analytical yet simple model for high buildings whose structure is made of three-dimensional frames; it turned out that the homogenization technique was one of the best ways to do that.

There are many works in literature based on this technique which follow different approaches in function of their goals. Since the objective of this section is to have a model whose results (in terms of natural frequencies and mode shapes) can be compared to those obtained for the available real buildings, with the future idea of updating the model itself to better catch the building dynamics, the methodology used in [108] is mainly followed and equations developed there are here recalled. In particular, the three-dimensional frame is considered equivalent (in terms of energy) to a Timoshenko beam with some fundamental hypotheses; thus, the Timoshenko beam is studied and, once its response is known, that of the three-dimensional frame can be derived.

5.2.1 Formulation

The two fundamental hypotheses at the base of the model of the 3D Timoshenko beam used in [108] are that the building is made of rigid floors connected by deformable columns and that both displacements and strains are assumed to be small. As a consequence of the first hypothesis, even if a three-dimensional frame is formally studied, the contribution in terms of stiffness is given only by vertical elements (columns and shear walls), while horizontal elements (like beams and floors) are accounted only in terms of mass contribution. A generic representation of the building can be seen in Fig. 5.1(a) (it has to be noted that symmetry is not required), while in Fig. 5.1(b) the equivalent beam is depicted with its displacement field. Throughout the entire chapter, the y and z axes are referred to the cross-section, while the x axis (from 0 to the total length of the beam L, which is also the height of the building) represents the longitudinal direction; the orthogonal basis $\mathbf{a}_x, \mathbf{a}_y, \mathbf{a}_z$ is associated to those directions.

Starting from the kinematics, being the Timoshenko beam embedded in space, 6 parameters are used to describe its displacement field, here written (in m and rad respectively):

$$\mathbf{u} = u(x,t)\mathbf{a}_x + v(x,t)\mathbf{a}_y + w(x,t)\mathbf{a}_z \tag{5.1}$$

$$\boldsymbol{\theta} = \theta_x(x,t)\mathbf{a}_x + \theta_y(x,t)\mathbf{a}_y + \theta_z(x,t)\mathbf{a}_z \tag{5.2}$$

It follows that the linear strain field is:

$$\begin{aligned} &\varepsilon = u'; \quad \gamma_y = v' - \theta_z; \quad \gamma_z = w' + \theta_y; \\ &\kappa_x = \theta_x'; \quad \kappa_y = \theta_y'; \quad \kappa_z = \theta_z' \end{aligned} \tag{5.3}$$

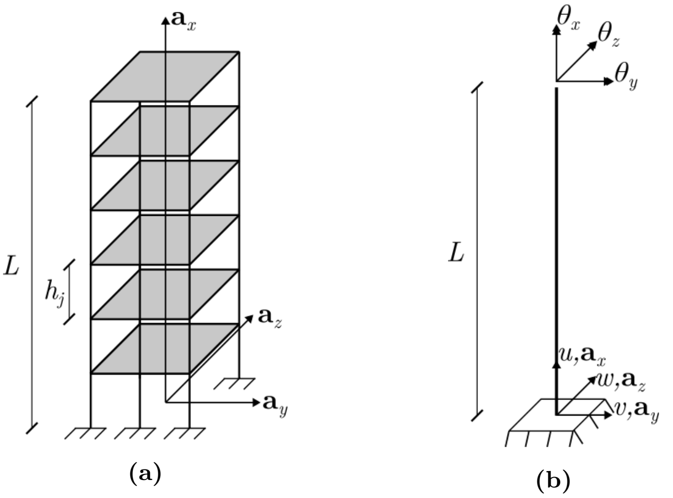

Figure 5.1. Schematic representation of the homogenization procedure: (a) Three-dimensional frame; (b) Equivalent Timoshenko beam.

where, $()'$ denotes derivative with respect to x, ε is the unit extension, γ_y, γ_z are the shear strains, κ_x is the torsional curvature and κ_y, κ_z are the bending ones. Since the beam is clamped at $x = 0$, the geometrical boundary conditions are:

$$\begin{aligned} &u(0,t) = v(0,t) = w(0,t) = 0 \\ &\theta_x(0,t) = \theta_y(0,t) = \theta_z(0,t) = 0 \end{aligned} \tag{5.4}$$

Then, considering the vector of external forces and couples (which includes the inertia terms too) as:

$$\mathbf{p} = p_x(x,t)\mathbf{a}_x + p_y(x,t)\mathbf{a}_y + p_z(x,t)\mathbf{a}_z \tag{5.5}$$

$$\mathbf{c} = c_x(x,t)\mathbf{a}_x + c_y(x,t)\mathbf{a}_y + c_z(x,t)\mathbf{a}_z \tag{5.6}$$

in N/m and Nm/m respectively, the equations of motion of the Timoshenko beam are written as:

$$\begin{aligned} &N' + p_x = 0; \\ &T_y' + p_y = 0; \quad T_z' + p_z = 0; \\ &M_x' + c_x = 0; \\ &M_y' - T_z + c_y = 0; \quad M_z' + T_y + c_z = 0 \end{aligned} \tag{5.7}$$

where N, T_y and T_z are the axial and shear stresses along the respective directions and M_x, M_y and M_z are torsional and bending moments. Being the beam free at $x = L$, the mechanical boundary conditions read:

$$\begin{aligned} &N(L,t) = T_y(L,t) = T_z(L,t) = 0 \\ &M_x(L,t) = M_y(L,t) = M_z(L,t) = 0 \end{aligned} \tag{5.8}$$

Finally, postulating the existence of an elastic potential energy density ϕ_b, the linear hyperelastic constitutive law is obtained following the procedure explained in Appendix B as:

$$\begin{pmatrix} N \\ T_y \\ T_z \\ M_x \\ M_y \\ M_z \end{pmatrix} = h \begin{bmatrix} D & 0 & 0 & 0 & Dz_E & -Dy_E \\ 0 & S_y & 0 & -S_y z_S & 0 & 0 \\ 0 & 0 & S_z & S_z y_S & 0 & 0 \\ 0 & -S_y z_S & S_z y_S & C & 0 & 0 \\ Dz_E & 0 & 0 & 0 & B_y & -B_{yz} \\ -Dy_E & 0 & 0 & 0 & -B_{yz} & B_z \end{bmatrix} \begin{pmatrix} \varepsilon \\ \gamma_y \\ \gamma_z \\ \kappa_x \\ \kappa_y \\ \kappa_z \end{pmatrix} \tag{5.9}$$

where h is the floor height and D, S_y, S_z, C, B_y, B_z and B_{yz} are in the order the extensional, shear along y, shear along z, torsional, bending around y, bending around z and cross-bending stiffness coefficients of the equivalent beam. Moreover, y_E, z_E are the coordinates of the center of extensional stiffness, while y_S, z_S those of the center of shear stiffness of the cross-section. As already highlighted in the original work ([108]), from Eq. (5.9) it is evident that the axial and bending behaviors are coupled as long as the shear and torsional ones.

Finally, in order to obtain equilibrium equations in terms of the displacement field, putting Eqs. (5.3) into Eq. (5.9) and then substituting them inside Eqs. (5.7), one gets, explicitly expressing the inertia terms, the following equations of motion:

$$\begin{aligned}
&hDu'' + hDz_E\theta_y'' - hDy_E\theta_z'' + p_x - m\ddot{u} - c_u\dot{u} = 0 \\
&hS_y\left(v'' - \theta_z'\right) - hS_y z_S\theta_x'' + p_y - m\ddot{v} - c_v\dot{v} = 0 \\
&hS_z\left(w'' + \theta_y'\right) + hS_z y_S\theta_x'' + p_z - m\ddot{w} - c_w\dot{w} = 0 \\
&hC\theta_x'' - hS_y z_S\left(v'' - \theta_z'\right) + hS_z y_S\left(w'' + \theta_y'\right) + c_x - I_x\ddot{\theta}_x - c_{\theta x}\dot{\theta}_x = 0 \\
&hB_y\theta_y'' + hDz_E u'' - hB_{yz}\theta_z'' - hS_z\left(w' + \theta_y\right) - hS_z y_S\theta_x' + c_y - I_y\ddot{\theta}_y - c_{\theta y}\dot{\theta}_y = 0 \\
&hB_z\theta_z'' - hDy_E u'' - hB_{yz}\theta_y'' + hS_y\left(v' - \theta_z\right) - hS_y z_S\theta_x' + c_z - I_z\ddot{\theta}_z - c_{\theta z}\dot{\theta}_z = 0
\end{aligned} \tag{5.10}$$

where c_u, c_v, $\ldots$ are the viscous damping coefficients and m is the mass per unit length (in kg/m) with I_x, I_y and I_z being mass inertia moments (of the floors) per unit length (in kg m^2/m), found as:

$$m = \sum_{i=1}^{N_c} m_i; \quad I_x = \sum_{i=1}^{N_c} m_i\left(y_i^2 + z_i^2\right); \quad I_y = \sum_{i=1}^{N_c} m_i z_i^2; \quad I_z = \sum_{i=1}^{N_c} m_i y_i^2 \tag{5.11}$$

Here, m_i is the mass per unit length acting on each column $i = 1, \ldots, N_c$ of coordinates (y_i, z_i). It should be noted that, in calculating the mass of each cell, the horizontal masses (beams and floors) corresponding to the upper floor of the cell were included. As for the vertical masses (columns, infill walls, partition walls and stairs), half of the mass of the elements belonging to the story above and half of those belonging to the current story were considered.

Geometrical boundary conditions, in absence of settlements, are the same written in Eq. (5.4), here rewritten:

$$\begin{aligned} &u(0,t)=0; \quad v(0,t)=0; \quad w(0,t)=0 \\ &\theta_x(0,t)=0; \quad \theta_y(0,t)=0; \quad \theta_z(0,t)=0 \end{aligned} \tag{5.12}$$

and mechanical boundary conditions of Eq. (5.8) are rewritten in terms of displacements as:

$$\begin{aligned} &hDu'(L,t)+hDz_E\theta_y'(L,t)-hDy_E\theta_z'(L,t)=0 \\ &hS_y\left(v'(L,t)-\theta_z(L,t)\right)-hS_yz_S\theta_x'(L,t)=0 \\ &hS_z\left(w'(L,t)+\theta_y(L,t)\right)+hS_zy_S\theta_x'(L,t)=0 \\ &hC\theta_x'(L,t)-hS_yz_S\left(v'(L,t)-\theta_z(L,t)\right)+hS_zy_S\left(w'(L,t)+\theta_y(L,t)\right)=0 \\ &hB_y\theta_y'(L,t)+hDz_Eu'(L,t)-hB_{yz}\theta_z'(L,t)=0 \\ &hB_z\theta_z'(L,t)-hDy_Eu'(L,t)-hB_{yz}\theta_y'(L,t)=0 \end{aligned} \tag{5.13}$$

If the columns position is symmetric with respect to the inertial principal axes $(\mathbf{a}_y, \mathbf{a}_z)$, the extensional centroid E, the shear centroid S and the center of mass G are coincident and the equations are considerably simplified. As can be seen from the previous equations, this Timoshenko beam model is extremely rich and can account for limit behaviors which are described by "poorer" models as the Euler-Bernoulli beam (with the floors that rigidly rotate out-of-plane) or the shear beam (with the floors that translate and rotate in-plane). It is shown in [108] that for a building with columns only (no shear walls), a pure bending (Euler-Bernoulli) response is highlighted for slender buildings with squat columns, while on the contrary a pure shear response can happen for squat buildings with slender columns; however, the great majority of buildings manifest a mixed response which thus require to account the complete model here used.

Once the displacements of the equivalent Timoshenko beam at each stage are found, solving the previous problem as explained in Sects. 5.2.2, 5.2.3, the displacements, strains and internal stresses fields on each column can be reconstructed. In particular, recalling the hypothesis of rigid floors, one can obtain the displacements at the head (H) and at the foot (F) of the column i of coordinates (y_i, z_i) of cell j

delimited by floors $j-1$ and j from Eq. (B.9) as:

$$\begin{cases} u_{F_{i,j}} = u(h_{j-1}) - \theta_z(h_{j-1})y_i + \theta_y(h_{j-1})z_i \\ v_{F_{i,j}} = v(h_{j-1}) - \theta_x(h_{j-1})z_i \\ w_{F_{i,j}} = w(h_{j-1}) + \theta_x(h_{j-1})y_i \\ \theta_{xF_{i,j}} = \theta_x(h_{j-1}) \\ \theta_{yF_{i,j}} = \theta_y(h_{j-1}) \\ \theta_{zF_{i,j}} = \theta_z(h_{j-1}) \end{cases} ; \quad \begin{cases} u_{H_{i,j}} = u(h_j) - \theta_z(h_j)y_i + \theta_y(h_j)z_i \\ v_{H_{i,j}} = v(h_j) - \theta_x(h_j)z_i \\ w_{H_{i,j}} = w(h_j) + \theta_x(h_j)y_i \\ \theta_{xH_{i,j}} = \theta_x(h_j) \\ \theta_{yH_{i,j}} = \theta_y(h_j) \\ \theta_{zH_{i,j}} = \theta_z(h_j) \end{cases} \tag{5.14}$$

where h_{j-1} and h_j are the height of the floors j and $j-1$ which correspond to specific longitudinal abscissas of the equivalent Timoshenko beam. Then, the displacement field along the column can be reconstructed. In fact, if each column is modeled as a Timoshenko beam too, the displacement field can be found as:

$$\begin{aligned} u_{i,j}(x) &= u_{F_{i,j}} + \frac{x}{h_j}\left(u_{H_{i,j}} - u_{F_{i,j}}\right) \\ v_{i,j}(x) &= v_{F_{i,j}} + \frac{1}{1+\alpha_{iz,j}}\left[\left(-2\frac{x^3}{{h_j}^3} + 3\frac{x^2}{{h_j}^2} + \frac{x}{h_j}\alpha_{iz,j}\right)\left(v_{H_{i,j}} - v_{F_{i,j}}\right)\right. \\ &\quad \left. + \frac{x}{2}\left(\frac{x}{h_j} - 1\right)\left(2\frac{x}{h_j} + \alpha_{iz,j}\right)\left(\theta_{zH_{i,j}} - \theta_{zF_{i,j}}\right)\right] \\ w_{i,j}(x) &= w_{F_{i,j}} + \frac{1}{1+\alpha_{iy,j}}\left[\left(-2\frac{x^3}{{h_j}^3} + 3\frac{x^2}{{h_j}^2} + \frac{x}{h_j}\alpha_{iy,j}\right)\left(w_{H_{i,j}} - w_{F_{i,j}}\right)\right. \\ &\quad \left. + \frac{x}{2}\left(\frac{x}{h_j} - 1\right)\left(2\frac{x}{h_j} + \alpha_{iy,j}\right)\left(\theta_{yH_{i,j}} - \theta_{yF_{i,j}}\right)\right] \\ \theta_{xi,j}(x) &= \theta_{xF_{i,j}} + \frac{x}{h_j}\left(\theta_{xH_{i,j}} - \theta_{xF_{i,j}}\right) \\ \theta_{yi,j}(x) &= \theta_{yF_{i,j}} + \frac{1}{1+\alpha_{iy,j}}\left[6\left(\frac{x}{h_j} - 1\right)\frac{x}{h_j}\frac{\left(w_{H_{i,j}} - w_{F_{i,j}}\right)}{h_j}\right. \\ &\quad \left. + \frac{x}{h_j}\left(3\frac{x}{h_j} - 2 + \alpha_{iy,j}\right)\left(\theta_{yH_{i,j}} - \theta_{yF_{i,j}}\right)\right] \\ \theta_{zi,j}(x) &= \theta_{zF_{i,j}} + \frac{1}{1+\alpha_{iz,j}}\left[6\left(-\frac{x}{h_j} - 1\right)\frac{x}{h_j}\frac{\left(v_{H_{i,j}} - v_{F_{i,j}}\right)}{h_j}\right. \\ &\quad \left. + \frac{x}{h_j}\left(3\frac{x}{h_j} - 2 + \alpha_{iz,j}\right)\left(\theta_{zH_{i,j}} - \theta_{zF_{i,j}}\right)\right] \end{aligned} \tag{5.15}$$

and, through Eq. (5.3) before and Eq. (5.9) after (which hold for the columns as for the equivalent beam since they were considered as Timoshenko beams too) it is possible to obtain the strain and stress field in each of them.

5.2.2 Solution strategy: equal cells

The solution of the equations derived in Sect. 5.2.1 in the general case of non-symmetric structure can be analytically found but the resulting expressions are rather complex. As a consequence, a numerical solution can be obtained, for example through Finite Differences (FD) as done in [40]. In particular, in this section the approach is recalled, while in the following an addition is made that permits to consider different properties for each cell/floor of the three-dimensional frame as in real buildings.

First of all, Eqs. (5.10), (5.12) and (5.13) can be recast in matrix form and written as a system:

$$\begin{cases} -\mathbf{M}\ddot{\mathbf{u}} - \mathbf{C}\dot{\mathbf{u}} + \mathbf{K}_2\mathbf{u}'' + \mathbf{K}_1\mathbf{u}' + \mathbf{K}_0\mathbf{u} + \mathbf{p} = \mathbf{0} \\ \mathbf{u}_A = \mathbf{0} \\ \mathbf{K}_{1B}\mathbf{u}'_B + \mathbf{K}_{0B}\mathbf{u}_B = \mathbf{0} \end{cases} \tag{5.16}$$

where the vectors $\mathbf{u}$ and $\mathbf{p}$ comprehend here the entire displacement fields, Eqs. (5.1), (5.2) as $\mathbf{u} = (u, v, w, \theta_x, \theta_y, \theta_z)^T$, and all the external distributed loads, Eqs. (5.5), (5.6) as $\mathbf{p} = (p_x, p_y, p_z, c_x, c_y, c_z)^T$; the subscript A represents the clamped section at $x = 0$ while B is the free section at $x = L$. Then, the mass, stiffness and damping matrices are:

$$\mathbf{M} = \begin{bmatrix} m & 0 & 0 & 0 & 0 & 0 \\ 0 & m & 0 & 0 & 0 & 0 \\ 0 & 0 & m & 0 & 0 & 0 \\ 0 & 0 & 0 & I_x & 0 & 0 \\ 0 & 0 & 0 & 0 & I_y & 0 \\ 0 & 0 & 0 & 0 & 0 & I_z \end{bmatrix} \tag{5.17}$$

$$\mathbf{K}_0 = \begin{bmatrix} 0 & 0 & 0 & 0 & 0 & 0 \\ 0 & 0 & 0 & 0 & 0 & 0 \\ 0 & 0 & 0 & 0 & 0 & 0 \\ 0 & 0 & 0 & 0 & 0 & 0 \\ 0 & 0 & 0 & 0 & -hS_z & 0 \\ 0 & 0 & 0 & 0 & 0 & -hS_y \end{bmatrix} \tag{5.18}$$

$$\mathbf{K}_1 = \begin{bmatrix} 0 & 0 & 0 & 0 & 0 & 0 \\ 0 & 0 & 0 & 0 & 0 & -hS_y \\ 0 & 0 & 0 & 0 & hS_z & 0 \\ 0 & 0 & 0 & 0 & hS_z y_S & hS_y z_S \\ 0 & 0 & -hS_z & -hS_z y_S & 0 & 0 \\ 0 & hS_y & 0 & -hS_y z_S & 0 & 0 \end{bmatrix} \tag{5.19}$$

$$\mathbf{K}_2 = \mathbf{K}_{1B} = \begin{bmatrix} hD & 0 & 0 & 0 & hDz_E & -hDy_E \\ 0 & hS_y & 0 & -hS_y z_S & 0 & 0 \\ 0 & 0 & hS_z & hS_z y_S & 0 & 0 \\ 0 & -hS_y z_S & hS_z y_S & hC & 0 & 0 \\ hDz_E & 0 & 0 & 0 & hB_y & -hB_{yz} \\ -hDy_E & 0 & 0 & 0 & -hB_{yz} & hB_z \end{bmatrix} \tag{5.20}$$

$$\mathbf{K}_{0B} = \begin{bmatrix} 0 & 0 & 0 & 0 & 0 & 0 \\ 0 & 0 & 0 & 0 & 0 & -hS_y \\ 0 & 0 & 0 & 0 & hS_z & 0 \\ 0 & 0 & 0 & 0 & hS_z y_S & hS_y z_S \\ 0 & 0 & 0 & 0 & 0 & 0 \\ 0 & 0 & 0 & 0 & 0 & 0 \end{bmatrix} \tag{5.21}$$

$$\mathbf{C} = \begin{bmatrix} c_u & 0 & 0 & 0 & 0 & 0 \\ 0 & c_v & 0 & 0 & 0 & 0 \\ 0 & 0 & c_w & 0 & 0 & 0 \\ 0 & 0 & 0 & c_{\theta x} & 0 & 0 \\ 0 & 0 & 0 & 0 & c_{\theta y} & 0 \\ 0 & 0 & 0 & 0 & 0 & c_{\theta z} \end{bmatrix} \tag{5.22}$$

Since the goal of the entire section is to study the free dynamics, the terms related to the external loads and to damping in Eq. (5.16) are set equal to 0 and the problem becomes:

$$\begin{cases} -\mathbf{M}\ddot{\mathbf{u}} + \mathbf{K}_2\mathbf{u}'' + \mathbf{K}_1\mathbf{u}' + \mathbf{K}_0\mathbf{u} = \mathbf{0} \\ \mathbf{u}_A = \mathbf{0} \\ \mathbf{K}_{1B}\mathbf{u}'_B + \mathbf{K}_{0B}\mathbf{u}_B = \mathbf{0} \end{cases} \tag{5.23}$$

In order to solve Eq. (5.23), one can consider $\mathbf{u}(x,t) = \hat{\mathbf{u}}(x)e^{\lambda t}$, thus the problem is rewritten as:

$$\begin{cases} -\lambda^2\mathbf{M}\hat{\mathbf{u}} + \mathbf{K}_2\hat{\mathbf{u}}'' + \mathbf{K}_1\hat{\mathbf{u}}' + \mathbf{K}_0\hat{\mathbf{u}} = \mathbf{0} \\ \hat{\mathbf{u}}_A = \mathbf{0} \\ \mathbf{K}_{1B}\hat{\mathbf{u}}'_B + \mathbf{K}_{0B}\hat{\mathbf{u}}_B = \mathbf{0} \end{cases} \tag{5.24}$$

This problem can be solved making use of Finite Differences (FD). In particular, the Timoshenko beam is divided in n_i elements of dimensions $\Delta = L/n_i$, which implies that $n_i + 1$ real nodes exist. Since central differences are used, the displacement in correspondence of each node and its derivatives are written as:

$$\hat{\mathbf{u}}_i = \hat{\mathbf{u}}(x_i); \quad \hat{\mathbf{u}}'_i = \frac{\hat{\mathbf{u}}_{i+1} - \hat{\mathbf{u}}_{i-1}}{2\Delta}; \quad \hat{\mathbf{u}}''_i = \frac{\hat{\mathbf{u}}_{i+1} - 2\hat{\mathbf{u}}_i + \hat{\mathbf{u}}_{i-1}}{\Delta^2} \tag{5.25}$$

This new writing, together with Eq. (5.24) implies that when considering the node $n_i + 1$, where both the equation of motion and the mechanical boundary condition have to be imposed, a new virtual node $n_i + 2$ has to be introduced, as shown in Fig. 5.2.

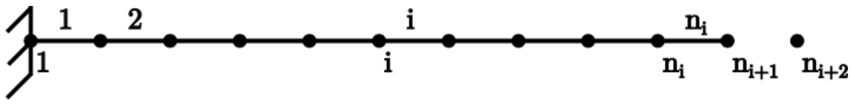

Figure 5.2. Equivalent Timoshenko beam studied through FD divided in n_i elements, with $n_i + 1$ physical nodes (the node $n_i + 2$ is a virtual one).

So, the problem in Eq. (5.24) introducing FD of Eq. (5.25), rewritten in the correct order, becomes:

$$\begin{cases} \hat{\mathbf{u}}_1 = \mathbf{0} \qquad i = 1 \\ -\lambda^2\mathbf{M}\hat{\mathbf{u}}_i + \left(\dfrac{\mathbf{K}_2}{\Delta^2} - \dfrac{\mathbf{K}_1}{2\Delta}\right)\hat{\mathbf{u}}_{i-1} + \left(\mathbf{K}_0 - \dfrac{2\mathbf{K}_1}{\Delta^2}\right)\hat{\mathbf{u}}_i \\ + \left(\dfrac{\mathbf{K}_2}{\Delta^2} + \dfrac{\mathbf{K}_1}{2\Delta}\right)\hat{\mathbf{u}}_{i+1} = \mathbf{0} \qquad i = 2, \ldots, n_i + 1 \\ -\dfrac{\mathbf{K}_{1B}}{2\Delta}\hat{\mathbf{u}}_{n_i} + \mathbf{K}_{0B}\hat{\mathbf{u}}_{n_i+1} + \dfrac{\mathbf{K}_{1B}}{2\Delta}\hat{\mathbf{u}}_{n_i+2} = \mathbf{0} \qquad i = n_i + 1 \end{cases} \tag{5.26}$$

This equation can be rewritten in the usual form as:

$$\left(\mathbf{K}_T - \lambda^2\mathbf{M}_T\right)\hat{\mathbf{u}}_T = \mathbf{0} \tag{5.27}$$

where the subscript T stands for Timoshenko beam and $\hat{\mathbf{u}}_T = (\hat{\mathbf{u}}_1, \ldots, \hat{\mathbf{u}}_{n_i+2})^T$ is the vibration mode of length $6(n_i + 2)$ for each mode and the mass and stiffness matrices have dimensions $6(n_i + 2) \times 6(n_i + 2)$. The resolution of Eq. (5.27) gives the sought eigenvalues and eigenvectors, i.e. vibration modes in correspondence of the discretized nodes of the beam Then, applying the procedure explained at the end of Sect. 5.2.1 (Eq. (5.14), (5.15)), one can reconstruct the properties along each column.

5.2.3 Solution strategy: different cells

In case one wants to consider different properties at each stage (thus for each cell), which can be representative of different cross-section or length of columns, different number or position of them and different mass distribution, it is possible to slightly modify the formulation reported in Sect. 5.2.2 as here explained.

If one consider different properties at each floor j (Fig. 5.3), the equations of the Timoshenko beam deduced in Sect. 5.2.1 can be extended to a piece-wise constant beam by considering different properties (h_j, D_j, m_j, ...) and different displacement fields (u_j, v_j, ...) at each floor.

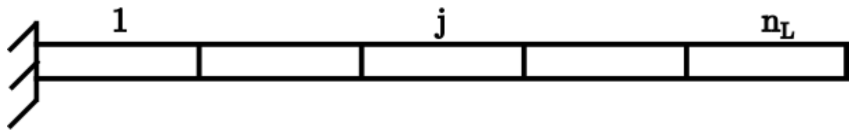

Figure 5.3. Piecewise Timoshenko beam divided in n_L elements, each with constant properties.

This means that, considering that the Timoshenko beam is made of n_L pieces with different (but constant) properties (corresponding to the stages), using the matrix form as done in Eq. (5.16), one can rewrite Eqs. (5.10), (5.12) and (5.13) as:

$$\begin{cases} -\mathbf{M}_1\ddot{\mathbf{u}}_1 - \mathbf{C}_1\dot{\mathbf{u}}_1 + \mathbf{K}_{2,1}\mathbf{u}_1'' + \mathbf{K}_{1,1}\mathbf{u}_1' + \mathbf{K}_{0,1}\mathbf{u}_1 + \mathbf{p}_1 = \mathbf{0} \\ \mathbf{u}_{A,1} = \mathbf{0} \end{cases} \tag{5.28}$$

$$\begin{cases} \mathbf{u}_{B,1} = \mathbf{u}_{A,2} \\ \mathbf{K}_{1B,1}\mathbf{u}_{B,1}' + \mathbf{K}_{0B,1}\mathbf{u}_{B,1} = \mathbf{K}_{1A,2}\mathbf{u}_{A,2}' + \mathbf{K}_{0A,2}\mathbf{u}_{A,2} \end{cases} \tag{5.29}$$

$$\begin{cases} -\mathbf{M}_2\ddot{\mathbf{u}}_2 - \mathbf{C}_2\dot{\mathbf{u}}_2 + \mathbf{K}_{2,2}\mathbf{u}_2'' + \mathbf{K}_{1,2}\mathbf{u}_2' + \mathbf{K}_{0,2}\mathbf{u}_2 + \mathbf{p}_2 = \mathbf{0} \end{cases} \tag{5.30}$$

$$\begin{cases} \mathbf{u}_{B,2} = \mathbf{u}_{A,3} \\ \mathbf{K}_{1B,2}\mathbf{u}_{B,2}' + \mathbf{K}_{0B,2}\mathbf{u}_{B,2} = \mathbf{K}_{1A,3}\mathbf{u}_{A,3}' + \mathbf{K}_{0A,3}\mathbf{u}_{A,3} \end{cases} \tag{5.31}$$

$$\begin{cases} \dots \end{cases} \tag{5.32}$$

$$\begin{cases} \mathbf{K}_{1B,n_L}\mathbf{u}_{B,n_L}' + \mathbf{K}_{0B,n_L}\mathbf{u}_{B,n_L} = \mathbf{0} \end{cases} \tag{5.33}$$

where $\mathbf{K}_{0A,j} = \mathbf{K}_{0B,j}$, $\mathbf{K}_{1A,j} = \mathbf{K}_{1B,j}$ and, as already written, the subscript j

indicates the piece of beam (floor) $j = 1, \dots, n_L$. Eq. (5.28) contains the field equation of the first element of beam, together with the clamped boundary condition at the basis, Eq. (5.29) introduces the continuity condition between the first and the second piece of beam in terms of displacements and of internal stresses respectively, and so on for the other beam pieces until Eq. (5.33) which represents the free-end boundary condition at the end of the last element of the beam (on the tip of the beam).

So, as for the constant Timoshenko beam, it is considered that $\mathbf{u}_j(x,t) = \hat{\mathbf{u}}_j(x)e^{\lambda t}$ and FD are used once again with $\hat{\mathbf{u}}_{j,i}$ being the displacement in correspondence of node i of element j (the node is referred to as i^j), considering that each constant piece of beam j is divided into a certain number of (not necessarily equal) elements n_i^j with length $\Delta_j = h_j/n_i^j$. Thus, n_{i+1}^j real nodes exist plus the virtual node n_{i+2}^j for all beam elements and the virtual node 0^j for all beam elements j but the first one. A graphical explanation is given in Fig. 5.4, where the nodes of the beam element j corresponding to a stage of the building are represented, together with some of the nodes of the elements $j-1$ and $j+1$ (outside the beam for representational clarity).

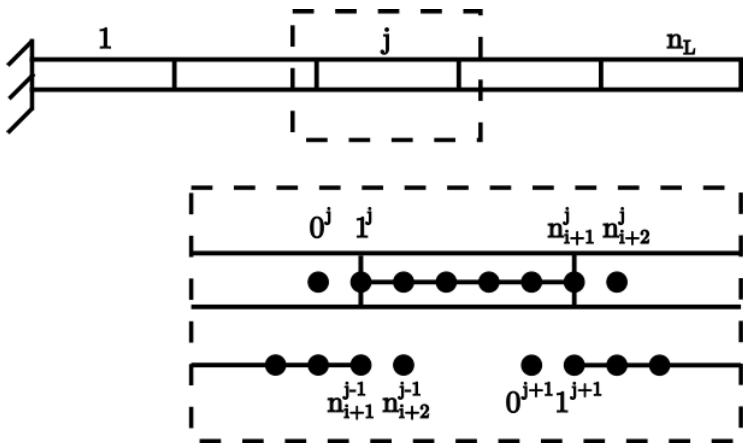

Figure 5.4. Piecewise Timoshenko beam divided in n_L elements studied through FD dividing each of them in n_i^j elements, with n_{i+1}^j physical nodes (the nodes 0^j and n_{i+2}^j are virtual ones).

With reference to Fig. 5.4, it should be noted that in general nodes n_{i+2}^j and node 2^{j+1} do not coincide and neither do nodes 0^j and node n_i^{j-1} (the relative stages should have the same height h_j and be divided in the same number of elements and, in order to have the same displacement, the stiffness and mass matrices of the two cells should be the same). So, the problem of free dynamics in FD becomes the following:

$$\begin{cases} \hat{\mathbf{u}}_{1,1} = \mathbf{0} \qquad \text{node } 1^1 \\ -\lambda^2 \mathbf{M}_1 \hat{\mathbf{u}}_{1,i} + \left(\dfrac{\mathbf{K}_{2,1}}{{\Delta_1}^2} - \dfrac{\mathbf{K}_{1,1}}{2\Delta_1} \right) \hat{\mathbf{u}}_{1,i-1} + \left(\mathbf{K}_{0,1} - \dfrac{2\mathbf{K}_{1,1}}{{\Delta_1}^2} \right) \hat{\mathbf{u}}_{1,i} \\ + \left(\dfrac{\mathbf{K}_{2,1}}{{\Delta_1}^2} + \dfrac{\mathbf{K}_{1,1}}{2\Delta_1} \right) \hat{\mathbf{u}}_{1,i+1} = \mathbf{0} \qquad \text{nodes } 2^1, \ldots, n_{i+1}^1 \end{cases} \tag{5.34}$$

$$\begin{cases} \hat{\mathbf{u}}_{1,n_i+1} = \hat{\mathbf{u}}_{2,1} \qquad \text{nodes } n_{i+1}^1, 1^2 \\ -\dfrac{\mathbf{K}_{1B,1}}{2\Delta_1} \hat{\mathbf{u}}_{1,n_i} + \mathbf{K}_{0B,1} \hat{\mathbf{u}}_{1,n_i+1} + \dfrac{\mathbf{K}_{1B,1}}{2\Delta_1} \hat{\mathbf{u}}_{1,n_i+2} \\ = -\dfrac{\mathbf{K}_{1A,2}}{2\Delta_2} \hat{\mathbf{u}}_{2,0} + \mathbf{K}_{0A,2} \hat{\mathbf{u}}_{2,1} + \dfrac{\mathbf{K}_{1A,2}}{2\Delta_2} \hat{\mathbf{u}}_{2,2} \qquad \text{nodes } n_{i+1}^1, 1^2 \end{cases} \tag{5.35}$$

$$\begin{cases} -\lambda^2 \mathbf{M}_2 \hat{\mathbf{u}}_{2,i} + \left(\dfrac{\mathbf{K}_{2,2}}{{\Delta_2}^2} - \dfrac{\mathbf{K}_{1,2}}{2\Delta_2} \right) \hat{\mathbf{u}}_{2,i-1} + \left(\mathbf{K}_{0,2} - \dfrac{2\mathbf{K}_{1,2}}{{\Delta_2}^2} \right) \hat{\mathbf{u}}_{2,i} \\ + \left(\dfrac{\mathbf{K}_{2,2}}{{\Delta_2}^2} + \dfrac{\mathbf{K}_{1,2}}{2\Delta_2} \right) \hat{\mathbf{u}}_{2,i+1} = \mathbf{0} \qquad \text{nodes } 1^2, \ldots, n_{i+1}^2 \end{cases} \tag{5.36}$$

$$\begin{cases} \hat{\mathbf{u}}_{2,n_i+1} = \hat{\mathbf{u}}_{3,1} \qquad \text{nodes } n_{i+1}^2, 1^3 \\ -\dfrac{\mathbf{K}_{1B,2}}{2\Delta_2} \hat{\mathbf{u}}_{2,n_i} + \mathbf{K}_{0B,2} \hat{\mathbf{u}}_{2,n_i+1} + \dfrac{\mathbf{K}_{1B,2}}{2\Delta_2} \hat{\mathbf{u}}_{2,n_i+2} \\ = -\dfrac{\mathbf{K}_{1A,3}}{2\Delta_3} \hat{\mathbf{u}}_{3,0} + \mathbf{K}_{0A,3} \hat{\mathbf{u}}_{3,1} + \dfrac{\mathbf{K}_{1A,3}}{2\Delta_3} \hat{\mathbf{u}}_{3,2} \qquad \text{nodes } n_{i+1}^2, 1^3 \end{cases} \tag{5.37}$$

$$\begin{cases} \ldots \end{cases} \tag{5.38}$$

$$\begin{cases} -\dfrac{\mathbf{K}_{1B,n_L}}{2\Delta_{n_L}} \hat{\mathbf{u}}_{n_L,n_i} + \mathbf{K}_{0B,n_L} \hat{\mathbf{u}}_{n_L,n_i+1} + \dfrac{\mathbf{K}_{1B,n_L}}{2\Delta_{n_L}} \hat{\mathbf{u}}_{n_L,n_i+2} = \mathbf{0} \qquad \text{nodes } n_{i+1}^{n_L} \end{cases} \tag{5.39}$$

Once again, this problem can be rewritten as:

$$\left(\mathbf{K}_T - \lambda^2 \mathbf{M}_T \right) \hat{\mathbf{u}}_T = \mathbf{0} \tag{5.40}$$

where the vector of vibration modes $\hat{\mathbf{u}}_T = (\hat{\mathbf{u}}_{1,1}, \hat{\mathbf{u}}_{1,2}, \ldots, \hat{\mathbf{u}}_{1,n_i+2}, \hat{\mathbf{u}}_{2,0}, \hat{\mathbf{u}}_{2,1}, \ldots, \hat{\mathbf{u}}_{n_L,n_i+2})^T$ has dimension $6\sum_{j=1}^{n_L}(n_i^j + 3) - 6$ for each mode, since three virtual nodes are added for each element $\hat{\mathbf{u}}_{j,0}, \hat{\mathbf{u}}_{j,n_i+1}, \hat{\mathbf{u}}_{j,n_i+2}$ except for the first element that does not have $\hat{\mathbf{u}}_{1,0}$ (6 because each node of the equivalent beam has 6 d.o.f.) and the mass and stiffness matrices are square matrices with the same dimensions. As before, once Eq. (5.40) is solved, thus eigenvalues and eigenvectors (i.e. vibration modes in correspondence of the discretized nodes) are obtained, the solution in terms of displacement, strain and stress fields can be reconstructed as explained at the end of Sect. 5.2.1 (applying in the order Eq. (5.14), (5.15), (5.3), (5.9)).

5.2.4 Case study 1

In this section the Building case study number 1 (CS1) is briefly described in terms of geometry, material properties and load distribution, also explaining some simplifications which were made.

This building was chosen since it is quite compact, as can be noted from the plan view of a generic floor reported in Fig. 5.5 and this is important since the model which was used in the previous section is not able to capture the floor deformability, thus, a higher ratio between the sides of the building, as well as the presence of significant concavity in plan, makes the model less appropriate. In Fig. 5.6 the front and side elevations show that also the development in elevation of the building is quite regular.

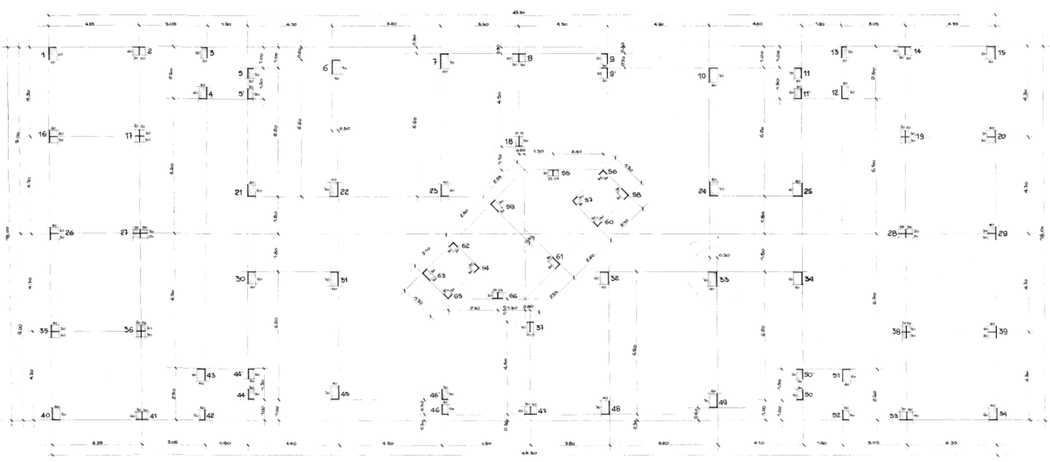

Figure 5.5. Plan view of building case study number 1 (courtesy of Dimensione Solare s.r.l.).

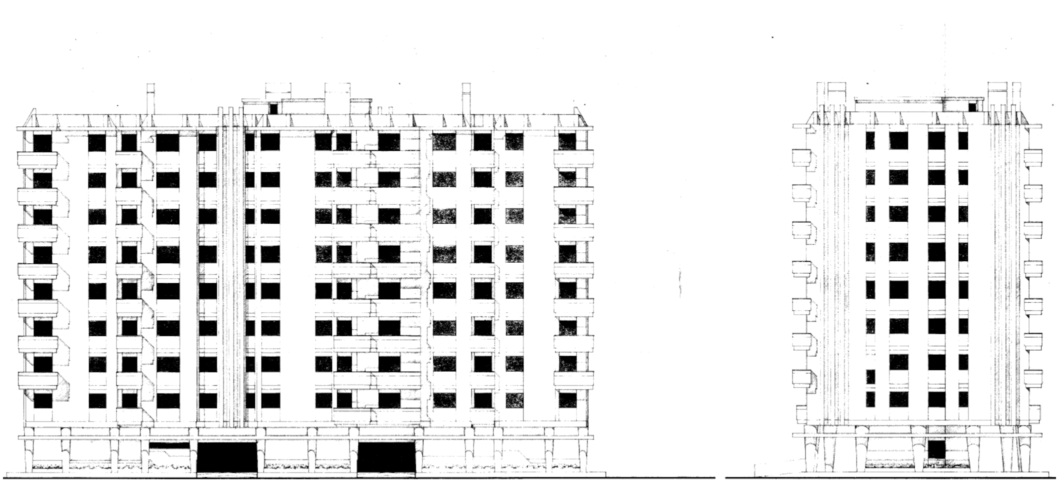

Figure 5.6. Front and side elevation of building case study number 1 (courtesy of Dimensione Solare s.r.l.).

The sides of the building are 45.30 m along y and 18.00 m along z (using the same reference system of the model), while its height (dimension along x) is of 27.80 m, with a ground floor of 3.80 m and 8 floors of 3.00 m each. The cross-section dimensions of the columns at ground floor (which are reduced on the upper floors) and their exact positions can be deducted from Fig. 5.5. Moreover, the same figure shows that the columns are arranged in a regular way along y and z, except for the central part of the building in correspondence of the stairs.

The properties of the material used to model the reinforced concrete columns and the loads acting on the structure, converted in masses for the dynamic analysis, were taken from the available documents of the building design and are resumed in Tab. 5.1.

Table 5.1. Material properties and amplitudes of the loads acting on building case study number 1.

r.c. properties:	$E = 3.12 \times 10^{10}$ N/m^2	$\nu = 0.2$	$\rho_c = 25$ kN/m^3
Type	Permanent (kN/m^2)	Non-perm. (kN/m^2)	Variable (kN/m^2)
Floor	3.28	2.36	2.00
Balcony	2.80	1.36	4.00
Stairs	3.75	1.36	4.00
Infill wall	-	2.97	-

As already written, some simplifications were made in this model which however, in the author's opinion do not significantly influence the results since, as will be clearer in Sect. 5.3, major simplifications exist. In particular, the columns of the last level were considered all having the same length, even if those on the perimeter are shorter due to the shape of the roof (inclined), the stairs were not directly modeled, but their weight was applied on the nearby columns, since it was verified that modeling them as columns having equivalent properties only slightly influences the final result and finally, the last hypothesis is that the mass of the roof was assumed to be the same of regular floors.

5.2.5 Model results

In this section the results in terms of frequencies and vibration modes for the building presented in the previous section, obtained through the homogenization procedure are commented. In particular, in Tab. 5.2 the first three frequencies obtained through the model, associated to the first three global vibration modes of the structure, are reported; they are represented in Figs. 5.7, 5.8 and 5.9. In particular, in all the three figures, on the left the three-dimensional representation of the vibration modes is shown, with the undeformed columns in dark gray and the deformed ones in red (black dots identify floors) and also a reconstruction of the undeformed and deformed beams of the last floor is given (in dark gray and blue respectively): the beam displacements were simply derived from those of the columns and are depicted just to give a clearer visualization of the modes since as already said they do not appear in the model. It is evident that Fig. 5.7 is the first bending mode along y, Fig. 5.8 is the first torsional mode and Fig. 5.9 is the first bending mode along z; the hypothesis of rigid floor is evident in the three cases and the frequencies assume quite close values.

Results obtained in this section using the homogenization technique to model a full-scale reinforced concrete building will be compared to those obtained on the same building in operational condition, to understand if the model is able to reconstruct the building dynamics and which are its limitations.

Table 5.2. Modal properties of building case study number 1 found with the homogenization model.

Mode	Type	f (Hz)
1	Bending (along y)	1.14
2	Torsional	1.63
3	Bending (along z)	1.66

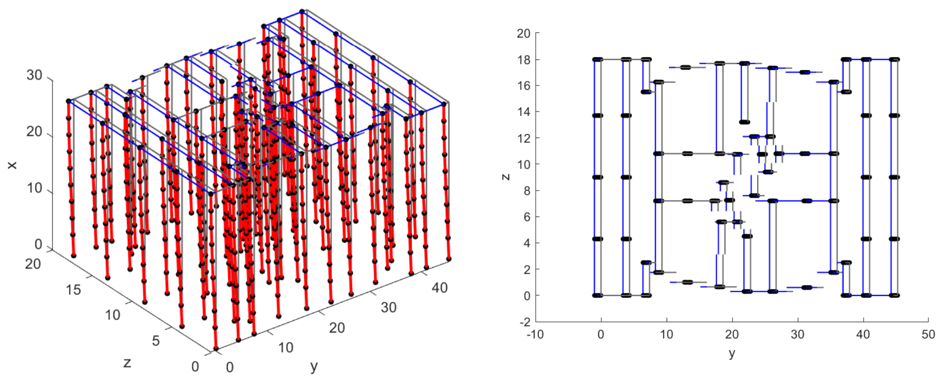

(a)

(b)

Figure 5.7. First vibration mode of building case study number 1 obtained through the homogenization model: (a) Three-dimensional view; (b) Plan view.

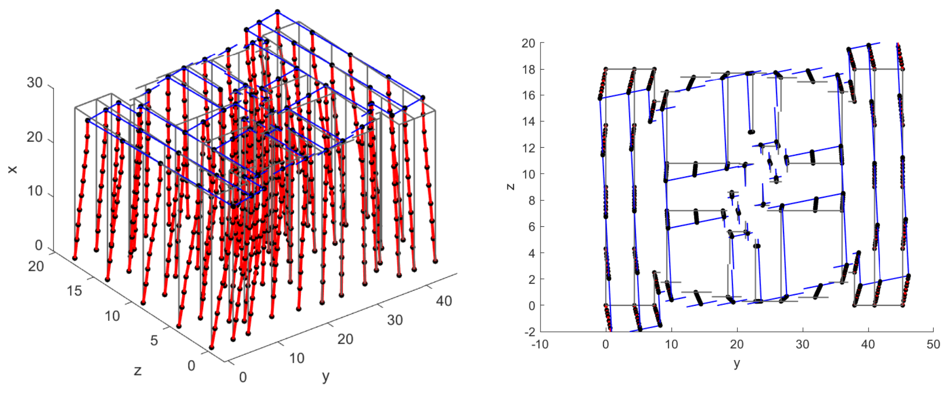

(a) (b)

Figure 5.8. Second vibration mode of building case study number 1 obtained through the homogenization model: (a) Three-dimensional view; (b) Plan view.

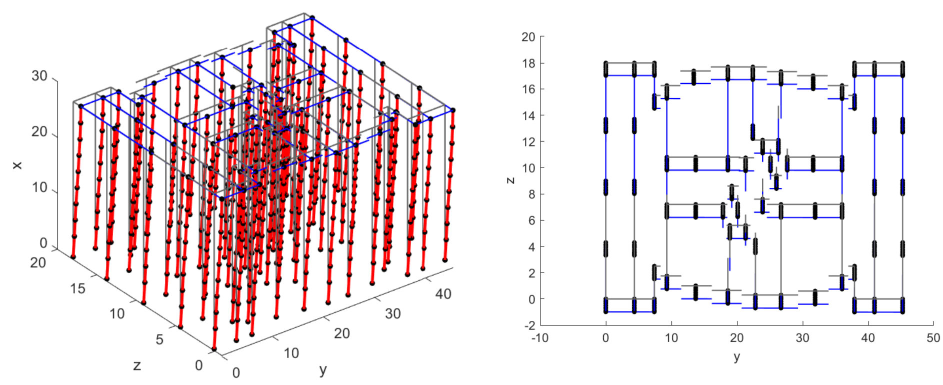

(a) (b)

Figure 5.9. Third vibration mode of building case study number 1 obtained through the homogenization model: (a) Three-dimensional view; (b) Plan view.

5.3 Monitoring

In this section, using the same OMA algorithms introduced for beams, the modal properties of two three-dimensional frames are obtained. In particular, the SSI-COV algorithm is used, thus the identification is performed in time domain. Two case studies are considered among some available instrumented buildings. The first one is the same already investigated in Sect. 5.2 called CS1 and a comparison is made between the model and the experimental results. The second one, here called Building case study number 2 (CS2), is of interest too, since for this building data measured every two weeks were available without long-term interruptions, along with information on temperature, thus allowing to track their evolution and the relation between them.

5.3.1 Case study 1

Recalling CS1 from Sect. 5.2.4, the position of the accelerometers is depicted in Fig. 5.10 in plan and in Fig. 5.11 in elevation. The building is monitored through FBA accelerometers at stages; in particular, the blue ones represent bi-axial sensors, while the orange ones are mono-axial accelerometers. As can be seen from the figures, two bi-axial and one mono-axial accelerometers are installed at the top of stages 2, 4, 6 and 8; finally, a Micro-ElectroMechanical Systems (MEMS) sensor at the basis, for the measurement of the PGA, is implemented too.

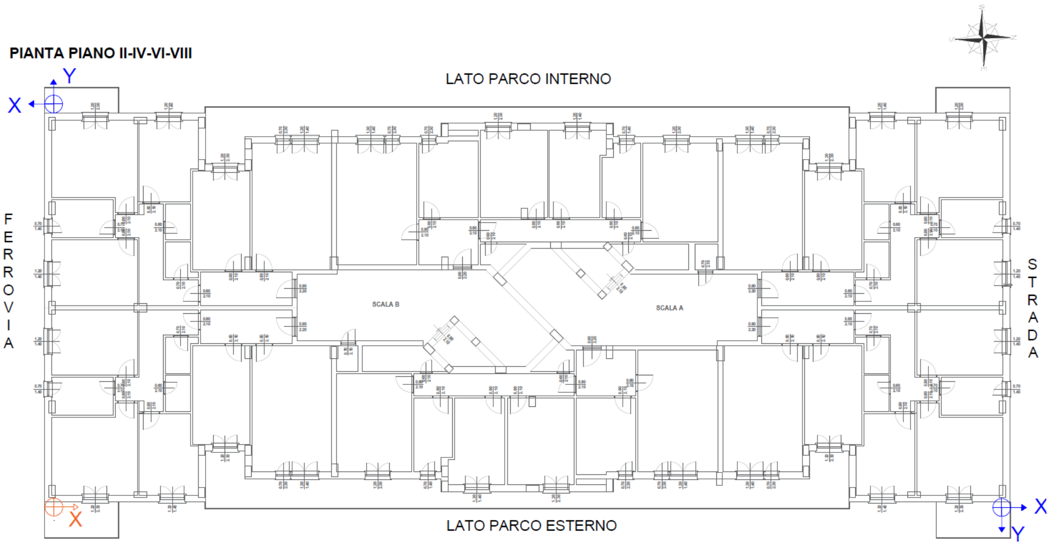

Figure 5.10. Position of sensors in plan for building case study number 1 (courtesy of Dimensione Solare s.r.l.).

Figure 5.11. Position of sensors in east elevation for building case study number 1 (courtesy of Dimensione Solare s.r.l.).

The stabilization diagram of SSI-COV, which allows to identify the first modes of the structure, is depicted in Fig. 5.12: it can be seen that there are really close modes in terms of frequency around 2 Hz, but they are classified as representative of different physical modes as also found with the model.

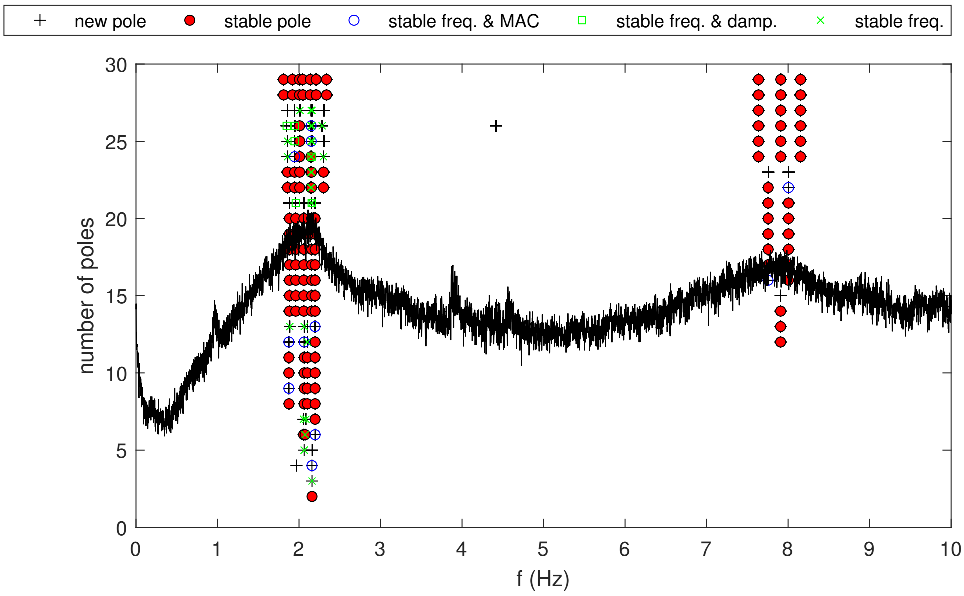

Figure 5.12. Stabilization Diagram with identified vibrations modes using SSI-COV on time series acquired on building case study number 1.

These results are examined and reported in Tab. 5.3 in terms of frequencies of the vibration modes of interest, with the indication of the type of mode which has been identified.

Table 5.3. Modal properties of building case study number 1 found with OMA in time domain.

Mode	Type	f (Hz)
1	Torsional	1.88
2	Bending ($\approx$ along z)	2.16
3	Bending ($\approx$ along y)	2.20

The natural frequencies are quite close and, about the vibration modes, looking at Fig. 5.13, keeping in mind that at each monitored stage two of the sensors are bi-axial and one is mono-axial (thus the information given by the the last one is in some way incomplete), it is reasonable to assume that the first vibration mode (Fig. 5.13(a)) is of torsional nature, the second one (Fig. 5.13(b)) could represent a global bending mode of the structure almost along z (i.e. bending along the "weak direction"), while the third one (Fig. 5.13(b)) is indicative of a bending mode almost along y (i.e. bending along the "strong direction").

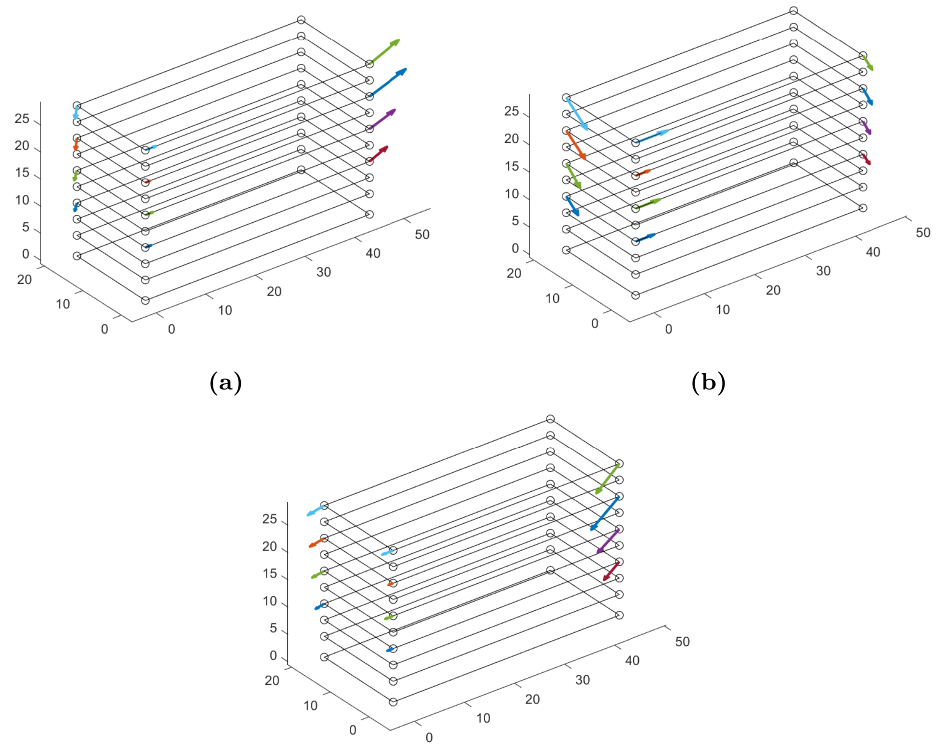

(a) (b) (c)

Figure 5.13. Schematic representation of vibration modes of building case study number 1 obtained through OMA.

5.3.2 Comparison with the model

At this point, the free dynamics properties of CS1 obtained with the analytical model based on the homogenization theory in Sect. 5.2.5 and with the OMA algorithm in time domain in Sect. 5.3.1 are compared, to assess how accurately the model reproduces the real behavior of the building and to identify the sources of discrepancy. Modes in Tab. 5.4 are ordered following those found with OMA.

Table 5.4. Comparison between modal properties of building case study number 1 found with OMA and homogenization model.

Mode type	OMA		Model	
	f (Hz)	-	f (Hz)	MAC
Torsional	1.88	-	1.63	0.47
Bending (along z)	2.16	-	1.66	0.63
Bending (along y)	2.20	-	1.14	0.56

First of all, the model does not give exactly the same values of frequencies of the real building and also the values of the Modal Assurance Criterion (MAC) are far from being 0.8 or higher but this was to be expected, due to the simplifications of the model compared to the complexity of the real structure. In particular, a deeper analysis of the single modes is performed one at a time. The vibration mode labeled as "torsional" is represented in Fig. 5.8 for the model and in Fig. 5.13(a) for the OMA. First of all, a general comment, which holds true also for other cases, is that for the experimental modes, the mono-axial accelerometers placed in correspondence of the column 40 cannot give exhaustive information, meaning that the value of the MAC could be higher (but also lower) if the component in the orthogonal direction is considered too. However, from Fig. 5.13(a) and with the available information, the mode can be classified as torsional and, a comparison of the frequencies (1.88 Hz versus 1.63 Hz) tells that they are not so far. Then, moving to the second row of Tab. 5.4, the value of the MAC is the highest one (0.63) as can be seen from the comparison of Fig. 5.9 for the model and of Fig. 5.13(b), showing a prevalent translation along the direction z; once again, the component of the accelerometer in correspondence of the column 40 in that direction would be fundamental to confirm this statement. Finally, the last comparison is between Fig. 5.7 for the model and in Fig. 5.13(c), identified as bending modes along y; more or less the same considerations made for the previous mode hold here; however, in this case the difference in terms of frequency is definitely higher compared to the other two cases and this may suggest a lack of stiffness in the y direction of the model, meaning that something was not accounted for.

Other considerations have to be made in order to correctly interpret these results and above all to understand their differences. Of course, the model based on the homogenization technique described in this Thesis has some limitations in describing a full-scale building, some of which could be bypassed through an adequate model updating procedure as discussed later. For example, the model considers a rigid behavior of the floors in and out-of-plane: to respect the in-plane rigid behavior, the slab should be quite thick and the plan of the building should be as compact as possible, similar to a square and, the more the shape is different, the higher the difference is between the two; on the other hand, about the out-of-plane behavior, this hypothesis implies that the stiffness of the horizontal elements is sufficiently higher than that of the columns, in order to consider them clamped at both ends (at the head and at the foot) when deriving the problem equations: also this hypothesis is not perfectly respected since the stiffness of the floor (hollow-clay-block reinforced concrete slabs) is not "infinite", being the thickness of the slab of just 4 cm, and also the beams are slab-depth beams (thus having the same height of the floor), except those on the perimeter. This means that the stiffness of the horizontal elements is low and is not really able to prevent the rotation of the columns at foot and head. So, some implementations have to be done in the model in a second stage, to account for the in-plane and out-of-plane behavior. In this Thesis, only the "basic" model was used, since the real goal was to determine whether, even with all these simplifications, it was possible to obtain realistic results: the outcomes are encouraging. Moreover, all the available case studies of real buildings had similar properties, so it was not possible to find a better candidate (e.g. lower ratio between the sides of the building, deeper beams) for the comparison with the model.

Another important simplification of the model – which, however, is not specific to homogenization theory but is also a common feature of FE models in general – is that infill walls, and consequently the increase in stiffness they provide to the structure, were not considered. In fact, they were considered as masses acting on the beams where they are actually applied, but their contribution in terms of stiffness was neglected. Of course, this contribution is far from negligible and there are many works highlighting how on real buildings a significant reduction of frequency can be registered if the infill walls are not present or damaged, as in [75, 96] while a sudden increase is registered when they are built.

Another important difference between the model and the real structure are the loads applied on it. In fact, as written, the loads (converted into masses) applied on the model are taken from the available documentation. However, in general their effective distribution on the structure is different from the assumed one, especially for those loads classified as permanent non-structural like finishes, partition walls and the variable ones like furniture, appliances, people, whose values and positions can influence the free dynamics. In addition to this point, the elastic modulus of all elements was considered the same and it is evident that this is another important simplification.

However, despite all these simplifications, with a relatively simple model, interesting results were obtained and the comparison with the modal properties found from ambient vibration data, processed with OMA, is definitely encouraging.

Thinking to future experimental campaigns, based on what was found for this case study (and for other not reported in the Thesis) it should be underlined that, if one wants to install sensors on a building with the objective of finding its modal properties, i.e. natural frequencies and especially mode shapes, for buildings as the one investigated in this section, taking also into consideration the economic aspect, the right compromise should be the the installation of four bi-axial accelerometers (one at each corner), thus having eight channels per floor, every two stages. In fact, it was demonstrated in this section that 5 channels (given by two bi-axial and one mono-axial sensors) are not enough to fully characterize the mode shape, requiring some further hypotheses. On the other side, the implementation of less sensors, for example just three channels per floor (one bi-axial and one mono-axial sensors) is useless for the mode shapes characterization whilst it can be useful to find the first natural frequencies of a building. Finally, if one side of the building is particularly longer than the other one (meaning that the floor is particularly flexible in plane), it would be recommended to place some sensors also in the middle of the long sides.

To conclude, in order to make the model more accurate in the identification of the modal properties of the building, a model updating procedure has to be developed. Something was already done for the case under study, but results are not reported in this Thesis since further analyses have to be carried out. However, just to give an idea, it was decided to follow the procedure introduced in [63] which was originally developed for FE and to adapt it to a model realized through the homogenization procedure. In brief, it consists in the choice of some parameters to update and in the definition of an objective function accounting for the deviation between the prediction of the model and the real structure behavior, in terms of difference between eigenvalues, mode shapes or other criteria. Then, the constrained objective function has to be minimized, being the constraints for example on the value assumed by the parameters to be updated, on the difference between eigenvalues from the real structure and those of the model and on the values assumed by the MAC comparing the mode shapes of the two. In the proposed procedure, penalty functions are introduced to make the problem unconstrained and adequate techniques are proposed to minimize the objective function.

A first attempt to apply the algorithm to the problem under study is currently underway, considering as updating parameters the Young modulus of each cell E_j (or alternatively the shear areas or the torsional inertia), trying to minimize as a first try the difference between the eigenvalues of Tab. 5.4, also trying to invert their order. The analysis has also the goal to understand if this kind of algorithm is adequate for the model based on the homogenization technique: there is no guarantee that it works, given the limited amount of experimental data available, which suggests that other model updating procedures might be more suitable.

5.3.3 Case study 2

Another case study, here identified as CS2, is investigated just in terms of OMA. In fact, being this building in masonry, the model developed in Sect. 5.2, which considers frame structures, would not be useful. However, in addition to the identification of modal properties already presented for CS1, in this case they are tracked in time to understand if their evolution is due to normal seasonal effects (related to temperature) or if something unexpected is happening.

The sides of the building are 27.50 m along y and 11.30 m along z and its above-ground height is about 15.00 m, distributed over 4 floors. The structural system consists of masonry walls which, in combination with the low height of the building, make it quite stiff.

The position of the FBA accelerometers is indicated in plan and in elevation in Fig. 5.14 and in Fig. 5.15 respectively. In this case, in addition to the MEMS sensor at the basis, whose only goal is to measure the PGA, one bi-axial and one mono-axial FBA are placed at the top of what can be identified as ground and last stages of the building.

Fig. 5.16 shows the stabilization diagram of this building. Less modes are identified with respect to CS1, mainly due to its simpler architectural layout, due to the use of a different structural systems made of masonry walls which are stiffer and thus require higher excitation levels and/or more sensors and, of course, due to the use o a reduced number of accelerometers.

Finally, in Tab. 5.5 the identified frequencies of the first three vibration modes of the building, found from the recordings of a certain time window of a certain date are resumed. The vibration modes are illustrated in Fig. 5.17 even if it is difficult to define what they represent, likely mixed modes.

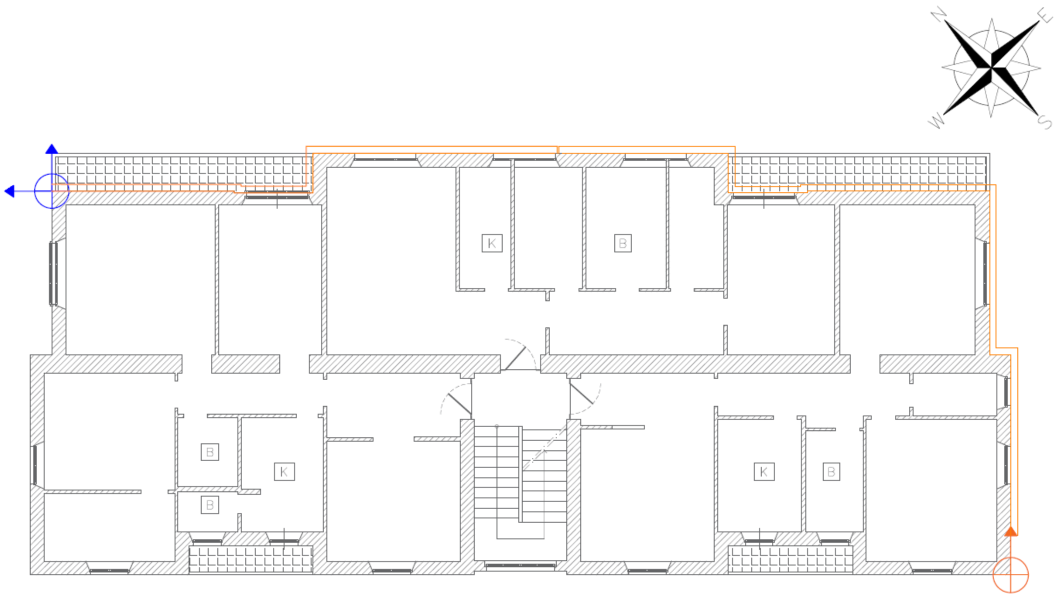

Figure 5.14. Position of sensors in plan for building case study number 2 (courtesy of Dimensione Solare s.r.l.).

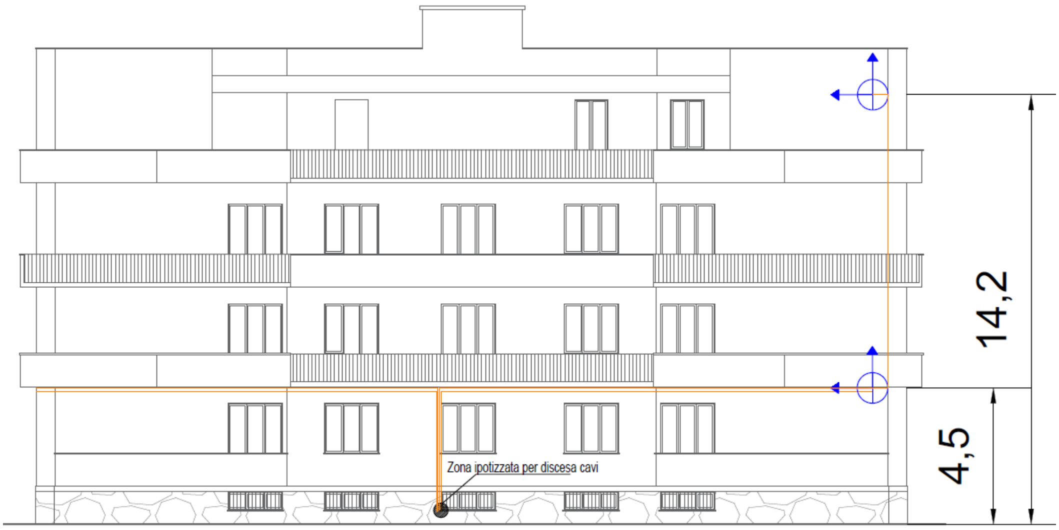

Figure 5.15. Position of sensors in north-east elevation for building case study number 2 (courtesy of Dimensione Solare s.r.l.).

Table 5.5. Modal properties of building case study number 2 found with OMA in time domain.

Mode	Type	f (Hz)
1	-	4.06
2	-	5.32
3	-	14.01

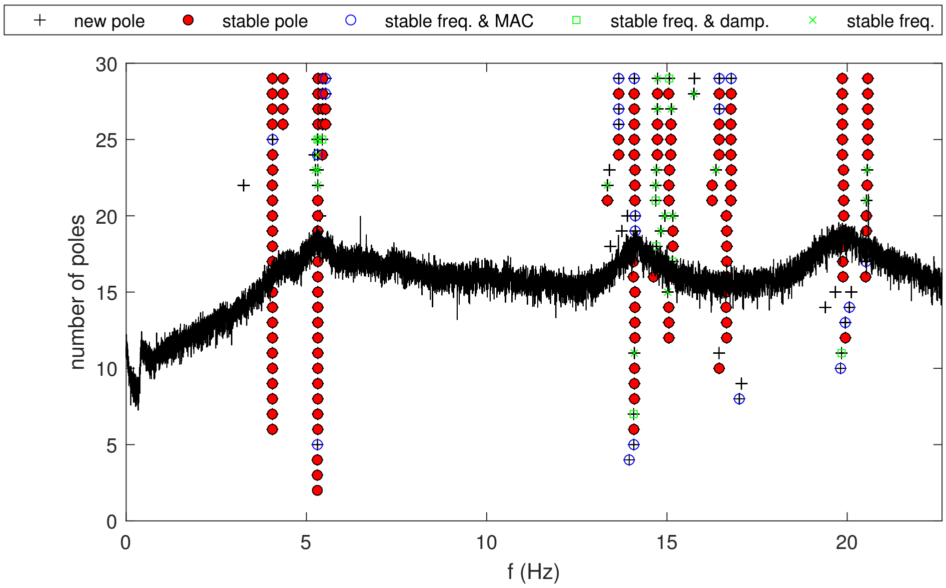

Figure 5.16. Stabilization Diagram with identified vibrations modes using SSI-COV for building case study number 2.

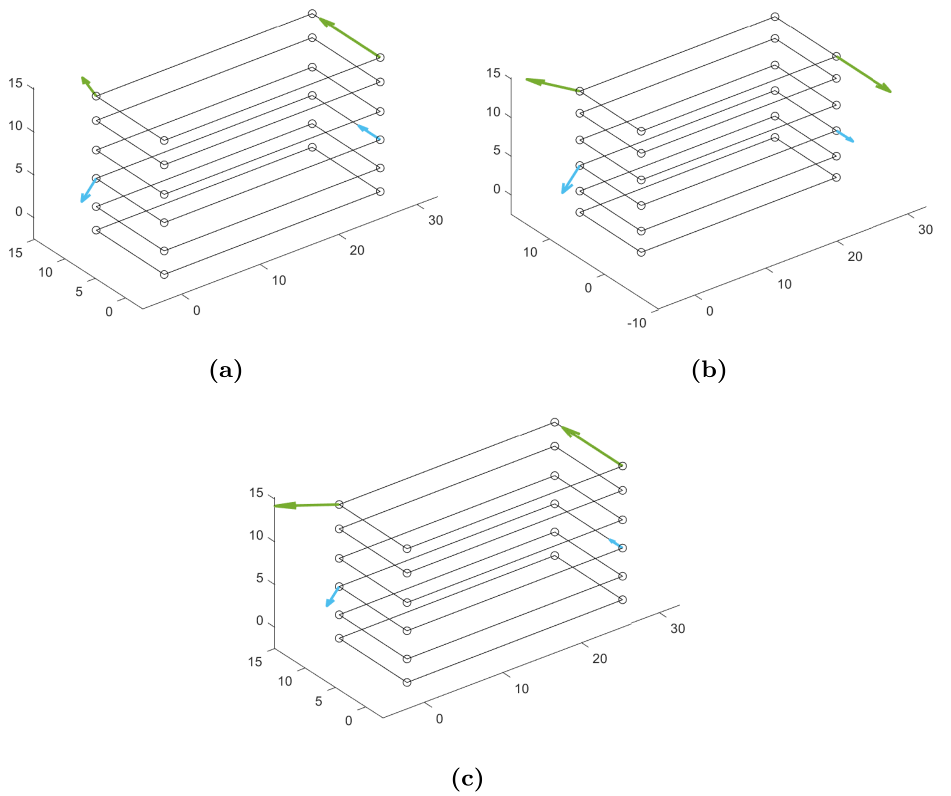

Figure 5.17. Schematic representation of vibration modes of building case study number 2 obtained through OMA.

5.3.4 Tracking of modal properties

In this section the modal properties of CS2 found at different times through the same OMA algorithm are put together in order to track their evolution in time as done for example in [3, 16].

The tracking of modal properties was realized in a period of 19 months from the 15^{th} of January 2024 to the 30^{th} of July 2025 and, in the figures, data collected every two weeks are represented. First, a clustering procedure was realized in order to correctly associate the same modes at different time instants (the word event is here used to indicate the records at a certain time instant). To do that, a reference event was chosen and both the frequencies and the MAC values of each mode of each event were compared to each mode of the reference event. The differences in terms of frequencies and MAC were calculated and the mode k of the event j whose difference was minimum with respect to the mode i of the reference event (excluding those whose difference was greater then a threshold, which was kept fixed but can also be updated as in [16]) was considered to be the same mode of i; this was done in order to correctly associate the same vibration mode recorder at different time instants (in other words to create clusters).

The results of this procedure can be seen in Fig. 5.18 for the first two vibration modes. There, the orange triangles are the values of temperature (which were acquired through a sensor placed inside the building in an unheated zone at the ground floor) not always available due to technical issues, while the blue circles are the frequencies and the red line is a trend line for them. It is evident that the 1^{st} and 2^{nd} vibration modes behave the same way: in fact, it can be seen that the frequencies have the same harmonic trend of temperatures, with lower values in correspondence of cold months and higher values in warmer periods. The oscillation of values is around a mean value (black horizontal line) and it is not possible to highlight a different trend in addition to the seasonal one, as could be for example a linear decrease of frequencies related to damage, giving the idea that nothing dangerous in happening on the building (at least globally).

Finally, a metric was introduced, called Mahalanobis distance [36], which can be useful to find anomalous values, also called outliers, which are basically unexpected values which require a further investigation. In particular, if one considers the set of n events, each containing the same number p of frequencies coming from the cluster

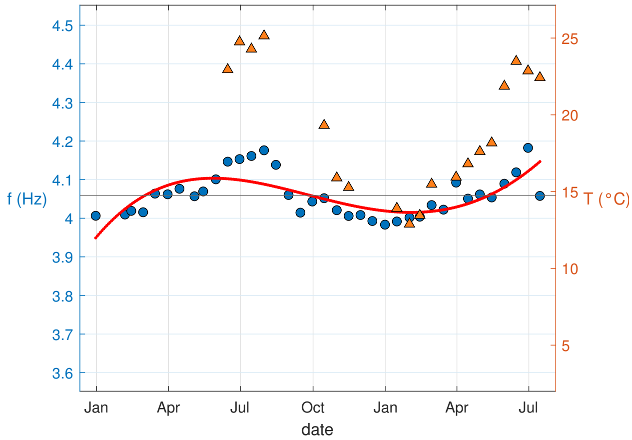

(a)

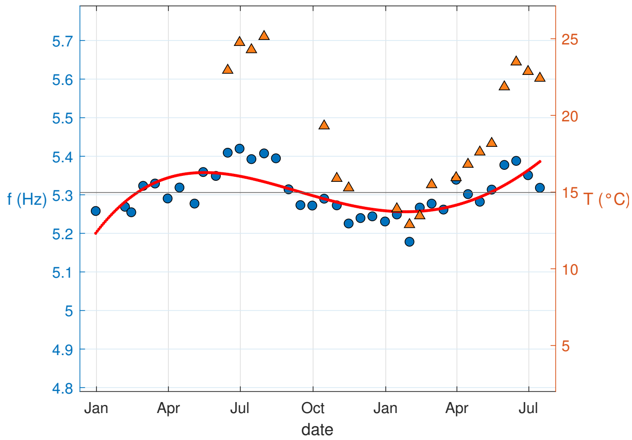

(b)

Figure 5.18. Tracking of vibration modes in time for building case study number 2: (a) First mode; (b) Second mode.

algorithm, the Mahalanobis distance $D_{\bar{t}}$ for the event recorded at time $\bar{t}$ is:

$$D_{\bar{t}} = \left(\mathbf{f}_{\bar{t}} - \bar{\mathbf{f}}\right)^T \mathbf{S}^{-1} \left(\mathbf{f}_{\bar{t}} - \bar{\mathbf{f}}\right) \tag{5.41}$$

where $\mathbf{f}_{\bar{t}}$ is the vector containing the frequencies measured at time $\bar{t}$ which is suspected to be an outlier, $\bar{\mathbf{f}}$ is the vector of the mean frequencies considering the entire set of n events (one can chose to include or exclude the suspected outlier from the calculation of the mean vector and the covariance matrix) and $\mathbf{S}$ is their covariance matrix of dimensions $p \times p$. This measure is particularly interesting since it entails a correlation between the different frequencies evaluated at the same time instant $\bar{t}$.

Given that a procedure has to be established in order to define the threshold beyond which the event can be classified as an outlier, the application of Eq. (5.41) on the data set considered in this section while retaining only the first three frequencies, did not yield any values that could be associated with anomalies at any time.

5.4 Conclusions and future developments

In this chapter, three-dimensional frames were studied. First, an analytical model based on the homogenization technique was recalled. The model considers the three-dimensional frame as an equivalent Timoshenko beam (with 6 d.o.f.) and is valid under certain hypotheses. Equations were recalled and a novel contribution was given to take into account different properties (in terms of mass and stiffness) at each floor, modeling the beam as a piecewise beam. The free dynamics problem was solved through Finite Differences (FD) and results are presented for a first case study, called CS1 based on a full-scale existing building.

Then, in order to identify the dynamical properties on the real building, data collected from accelerometers placed on CS1 are processed through the usual OMA algorithm in time domain (SSI-COV) and a comparison is made with the frequencies and mode shapes found with the model. An extensive discussion of the similarities and of the differences is realized, trying to understand how the model can be improved, also relying on a well established model updating algorithm.

Moving on, in the framework of monitoring, the attention turned to another case study, CS2, for which a big amount of data was available, with the goal of identifying its modal properties and track them over time to study their evolution. Focusing on the first two vibration modes, it was found that their variation over time follows the temperature oscillation and does not present any other trend which could suggest the presence of damage; moreover, the Mahalanobis distance was calculated arriving at the same conclusion: no outliers were found.

So, the main findings of this chapter involve the attempt to use the homogenization technique to model a full-scale existing building, establishing the basis for its updating: encouraging results were found. Moreover, the tracking of modal properties can be defined in a specific algorithm that can be implemented in similar cases.

Future perspectives are obviously aimed to complete the model updating process already in progress or to use other strategies if this one will not give satisfying results. Moreover, since the model is now available, it would be interesting to study the forced dynamics of the building, considering existing accelerograms of past earthquakes, to determine the demand in terms of displacement and of internal stresses in the most stressed columns from a design perspective.

Conclusions

In this Thesis, models for beams, cables and three-dimensional frames were discussed with the main objective of developing and extending efficient ROM to study linear and nonlinear systems with a specific focus in the structural dynamics field. In this chapter the novelties introduced in the Thesis are highlighted, providing answers to the research questions, and future perspectives are discussed.

In Ch. 3, Thin-Walled Beams (TWB) were modeled through Generalized Beam Theory (GBT-D) and static and dynamic results compared with experimental ones processed through OMA algorithms. Later, the beam vibrations were controlled with a Nonlinear Energy Sink (NES) and at the end a newly developed model-based identification procedure was presented and tested on a nonlinear Euler-Bernoulli beam using numerical or experimental signals.

In Ch. 4, the nonlinear model of suspended cable was recalled and its interaction with the wind in terms of Vortex-Induced Vibrations (VIV) was studied using the MSM directly on the continuous problem. Finally, the same identification procedure developed for beams was successfully tested on cables.

In Ch. 5, a ROM for three-dimensional frames based on the homogenization technique was considered and extended. Its modal properties were compared to those obtained from experimental signals on a full-scale building and limitations and perspectives of the method discussed. Finally, the modal properties of another building were tracked over time.

6.1 Conclusions

The main goal of this PhD Thesis was the development or the extension of accurate mathematical Reduced-Order Models (ROM) to study different kinds of structures in civil engineering related to dynamics in its various facets: linear, nonlinear, experimental, inverse. These models had to give answers to research questions highlighted in Ch. 2, arising from problems not yet investigated.

Here, among civil engineering structures, beams, cables, and three-dimensional frames were investigated. About beams, given their extensive use, different possible research paths were identified, from the validation of ROM with experimental results, to vibration control, to the identification of parameters. Then, about cables, the main focus was on the investigation of their interaction with wind in terms of VIV. Finally, for three-dimensional frames the feasibility of employing the homogenization technique to describe full-scale buildings was investigated.

About beams, the study set out to investigate whether a Thin-Walled Beam (TWB), analytically modeled through the Generalized Beam Theory, in the GBT-D version, was able to faithfully catch the response in statics and dynamics of full-scale prestressed reinforced concrete girder bridges. This was proven to be true modeling a beam part of the highway A24 (in Italy) with a small number of deformation modes, as shown in convergence analyses, and comparing its results to those obtained through OMA algorithms, while a linear Euler–Bernoulli beam model was proven to be less suitable. Within this framework, it was observed that an increase of the static load on the real bridge leads to experimental displacements exhibiting slight nonlinear behavior, thus future studies could regard the incorporation of material nonlinearities into the GBT-D model, to further improve its capability to represent the actual structural response.

In the framework of vibration control, the same GBT-D model was used to passively reduce vibrations in prestressed reinforced concrete box-girder bridges through the use of a Nonlinear Energy Sink (NES) with cubic nonlinearity. It was shown that the device is able to effectively control beam vibrations under different loading scenarios and in a wide range of natural frequencies, both in resonant cases and in non-resonant ones, for which obviously a reduced level of vibration mitigation was observed. This approach could be further enhanced by optimizing the NES parameter and by considering nonlinear restoring forces more complex than the cubic one.

Subsequently, moving to the inverse problem, a novel model-based procedure was proposed for the identification of parameters of nonlinear continuous systems (like nonlinear Euler-Bernoulli beams), based on the combined use of the Hilbert–Huang Transform (HHT) and the Multiple Scale Method (MSM). The proposed method, which differently from existing methods can operate directly on the continuous (non-discretized) problem, avoiding possible mistakes, was shown to be effective in several scenarios and was also subjected to an experimental validation on a nonlinear clamped-clamped beam. Several directions are envisaged for future research, including the consideration of internal resonances and slower time scales to improve the procedure, and the possible extension to the GBT-D model within a damage detection framework.

Attention was then directed to cables, with particular focus on the nonlinear (both quadratic and cubic) model of a suspended cable. Its interaction with the wind action in terms of Vortex-Induced Vibrations (VIV), modeled through a wake oscillator, was investigated. Differently from past works, the equations of motion of the nonlinear cable were tackled using the MSM directly on the continuous problem, finding good agreement between analytical and numerical results. This study serves as a starting point for the investigation of long cables, which may suffer of more complicated phenomena, and to think to the adoption of vibration control devices, such as NES, to reduce the amplitude of these vibrations as an alternative to existing devices.

Finally, always related to cables, the model-based identification procedure based on the combination of HHT and MSM was applied to the nonlinear cable model, proving effective, while future improvements are envisaged to account for higher-frequency Intrinsic Mode Functions (IMF)which could improve the procedure.

The final chapter of the Thesis was devoted to the use of a ROM, based on the homogenization technique, to three-dimensional frames, with some improvements helping to better represent the behavior of full-scale reinforced concrete three-dimensional frames. Owing to the complexity of the problem and the intentionally reduced complexity of the model, several simplifying assumptions were required as considering rigid floors (in-plane and out-of-plane). Results, in terms of natural frequencies and mode shapes were compared with those derived from the application of OMA algorithms on signals recorded on monitored buildings. This comparison highlighted the limitations of the model in describing full-scale structures, mainly due to the simplifying assumptions adopted, the limited knowledge of the actual mechanical properties and mass distribution of the buildings, and the inability to account for the stiffness contribution of infill walls. Nevertheless, despite all these limitations, results proved encouraging, and it was concluded that a model updating procedure could represent an effective strategy to improve the model response and bring it closer to the actual structural one, without the necessity of recurring to Finite Element Analyses. An updated model could also be employed to investigate the seismic response of the structure from a design perspective.

Finally, after making some considerations on the positioning of sensors on buildings monitored by accelerometers, a tracking of the modal properties of monitored buildings was performed on another structure, revealing a clear seasonal trend, with no additional patterns that could indicate the presence of damage – at least at a global level – in the monitored building.

In conclusion, this Thesis highlights the numerous challenges that still characterize civil engineering structures and that deserve further investigation, particularly with regard to complex phenomena in nonlinear dynamics. The results also confirm the fundamental role of models in describing such phenomena and in guiding the development of effective solutions. While current methodologies increasingly rely on data-driven approaches, building on the remarkable advances achieved in recent years in computational intelligence and data analytics, this perspective, though undoubtedly valuable, should in the author's view be consistently complemented by physics-based models, which ought to represent the backbone of any rigorous analysis.

Bibliography

[1] Decreto-Legge 4 giugno 2013, n. 63. Gazzetta Ufficiale della Repubblica Italiana, 2013. Art. 16.

[2] Decreto-Legge 19 maggio 2020, n. 34. Gazzetta Ufficiale della Repubblica Italiana, 2020. Art. 119.

[3] R. Alaggio, A. Aloisio, E. Antonacci, and R. Cirella. Two-years static and dynamic monitoring of the Santa Maria di Collemaggio basilica. *Construction and Building Materials*, 268:121069, 2021. URL `https://doi.org/10.1016/j.conbuildmat.2020.121069`.

[4] R.J. Allemang. The Modal Assurance Criterion – Twenty Years of Use and Abuse. *Sound & Vibration*, 37(8):14–23, 2003. URL `http://www.sandv.com/downloads/0308alle.pdf`.

[5] R.J. Allemang and D.L. Brown. A Correlation Coefficient for Modal Vector Analysis. In *Proceedings of the 1st International Modal Analysis Conference*, pages 110–116, Orlando, FL, USA, 1982.

[6] S.V. Bakre and R.S. Jangid. Optimum parameters of tuned mass damper for damped main system. *Structural Control and Health Monitoring*, 14(3): 448–470, 2007. URL `https://doi.org/10.1002/stc.166`.

[7] C. Basaglia, D. Camotim, and N. Silvestre. Non-linear GBT formulation for open-section thin-walled members with arbitrary support conditions. *Computers & Structures*, 89(21):1906–1919, 2011. URL `https://doi.org/10.1016/j.compstruc.2011.07.001`. Civil-Comp.

[8] R. Bebiano, D. Camotim, and N. Silvestre. Dynamic analysis of thin-walled members using Generalised Beam Theory (GBT). *Thin-Walled Structures*, 72:188–205, 2013. URL `https://doi.org/10.1016/j.tws.2013.07.004`.

[9] R. Bebiano, R. Gonçalves, and D. Camotim. A cross-section analysis procedure to rationalise and automate the performance of GBT-based structural analyses. *Thin-Walled Structures*, 92:29–47, 2015. URL `https://doi.org/10.1016/j.tws.2015.02.017`.

[10] F. Benedettini, G. Rega, and F. Vestroni. Modal coupling in the free nonplanar finite motion of an elastic cable. *Meccanica*, 21:38–46, 1986. URL `https://doi.org/10.1007/BF01556315`.

[11] F. Benedettini, G. Rega, and R. Alaggio. Non-linear oscillations of a four-degree-of-freedom model of a suspended cable under multiple internal resonance conditions. *Journal of Sound and Vibration*, 182(5):775–798, 1995. URL `https://doi.org/10.1006/jsvi.1995.0232`.

[12] E. Boroson, S. Missoum, P.-O. Mattei, and C. Vergez. Optimization under uncertainty of parallel nonlinear energy sinks. *Journal of Sound and Vibration*, 394:451–464, 2017. URL `https://doi.org/10.1016/j.jsv.2016.12.043`.

[13] R. Brincker, L. Zhang, and P. Andersen. Modal identification of output-only systems using frequency domain decomposition. *Smart Materials and Structures*, 10(3):441–445, jun 2001. URL `https://doi.org/10.1088/0964-1726/10/3/303`.

[14] S.L. Brunton and J.N. Kutz. *Data-Driven Science and Engineering: Machine Learning, Dynamical Systems, and Control*. Cambridge University Press, 2 edition, 2022. URL `https://doi.org/10.1017/9781009089517`.

[15] S.L. Brunton, J.L. Proctor, and J.N. Kutz. Discovering governing equations from data by sparse identification of nonlinear dynamical systems. *Proceedings of the National Academy of Sciences*, 113(15):3932–3937, 2016. URL `https://doi.org/10.1073/pnas.1517384113`.

[16] A. Cabboi, F. Magalhães, C. Gentile, and Á. Cunha. Automated modal identification and tracking: Application to an iron arch bridge. *Structural Control and Health Monitoring*, 24(1):e1854, 2017. URL `https://doi.org/10.1002/stc.1854`.

[17] D. Camotim, N. Silvestre, C. Basaglia, and R. Bebiano. Gbt-based buckling analysis of thin-walled members with non-standard support conditions. *Thin-*

Walled Structures, 46(7-9):800–815, 2008. URL https://doi.org/10.1016/j.tws.2008.01.019.

[18] J. Carr. *Applications of Centre Manifold Theory.*, volume 35. Applied Mathematical Sciences. Springer-Verlag, New York - Heidelberg - Berlin, 1981. URL https://doi.org/10.1007/978-1-4612-5929-9.

[19] G. Carta and F. Stochino. Theoretical models to predict the flexural failure of reinforced concrete beams under blast loads. *Engineering Structures*, 49:306–315, 2013. URL https://doi.org/10.1016/j.engstruct.2012.11.008.

[20] A. Casalotti, A. Arena, and W. Lacarbonara. Mitigation of post-flutter oscillations in suspension bridges by hysteretic tuned mass dampers. *Engineering Structures*, 69:62–71, 2014. URL https://doi.org/10.1016/j.engstruct.2014.03.001.

[21] B. Chen, S.-L. Zhao, and P.-Y. Li. Application of Hilbert-Huang Transform in Structural Health Monitoring: A State-of-the-Art Review. *Mathematical Problems in Engineering*, 2014(1):317954, 2014. URL https://doi.org/10.1155/2014/317954.

[22] W.-L. Chen, Q.-Q. Zhang, H. Li, and H. Hu. An experimental investigation on vortex induced vibration of a flexible inclined cable under a shear flow. *Journal of Fluids and Structures*, 54:297–311, 2015. URL https://doi.org/10.1016/j.jfluidstructs.2014.11.007.

[23] W.-L. Chen, D. Gao, S. Laima, and H. Li. A Field Investigation on Vortex-Induced Vibrations of Stay Cables in a Cable-Stayed Bridge. *Applied Sciences*, 9(21), 2019. URL https://doi.org/10.3390/app9214556.

[24] Y. Chen, Z. Qian, K. Chen, P. Tan, and S. Tesfamariam. Seismic performance of a nonlinear energy sink with negative stiffness and sliding friction. *Structural Control and Health Monitoring*, 26(11):e2437, 2019. URL https://doi.org/10.1002/stc.2437.

[25] M. Corbetta. Application of sparse identification of nonlinear dynamics for physics-informed learning. In *2020 IEEE Aerospace Conference*, pages 1–8, 2020. URL https://doi.org/10.1109/AERO47225.2020.9172386.

[26] C. da Silveira Zanin, A. Ture Savadkoohi, S. Baguet, R. Dufour, and G. Hurel. Nonlinear vibratory energy exchanges in a meta-cell. *International Journal of Non-Linear Mechanics*, 146:104148, 2022. URL `https://doi.org/10.1016/j.ijnonlinmec.2022.104148`.

[27] H.L. Dai, A. Abdelkefi, and L. Wang. Vortex-induced vibrations mitigation through a nonlinear energy sink. *Communications in Nonlinear Science and Numerical Simulation*, 42:22–36, 2017. URL `https://doi.org/10.1016/j.cnsns.2016.05.014`.

[28] F. D'Annibale, M. Ferretti, and A. Luongo. Shear-shear-torsional homogenous beam models for nonlinear periodic beam-like structures. *Engineering Structures*, 184:115–133, 2019. URL `https://doi.org/10.1016/j.engstruct.2019.01.039`.

[29] F. D'Annibale, M. Ferretti, and A. Luongo. Static and Dynamic Responses of Micro-Structured Beams. *Applied Sciences*, 10(19), 2020. URL `https://doi.org/10.3390/app10196836`.

[30] J.M. Davies and P. Leach. Some applications of Generalized Beam Theory., 1992. International Specialty Conference on Cold-Formed Steel Structures. 2.

[31] J.M. Davies and P. Leach. First-order Generalised Beam Theory. *Journal of Constructional Steel Research*, 31(2):187–220, 1994. URL `https://doi.org/10.1016/0143-974X(94)90010-8`.

[32] J.P. Den Hartog. *Mechanical Vibrations.* McGraw-Hill Book Company, New York and London, 1947.

[33] H. Ding and L.-Q. Chen. Designs, analysis, and applications of nonlinear energy sinks. *Nonlinear Dynamics*, 100:3061–3107, 2020. URL `https://doi.org/10.1007/s11071-020-05724-1`.

[34] E.J. Doedel and B.D. Oldeman. *AUTO-07p: Continuation and bifurcation software for ordinary differential equations.* Montreal, Canada, 2007.

[35] M.L. Facchinetti, E. de Langre, and F. Biolley. Coupling of structure and wake oscillators in vortex-induced vibrations. *Journal of Fluids and Structures*, 19(2):123–140, 2004. URL `https://doi.org/10.1016/j.jfluidstructs.2003.12.004`.

[36] C.R. Farrar and K. Worden. *Structural Health Monitoring: A Machine Learning Perspective*. John Wiley & Sons, 2012. URL https://doi.org/10.1002/9781118443118.

[37] M. Feldman. Time-varying vibration decomposition and analysis based on the Hilbert transform. *Journal of Sound and Vibration*, 295(3):518–530, 2006. ISSN 0022-460X. URL https://doi.org/10.1016/j.jsv.2005.12.058.

[38] A. Ferrarotti, G. Piccardo, and A. Luongo. A novel straightforward dynamic approach for the evaluation of extensional modes within GBT 'cross-section analysys'. *Thin-Walled Structures*, 114:52–69, 2017. ISSN 0263-8231. URL https://doi.org/10.1016/j.tws.2017.01.001.

[39] M. Ferretti, D. Zulli, and A. Luongo. A Continuum Approach to the Nonlinear In-Plane Galloping of Shallow Flexible Cables. *Advances in Mathematical Physics*, 2019(1):6865730, 2019. URL https://doi.org/10.1155/2019/6865730.

[40] M. Ferretti, F. D'Annibale, and A. Luongo. Modeling beam-like planar structures by a one-dimensional continuum: an analytical-numerical method. *Journal of Applied and Computational Mechanics*, 7(Special Issue):1020–1033, 2021. URL https://doi.org/10.22055/jacm.2020.33100.2150.

[41] H. Frahm. Device for damping vibrations of bodies. *US Patent 989,958*, 1911.

[42] Y. Fujino and M. Abé. Design formulas for tuned mass dampers based on A perturbation technique. *Earthquake Engineering & Structural Dynamics*, 22 (10):833–854, 1993. URL https://doi.org/10.1002/eqe.4290221002.

[43] A. Gallet, S. Rigby, T.N. Tallman, X. Kong, I. Hajirasouliha, A. Liew, D. Liu, L. Chen, A. Hauptmann, and D. Smyl. Structural engineering from an inverse problems perspective. *Proceeding of the Royal Society A: Mathematical, Physical and Engineering Sciences*, 478:20210526, 2022. URL https://doi.org/10.1098/rspa.2021.0526.

[44] V. Gattulli, F. Di Fabio, and A. Luongo. Simple and double Hopf bifurcations in aeroelastic oscillators with tuned mass dampers. *Journal of the Franklin Institute*, 338(2):187–201, 2001. URL https://doi.org/10.1016/S0016-0032(00)00077-6.

[45] O.V. Gendelman and Y. Starosvetsky. Quasi-Periodic Response Regimes of Linear Oscillator Coupled to Nonlinear Energy Sink Under Periodic Forcing. *Journal of Applied Mechanics*, 74(2):325–331, 2006. URL https://doi.org/10.1115/1.2198546.

[46] O.V. Gendelman, L.I. Manevitch, A.F. Vakakis, and R. M'Closkey. Energy Pumping in Nonlinear Mechanical Oscillators: Part I—Dynamics of the Underlying Hamiltonian Systems. *Journal of Applied Mechanics*, 68(1):34–41, 2000. URL https://doi.org/10.1115/1.1345524.

[47] O.V. Gendelman, Y. Starosvetsky, and M. Feldman. Attractors of harmonically forced linear oscillator with attached nonlinear energy sink I: Description of response regimes. *Nonlinear Dynamics*, 51:31–46, 2008. URL https://doi.org/10.1007/s11071-006-9167-0.

[48] F. Georgiades and A.F. Vakakis. Dynamics of a linear beam with an attached local nonlinear energy sink. *Communications in Nonlinear Science and Numerical Simulation*, 12(5):643–651, 2007. URL https://doi.org/10.1016/j.cnsns.2005.07.003.

[49] R. Gonçalves, D. Camotim, C. Basaglia, A.D. Martins, and N. Peres. Latest developments on the analysis of thin-walled structures using Generalised Beam Theory (GBT). *Journal of Constructional Steel Research*, 204:107858, 2023. URL https://doi.org/10.1016/j.jcsr.2023.107858.

[50] E. Gourdon and C.-H. Lamarque. Energy Pumping with Various Nonlinear Structures: Numerical Evidences. *Nonlinear Dynamics*, 40:281–307, 2005. URL https://doi.org/10.1007/s11071-005-6610-6.

[51] H. Guo, T. Yang, Y. Chen, and L.-Q. Chen. Singularity analysis on vibration reduction of a nonlinear energy sink system. *Mechanical Systems and Signal Processing*, 173:109074, 2022. URL https://doi.org/10.1016/j.ymssp.2022.109074.

[52] T. Guo and G. Rega. Direct and discretized perturbations revisited: A new error source interpretation, with application to moving boundary problem. *European Journal of Mechanics - A/Solids*, 81:103936, 2020. URL https://doi.org/10.1016/j.euromechsol.2019.103936.

[53] R.T. Hartlen and I.G. Currie. Lift-Oscillator Model of Vortex-Induced Vibration. *Journal of the Engineering Mechanics Division*, 96(5):577–591, 1970. URL https://doi.org/10.1061/JMCEA3.0001276.

[54] H. Hasani and F. Freddi. Operational Modal Analysis on Bridges: A Comprehensive Review. *Infrastructures*, 8(12), 2023. URL https://doi.org/10.3390/infrastructures8120172.

[55] N.E. Huang, Z. Shen, S.R. Long, M.C. Wu, H.H. Shih, Q. Zheng, N.-C. Yen, C.C. Tung, and H.H Liu. The empirical mode decomposition and the Hilbert spectrum for nonlinear and non-stationary time series analysis. *Proceeding of the Royal Society A: Mathematical, Physical and Engineering Sciences*, 454: 903–995, 1998. URL https://doi.org/10.1098/rspa.1998.0193.

[56] G. Hurel, A. Ture Savadkoohi, and C.-H. Lamarque. Nonlinear Vibratory Energy Exchanges between a Two-Degree-of-Freedom Pendulum and a Nonlinear Absorber. *Journal of Engineering Mechanics*, 145(8):04019058, 2019. URL https://doi.org/10.1061/(ASCE)EM.1943-7889.0001620.

[57] G. Hurel, A. Ture Savadkoohi, and C.-H. Lamarque. Passive control of a two degrees-of-freedom pendulum by a non-smooth absorber. *Nonlinear dynamics*, 98:3025–3036, 2019. URL https://doi.org/10.1007/s11071-019-04891-0.

[58] P. Ibáñez. Identification of dynamic parameters of linear and non-linear structural models from experimental data. *Nuclear Engineering and Design*, 25(1): 30–41, 1973. URL https://doi.org/10.1016/0029-5493(73)90059-9.

[59] T. Ioi and K. Ikeda. On the Dynamic Vibration Damped Absorber of the Vibration System. *Bulletin of JSME*, 21(151):64–71, 1978. URL https://doi.org/10.1299/jsme1958.21.64.

[60] H. M. Irvine and T. K. Caughey. The linear theory of free vibrations of a suspended cable. *Proceedings of the Royal Society of London. A. Mathematical and Physical Sciences*, 341(1626):299–315, 1974. URL https://doi.org/10.1098/rspa.1974.0189.

[61] H.M. Irvine. *Cable Structures*. MIT Press, Cambridge, MA, 1981.

[62] M. Jafari, F. Hou, and A. Abdelkefi. Wind-induced vibration of structural

cables. *Nonlinear Dynamics*, 100:351–421, 2020. URL https://doi.org/10.1007/s11071-020-05541-6.

[63] B. Jaishi and W.-X. Ren. Structural Finite Element Model Updating Using Ambient Vibration Test Results. *Journal of Structural Engineering*, 131(4):617–628, 2005. URL https://doi.org/10.1061/(ASCE)0733-9445(2005)131:4(617).

[64] G. Kerschen, K. Worden, A.F. Vakakis, and J.-C. Golinval. Past, present and future of nonlinear system identification in structural dynamics. *Mechanical Systems and Signal Processing*, 20(3):505–592, 2006. URL https://doi.org/10.1016/j.ymssp.2005.04.008.

[65] G. Kerschen, A.F. Vakakis, Y.S. Lee, D.M. McFarland, and L.A. Bergman. Toward a Fundamental Understanding of the Hilbert-Huang Transform in Nonlinear Structural Dynamics. *Journal of Vibration and Control*, 14(1-2):77–105, 2008. URL https://doi.org/10.1177/1077546307079381.

[66] S. Kim, S. Kim, and H.-K. Kim. High-mode vortex-induced vibration of stay cables: monitoring, cause investigation, and mitigation. *Journal of Sound and Vibration*, 524:116758, 2022. URL https://doi.org/10.1016/j.jsv.2022.116758.

[67] W.-J. Kim and N.C. Perkins. Two-Dimensional Vortex-Induced Vibration of Cable Suspension. *Journal of Fluids and Structures*, 16(2):229–245, 2002. URL https://doi.org/10.1006/jfls.2001.0418.

[68] R.J. Kuether, L. Renson, T. Detroux, C. Grappasonni, G. Kerschen, and M.S. Allen. Nonlinear normal modes, modal interactions and isolated resonance curves. *Journal of Sound and Vibration*, 351:299–310, 2015. URL https://doi.org/10.1016/j.jsv.2015.04.035.

[69] W. Lacarbonara. *Nonlinear Structural Mechanics. Theory, Dynamical Phenomena and Modeling.* Springer, New York, 2013. URL https://doi.org/10.1007/978-1-4419-1276-3.

[70] W. Lacarbonara and A. Pacitti. Nonlinear Modeling of Cables with Flexural Stiffness. *Mathematical Problems in Engineering*, 2008(1):370767, 2008. URL https://doi.org/10.1155/2008/370767.

[71] C.-H. Lamarque, O.V. Gendelman, A. Ture Savadkoohi, and E. Etcheverria. Targeted energy transfer in mechanical systems by means of non-smooth nonlinear energy sink. *Acta Mechanica*, 221:175–200, 2011. URL https://doi.org/10.1007/s00707-011-0492-0.

[72] J. Latalski and D. Zulli. Generalized Beam Theory for Thin-Walled Beams with Curvilinear Open Cross-Sections. *Applied Sciences*, 10(21), 2020. URL https://doi.org/10.3390/app10217802.

[73] S. Lenci and G. Rega. Nonlinear Free Vibrations of Planar Elastic Beams: A Unified Treatment of Geometrical and Mechanical Effects. *Procedia IUTAM*, 19:35–42, 2016. URL https://doi.org/10.1016/j.piutam.2016.03.007. IUTAM Symposium Analytical Methods in Nonlinear Dynamics.

[74] L. Leroux, S. Langlois, and A. Ture Savadkoohi. Investigation of a nonlinear control of galloping with a linear beam with elastic boundary conditions. *International Journal of Non-Linear Mechanics*, 156:104484, 2023. URL https://doi.org/10.1016/j.ijnonlinmec.2023.104484.

[75] A. Lubrano Lobianco, M. Del Zoppo, C. Rainieri, G. Fabbrocino, and M. Di Ludovico. Damage Estimation of Full-Scale Infilled RC Frames under Pseudo-Dynamic Excitation by Means of Output-Only Modal Identification. *Buildings*, 13(4), 2023. URL https://doi.org/10.3390/buildings13040948.

[76] A. Luongo. Analisi del comportamento strutturale sotto carichi di esercizio degli impalcati di n. sette viadotti dell'autostrada A24 ubicati nella provincia di Teramo. *Relazione Generale*, 1/RG, 2019.

[77] A. Luongo and D. Zulli. Dynamic analysis of externally excited NES-controlled systems via a mixed Multiple Scale/Harmonic Balance algorithm. *Nonlinear Dynamics*, 70:2049–2061, 2012. URL https://doi.org/10.1007/s11071-012-0597-6.

[78] A. Luongo and D. Zulli. *Mathematical Models of Beams and Cables*. John Wiley & Sons, 2013. URL https://doi.org/10.1002/9781118577554.

[79] A. Luongo and D. Zulli. Aeroelastic instability analysis of NES-controlled systems via a mixed multiple scale/harmonic balance method. *Journal of Vibra-*

tion and Control, 20(13):1985–1998, 2014. URL `https://doi.org/10.1177/1077546313480542`.

[80] A. Luongo and D. Zulli. Nonlinear energy sink to control elastic strings: the internal resonance case. *Nonlinear Dynamics*, 81:425–435, 2015. URL `https://doi.org/10.1007/s11071-015-2002-8`.

[81] A. Luongo and D. Zulli. Free and forced linear dynamics of a homogeneous model for beam-like structures. *Meccanica*, 55:907–925, 2020. URL `https://doi.org/10.1007/s11012-019-01070-8`.

[82] A. Luongo, G. Rega, and F. Vestroni. Monofrequent oscillations of a non-linear model of a suspended cable. *Journal of Sound and Vibration*, 82(2): 247–259, 1982. URL `https://doi.org/10.1016/0022-460X(82)90533-8`.

[83] A. Luongo, G. Rega, and F. Vestroni. Planar non-linear free vibrations of an elastic cable. *International Journal of Non-Linear Mechanics*, 19(1):39–52, 1984. URL `https://doi.org/10.1016/0020-7462(84)90017-9`.

[84] A. Luongo, G. Rega, and F. Vestroni. On Nonlinear Dynamics of Planar Shear Indeformable Beams. *Journal of Applied Mechanics*, 53(3):619–624, 1986. URL `https://doi.org/10.1115/1.3171821`.

[85] A. Luongo, D. Zulli, M. Ferretti, and F. D'Annibale. *Perturbation Methods and Nonlinear Phenomena: Applications to Continuous Mechanical Systems*. Springer, Cham, 2024. URL `https://doi.org/10.1007/978-3-031-49397-3`.

[86] F. Magalhães, Á. Cunha, and E. Caetano. Online automatic identification of the modal parameters of a long span arch bridge. *Mechanical Systems and Signal Processing*, 23(2):316–329, 2009. URL `https://doi.org/10.1016/j.ymssp.2008.05.003`.

[87] L.I. Manevitch. The Description of Localized Normal Modes in a Chain of Nonlinear Coupled Oscillators Using Complex Variables. *Nonlinear Dynamics*, 25:95–109, 2001. URL `https://doi.org/10.1023/A:1012994430793`.

[88] Matlab. *The MathWorks Inc. MATLAB version R2023b*. The MathWorks Inc., Natick, Massachusetts, United States, 2023.

[89] D.M. McFarland, L.A. Bergman, and A.F. Vakakis. Experimental study of non-linear energy pumping occurring at a single fast frequency. *International Journal of Non-Linear Mechanics*, 40(6):891–899, 2005. URL `https://doi.org/10.1016/j.ijnonlinmec.2004.11.001`.

[90] A. Mehmood, A.H. Nayfeh, and M.R. Hajj. Effects of a non-linear energy sink (NES) on vortex-induced vibrations of a circular cylinder. *Nonlinear Dynamics*, 77(3):667–680, 2014. URL `https://doi.org/10.1007/s11071-014-1329-x`.

[91] L. Mi and O. Gottlieb. Asymptotic model-based estimation of a wake oscillator for a tethered sphere in uniform flow. *Journal of Fluids and Structures*, 54:361–389, 2015. URL `https://doi.org/10.1016/j.jfluidstructs.2014.11.012`.

[92] M. Morell, E. Gourdon, M. Collet, A. Ture Savadkoohi, E. De Bono, and C.-H. Lamarque. Towards digitally programmed nonlinear electroacoustic resonators for low amplitude sound pressure levels: Modeling and experiments. *Journal of Sound and Vibration*, 584:118437, 2024. URL `https://doi.org/10.1016/j.jsv.2024.118437`.

[93] G. Mu, W. Zhu, and M. Deng. Random vortex induced vibration response of suspended flexible cable to fluctuating wind. *Applied Mathematics and Mechanics (English Edition)*, 44(12):2207–2226, 2023. URL `https://doi.org/10.1007/s10483-023-3058-8`.

[94] A.H. Nayfeh and W. Lacarbonara. On the Discretization of Distributed-Parameter Systems with Quadratic and Cubic Nonlinearities. *Nonlinear Dynamics*, 13(3):203–220, 1997. URL `https://doi.org/10.1023/A:1008253901255`.

[95] A.H. Nayfeh and D.T. Mook. *Nonlinear Oscillations.* John Wiley & Sons, New York, 1995.

[96] V. Nicoletti, D. Arezzo, S. Carbonari, and F. Gara. Dynamic monitoring of buildings as a diagnostic tool during construction phases. *Journal of Building Engineering*, 46:103764, 2022. URL `https://doi.org/10.1016/j.jobe.2021.103764`.

[97] J.P. Noël and G. Kerschen. Nonlinear system identification in structural dynamics: 10 more years of progress. *Mechanical Systems and Signal Processing*, 83:2–35, 2017. URL https://doi.org/10.1016/j.ymssp.2016.07.020.

[98] N. Novelli, P. Belardinelli, and S. Lenci. Identification of hybrid dynamic systems via a sparse regression algorithm. *Nonlinear Dynamics*, 113:20565–20588, 2025. URL https://doi.org/10.1007/s11071-025-11253-6.

[99] V. Ondra, I.A. Sever, and C.W. Schwingshackl. Non-linear System Identification Using the Hilbert-Huang Transform and Complex Non-linear Modal Analysis. In Gaetan Kerschen, editor, *Nonlinear Dynamics, Volume 1*, pages 77–86, Cham, 2017. Springer. URL https://doi.org/10.1007/978-3-319-54404-5_8.

[100] V. Ondra, I.A. Sever, and C.W. Schwingshackl. Identification of complex non-linear modes of mechanical systems using the Hilbert-Huang Transform from free decay responses. *Journal of Sound and Vibration*, 495:115912, 2021. URL https://doi.org/10.1016/j.jsv.2020.115912.

[101] P.F. Pai and A.N. Palazotto. Detection and identification of nonlinearities by amplitude and frequency modulation analysis. *Mechanical Systems and Signal Processing*, 22(5):1107–1132, 2008. URL https://doi.org/10.1016/j.ymssp.2007.11.006.

[102] T.S. Parker and L.O. Chua. *Practical Numerical Algorithms for Chaotic Systems*. Springer, New York, 1989. URL https://doi.org/10.1007/978-1-4612-3486-9.

[103] B. Peeters and G. De Roeck. *System Identification and Damage Detection in Civil Engineering*. PhD thesis, Katholieke Universiteit Leuven, 2000.

[104] N.C. Perkins. Modal interactions in the non-linear response of elastic cables under parametric/external excitation. *International Journal of Non-Linear Mechanics*, 27(2):233–250, 1992. URL https://doi.org/10.1016/0020-7462(92)90083-J.

[105] G. Piccardo, G. Ranzi, and A. Luongo. A complete dynamic approach to the Generalized Beam Theory cross-section analysis including extension and

shear modes. *Mathematics and Mechanics of Solids*, 19(8):900–924, 2013. URL `https://doi.org/10.1177/1081286513493107`.

[106] G. Piccardo, G. Ranzi, and A. Luongo. A direct approach for the evaluation of the conventional modes within the GBT formulation. *Thin-Walled Structures*, 74:133–145, 2014. URL `https://doi.org/10.1016/j.tws.2013.09.008`.

[107] G. Piccardo, A. Ferrarotti, and A. Luongo. Nonlinear Generalized Beam Theory for open thin-walled members. *Mathematics and Mechanics of Solids*, 22 (10):1907–1921, 2017. URL `https://doi.org/10.1177/1081286516649990`.

[108] G. Piccardo, F. Tubino, and A. Luongo. Equivalent Timoshenko linear beam model for the static and dynamic analysis of tower buildings. *Applied Mathematical Modelling*, 71:77–95, 2019. URL `https://doi.org/10.1016/j.apm.2019.02.005`.

[109] G. Ranzi and A. Luongo. A new approach for thin-walled member analysis in the framework of GBT. *Thin-Walled Structures*, 49(11):1404–1411, 2011. URL `https://doi.org/10.1016/j.tws.2011.06.008`.

[110] G. Rega. Nonlinear vibrations of suspended cables—Part II: Deterministic phenomena. *Applied Mechanics Reviews*, 57(6):479–514, 2005. URL `https://doi.org/10.1115/1.1777225`.

[111] G. Rega. Nonlinear vibrations of suspended cables—Part I: Modeling and analysis. *Applied Mechanics Reviews*, 57(6):443–478, 2005. URL `https://doi.org/10.1115/1.1777224`.

[112] G. Rega and A. Luongo. Natural vibrations of suspended cables with flexible supports. *Computers & Structures*, 12(1):65–75, 1980. URL `https://doi.org/10.1016/0045-7949(80)90094-2`.

[113] G. Rega, W. Lacarbonara, A.H. Nayfeh, and C.M. Chin. Multiple resonances in suspended cables: direct versus reduced-order models. *International Journal of Non-Linear Mechanics*, 34(5):901–924, 1999. URL `https://doi.org/10.1016/S0020-7462(98)00065-1`.

[114] E. Reynders and G. De Roeck. Reference-based combined deterministic–stochastic subspace identification for experimental and operational modal

analysis. *Mechanical Systems and Signal Processing*, 22(3):617–637, 2008. URL https://doi.org/10.1016/j.ymssp.2007.09.004.

[115] R.E. Roberson. Synthesis of a nonlinear dynamic vibration absorber. *Journal of the Franklin Institute*, 254(3):205–220, 1952. URL https://doi.org/10.1016/0016-0032(52)90457-2.

[116] L. Rosafalco, P. Conti, A. Manzoni, S. Mariani, and A. Frangi. Online learning in bifurcating dynamic systems via SINDy and Kalman filtering. *Nonlinear Dynamics*, 113:14201–14221, 2025. URL https://doi.org/10.1007/s11071-025-11029-y.

[117] N. Roveri and A. Carcaterra. Damage detection in structures under traveling loads by Hilbert–Huang transform. *Mechanical Systems and Signal Processing*, 28:128–144, 2012. URL https://doi.org/10.1016/j.ymssp.2011.06.018.

[118] A.S. Saeed, R. Abdul Nasar, and M.A. AL-Shudeifat. A review on nonlinear energy sinks: designs, analysis and applications of impact and rotary types. *Nonlinear Dynamics*, 111:1–37, 2023. URL https://doi.org/10.1007/s11071-022-08094-y.

[119] R. Schardt. Eine Erweiterung der Technischen Biegetheorie zur Berechnung prismatischer Faltwerke. *Der Stahlbau*, 35:161–171, 1966. (In German).

[120] R. Schardt. Generalized beam theory—an adequate method for coupled stability problems. *Thin-Walled Structures*, 19(2):161–180, 1994. URL https://doi.org/10.1016/0263-8231(94)90027-2.

[121] F. Scozzese and A. Dall'Asta. Nonlinear Response Characterization of Post-Tensioned R.C. Bridges through Hilbert–Huang Transform Analysis. *Structural Control and Health Monitoring*, 2024(1):5960162, 2024. URL https://doi.org/10.1155/2024/5960162.

[122] N. Silvestre and D. Camotim. First-order generalised beam theory for arbitrary orthotropic materials. *Thin-Walled Structures*, 40(9):755–789, 2002. URL https://doi.org/10.1016/S0263-8231(02)00025-3.

[123] N. Silvestre and D. Camotim. Second-order generalised beam theory for arbitrary orthotropic materials. *Thin-Walled Structures*, 40(9):791–820, 2002. ISSN 0263-8231. URL https://doi.org/10.1016/S0263-8231(02)00026-5.

[124] N. Silvestre and D. Camotim. Nonlinear Generalized Beam Theory for Cold-formed Steel Members. *International Journal of Structural Stability and Dynamics*, 3(4):461–490, 2003. URL https://doi.org/10.1142/S0219455403001002.

[125] R.A. Skop and S. Balasubramanian. A New Twist on an Old Model for Vortex-Excited Vibrations. *Journal of Fluids and Structures*, 11(4):395–412, 1997. URL https://doi.org/10.1006/jfls.1997.0085.

[126] G. Stabile, H.G. Matthies, and C. Borri. A novel reduced order model for vortex induced vibrations of long flexible cylinders. *Ocean Engineering*, 156: 191–207, 2018. URL https://doi.org/10.1016/j.oceaneng.2018.02.064.

[127] Y. Starosvetsky and O.V. Gendleman. Strongly modulated response in forced 2DOF oscillatory system with essential mass and potential asymmetry. *Physica D: Nonlinear Phenomena*, 237(13):1719–1733, 2008. URL https://doi.org/10.1016/j.physd.2008.01.019.

[128] Y. Starosvetsky and O.V. Gendleman. Response regimes in forced system with non-linear energy sink: quasi-periodic and random forcing. *Nonlinear Dynamics*, 64:177–195, 2011. URL https://doi.org/10.1007/s11071-010-9856-6.

[129] Y. Tamura. Mathematical models for understanding phenomena: Vortex-induced vibrations. *Japan Architectural Review*, 3(4):398–422, 2020. URL https://doi.org/10.1002/2475-8876.12180.

[130] M.S. Triantafyllou, R. Gopalkrishnan, and M.A. Grosenbaugh. Vortex-Induced Vibrations in a Sheared Flow: A New Predictive Method. In E. Naudascher and D. Rockwell, editors, *Flow-Induced Vibrations: An Engineering Guide*, chapter 4, pages 129–146. CRC Press, 1994. URL https://doi.org/10.1201/9780203751503-4.

[131] H. Troger and A. Steindl. *Nonlinear Stability and Bifurcation Theory. An Introduction for Engineers and Applied Scientists*. Springer, Wien, 1991. URL https://doi.org/10.1007/978-3-7091-9168-2.

[132] A. Ture Savadkoohi, C.-H. Lamarque, M. Weiss, B. Vaurigaud, and S. Charlemagne. Analysis of the 1:1 resonant energy exchanges between coupled os-

cillators with rheologies. *Nonlinear Dynamics*, 86(4):2145–2159, 2016. URL https://doi.org/10.1007/s11071-016-2792-3.

[133] Computers & Structures, Inc. v26. *CSI Analysis Reference Manual For SAP2000®, ETABS®, SAFE® and CSiBridge®*. Berkeley, California, United States, 2025.

[134] A.F. Vakakis, O.V. Gendelman, L.A. Bergman, D.M. McFarland, G. Kerschen, and Y.S. Lee. *Nonlinear targeted energy transfer in mechanical and structural systems I & II*. Springer, Germany, 2008.

[135] P. van Overschee and B. De Moor. *Subspace Identification for Linear Systems*. Springer, New York, 1996. URL https://doi.org/10.1007/978-1-4613-0465-4.

[136] B. Vaurigaud, A. Ture Savadkoohi, and C.-H. Lamarque. Targeted energy transfer with parallel nonlinear energy sinks. Part I: Design theory and numerical results. *Nonlinear Dynamics*, 66:763–780, 2011. URL https://doi.org/10.1007/s11071-011-9949-x.

[137] R. Violette, E. de Langre, and J. Szydlowski. Computation of vortex-induced vibrations of long structures using a wake oscillator model: Comparison with DNS and experiments. *Computers & Structures*, 85(11):1134–1141, 2007. URL https://doi.org/10.1016/j.compstruc.2006.08.005. Fourth MIT Conference on Computational Fluid and Solid Mechanics.

[138] A.-P. Wang, R.-F. Fung, and S.-C. Huang. Dynamic analysis of a tall building with a tuned-mass-damper device subjected to earthquake excitations. *Journal of Sound and Vibration*, 244(1):123–136, 2001. URL https://doi.org/10.1006/jsvi.2000.3480.

[139] D. Wang, Z. Hao, E. Pavlovskaia, and M. Wiercigroch. Bifurcation analysis of vortex-induced vibration of low-dimensional models of marine risers. *Nonlinear Dynamics*, 106:147–167, 2021. URL https://doi.org/10.1007/s11071-021-06808-2.

[140] Y. Wang, H. Kang, Y. Cong, T. Guo, and W. Zhu. Vibration suppression of a cable under harmonic excitation by a nonlinear energy sink. *Commu-*

nications in Nonlinear Science and Numerical Simulation, 117:106988, 2023. URL https://doi.org/10.1016/j.cnsns.2022.106988.

[141] P. Welch. The use of fast Fourier transform for the estimation of power spectra: A method based on time averaging over short, modified periodograms. *IEEE Transactions on Audio and Electroacoustics*, 15(2):70–73, 1967. URL https://doi.org/10.1109/TAU.1967.1161901.

[142] S. Wiggins. *Introduction to Applied Nonlinear Dynamical Systems and Chaos*. Springer, New York, 2003. URL https://doi.org/10.1007/b97481.

[143] K. Worden and G.R. Tomlinson. *Nonlinearity in Structural Dynamics: Detection, Identification and Modelling*. CRC Press, Bristol, UK, 2001.

[144] X. Wu, F. Ge, and Y. Hong. A review of recent studies on vortex-induced vibrations of long slender cylinders. *Journal of Fluids and Structures*, 28:292–308, 2012. URL https://doi.org/10.1016/j.jfluidstructs.2011.11.010.

[145] K. Xu, Y. Ge, and D. Zhang. Wake oscillator model for assessment of vortex-induced vibration of flexible structures under wind action. *Journal of Wind Engineering and Industrial Aerodynamics*, 136:192–200, 2015. URL https://doi.org/10.1016/j.jweia.2014.11.002.

[146] Y.B. Yang, J.D. Yau, and Y.S. Wu. *Vehicle–Bridge Interaction Dynamics*. World Scientific, 2004.

[147] J. Zhang, Z. Feng, J. Dai, Y. Wang, X. Hua, and W.-J. Yan. Bayesian Approach for Damping Identification of Stay Cables Under Vortex-Induced Vibrations. *Structural Control and Health Monitoring*, 2025(1):5532528, 2025. URL https://doi.org/10.1155/stc/5532528.

[148] M. Zhang, T. Wu, and O. Øiseth. Vortex-induced vibration control of a flexible circular cylinder using a nonlinear energy sink. *Journal of Wind Engineering and Industrial Aerodynamics*, 229:105163, 2022. URL https://doi.org/10.1016/j.jweia.2022.105163.

[149] Y.-W. Zhang, S. Hou, Z. Zhang, J. Zang, Z.-Y. Ni, Y.-Y. Teng, and L.-Q. Chen. Nonlinear vibration absorption of laminated composite beams in complex environment. *Nonlinear Dynamics*, 99:2605–2622, 2020. URL https://doi.org/10.1007/s11071-019-05442-3.

[150] D. Zulli and A. Luongo. Non linear energy sink to control vibrations of an internally non resonant elastic string. *Meccanica*, 50:781–794, 2015. URL https://doi.org/10.1007/s11012-014-0057-0.

[151] D. Zulli and A. Luongo. Control of primary and subharmonic resonances of a Duffing oscillator via non-linear energy sink. *International Journal of Non-Linear Mechanics*, 80:170–182, 2016. URL https://doi.org/10.1016/j.ijnonlinmec.2015.08.014.

List of Terms

AME Amplitude Modulation Equation. 87, 90–92, 94–98, 102, 104, 117, 129, 130, 136, 141, 216

b.c. boundary conditions. 7, 98

CS1 Building case study number 1. 160, 163, 164, 166, 170, 175

CS2 Building case study number 2. 163, 170, 173, 175

Cx-A Complexification-Averaging Method. 14, 63, 83, 86, 89, 101–104, 108, 117, 215–217

d.o.f. degree(s)-of-freedom. 28, 31, 34, 87, 89, 91, 101–103, 108, 159, 175, 215–217

EMD Empirical Mode Decomposition. 84, 85, 108

FBA Force Balance Accelerometers. 57, 58, 164, 170

FD Finite Differences. 34, 39, 154, 156, 158, 175

FDD Frequency Domain Decomposition. 58, 59, 117

FE Finite Elements. 2, 11, 12, 17–19, 28, 34, 40, 42, 46–48, 50, 52, 56, 168, 169

FEA Finite Element Analysis. 2, 6, 29, 39, 41

FRC Frequency Responce Curve. 70, 71, 74, 75, 130, 131, 138

GBT Generalized Beam Theory. 7, 10–12, 14, 19–24, 28, 40, 61, 63, 115, 116

GBT-D GBT with complete dynamic approach in cross-section analysis. 7, 11, 12, 14, 20–23, 28, 39, 46–48, 50, 52–57, 60, 62, 63, 78, 83, 115–117, 177–179

HHT Hilbert-Huang Transform. 7, 13, 19, 20, 83, 84, 86, 88, 91, 92, 96, 98, 101, 104, 105, 108, 110, 117, 118, 140, 142, 143, 145, 179, 216

HT Hilbert Transform. 84, 85

i.c. initial conditions. 74, 75, 88, 90, 92, 93, 95, 101, 102, 138, 143, 216, 217

IMF Intrinsic Mode Functions. 84, 85, 92, 96, 108, 143, 146, 179

MA1 Member analysis with analytical solution. 34, 35, 39, 48, 64, 71

MA2 Member analysis with finite differences. 34, 39, 48

MA3 Member analysis with finite elements. 35, 39, 40, 48, 50

MAC Modal Assurance Criterion. 49, 50, 52, 58, 59, 62, 167, 169, 173

MEMS Micro-ElectroMechanical Systems. 164, 170

MSM Multiple Scale Method. 6–8, 13, 15–17, 19, 20, 66, 83, 84, 86, 88, 89, 96, 98, 99, 101, 104, 105, 108, 110, 117, 118, 120, 126, 134, 139, 140, 142–145, 177, 179

NES Nonlinear Energy Sink. 7, 14, 19, 20, 63–65, 68, 71, 72, 74–76, 78, 80–82, 117, 118, 120, 133, 140, 145, 177–179

OMA Operational Modal Analysis. 7, 8, 12, 17–20, 58–60, 117, 145, 147, 148, 163, 166–168, 170, 173, 175, 177–179

PEP Planar Eigenvalue Problem. 28, 30, 32–34, 45, 46

PGA Peak Ground Acceleration. 82, 164, 170

PSD Power Spectral Density. 58, 59

ROM Reduced-Order Models. 2, 3, 19, 21, 22, 177–179

SHM Structural Health Monitoring. 2, 3, 10, 12, 13, 117

SIM Slow Invariant Manifold. 67–70, 74, 75, 78

SSI Stochastic Subspace Identification. 58, 59

SSI-COV Covariance-driven SSI. 59, 117, 163, 165, 175

SVD Singular Value Decomposition. 58, 59

TMD Tuned Mass Damper. 14, 63, 80

TWB Thin-Walled Beams. 7, 10, 11, 14, 19–21, 24, 36, 38, 40, 46, 48, 63, 84, 115, 117, 177, 178

VIV Vortex-Induced Vibrations. 8, 16, 17, 119, 120, 133, 139, 144, 145, 177–179

WEP Warping Eigenvalue Problem. 28, 33, 34, 45, 46

[Blank page]

List of Symbols

Since many symbols appear in the Thesis, they are here resumed to improve the readability of the text. In addition, an indication of the section where each of them is introduced for the first time in each chapter is given.

a, a_k, a_{x_k}	amplitudes of signals in polar form	(3.5-4.2)
$\hat{a}, \hat{b}$	initial conditions of the 1-d.o.f. system	(3.5)
$\hat{a}_k, \hat{b}_k$	initial conditions on the modal basis	(3.5-4.4)
$\mathbf{a}_{n_j}, \mathbf{b}_{n_j}$	unknown constants for $\boldsymbol{\varphi}(z)$ and $\boldsymbol{\Psi}(z)$ in MA1	(3.2)
$\mathbf{a}_t, \mathbf{a}_n, \mathbf{a}_b$	orthonormal basis of the cable in the current configuration	(4.2)
$\bar{\mathbf{a}}_t, \bar{\mathbf{a}}_n, \bar{\mathbf{a}}_b$	orthonormal basis of the cable in the reference configuration	(4.2)
$\mathbf{a}_x, \mathbf{a}_y, \mathbf{a}_z$	orthonormal basis of the equivalent Timoshenko beam	(5.2)
A, A_k	amplitude of the generating solution with MSM	(3.5-4.2)
A	amplitude of the load acting on the wake oscillator	(4.3)
A_b, A_c	areas in the moment-curvature relationships	(3.5)
A_e, h_e, I_e, L_e	geometric properties of the cross-section elements	(3.2)
A_i, A_{iy}, A_{iz}	area and shear areas of column i	(5.2)
$\mathbf{A}$	matrix of coefficients in the parameter identification	(3.5-4.4)
$\mathbf{A}_{FE}, \mathbf{A}_{FE,M}, \mathbf{A}_{FE,S}$	total, master and slave coefficient matrices in MA3	(3.2)
$\mathbf{A}_i, \mathbf{A}_{iM}, \mathbf{A}_{iS}$	total, master and slave coefficient matrices in the 1^{st} PEP	(3.2)
b_1	characteristic length of the beam equipped with NES	(3.4)
$\mathbf{b}$	known terms in the parameter identification	(3.5-4.4)
B_{iy}, B_{iz}	bending stiffness coefficients of column i	(5.2)
B^e_{hk}, B^f_{hk}	extensional and flexural stiffness components of the cross-section	(3.2)
B_y, B_z, B_{yz}	bending stiffness coefficients of the equivalent Timoshenko beam	(5.2)
$\mathbf{B}^e, \mathbf{B}^f$	extensional and flexural stiffness matrices of the cross-section	(3.2)
c, c_1, c_2, c_{12}	damping coefficients of discrete and continuous systems	(3.5)
c_e	linear external damping on the cable	(4.2)
c_F	damping added by wind on the cable	(4.3)
c_i	viscous damping coefficients with $i = u, v, w, \theta x, \theta y, \theta z$	(5.2)
c_{L0}	reference lift coefficient	(4.3)

c_N	damping of the NES	(3.4)
$\bar{c}_1, \bar{c}_2, \bar{c}_3$	coefficients of the second order equation of σ	(3.4)
$\mathbf{c}$	external couples (and inertia terms) with components c_x, c_y, c_z	(5.2)
C	torsional stiffness coefficient of the equivalent Timoshenko beam	(5.2)
C^a_{hk}, C^f_{hk}	axial and flexural stiffness components of the cross-section	(3.2)
C_i	torsional stiffness coefficient of column i	(5.2)
$C_j, \hat{C}_j$	damping coefficient of mode j of the beam	(3.4)
$\mathbf{C}$	damping matrix in the homogenization technique	(5.2)
$\mathbf{C}^a, \mathbf{C}^f$	axial and flexural stiffness matrices of the cross-section	(3.2)
$\mathcal{C}$	middle line at the end cross-sections of TWB	(3.2)
$\mathcal{C}, \bar{\mathcal{C}}$	current and reference configurations of the cable	(4.2)
d	sag of the suspended cable	(4.2)
$d_{k,\alpha}$	generalized displ. α of the FE e for deformation mode k in MA3	(3.2)
d_v	distance between two subsequent vehicles of the moving load	(3.4)
$\mathbf{d}_{FE}, \mathbf{d}_{FE,M}, \mathbf{d}_{FE,S}$	total, master and slave generalized displacements in MA3	(3.2)
$\mathbf{d}_y$	displacement of a point in the thickness of a generic element	(3.2)
D	diameter of the cable	(4.3)
D	extensional stiffness coefficient of the equivalent Timoshenko beam	(5.2)
$D^f_{hk}, D^s_{hk}, D^t_{hk}$	flexural, shear and torsional stiffness components of the cross-section	(3.2)
D_i	extensional stiffness coefficient of column i	(5.2)
D_j	non-dimensional parameter of the beam with NES equal to $1+\varepsilon\chi_j$	(3.4)
$D_{\bar{t}}$	Mahalanobis distance	(5.3)
$\mathbf{D}^f, \mathbf{D}^s, \mathbf{D}^t$	flexural, shear and torsional stiffness matrices of the cross-section	(3.2)
e	dynamic unit extension of the cable	(4.2)
$\mathbf{e}_s, \mathbf{e}_y, \mathbf{e}_z$	orthonormal basis for the TWB	(3.2)
E	Young modulus	(3.2-4.2-5.2)
E_e, G_e, m_e	mechanical properties of the elements of the cross-section	(3.2)
EA	axial stiffness of a beam/cable	(3.5-4.2)
EI_1, EI_2	first and second branch stiffness for the bilinear relationship	(3.5)
EI_c	tangent stiffness of the beam at the origin, equal to EI_1	(3.5)
$\mathbb{E}$	derivative of β_1 with respect to τ_1 for the TWB with NES	(3.4)
$f_{s,n_j}, f_{y,n_j}, f_{z,n_j}$	coefficients for the external load in MA1	(3.2)
f_V	non-dimensional effect of the cable on the wake oscillator	(4.3)
$\mathbf{f}$	forces per unit area applied on $\mathcal{S}$ with components f_s, f_y, f_z	(3.2)
$\mathbf{f}_k$	secular terms for the k^{th} vibration mode	(3.5)
$\mathbf{f}_{\bar{t}}$	suspected outliers in the Mahalanobis distance calculation	(5.3)
$\bar{\mathbf{f}}$	mean frequencies in the Mahalanobis distance calculation	(5.3)
F	vertical load per unit length on beam/cable	(3.5-4.2)

F	effect of the cable on the wake oscillator	(4.3)
F_V	vertical punctual load on the beam	(3.5)
$\bar{F}$	parameter introduced for the beam with NES	(3.4)
$\mathbf{F}_H$	forces per unit length applied on $\mathcal{C}$ with compon. F_{Hs}, F_{Hy}, F_{Hz}	(3.2)
g	gravitational acceleration	(3.4-4.2)
G	shear modulus	(3.2-5.2)
h	thickness of the generic element of cross-section	(3.2)
h	dynamic unit tension of the cable	(4.2)
h, h_j	height of floor j	(5.2)
$h_1, \ldots, h_3$	solutions of h (cable) at different time scales	(4.2)
H_k	constant in the symmetric vibration mode k of the cable	(4.2)
$\mathcal{H}$	total energy of the system	(3.2)
i	imaginary unit	(3.4-4.2)
I_x, I_y, I_z	mass inertia moments per unit length	(5.2)
J_i, J_{iy}, J_{iz}	torsional and bending inertia moments of column i	(5.2)
$\mathbf{J}$	Jacobian matrix of the cable	(4.2)
$\mathbf{J_2}$	Jacobian matrix of the SIM in the TWB with NES	(3.4)
k, k_1, k_2, k_{12}	stiffness terms	(3.5)
k_3	elastic coefficient describing the material nonlinearity of the beam	(3.5)
k_{nl}	nonlinear stiffness term	(3.5)
k_N	stiffness of the NES	(3.4)
$\bar{k}$	limit curvature in the bilinear elastic law	(3.5)
$\bar{k}$	prestress curvature of the cable	(4.2)
K_j	beam stiffness matrices projected on mode j	(3.4)
$\mathbf{K}_0, \mathbf{K}_1, \mathbf{K}_2$	stiffness matrices in the homogenization technique	(5.2)
$\mathbf{K}_{0A}, \mathbf{K}_{0B}, \mathbf{K}_{1A}, \mathbf{K}_{1B}$	boundary stiffness matrices in the homogenization technique	(5.2)
$\mathbf{K}_{cs}^e$	EB stiffness matrix of the cross-section for the element e in the PEP	(3.2)
$\mathbf{K}_{cs}$	global EB stiffness matrix of the cross-section in the PEP	(3.2)
$\mathbf{K}_e$	constrained stiffness matrix for the 2^{nd} PEP	(3.2)
$\mathbf{K}_{FE}^e$	stiffness matrix of the generic element in MA3	(3.2)
$\mathbf{K}_{FE}$	global stiffness matrix in MA3	(3.2)
$\mathbf{K}_{FE,r}$	constrained global stiffness matrix in MA3	(3.2)
$\mathbf{K}_{hk}^e$	4×4 stiffness matrix in MA3	(3.2)
$\mathbf{K}_i$	constrained stiffness matrix for the 1^{st} PEP	(3.2)
$\mathbf{K}_{ID}$	stiffness matrix of the 2-d.o.f. system	(3.2)
$\mathbf{K}_j$	beam stiffness matrix in MA1	(3.2)
$\mathbf{K}_w^e$	shear beam stiffness matrix of the c.-s. for the element e in the WEP	(3.2)
$\mathbf{K}_w$	global shear beam stiffness matrix of the cross-section in the WEP	(3.2)

$\mathbf{K}_{Wa}, \mathbf{K}_{Wb}$	stiffness matrices for shear modes in MA1	(3.2)
$\mathbf{K}_{\Omega a}, \mathbf{K}_{\Omega b}$	stiffness matrices for conv. and ext. modes in MA1	(3.2)
$\mathbf{K}_T$	Timoshenko beam stiffness matrix in FD	(5.2)
L	length of a beam/cable	(3.2-4.2)
m	mass per unit area	(3.2)
m	mass per unit length	(4.2-5.2)
m_1, m_2	mass terms of discrete systems	(3.5)
m_i	mass per unit length of the column i	(5.2)
m_N	mass of the NES	(3.4)
M_e, M_u	first branch and ultimate limit moments for the bilinear law	(3.5)
M_{hk}	in-plane mass component of the cross-section	(3.2)
M_j	beam mass matrices projected on mode j	(3.4)
M_x, M_y, M_z	torsional and bending moments	(5.2)
$\mathbf{M}$	mass matrix in the homogenization technique	(5.2)
$\mathbf{M}$	in-plane mass matrix of the cross-section	(3.2)
$\mathbf{M}_{cs}^e$	EB mass matrix of the cross-section for the element e in the PEP	(3.2)
$\mathbf{M}_{cs}$	global EB mass matrix of the cross-section in the PEP	(3.2)
$\mathbf{M}_e$	constrained mass matrix for the 2^{nd} PEP	(3.2)
$\mathbf{M}_{FE}^e$	mass matrix of the generic element in MA3	(3.2)
$\mathbf{M}_{FE}$	global mass matrix in MA3	(3.2)
$\mathbf{M}_{FE,r}$	constrained global mass matrix in MA3	(3.2)
$\mathbf{M}_{hk}^e$	4×4 mass matrix in MA3	(3.2)
$\mathbf{M}_i$	constrained mass matrix for the 1^{st} PEP	(3.2)
$\mathbf{M}_{ID}$	mass matrix of the 2-d.o.f. system	(3.2)
$\mathbf{M}_j$	beam mass matrix in MA1	(3.2)
$\mathbf{M}_w^e$	shear beam mass matrix of the c.s. for the element e in the WEP	(3.2)
$\mathbf{M}_w$	global shear beam mass matrix of the cross-section in the WEP	(3.2)
$\mathbf{M}_T$	Timoshenko beam mass matrix in FD	(5.2)
n_c	number of punctual restraints in MA3	(3.2)
n_d	number of deformation modes considered in the member analysis	(3.2)
n_e	total number of elements of the cross-section	(3.2)
n_i	number of beam elements of length $\Delta = L/n_i$ in FD	(5.2)
n_i^j	number of constant beam elements of length $\Delta_j = h_j/n_i^j$ in FD	(5.2)
n_j	longitudinal half-wave number of the j^{th} vibration mode	(3.2)
n_L	number of piecewise constant elements of Timoshenko beam	(5.2)
n_n	total number of nodes of the cross-section	(3.2)
n_v	total number of vibration modes in MA1	(3.2)
n_z	total number of nodes along z in MA3	(3.2)

N	axial stress	(5.2)
N_1, N_2	amplitudes of β_1, β_2 in polar form	(3.4)
N_c	number of columns of a cell	(5.2)
N_j	maximum half-wave number considered in MA1	(3.2)
N_T	total number of d.o.f. of the unrestrained cross-section	(3.2)
N_v	number of vehicles of the moving load	(3.4)
p_v	transversal (in-plane) distributed load on the cable	(4.2)
p_w	transversal (out-of-plane) distributed load on the cable	(4.2)
$p_{\Omega h}, p_{Wh}$	components of the field loads acting on the cross-section	(3.2)
$\mathbf{p}$	external forces (and inertia terms) with components p_x, p_y, p_z	(5.2)
$\mathbf{p}, \mathbf{P}_H$	external loads in the current configuration of the cable	(4.2)
$\bar{\mathbf{p}}, \bar{\mathbf{P}}_H$	external loads in the reference configuration of the cable	(4.2)
$\mathbf{p}_\Omega, \mathbf{p}_W$	field loads acting on the cross-section	(3.2)
$\mathbf{p}_{\Omega,n_j}, \mathbf{p}_{W,n_j}$	field loads acting on the cross-section in MA1	(3.2)
$\mathbf{p}_\Omega^0$	field load $\mathbf{p}_\Omega$ considered for the TWB with NES	(3.4)
$P_{Mh}, P_{Wh}, P_{\Omega h}$	components of the end-sections loads acting on the cross-section	(3.2)
$\mathbf{P}_{FE}^e$	loads acting on the generic element in MA3	(3.2)
$\mathbf{P}_{FE}$	global load vector in MA3	(3.2)
$\mathbf{P}_{FE,r}$	constrained global load vector in MA3	(3.2)
$\mathbf{P}_h^e$	4×1 load vector in MA3	(3.2)
$\mathbf{P}_M, \mathbf{P}_W, \mathbf{P}_\Omega$	end-sections loads acting on the cross-section	(3.2)
q	wake oscillator variable	(4.3)
$q_0, \ldots, q_2$	solutions of q (wake oscillator) at different time scales	(4.3)
$\mathbf{q}_e, \mathbf{q}_{eM}, \mathbf{q}_{eS}$	total, master and slave d.o.f. for the 2^{nd} PEP	(3.2)
$\mathbf{q}_i, \mathbf{q}_{iM}, \mathbf{q}_{iS}$	total, master and slave d.o.f. for the 1^{st} PEP	(3.2)
$\mathbf{q}_w$	d.o.f. for the WEP	(3.2)
Q_{hk}^m	out-of-plane mass component of the cross-section	(3.2)
Q_k	amplitude of the generating solution (wake)	(4.3)
Q_k^l	tangential stress flow for the cross-section analysis	(3.2)
Q_{x_k}	amplitude of the signal z_k whose real part is x_k	(3.5)
$\mathbf{Q}^m$	out-of-plane mass matrix of the cross-section	(3.2)
$\mathbf{Q}_i, \mathbf{Q}_{iM}, \mathbf{Q}_{iS}$	total, master and slave coefficient matrices in the 2^{nd} PEP	(3.2)
r_1	displacement of the center of mass of the beam with the NES	(3.4)
r_2	relative displacement between beam and NES	(3.4)
Re	Reynolds' number	(4.3)
$\mathbf{R}_e$	constraint matrix for the extensional (2^{nd}) PEP	(3.2)
$\mathbf{R}_i$	constraint matrix for the inextensional (1^{st}) PEP	(3.2)
s	tangential coordinate of TWB	(3.2)

s	curvilinear abscissa of the cable	(4.2)
s_V	non-dimensional effect of the wake oscillator on the cable	(4.3)
$\mathbf{s}, \hat{\mathbf{s}}$	settlements in MA3	(3.2)
S	effect of the wake oscillator on the cable	(4.3)
S_{iy}, S_{iz}	shear stiffness coefficients of column i	(5.2)
S_y, S_z	equivalent shear stiffness coefficients	(5.2)
St	Strouhal number	(4.3)
$\mathbf{S}$	covariance matrix	(5.3)
$\mathcal{S}$	middle surface of TWB	(3.2)
$\mathbb{S}$	Slow Invariant Manifold	(3.4)
t	time	(3.2-4.2-5.2)
t_j	arriving time of the j^{th} moving load on the beam	(3.4)
$\mathbf{t}$	internal stresses in the current configuration of the cable	(4.2)
$\bar{\mathbf{t}}$	internal stresses in the reference configuration of the cable	(4.2)
T_i	time scale i in MSM	(3.5-4.2)
T_y, T_z	shear stresses	(5.2)
$\bar{T}$	prestress of the cable	(4.2)
$\mathcal{T}$	kinetic energy	(3.2)
u	displacement at the middle surface $\mathcal{S}$ along s	(3.2)
(u_i, v_i)	in-plane displacements of node i of the cross-section in (x_e, y_e)	(3.2)
$\bar{u}_k$	component of the k^{th} deformation mode of the cross-section along s	(3.2)
$\mathbf{u}$	vector of displacement at the middle surface $\mathcal{S}$	(3.2)
$\mathbf{u}$	displacement vector of components u, v, w	(4.2-5.2)
$\bar{\mathbf{u}}$	deformation modes of the cross-section along s	(3.2)
$\hat{\mathbf{u}}_i$	vector of displacements at node i of the beam in FD	(5.2)
$\hat{\mathbf{u}}_{j,i}$	vector of displacements at node i of constant element j in FD	(5.2)
$\hat{\mathbf{u}}_T$	vector of total displacements of the Timoshenko beam in FD	(5.2)
U	wind velocity	(4.3)
(U_i, V_i)	in-plane displacements of node i of the cross-section in (X, Y)	(3.2)
$\mathcal{U}$	elastic energy of the cell	(5.2)
$\mathcal{U}_e$	elastic potential energy	(3.2)
$\mathcal{U}_i$	elastic energy of column i	(5.2)
$\mathcal{U}_l$	potential energy of conservative external loads	(3.2)
v	displacement at the middle surface $\mathcal{S}$ along y	(3.2)
v	transversal (in-plane) displacement of the cable	(4.2)
$v_1, \ldots, v_3$	solutions of v (cable) at different time scales	(4.2)
$v_g, \ddot{v}_g$	vertical ground displacement and acceleration due to the earthquake	(3.4)
$\bar{v}_k$	component of the k^{th} deformation mode of the cross-section along y	(3.2)

v_v	speed of vehicles of the moving load	(3.4)
$\mathbf{v}_k$	right k^{th} eigenvector with components $(v_{k,x}, v_{k,y})$	(3.5)
$\bar{\mathbf{v}}$	deformation modes of the cross-section along y	(3.2)
$\mathcal{V}$	total volume of TWB	(3.2)
w	displacement at the middle surface $\mathcal{S}$ along z	(3.2)
w	vertical displacement of the EB beam	(3.5)
w	transversal (out-of-plane) displacement of the cable	(4.2)
w_0, w_1	solutions of displacement w (beam) at different time scales	(3.5)
$\bar{w}_j$	compon. of the j^{th} shear deform. mode of the cross-section along z	(3.2)
w''_e, w''_u	first branch and ultimate curvatures for the bilinear law	(3.5)
$\bar{\mathbf{w}}$	shear deformation modes of the cross-section along z	(3.2)
x	d.o.f. of discrete systems or name of the generic signal	(3.5)
x	longitudinal coordinate of the EB beam	(3.5)
x	longitudinal coordinate of 3D frame and Timoshenko beam	(5.2)
x_0, x_1	solutions of the d.o.f. x at different time scales	(3.5)
(x_e, y_e)	local reference systems of the generic element of the cross-section	(3.2)
x_k	k^{th} IMF obtained from the EMD of the signal x	(3.5)
x_V	application point of the punctual force F_V	(3.5)
$\hat{x}, \hat{y}$	initial conditions of the 2-d.o.f. system	(3.5)
$\mathbf{x}, \bar{\mathbf{x}}$	position of a point on the cable in $\mathcal{C}, \bar{\mathcal{C}}$ configurations	(4.2)
$\mathbf{x}_0$	vector of the the discrete system with components x_0, y_0	(3.5)
(X, Y)	global reference systems of the cross-section of TWB	(3.2)
$\hat{X}, \hat{Y}$	initial conditions of the 2-d.o.f. system	(3.5)
y	transversal coordinate of TWB	(3.2)
y	d.o.f. of discrete systems	(3.5)
y	in-plane coordinate of 3D frame and Timoshenko beam	(5.2)
y_0, y_1	solutions of the d.o.f. y at different time scales	(3.5)
y_E, z_E	coordinates of the center of extensional stiffness	(5.2)
y_i, z_i	coordinates of the generic column i	(5.2)
y_k	Hilbert Transform of the mono-component signal x_k	(3.5)
y_N	absolute vertical displacement of the NES	(3.4)
y_S, z_S	coordinates of the center of shear stiffness	(5.2)
Y_j	time response relative to the j^{th} vibration mode in MA1	(3.2)
$\mathbf{Y}$	n_v-column vector representing the time response in MA1	(3.2)
z	longitudinal coordinate of TWB	(3.2)
z	in-plane coordinate of 3D frame and Timoshenko beam	(5.2)
z_k	complex signal obtained from x_k and y_k	(3.5)
z_k	amplitude of signal in polar form (wake)	(4.3)

z_N	position of the NES along the beam axis	(3.4)
$\mathbf{Z}$	Jacobian matrix of the TWB with NES	(3.4)

α	non-dimensional term related to the geometric nonlinearity	(3.5)
α	van der Pol parameter of the wake oscillator	(4.3)
α_e	angle between X and the direction of the cross-section element e	(3.2)
α_{iy}, α_{iz}	ratio between bending and shear stiffness of column i	(5.2)
$\beta, \beta_k, \beta_{x_k}$	phase of the signal in polar form	(3.5-4.2)
β_1, β_2	complex variables by Manevitch for the beam with the NES	(3.4)
γ	stall term related to the wind action	(4.3)
γ_k	phase of the signal in polar form in presence of resonant load	(3.5-4.2)
γ_y, γ_z	shear strains	(5.2)
$\bar{\gamma}$	parameter introduced for the beam with NES	(3.4)
Γ	non-dimensional external load on the TWB with NES	(3.4)
Γ_p	amplitude of the non-dimensional load on the TWB with NES	(3.4)
$\mathbf{\Gamma}_{FE}$	constraint matrix for the FEA of MA3	(3.2)
δ	variation or Dirac's delta (based on context)	(3.2-3.4)
δ_1, δ_2	phase of β_1, β_2 in polar form	(3.4)
ε	mass ratio	(3.4)
ε	bookkeeping parameter	(3.5-4.2)
ε	unit extension	(5.2)
$\varepsilon_s^f, \varepsilon_z^f, \gamma_{zs}^f$	flexural strain field of TWB	(3.2)
$\varepsilon_s^m, \varepsilon_z^m, \gamma_{zs}^m$	membrane strain field of TWB	(3.2)
η_{20}, η_{22}	shape corrections of the cable	(4.2)
$\boldsymbol{\eta}$	vector of parameters in the parameter identifications	(3.5-4.4)
θ_i	rotation of node i of the cross-section	(3.2)
θ_k	phase of the signal in polar form (wake)	(4.3)
θ_{x_k}	instantaneous frequency of the signal z_k whose real part is x_k	(3.5)
$\boldsymbol{\theta}$	rotation vector of components $\theta_x, \theta_y, \theta_z$	(5.2)
$\mathbf{\Theta}_j$	magnitude of the j^{th} vibration mode in MA1	(3.2)
$\kappa_x, \kappa_y, \kappa_z$	torsional and bending curvatures	(5.2)
λ, λ_k	eigenvalue	(3.2-4.2-5.2)
λ^2	Irvine's parameter of the cable	(4.2)
ν	Poisson's ratio	(3.2)
ξ	non-dimensional damping coefficient	(3.5)
ξ_j	modal damping coefficient	(3.4)
ρ	mass per unit length	(3.5)
ρ	density of the fluid (air)	(4.3)
ρ_c	specific weight of reinforced concrete	(3.2)

σ	detuning parameter (angular frequency)	(3.4-4.2)
$\sigma_s^f, \sigma_z^f, \tau_{zs}^f$	flexural stress field	(3.2)
$\sigma_s^m, \sigma_z^m, \tau_{zs}^m$	membrane stress field	(3.2)
τ	non-dimensional time	(3.4-4.2)
τ_i	i^{th} time scale of MSM	(3.4)
φ_k	component of the k^{th} conventional or extensional amplitude function	(4.2)
φ_k	vibration mode of the linear beam/cable	(3.5-4.2)
ϕ_b	elastic potential energy density of the Timoshenko beam	(5.2)
ϕ_{x_k}	phase of the signal z_k whose real part is x_k	(3.5)
$\boldsymbol{\varphi}$	conventional or extensional amplitude functions	(3.2)
$\bar{\boldsymbol{\varphi}}_1, \dots, \bar{\boldsymbol{\varphi}}_4$	amplitude functions for the bvp of MA2	(3.2)
$\boldsymbol{\varphi}_j$	amplitude funct. of TWB associated to the j^{th} vibr. mode in MA1	(3.2)
$\mathbf{\Phi}$	matrix accounting for deformation and vibration modes in MA1	(3.2)
$\mathbf{\Phi}_j$	n_d-column vect. of the long. evolution of the j^{th} vibr. mode in MA1	(3.2)
χ	non-dimensional term related to the material nonlinearity	(3.5)
χ_{20}, χ_{22}	shape corrections of the cable	(4.2)
χ_j	non-dimensional parameter introduced for the beam with the NES	(3.4)
ψ_{x_k}	slow component of Ψ_{x_k} in Cx-A	(3.5)
Ψ_1, Ψ_2	linear interpolation functions	(3.2)
$\Psi_3, \dots, \Psi_6$	cubic interpolation functions	(3.2)
Ψ_j	component of the j^{th} shear amplitude function	(3.2)
Ψ_{x_k}	complex variable by Manevitch in Cx-A	(3.5)
$\mathbf{\Psi}$	shear amplitude functions	(3.2)
ω, ω_k	angular frequency of linear systems	(3.5-4.2)
ω_j	angular frequency associated to the j^{th} vibration mode in MA1	(3.2)
$\bar{\omega}$	reference angular frequency of the beam/cable	(3.5-4.2)
Ω_F	angular frequency of the external load	(3.4-4.2)
Ω_k	component of the k^{th} conventional mode of the cross-section along z	(3.2)
Ω_R	non-dimensional angular frequency of the external load	(3.4-4.2)
$\mathbf{\Omega}$	conventional modes of the cross-section along z	(3.2)

$(\cdot)^T$	transpose	(-)
$(\cdot)'$	space derivative	(-)
$\dot{(\cdot)}$, d/dt	time derivative	(-)
$\bar{(\cdot)}$	complex conjugate	(-)
D_i	derivative with respect to the time scale T_i	(-)
$(\cdot)_{,s}, (\cdot)_{,z}$	derivative with respect to s or z	(3.2)
$(\cdot)_H$, $(\cdot)_F$	properties of column evaluated at its head (top) or foot (bottom)	(5.2)

[Blank page]

List of Publications

- A. De Flaviis, A. Ture Savadkoohi and D. Zulli. Passive vibration control of a beam modeled through Generalized Beam Theory using a Nonlinear Energy Sink under different loading scenarios. *European Journal of Mechanics - A/Solids*, 111:105552, 2025.

  `https://doi.org/10.1016/j.euromechsol.2024.105552`

- A. De Flaviis, R. Alaggio and D. Zulli. Generalized Beam Theory for the static and dynamic response of a bridge deck with Structural Health Monitoring purposes. *Procedia Structural Integrity*, 62:871 – 878, 2024. Proceedings of the 2nd Fabre Conference. Genova, Italy, 2024.

  `https://doi.org/10.1016/j.prostr.2024.09.117`

[Blank page]

Appendix A

A short description of the identification procedure using Cx-A is given here. For a detailed discussion, it is possible to refer to [65].

A.1 Discrete systems

A general m-d.o.f. dynamical system with cubic nonlinearity is considered as:

$$\mathbf{M}\ddot{\mathbf{x}} + \mathbf{C}\dot{\mathbf{x}} + \mathbf{K}\mathbf{x} + \mathbf{n}_3\left(\mathbf{x}, \mathbf{x}, \mathbf{x}\right) = \mathbf{F} \tag{A.1}$$

where $\mathbf{M}$, $\mathbf{C}$ and $\mathbf{K}$ are mass, damping and stiffness matrices respectively, $\mathbf{n}_3$ is the nonlinear cubic column vector, $\mathbf{F}$ is the vector of external loads, if present, and the vector $\mathbf{x}$ contains the m variables $\mathbf{x} = (x, y, z, \ldots)^T$. The generic variable x can be written as $x(t) = \sum_{k=1}^{m} x_k(t)$, being k the k-th monochromatic component of the signal, of frequency ω_k. Complex variables by Manevitch [87] are introduced as:

$$\Psi_{x_k}(t) = \dot{x}_k(t) + i\omega_k x_k(t) \tag{A.2}$$

and the decomposition of dynamics into slow and fast components is realized, as:

$$\Psi_{x_k}(t) = \psi_{x_k}(t)e^{i\omega_k t} \tag{A.3}$$

being $\psi_{x_k}(t)$ the slow component; then, averaging is realized over the fast frequency components $e^{i\omega_k t}$ and polar form is introduced as:

$$\psi_{x_k}(t) = a_{x_k}(t)e^{i\beta_{x_k}(t)} \tag{A.4}$$

to explicitly express amplitude $a_{x_k}(t)$ and phase $\beta_{x_k}(t)$, thus getting m AME. Then, the real and imaginary parts of the AME are written to obtain real-terms equations.

To identify the systems parameters, the real-terms AME are rewritten as $\mathbf{A}\boldsymbol{\eta} = \mathbf{b}$, where $\boldsymbol{\eta}$ is the vector of unknown parameters, which in this case contains linear and nonlinear stiffness and damping coefficients. Making use of Eq. (A.3) and Eq. (A.4), one can write:

$$\Psi_{x_k}(t) = a_{x_k}(t)e^{i(\omega_k t+\beta_{x_k}(t))} \tag{A.5}$$

Taking advantage of complex variables, thus using Eq. (A.2), the modal component k of the degree-of-freedom x can be written as $x_k = \dfrac{\Psi_{x_k} - \bar{\Psi}_{x_k}}{2i\omega_k}$ which, together with Eq. (A.5), gives:

$$x_k(t) = \frac{a_{x_k}(t)}{\omega_k}\sin\left(\omega_k t + \beta_{x_k}(t)\right) \tag{A.6}$$

As it was stated in [65], both HHT and Cx-A expand the multi-frequency signal in mono-component modes related to fast-frequency components. Thus, comparing the expression of $x_k(t)$ written in Eq. (A.6) to the analytical signal of Eq. (3.135), one gets the known correspondence between the two methods:

$$\begin{cases} a_{x_k}(t) = Q_{x_k}(t)\omega_k \\ \beta_{x_k}(t) = \phi_{x_k}(t) - \omega_k t + \dfrac{\pi}{2} \to \dot{\beta}_{x_k}(t) = \theta_{x_k}(t) - \omega_k \end{cases} \tag{A.7}$$

A.2 1-d.o.f. system results

The 1-d.o.f. dynamical system of Eq. (3.138), already studied in [65] is considered and the Cx-A is applied for comparison. The matrix of coefficients $\mathbf{A}$, which can be found in the original paper, obtained through the procedure described in this Appendix, can be pseudo-inverted to find the unknown parameters in Eq. (3.138). Results are reported in Tab. A.1 where the numerical solution was found by applying a non-zero i.c. on x. It can be seen that all parameters are well identified for different values of initial conditions, with a maximum difference of 8.5% on c.

Table A.1. Parameter identification for the 1-d.o.f. system of Eq. (3.138) using HHT+Cx-A.

	k (N/m)	k_{nl} (N/m^3)	c (Ns/m)
Real values	1.000	1.000	0.100
Identified values for $x(0) = 1.0$ m	0.997	0.954	0.098
Real values	1.000	2.000	0.050
Identified values for $x(0) = 0.5$ m	0.997	2.021	0.046

A.3 2-d.o.f. system results

The 2-d.o.f. dynamical system of Eq. (3.155), already studied in [65] is considered and the Cx-A is applied for comparison. The matrix of coefficients **A**, written in the original paper, can be pseudo-inverted to find the unknown parameters for the 2-d.o.f. case. Results are reported in Tab. A.2, where the numerical solution was found by applying a non-zero i.c. either on x, $\dot{x}$ or y. It can be seen that all parameters are well identified in all investigated cases, with a maximum difference of 38.7% on c_1 in the last case.

Table A.2. Parameter identification for the 2-d.o.f. system of Eq. (3.155) using HHT+Cx-A.

	m_1 (kg)	m_2 (kg)	k_1 (N/m)	k_2 (N/m)	k_{12} (N/m)	k_{nl} (N/m^3)	c_1 (Ns/m)	c_2 (Ns/m)	c_{12} (Ns/m)
Real values	1.000	1.000	1.000	1.000	1.000	2.000	0.050	0.050	0.000
Identified values for $x(0) = 1.0$ m	-	-	1.005	0.986	1.006	2.021	0.050	0.051	-0.001
Identified values for $y(0) = 0.5$ m	-	-	1.007	0.990	1.001	2.130	0.049	0.052	0.000
Identified values for $\dot{x}(0) = 1.0$ m/s	-	-	1.067	0.980	0.979	2.035	0.049	0.050	0.002
Real values	1.000	1.000	1.000	2.000	2.000	3.000	0.050	0.050	0.010
Identified values for $x(0) = 0.5$ m	-	-	1.011	1.982	2.010	3.025	0.050	0.054	0.008
Real values	1.000	1.300	2.000	1.000	1.000	5.000	0.050	0.030	0.000
Identified values for $x(0) = 0.5$ m	-	-	2.037	1.022	0.996	4.917	0.031	0.031	0.008

[Blank page]

Appendix B

This appendix clarifies the way the homogenization procedure between the three-dimensional frame and the equivalent Timoshenko beam is carried out and in which way the constitutive law of Eq. (5.9) is derived. This appendix is part of the homogenization formulation developed in [108].

B.1 Analysis of the single elastic column

First of all, a generic elastic column i of a generic floor j is investigated, in order to find its elastic stiffness coefficients.

The generic element i with length h_j (equal to the height of the floor) is considered with the same axes $(\mathbf{a}_x, \mathbf{a}_y, \mathbf{a}_z)$ already introduced in Sect. 5.2. The column is considered to be clamped at both ends (between two floors), subjected to an applied displacement and rotation field at its head (H), while no settlement occurs at its foot (F), as:

$$\mathbf{u}_{H_{i,j}} = u_{H_i}\mathbf{a}_x + v_{H_i}\mathbf{a}_y + w_{H_i}\mathbf{a}_z \tag{B.1}$$

$$\boldsymbol{\theta}_{H_{i,j}} = \theta_{xH_i}\mathbf{a}_x + \theta_{yH_i}\mathbf{a}_y + \theta_{zH_i}\mathbf{a}_z \tag{B.2}$$

where the subscript j is not repeated in the components to streamline the notation. Using the three-dimensional Timoshenko beam model, this assigned displacement produces a certain displacement field $(u_i(x),\ v_i(x),\ w_i(x),\ \theta_{xi}(x),\ \theta_{yi}(x),\ \theta_{zi}(x))$ whose expression can be found in the original paper, being x the longitudinal coordinate going from F to H as usual.

Then the strain field $(\varepsilon_i(x),\ \gamma_{yi}(x),\ \gamma_{zi}(x),\ \kappa_{xi}(x),\ \kappa_{yi}(x),\ \kappa_{zi}(x))$ can be derived through Eq. (5.3) from the displacement field and its expression is once again written in [108].

At this point, with the goal of deriving the stiffness coefficients of this Timoshenko beam, representative of the single columns clamped between two floors, it is possible to express the elastic energy of the column i as:

$$\mathcal{U}_i = \frac{1}{2}\int_0^{h_j} \left(EA_i\varepsilon_i^2 + GA_{iy}\gamma_{yi}^2 + GA_{iz}\gamma_{zi}^2 + GJ_i\kappa_{xi}^2 + EJ_{iy}\kappa_{yi}^2 + EJ_{iz}\kappa_{zi}^2\right) dx \tag{B.3}$$

where E and G are the Young and shear modulus (in N/m^2), A_i is the cross-section area (in m^2), A_{iy} and A_{iz} are the shear cross-section area along y and z, J_i is the torsional cross-section inertia and J_{iy} and J_{iz} are the bending cross-section inertia moments (in m^4) with respect to y and z respectively.

Once the strain field (here not reported) is substituted into Eq. (B.3), the elastic energy becomes:

$$\begin{aligned}\mathcal{U}_i = \frac{1}{2}\Big[&D_i u_{H_i}^2 + S_{iy}v_{H_i}^2 + S_{iz}w_{H_i}^2 + C_i\theta_{xH_i}^2 \\ &+\frac{(4+\alpha_{iy})}{(1+\alpha_{iy})}B_{iy}\theta_{yH_i}^2 + \frac{(4+\alpha_{iz})}{(1+\alpha_{iz})}B_{iz}\theta_{zH_i}^2 - S_{iy}hv_{H_i}\theta_{zH_i} + S_{iz}hw_{H_i}\theta_{yH_i}\Big]\end{aligned} \tag{B.4}$$

where the expressions of the different element stiffness coefficients are:

$$\begin{aligned}&D_i = \frac{EA_i}{h_j};\\ &S_{iy} = \frac{12EJ_{iz}}{(1+\alpha_{iz})\,h_j^3}; \quad S_{iz} = \frac{12EJ_{iy}}{(1+\alpha_{iy})\,h_j^3};\\ &C_i = \frac{GJ_i}{h_j};\\ &B_{iy} = \frac{EJ_{iy}}{h_j}; \quad B_{iz} = \frac{EJ_{iz}}{h_j}\end{aligned} \tag{B.5}$$

and the coefficients α_{iy} and α_{iz} representative of the ratio between bending and shear stiffness of the single columns are:

$$\alpha_{iy} = \frac{12EJ_{iz}}{GA_{iy}h_j^2}; \quad \alpha_{iz} = \frac{12EJ_{iy}}{GA_{iz}h_j^2} \tag{B.6}$$

B.2 Analysis of the cell

Once the single elastic column is analyzed, it is possible to analyze the cell which is made up of all the columns between two consecutive floors. It is considered that the upper floor undergoes a relative displacement (translation and rotation) with respect to the lower one equal to:

$$\mathbf{u}_G = u_G \mathbf{a}_x + v_G \mathbf{a}_y + w_G \mathbf{a}_z \tag{B.7}$$

$$\boldsymbol{\theta} = \theta_x \mathbf{a}_x + \theta_y \mathbf{a}_y + \theta_z \mathbf{a}_z \tag{B.8}$$

Making the fundamental hypothesis that all floors are rigid in and out-of-plane, the displacements at the head (H) of the generic column i can be written as:

$$\begin{aligned} u_{H_i} &= u_G - \theta_z y_i + \theta_y z_i \\ v_{H_i} &= v_G - \theta_x z_i \\ w_{H_i} &= w_G + \theta_x y_i \\ \theta_{xH_i} &= \theta_x \\ \theta_{yH_i} &= \theta_y \\ \theta_{zH_i} &= \theta_z \end{aligned} \tag{B.9}$$

Thus, the global elastic energy of the cell made up of N_c columns can be obtained recalling Eq. (B.4) as:

$$\begin{aligned} \mathcal{U} = \sum_{i=1}^{N_c} \mathcal{U}_i = \frac{1}{2} \sum_{i=1}^{N_c} & \left[D_i (u_G - \theta_z y_i + \theta_y z_i)^2 + S_{iy} (v_G - \theta_x z_i)^2 + S_{iz} (w_G + \theta_x y_i)^2 \right. \\ & + C_i \theta_x^2 + \frac{(4 + \alpha_{iy})}{(1 + \alpha_{iy})} B_{iy} \theta_y^2 + \frac{(4 + \alpha_{iz})}{(1 + \alpha_{iz})} B_{iz} \theta_z^2 \\ & \left. - S_{iy} h_j (v_G - \theta_x z_i) \theta_z + S_{iz} h_j (w_G + \theta_x y_i) \theta_y \right] \end{aligned} \tag{B.10}$$

B.3 Homogenization procedure

In order to represent the cell j as an element of Timoshenko beam, it has to be imposed that the elastic energy of the cell and that of the segment of beam having the same length h_j are equal when subjected to the same relative displacement. In case rigid floors are considered, the relative displacement is chosen considering a constant strain field on the beam element: this hypothesis is true for the cell when the variables under consideration vary at a (much) larger scale than the length of the cell itself. Thus, from Eq. (5.3), the displacement field of the beam element reads:

$$
\begin{aligned}
u_G &= \varepsilon h_j \\
v_G &= \gamma_y h_j + \kappa_z h_j^2/2 \\
w_G &= \gamma_z h_j - \kappa_y h_j^2/2 \\
\theta_x &= \kappa_x h_j \\
\theta_y &= \kappa_y h_j \\
\theta_z &= \kappa_z h_j
\end{aligned} \tag{B.11}
$$

The substitution of Eq. (B.11) inside Eq. (B.10) once the elastic energy per unit length (also known as elastic energy density) $\phi_b = \mathcal{U}/h_j$ is defined, leads to:

$$
\begin{aligned}
\phi_b = \frac{h_j}{2} &\left(D\varepsilon^2 + S_y\gamma_y^2 + S_z\gamma_z^2 + C\kappa_x^2 + B_y\kappa_y^2 + B_z\kappa_z^2\right. \\
&\left.+2Dz_E\varepsilon\kappa_y - 2Dy_E\varepsilon\kappa_z - 2S_yz_S\kappa_x\gamma_y + 2S_zy_S\kappa_x\gamma_z - 2B_{yz}\kappa_y\kappa_z\right)
\end{aligned} \tag{B.12}
$$

where the stiffness coefficients of the Timoshenko beam, with the same meaning of before, are:

$$
\begin{aligned}
&D = \sum_{i=1}^{N_c} D_i; \\
&S_y = \sum_{i=1}^{N_c} S_{iy}; \quad S_z = \sum_{i=1}^{N_c} S_{iz}; \\
&C = \sum_{i=1}^{N_c} \left(C_i + S_{iz}y_i^2 + S_{iy}z_i^2\right); \\
&B_y = \sum_{i=1}^{N_c} \left(B_{iy} + D_iz_i^2\right); \quad B_z = \sum_{i=1}^{N_c} \left(B_{iz} + D_iy_i^2\right); \quad B_{yz} = \sum_{i=1}^{N_c} D_iy_iz_i
\end{aligned} \tag{B.13}
$$

and the coordinates of the extensional centroid E and of the shear centroid S are found as:

$$
y_E = \frac{\sum_{i=1}^{N_c} D_iy_i}{D}; \quad z_E = \frac{\sum_{i=1}^{N_c} D_iz_i}{D} \tag{B.14}
$$

$$
y_S = \frac{\sum_{i=1}^{N_c} S_{iz}y_i}{S_z}; \quad z_S = \frac{\sum_{i=1}^{N_c} S_{iy}z_i}{S_y} \tag{B.15}
$$

At this point, in order to assume that the beam has a linear hyperelastic law, one can postulate the existence of an elastic potential energy density $\phi_b = \phi_b(\varepsilon, \gamma_y, \gamma_z, \kappa_x, \kappa_y, \kappa_z)$ and derive the stress field from it as $\left(N = \dfrac{\partial\phi_b}{\partial\varepsilon}, \ldots, M_z = \dfrac{\partial\phi_b}{\partial\kappa_z}\right)$

which finally gives the searched constitutive law of Eq. (5.9).

Tesi redatta con il cofinanziamento dell'Unione europea-*NextGeneration EU*
Piano Nazionale di Ripresa e Resilienza Missione 4, Componente 2 –
Investimento 3.3. del PNRR – "Dottorati innovativi che rispondono ai fabbisogni di innovazione delle imprese" – CUP E11I22000190001

Finanziato dall'Unione europea NextGenerationEU
Ministero dell'Università e della Ricerca
Italiadomani PIANO NAZIONALE DI RIPRESA E RESILIENZA
UNIVERSITÀ DEGLI STUDI DELL'AQUILA